Plasma Physics Reports, Vol. 27, No. 5, 2001, pp. 363–371. Translated from Fizika Plazmy, Vol. 27, No. 5, 2001, pp. 387–396.

PARTICLE ACCELERATION IN PLASMA

Computer Simulation of the Three-Dimensional Regime of Proton Acceleration in the Interaction of Laser Radiation with a Thin Spherical Target

H. Ruhl*, S. V. Bulanov, T. E. Cowan***, T. V. Liseĭkina****, P. Nickles*, F. Pegoraro*****, M. Roth******, and W. Sandner***

**Max-Born Institute, Max-Born Str. 2a, 12489 Berlin, Germany*

***Institute of General Physics, Russian Academy of Sciences, ul. Vavilova 38, Moscow, 117942 Russia*

****Lawrence Livermore National Laboratory, 5000 East Avenue, Livermore, CA 94550, P.O. Box 808, USA*

*****Institute of Computation Technologies, Siberian Division, Russian Academy of Sciences, ul. Lavrent'eva 6, Novosibirsk, 630090 Russia*

******Istituto Nazionale Fisica della Materia, Sez. 2, Piazza Torricelli, Pisa, Italy*

*******Gesellschaft für Schwerionenforschung mbH, Planckstrasse 1, D-64291 Darmstadt, Germany*

Received July 20, 2000; in final form, October 30, 2000

Abstract—Results from particle-in-cell simulations of the three-dimensional regime of proton acceleration in the interaction of laser radiation with a thin spherical target are presented. It is shown that the density of accelerated protons can be several times higher than that in conventional accelerators. The focusing of fast protons created in the interaction of laser radiation with a spherical target is demonstrated. The focal spot of fast protons is localized near the center of the sphere. The conversion efficiency of laser energy into fast ion energy attains 5%. The acceleration mechanism is analyzed and the electron and proton energy spectra are obtained. *© 2001 MAIK "Nauka/Interperiodica".*

1. INTRODUCTION

The development of laser technology has made it possible to create table-top superintense lasers, which may find applications in the field of charged-particle acceleration, nuclear fusion research, and medicine [1–5]. One of the most important applications is related to the acceleration of dense proton beams by ultraintense laser radiation. As was shown previously in two- and three-dimensional computer simulations of the interaction of laser radiation with thin dense targets [6–8], the ions are accelerated most efficiently at the back side of the target in the laser-pulse propagation direction. High-energy ions accelerated at the rare side of a thin foil were observed experimentally in [9]. Previous investigations showed that optimum conditions for efficient proton acceleration are created in a slab of marginally underdense plasma with a thickness of several tens of laser wavelengths [6–8, 10] or in a thin dense target (foil) with a thickness of several laser wavelengths [6–8]. This means that only the leading part of the pulse causes the generation of fast particles. Therefore, ultrashort (femtosecond) laser pulses seem to be the most appropriate for proton acceleration. This circumstance initiated a discussion of the modified fast ignition concept [11–13]. Recall that, according to the fast ignition concept, first formulated by Tabak *et al.* [2], the thermonuclear fuel is initially compressed by a long laser pulse up to a high density at a relatively low temperature. Then, a small fraction of compressed fuel is rapidly heated to the ignition temperature. The fast ignition concept implies that the thermonuclear reaction is ignited in the final stage of compression by relativistic electrons accelerated by a petawatt laser pulse (the third pulse) in a dense target, into which laser radiation penetrates through a thin channel produced by the second laser pulse. One can find a detailed discussion of this scheme in [2, 14–18] and the literature cited therein. In [11–13], it was proposed to ignite the thermonuclear reaction by high-energy ions (instead of electrons), which can be produced in the interaction of a petawatt laser pulse with a thin foil. The foil, which is to be deformed in a desired fashion, should ensure the focusing of the accelerated ions onto the target.

The goal of this paper is to quantitatively investigate the efficiency of proton acceleration in the interaction of a petawatt laser pulse with a thin dense spherical target, to identify the acceleration mechanism, and to study how the energy of fast protons depends on the radiation intensity. We present the results of three-dimensional particle-in-cell (PIC) simulations of the laser acceleration of protons. As applied to the problem under study, we emphasize the necessity of three-dimensional simulation, which is related to the qualitatively different behavior of the electrostatic potential in three-dimensional geometry as compared to one- or two-dimensional geometries.

1063-780X/01/2705-0363$21.00 © 2001 MAIK "Nauka/Interperiodica"

When formulating the initial and boundary conditions, we follow the approach used previously to simulate the interaction of laser radiation with a thin foil in one-dimensional geometry [19] and two- and three-dimensional geometries [6–8, 20]. In the problem as formulated, the ions are accelerated due to the irradiation of a part of a spherical target by a high-power laser. As was shown in [7, 8], a curved target ensures the efficient collimation of the fast-ion beam. Therefore, in our simulations, a thin spherical foil is used to focus proton beams.

2. FORMULATION OF THE PROBLEM FOR NUMERICAL SIMULATION

We use a fully three-dimensional, electromagnetic relativistic PIC code. At each time step, the coordinates and momenta of the particles and the electromagnetic field are calculated for the given initial and boundary conditions. All the variables to be calculated are functions of time and three spatial coordinates x, y, and z. The code used complies with the mass conservation law and the continuity equation. Adapting the particle form-factor to the spatial grid ensured that energy in the system was conserved with a high accuracy (about 0.1%) and substantially decreased artificial plasma heating inherent in the PIC method. The code will be described in more detail in a separate paper. One simulation run required about 10 h of a 32-processor Cray T3E supercomputer at about 14GB RAM.

The simulation box is 30 μm wide, 30 μm high, and 40 μm long. Inside the simulation box, a target—a spherical shell of radius 22 μm with the center at x = 15 μm, y = 15 μm, and z = 30 μm—is placed. The shell thickness is 5 μm. Since, at the laser intensities under consideration, the shell material is ionized almost instantaneously, we assume that the target consists of a dense electron–proton plasma. The proton-to-electron mass ratio is taken to be 1836. The initial electron and proton densities in the shell are equal to 1.6×10^{21} cm^{-3}. In this case, the ratio of the initial plasma density to the critical density is $n/n_c = 1.5$ for a laser wavelength of 1 μm. The spatial grid consists of 3.6×10^7 cells (300 cells along the x-axis, 300 cells along the y-axis, and 400 cells along the z-axis). Such spatial resolution corresponds to the collisionless skin depth c/ω_{pe}. The total number of quasi-particles is 1.6×10^7 for each plasma species (electrons and protons). This corresponds to about four particles per cell for electrons (protons) in the shell. Initially, both the electrons and ions are cold.

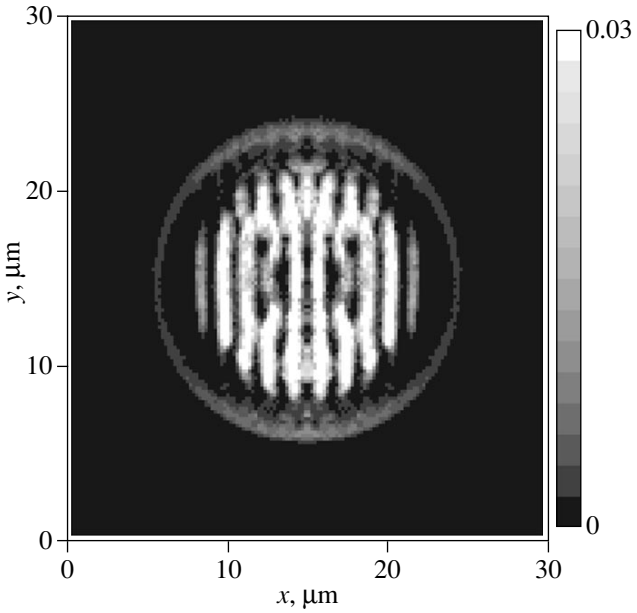

Fig. 1. Filamentation of laser radiation: distribution of $E_y^2(x, y)$ in the z = 8 μm plane (in the target shell) at t = 69 fs. The characteristic distance between the filaments is on the order of the laser wavelength.

The laser pulse is initialized in the vacuum region to the left of the target. The pulse is linearly polarized (the electric field is directed along the y-axis) and propagates along the z-axis. We consider linear polarization because we are interested in the effect of polarization on the collimation and transportation of fast protons. The transportation of fast protons toward the target requires a high degree of collimation as well as the neutralization of the electric charge of the accelerated proton beam by electrons. Obviously, azimuthal asymmetry can only worsen the beam collimation. The undesirable effect of azimuthal asymmetry should be most pronounced in the case of linear polarization. We assume that the laser wavelength is 1 μm. The laser pulse is Gaussian in shape. The pulse length is 24 μm (the duration is 70 fs), and the pulse width (at half-maximum of the intensity) is 15 μm. We carried out a series of runs for different laser intensities in the petawatt power range: 10^{21}, 5×10^{21}, and 10^{22} W cm^{-2}. These intensities correspond to dimensionless laser amplitudes of a = 27, 60, and 80, where $a = eE/m_e\omega c$.

We assume the periodical boundary condition over the x and y coordinates. At the left and right boundaries (the maximum and minimum values of z), we impose the absorption conditions for the field and particles.

The simulations are stopped at 400 fs. By this time, the laser pulse has left the box and the first protons have passed their focal spot near the center of the spherical shell.

3. SIMULATION RESULTS

As was mentioned above, we carried out simulations for several laser intensities. Figures 1–8 present the results for $I = 10^{21}$ W/cm^2 only, because the interaction pattern varies insignificantly in the intensity range under study.

Figure 1 shows the initial stage of the interaction of an intense laser with a thin dense shell. In this stage,

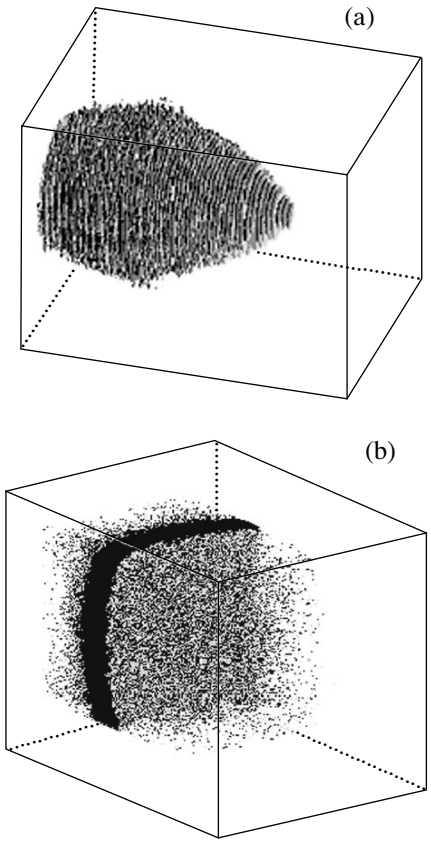

Fig. 2. (a) Surface of a constant value of $E_y^2(x, y)$, demonstrating the shape of the pulse, and (b) electron cloud produced by laser radiation near the target surface at $t = 139$ fs in the region (subbox) $5 < x < 24$ μm, $5 < y < 24$ μm, and $4 < z < 32$ μm.

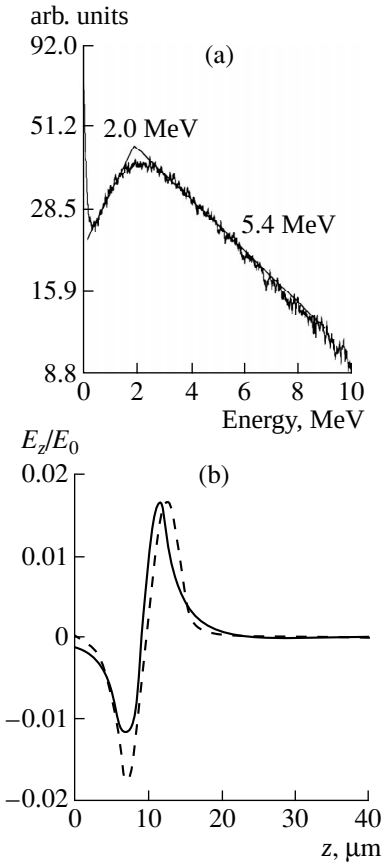

Fig. 3. (a) Electron energy distribution function averaged over the subbox shown in Fig. 2 and (b) the z-component of the electric field calculated by formula (1) ($E_z = -T_e\partial_x n_e/en_e$ with $T_e = 1.9$ MeV) as a function of z (dashed curve) and that obtained from computer simulations (solid curve) at $t = 69$ fs. The characteristic electric field is $E_0 = 10^{12}$ V/cm.

small-scale nonlinear self-modulation of laser radiation occurs. The figure presents the high-resolved distribution of the squared y-component of the electric field E_y^2 in the (x, y) plane at $z = 8$ μm. The laser field induces a strong electric current along the y-axis; the nonlinear evolution of this current results in the formation of thin current filaments with a transverse size of about the laser wavelength. These filaments survive throughout the entire process of the laser–target interaction and are still visible after the pulse has passed the target. Similar filamentation resulting in the electron density modulation along the electric field of a relativistically strong, linearly polarized electromagnetic wave in a dense plasma was observed in computer simulations reported in [21]. In that paper, it was shown theoretically that filamentation occurs due to the onset of a parametric instability in a dense plasma. It was also shown that, in a dense plasma, filamentation develops mainly in the polarization direction of the electromagnetic wave.

Figure 2a shows the laser pulse penetrating through the target. The pulse propagates from left to right. The figure presents the distribution of the squared y-component of the electric field E_y^2, but with a lower spatial resolution as compared to Fig. 1. For this reason, small-scale filaments are not seen here. Under the action of laser radiation, the electrons acquire mechanical momentum in the direction of the pulse propagation and leave the target. The resulting distribution of the electron density is shown in Fig. 2b. The characteristic electron density is 1.6×10^{21} cm^{-3}. Figure 2 shows the subbox $5 < x < 24$ μm, $5 < y < 24$ μm, and $4 < z < 32$ μm near the target.

At this intensity, heavy protons are not accelerated directly by the laser field but acquire mechanical momentum in the charge-separation field, mainly along the normal to the target surface. We note that, in addition to the acceleration in the charge-separation field, there may be other acceleration mechanisms such as Coulomb explosion [4, 6–8, 21, 22] and acceleration caused by eddy electric fields induced by rapidly varying quasistatic magnetic fields that are generated by fast electrons in a plasma [6, 23, 24]. The relative con-

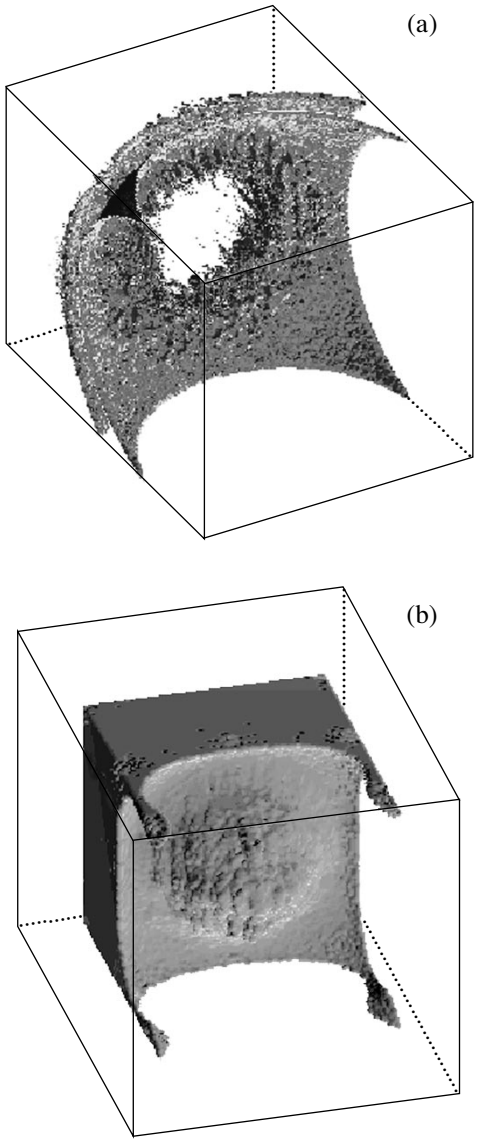

Fig. 4. Distributions of the proton density (a) at $t = 200$ fs and (b) by the time the laser pulse has already left the simulation box. The higher spatial resolution in plot (b) makes it possible to see the details of the fast ion distribution in the subbox shown in Fig. 2.

tributions from these mechanisms depend on the parameters characterizing the laser–target interaction. However, for the currently discussed laser intensities corresponding to at most multipetawatt laser pulses, the laser energy is first transferred to the electrons; then, the ions are accelerated by quasistatic collective fields arising due to the redistribution of the electron component (see the discussion in [25, 26]). The characteristic energy of fast electrons observed in experiments on the interaction of petawatt laser pulses with matter is 100 MeV [27].

For the parameters of the laser–target interaction under consideration, the ions are accelerated by the charge-separation field. This is confirmed by the dependences plotted in Fig. 3. Figure 3a presents the electron energy spectrum averaged over the subbox shown in Fig. 2. It is seen that the electron distribution function has the second maximum at an energy of 2 MeV. The *z*-component of the electric field can be calculated from the Vlasov equation with the known electron distribution function. After averaging over *x* and *y*, we obtain

$$E_z(z) \approx -\frac{1}{L_x L_y}\iint dxdy\left(\frac{\nabla \cdot \int d^3p\, p_z \mathbf{v} f}{e\int d^3p f}\right) \approx -T_{e,\,\mathrm{eff}}\frac{\partial_z n_e}{e n_e}, \quad (1)$$

where L_x and L_y are the subbox dimensions in the *x* and *y* directions.

Substituting as $T_{e,\,\mathrm{eff}}$ the energy corresponding to the second maximum in the electron distribution function into the right-hand side of expression (1) and calculating the partial derivative of the electron density over *z*, we obtain the electric field profile shown in Fig. 3b (dashed curve). The solid curve in Fig. 3b shows the dependence obtained from simulations. The satisfactory agreement of the two curves indicates that the main effect is the generation of the charge-separation electric field along the *z*-axis. The electric field is proportional to the mean electron energy and the effective electron density gradient. The field is approximately normal to the target surface.

The plasma density in the shell is higher than the critical one. Nevertheless, the laser pulse penetrates through the target due to nonlinear effects such that the change in the plasma refractive index in the relativistically strong electromagnetic field and the ponderomotive pressure, which leads to a local reduction of the density in the target. As a result, after the pulse has passed through the target, a region with a reduced plasma density is formed near the axis (Fig. 4a). Due to the destruction of the target, proton acceleration terminates. This is related to violating the conditions that are necessary for the formation of a strong charge-separation field due to the abrupt decrease in the plasma density. Although the accelerating field acts on the ions during a finite time, it is so strong that the ions start moving, as is seen in Fig. 4b. The figure presents the spatial distribution of the density of fast protons in the subbox shown in Fig. 2.

Fast protons form a well-collimated beam (Fig. 5). Protons are focused due to the spherical shape of the target. Figure 5 shows the distributions of the proton density in the (x, y) plane at distances of $\delta z = 11$ and 19 μm from the target surface. Since the left edge of the target is located at $z = 8$ μm, Fig. 5a shows the region in front of the focal spot and Fig. 5b shows the region just behind the focal spot. The geometric center of the spherical target is at $z = 30$ μm. Figures 5c and 5d present the distributions of the *x*-component of the pro-

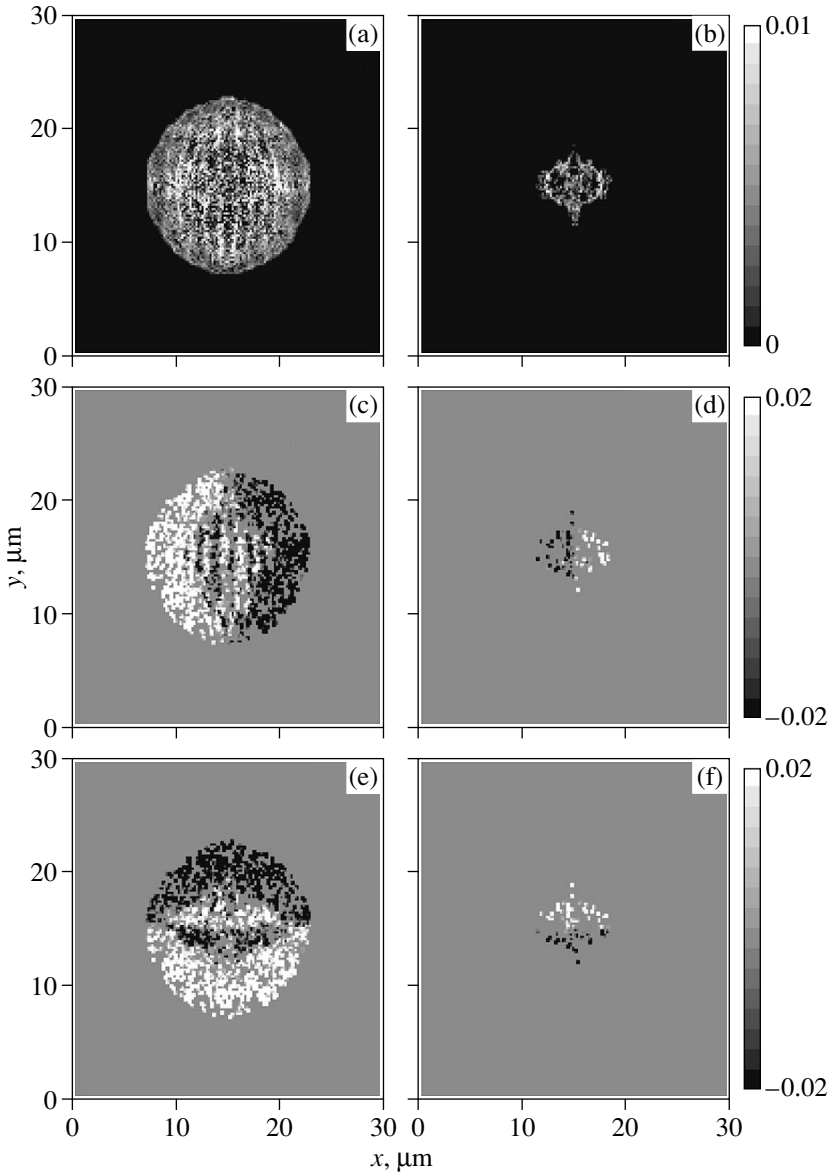

Fig. 5. Distributions of (a, b) the fast proton density and (c, d) *x*- and (e, f) *y*-components of the proton momentum (p_{xi} and p_{yi}) in the planes z = (a, c, e) 19 and (b, d, f) 27 μm at t = 347 fs. Plots (c, e) and (d, f) demonstrate the focusing and defocusing of protons, respectively. The geometric center of the spherical target is located at z = 30 μm.

ton momentum p_{xi} in the planes z = 19 and 27 μm, respectively. The distributions of the *y*-component of the proton momentum p_{yi} in the planes z = 19 and 27 μm are presented in Figs. 5e and 5f, respectively. The distributions are shown for a time of 347 fs. Figures 5c and 5e demonstrate the focusing of the proton beam, and Figs. 5d and 5f demonstrate the defocusing of the proton beam. The direction of the particle motion is shown by shades of gray, from which it is also seen that the plane δz = 19 μm lies behind the focal spot. The results of simulations demonstrate that the position of the proton focal spot is determined by the curvature of the target shell. It is seen in Figs. 5c–5f that the focal spot lies near the geometric center of the spherical target.

The gray scale on the right of Fig. 5b shows the proton density in units of 1.66×10^{21} cm^{-3}. Figure 5c presents the distribution of the transverse component of the proton momentum. It is seen that the proton density in the beam attains a value on the order of 10^{19} cm^{-3}. We note that the proton density changes insignificantly in the course of focusing (as it might be in the case of focusing a cold beam of noninteracting particles). This is related to the fact that, in our case, the particle distribution over momenta is nonuniform along the longitudinal coordinate. The distribution of fast ions over the

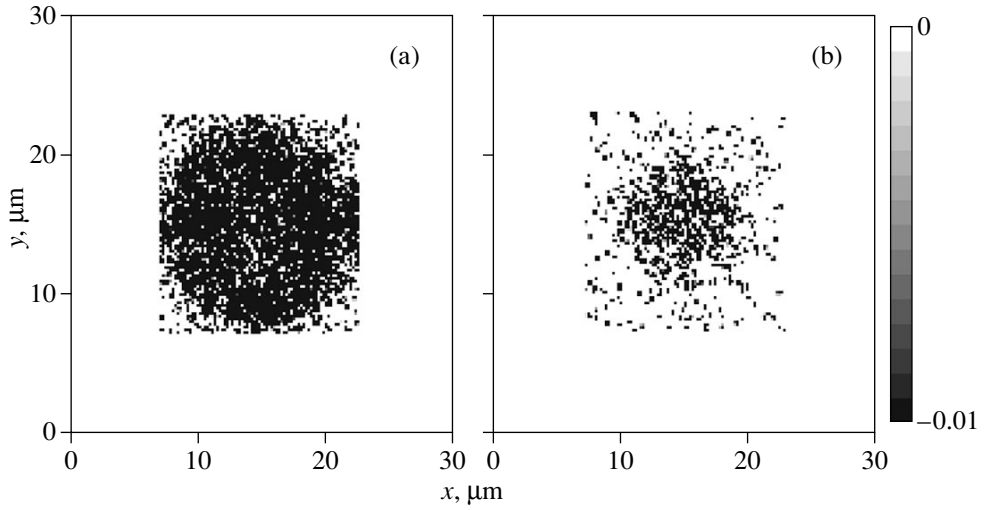

Fig. 6. Distribution of electrons in the planes z = (a) 19 and (b) z = 27 μm at t = 347 fs.

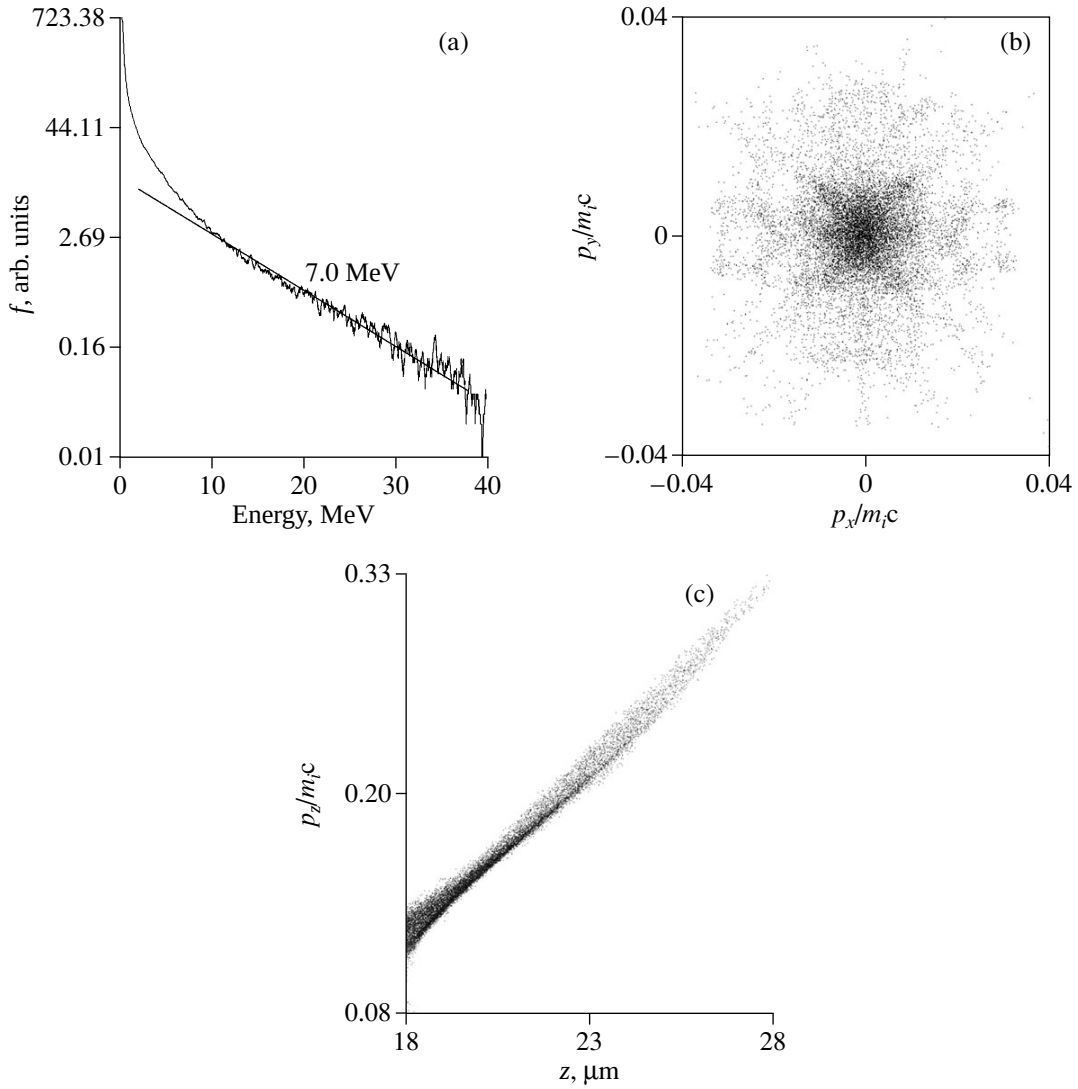

Fig. 7. (a) Proton energy distribution function and proton distributions in the phase planes (b) (p_x, p_y) and (c) (p_z, z) in the subbox shown in Fig. 5 at t = 347 fs.

longitudinal momenta is shown in Fig. 7c, which is discussed below. As a result, an elementary volume contracts in the transverse direction due to focusing and stretches in the longitudinal direction. The number of protons in the subbox $8 < x < 22$ μm, $8 < y < 22$ μm, and $18 < z < 28$ μm is approximately equal to 10^{10}. These are mainly fast protons with energies of 4–50 MeV. For comparison, the total number of protons in the simulation box is 7×10^{12}. The maximum value of the laser energy in the simulation box is about 50.2 J for a dimensionless amplitude of $a = 27$. By the time the laser pulse leaves the simulation box, the total energy of fast protons in the above subbox is ~2.4 J. Hence, in simulations with $a = 27$, the conversion efficiency of laser energy into the energy of fast protons is about 5%.

Another interesting result is that the fast protons polarize the electron component. Under the action of the radial electric field produced by the protons, the electron density changes and the local minimum of the electron density, which correlates with the maximum of the proton density, is formed at the axis. This is clearly seen in Fig. 6. We emphasize, however, that the electron density at the axis is much lower than the proton density. Note that, in simulations carried out for the other parameters of the laser–target interaction [6, 8, 10], the local values of the proton density were so high that the conditions for the Coulomb explosion mechanism for particle acceleration were satisfied (for details, see [26] and the literature cited therein).

The final proton distribution function and the structure of the proton distribution in phase space are shown in Fig. 7. The mean energy (effective temperature) of protons in the tail of the distribution function is 7 MeV (see Fig. 7a). At the same time, the mean energy of fast electrons is 5.4 MeV (Fig. 3a). The structure of the proton distribution in phase space (Figs. 7b, 7c) indicates that the divergence of the proton beam is relatively low. The characteristic value of the transverse component of the proton momentum is approximately ten times lower than that of the longitudinal component. For $a = 27$, the maximum kinetic energy of fast protons is approximately equal to $m_i c^2(\sqrt{1 + 0.1} - 1) \approx 50$ MeV (here, we take into account that the maximum value of the proton momentum is $0.33 m_i c$). This energy agrees with the estimate for the energy that the protons can acquire in the electric field E_z shown in Fig. 3.

As the laser intensity increases ($a = 60$ and 85), the maximum value of the longitudinal component of the proton momentum increases. The momentum and energy increase to $p_{zi} = 0.4 m_i c$ and 87 MeV for $a = 60$ and to $p_{zi} = 0.44 m_i c$ and 112 MeV for $a = 85$, respectively. The dependence of fast proton energy on the laser amplitude is described by the approximate formula $E_i = Ka^\beta$, where $K = 5$, $\beta = 0.7$, and energy is measured in MeV. This formula may also be written in the form

$$(E_i[\text{MeV}]) = 5(I[\text{W/cm}^2]\lambda^2[\mu\text{m}]/1.38 \times 10^{18})^{0.35}. \quad (2)$$

The directed electron flows produce the slowly varying electric current in the plasma, which, in turn, generates the magnetic field. In our case, the magnetic field whose structure is shown in Fig. 8 is generated near the target. Figure 8a presents the distribution in the (x, y) plane of the absolute value of the transverse component of the magnetic field $B_\perp(x, y) = \sqrt{B_x^2 + B_y^2}$, averaged over the region $11 < z < 16$ μm. Figure 8b shows the distribution of the z-component of the magnetic field in the (x, y) plane. It is seen that the magnetic field

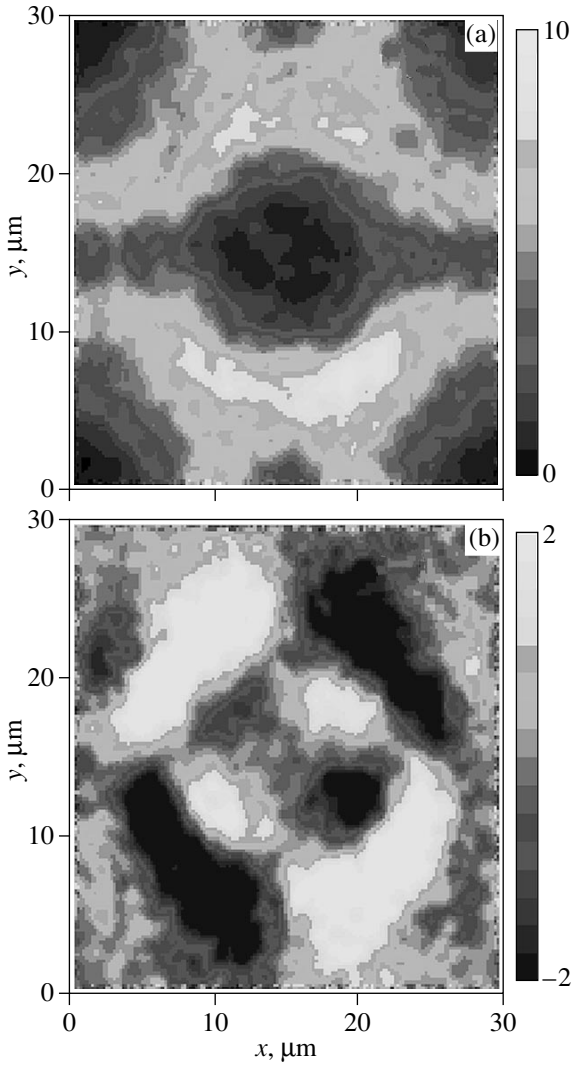

Fig. 8. Distributions of the (a) transverse and (b) longitudinal components of the quasistatic magnetic field (both averaged over the region $11 < z < 16$ μm) at $t = 347$ fs. The azimuthal component of the magnetic field is directed clockwise. The magnetic field is measured in units of 2.9×10^6 G.

possesses a pronounced multipole structure. The azimuthal component of the magnetic field is generated by the electric current produced by fast electrons as they move along the normal to the target surface. For this reason, the azimuthal magnetic field mainly defocuses fast protons. Various aspects of the influence of spontaneous magnetic fields on the dynamics of fast protons are discussed in [6, 7, 26, 27], where, in particular, the focusing effect of the magnetic field generated by fast protons was demonstrated for the other regimes of laser–plasma interaction.

4. CONCLUSIONS

We have presented the results of computer simulations of the three-dimensional regime of proton acceleration in the interaction of a high-intensity laser pulse with a thin spherical plasma shell. The beam of fast protons is almost axisymmetric, which indicates that the laser polarization insignificantly affects proton acceleration. The linear polarization of a laser pulse only affects the structure of small-scale filamentation, and does not cause the azimuthal asymmetry of the proton beam. In our simulations, the density of fast protons attains 10^{19} cm^{-3}. The maximum momentum of fast protons is $0.3m_ic$. Protons are accelerated for a relatively short time until the plasma is redistributed substantially and the plasma density in the axial region strongly decreases. The reduction of plasma density under the action of the ponderomotive force of laser radiation results in violating the conditions for the generation of a strong charge-separation electric field. It is shown that profiling the target in a proper manner creates the conditions for the generation of dense collimated beams of fast protons. Accelerated protons are focused near the geometric center of the spherical target. The linear polarization of laser radiation causes no appreciable azimuthal asymmetry of the focused fast-proton beam. It is worth noting the observed multipole structure of the longitudinal component of the magnetic field generated by fast electrons. It is found that, after the acceleration process comes to an end, the electric field of the proton beam leads to plasma polarization. The electric field attracts the electrons, which results in the regime of quasineutral propagation. This regime is more pronounced in three-dimensional simulations than in two-dimensional simulations. On the one hand, the transition to the quasineutral propagation regime results in the termination of acceleration. On the other hand, this regime makes possible the transportation of fast-ion beams over large distances. Obviously, this effect is favorable for igniting thermonuclear targets by fast ions. It is found that the energy of fast ions increases relatively slowly with increasing laser intensity. We anticipate that the use of multilayer targets substantially increases both the conversion efficiency of laser energy into the energy of fast particles and the number of accelerated protons, because, in such targets, the protons will be successively accelerated in each following shell.

ACKNOWLEDGMENTS

We are grateful for the opportunity to use the Cray T3E computing facility at NIC, Jülich, Germany. This work was supported by the European Commission through the TMR network SILASI (contract no. ERBFMRX-CT96-0043) and the Russian Foundation for Basic Research (project no. 99-02-16997).

REFERENCES

1. T. Tajima and J. Dawson, Phys. Rev. Lett. **43**, 267 (1979).
2. M. Tabak, J. Hammer, M. E. Glinsky, *et al.*, Phys. Plasmas **1**, 1626 (1994).
3. T. Ditmire, J. Zweiback, V. P. Yanovsky, *et al.*, Nature **398**, 489 (1999).
4. G. S. Sarkisov, V. Yu. Bychenkov, V. N. Novikov, *et al.*, Phys. Rev. E **59**, 7042 (1999).
5. V. S. Khoroshkov and E. I. Minakova, Eur. J. Phys. **19**, 523 (1998).
6. T. Zh. Esirkepov, Y. Sentoku, K. Mima, *et al.*, Pis'ma Zh. Éksp. Teor. Fiz. **70**, 80 (1999) [JETP Lett. **70**, 82 (1999)].
7. S. V. Bulanov, T. Zh. Esirkepov, F. Califano, *et al.*, Pis'ma Zh. Éksp. Teor. Fiz. **71**, 593 (2000) [JETP Lett. **71**, 407 (2000)].
8. Y. Sentoku, T. V. Lisseikina, T. Zh. Esirkepov, *et al.*, Phys. Rev. E **62**, 7271 (2000).
9. A. Maksimchuk, S. Gu, K. Flippo, *et al.*, Phys. Rev. Lett. **84**, 4108 (2000).
10. F. Pegoraro, S. Bulanov, F. Califano, *et al.*, IEEE Trans. Plasma Sci. **28**, 1226 (2000).
11. M. Roth, T. E. Cowan, M. D. Perry, *et al.*, in *Proceedings of the 4th International Workshop on Fast Ignition of Fusion Targets, Palaiseau, 2000*, Ed. by P. Mora and J. C. Gauthier (Ecole Politechnique, Palaiseau, 2000).
12. V. Yu. Bychenkov, W. Rozmus, A. Maksimchuk, and D. Umstadter, Comments Plasma Phys. Controlled Fusion (2001) (in press).
13. H. Ruhl, in *Proceedings of the International Workshop on the High-Intensity Laser Pulse Interaction with Plasmas, Albuquerque, NM, 2000*, Ed. by F. Pegoraro and I. Pogorelsky.
14. S. Atzeni, Phys. Plasmas **6**, 3316 (1999).
15. S. C. Wilks, W. L. Kruer, M. Tabak, and A. B. Langdon, Phys. Rev. Lett. **69**, 1383 (1992).
16. A. R. Piriz and M. M. Sánchez, Phys. Plasmas **5**, 4373 (1998).
17. C. Deutsch, Y. Furukawa, K. Mima, *et al.*, Phys. Rev. Lett. **77**, 2483 (1996).
18. P. A. Norreys, R. Allott, R. J. Clark, *et al.*, Phys. Plasmas **7**, 3721 (2000).
19. J. Denavit, Phys. Rev. Lett. **69**, 3052 (1992); S. Miyamoto, S. Kato, K. Mima, *et al.*, J. Plasma Fusion Res. **73**, 343 (1997).

20. A. V. Vshivkov, N. M. Naumova, F. Pegoraro, and S. V. Bulanov, Phys. Plasmas **5**, 2727 (1998).
21. T. Honda, K. Nishihara, T. Okamoto, *et al.*, J. Plasma Fusion Res. **75** (10-CD), 219 (1999).
22. K. Krushelnick, E. L. Clark, Z. Najmudin, *et al.*, Phys. Rev. Lett. **83**, 737 (1999); E. L. Clark, K. Krushelnik, M. Zepf, *et al.*, Phys. Rev. Lett. **85**, 1654 (2000).
23. A. V. Gordeev and T. V. Loseva, Pis'ma Zh. Éksp. Teor. Fiz. **70**, 669 (1999) [JETP Lett. **70**, 684 (1999)].
24. S. V. Bulanov and A. S. Sakharov, Fiz. Plazmy **26**, 1074 (2000) [Plasma Phys. Rep. **26**, 1005 (2000)].
25. S. V. Bulanov, V. A. Vshivkov, G. I. Dudnikova, *et al.*, Fiz. Plazmy **25**, 764 (1999) [Plasma Phys. Rep. **25**, 701 (1999)].
26. S. V. Bulanov, F. Califano, G. I. Dudnikova, *et al.*, in *Reviews of Plasma Physics*, Ed. by V. D. Shafranov (Consultants Bureau, New York, 2001), Vol. 22.
27. M. H. Key, M. D. Cable, T. E. Cowan, *et al.*, Phys. Plasmas **5**, 1966 (1998); R. A. Snavely, M. H. Key, S. P. Hatchett, *et al.*, Phys. Rev. Lett. **85**, 2945 (2000).
28. A. V. Kuznetsov, T. Zh. Esirkepov, F. F. Kamenets, and S. V. Bulanov, Fiz. Plazmy **27**, 225 (2001) [Plasma Phys. Rep. **27**, 211 (2001)].

Translated by A.S. Sakharov

Plasma Physics Reports, Vol. 27, No. 5, 2001, pp. 372–380. Translated from Fizika Plazmy, Vol. 27, No. 5, 2001, pp. 397–405.

PARTICLE ACCELERATION IN PLASMA

Dynamics of an Electron Bunch Accelerated by a Wakefield

S. V. Kuznetsov and N. E. Andreev

Institute for High Energy Densities, Associated Institute for High Temperatures, Russian Academy of Sciences, Izhorskaya ul. 13/19, Moscow, 127412 Russia

Received July 6, 2000; in final form, October 4, 2000

Abstract—The energy characteristics of an electron bunch accelerated by a wakefield are largely determined by the initial bunch dimensions. Present-day injectors are still incapable of ensuring the initial spatial parameters of the bunches required for their acceleration without increasing the energy spread of the bunch electrons. In connection with this, the possibility is studied of improving the energy characteristics of an accelerated bunch by precompressing it in the longitudinal direction in the stage of trapping by a wakefield. Analytic formulas are derived that describe the one-dimensional dynamics of the spatial and energy characteristics of a short (much shorter than the wakefield wavelength) electron bunch in both the trapping and acceleration stages. The analytical results obtained are shown to agree fairly well with the results from one-dimensional and three-dimensional simulations, provided that the electrons are injected into the region that is optimum for acceleration. The possibility is discussed of forming compressed bunches so as to ensure the high quality of the bunch in the course of its acceleration to high energies. *© 2001 MAIK "Nauka/Interperiodica".*

1. INTRODUCTION

Successful experiments on the generation of superstrong (~100 GV/m) accelerating fields by high-power short laser pulses in plasmas have stimulated increased interest in theoretical investigations of the main principles of electron acceleration by a wake plasma wave [1–5]. At present, one of the most important problems is that of providing a high quality of the electron bunches. Among the usual requirements for the quality of an accelerated bunch is the requirement that the relative energy spread of the bunch electrons be small (see, e.g., [6]). In many applications (see [7] and the literature cited therein), a very important parameter of the accelerated electrons is the smallness of the bunch length in the propagation direction. Previous investigations on the acceleration of electron bunches [8] have shown that the degree to which the bunch electrons are monoenergetic depends strongly on the bunch length. It is desirable that the bunch be as short as possible throughout the entire acceleration process for the relative energy spread of the accelerated electrons not to increase. However, present-day injectors are still incapable of forming bunches of the desired length. For this reason, before proceeding to acceleration, it is necessary to additionally shorten the bunch in the direction in which it is to be accelerated. In particular, the bunch can be precompressed in the longitudinal direction via the bunching of the electrons in the course of their trapping by the wakefield, provided that they are injected at a velocity much lower than the phase velocity of the wake wave. The effect of bunching on the electron distribution in the coordinate–velocity phase plane was demonstrated more than once in investigations of the dynamics of long electron bunches during their trapping and acceleration by a potential wave. Local bunching of electrons was found to occur not only in real space (along a physical coordinate) [7, 9] but also in energy space [9–11]. In particular, the possibility of using the bunching mechanism to additionally compress a fairly short injected electron bunch was demonstrated in our previous numerical [12] and theoretical [13] studies.

Here, we present a more detailed, analytic investigation of the main features of the dynamics of both the spatial and energy characteristics of a one-dimensional, short (in comparison with the wakefield wavelength) electron bunch during its trapping and acceleration by the wakefield, provided that the injection velocity of the electrons is lower than the phase velocity of the wake wave. In Section 2, we derive the main formulas, study the compression of a short electron bunch, and analyze the evolution of the energy characteristics of the bunch during its trapping by the wakefield. This stage of acceleration is usually referred to as the bunching stage. In Section 3, we study the evolution of the energy characteristics of a bunch during its injection into the accelerating stage, where the bunch electrons move with a velocity higher than the phase velocity of the wake wave. Our investigations may find important applications, e.g., in developing a multistage acceleration scheme, in which the bunch is accelerated to high energies in successive accelerating stages. The analytic formulas obtained in different limiting cases are compared with the results from both one-dimensional numerical simulations and simulations of the trapping and acceleration of three-dimensional (axisymmetric) bunches. In the Conclusion, we summarize the results obtained.

1063-780X/01/2705-0372$21.00 © 2001 MAIK "Nauka/Interperiodica"

2. BASIC EQUATIONS DESCRIBING THE LONGITUDINAL COMPRESSION OF A SHORT ELECTRON BUNCH BY A WAKEFIELD

The longitudinal compression of a monoenergetic electron bunch in the acceleration direction or, equivalently, in the direction of the wave phase velocity V_{ph} (the z-axis) is studied using a one-dimensional model. This approach is valid when the radius R_b of the injected bunch is much smaller than the characteristic radius of the optimum injection region [14]. We consider a spatial axisymmetric wake wave with the potential

$$\phi(\xi, r) = -\phi_0 \cos(\xi) \exp(-r^2/R_p^2), \quad (1)$$

where $\xi = k_p(z - V_{ph}t)$, $k_p = \omega_p/c$ is the wavenumber, $\omega_p = \sqrt{4\pi e^2 n_e/m_e}$ is the Langmuir frequency of the plasma electrons, R_p is the characteristic transverse scale length of the wakefield, and ϕ_0 is the maximum potential. In such a wave, the maximum radius of the optimum injection region for bunch electrons injected at an energy E_{inj} is estimated as [14]

$$R_{max,\,opt} = R_p \left\{ \ln \left[\frac{|e|\phi_0}{E_{inj} - \beta\sqrt{E_{inj}^2 - m^2c^4} - mc^2/\gamma} \right] \right\}^{1/2}. \quad (2)$$

For $R_b \ll R_{max,\,opt}$, we can assume that the wave potential ϕ is one-dimensional; i.e., in the laboratory frame, it depends only on the variable $\xi = k_p(z - V_{ph}t)$. It is assumed that the phase velocity of the wake wave is close to the speed of light ($V_{ph} \approx c$), as is the case with a wakefield generated by a laser pulse in an underdense plasma ($\omega_0 \gg \omega_p$, where ω_0 is the laser frequency).

In order for an electron bunch to be compressed by a wakefield, the energy E_{inj} of the injected electrons should be such that their velocity is lower than the wake phase velocity; i.e., $E_{inj} < mc^2\gamma$, where $\gamma = 1/\sqrt{1-\beta^2}$ and $\beta = V_{ph}/c$. Physically, the bunch is compressed by the longitudinally nonuniform force $F_z = |e|\partial\phi/\partial z$, in which case the leading part of the accelerated electron bunch experiences a weaker force than the trailing part. Consequently, the compression is most pronounced for the electrons that pass through the region where the negative force gradient is the largest, $\partial^2\phi/\partial z^2 < 0$. Usually, this region occurs in the vicinity of the maximum of the potential $\phi(\xi)$ of a plasma wave. On the other hand, it is desirable that the bunch energy in this region be as low as possible, in which case the relativistic electron mass will be lower and the longitudinally nonuniform force $F_z = |e|\partial\phi/\partial z$ will more strongly affect the electron trajectories and will better compress the bunch. Hence, in order for a bunch with the above injection energy to be compressed most efficiently, it should be injected into the vicinity of the point of the maximum wave potential. It is this situation that we will consider below.

In the rest frame of the wave, the motion of an individual electron is described by the equation

$$\frac{dp'}{dt'} = |e|\frac{d\phi'}{dz'}, \quad (3)$$

where p' is the longitudinal electron momentum, z' is the coordinate in the propagation direction of the wave, $\phi'(k_p'z')$ is the wave potential (which is time independent in this frame), and k_p' is the wavenumber. The injection conditions are such that the bunch electrons move initially in the negative direction along the z'-axis and start moving in the positive direction after reflection from the turning points.

Equation (3) has the first integral

$$E' - |e|\phi'(k_p'z') = E_{inj}' - |e|\phi'(k_p'z_{inj}'), \quad (4)$$

which indicates the conservation of electron energy in the potential wave. Solving Eq. (3) in quadratures yields the electron trajectory up to the turning point:

$$t' - t_{inj}' = -\frac{1}{c}\int_{z_{inj}'}^{z'} \frac{d\eta}{\sqrt{1 - \dfrac{m^2c^4}{[E_{inj}' + |e|(\phi'(k_p'\eta) - \phi'(k_p'z_{inj}'))]^2}}}, \quad (5)$$

where z' and E' are the instantaneous coordinate and energy of the electron at time t'.

Our formulas can be converted from the wave rest frame to the laboratory frame by means of relativistic transformations of the coordinates and time. In particular, the time interval $\Delta t' = t' - t_{inj}'$ in the wave rest frame satisfies the relationship

$$c\Delta t' = \gamma\{c\Delta t - \beta(z - z_{inj})\}. \quad (6)$$

The spatial coordinate z' satisfies the relationship $z' = \gamma\{z - V_{ph}t\}$; thus, it is expedient to introduce the self-similar variable $\xi = k_p(z - V_{ph}t)$ in the laboratory frame.

Using these relationships and applying relativistic transformations to the electron energy and wave potential, we reduce expressions (4) and (5) to

$$E - \beta\sqrt{E^2 - m^2c^4} - |e|\phi(\xi) = E_{inj} - \beta\sqrt{E_{inj}^2 - m^2c^4} - |e|\phi(\xi_{inj}), \quad (7)$$

$$\gamma^{-2}ck_p\Delta t - \beta(\xi - \xi_{\text{inj}}) = -\int_{\xi_{\text{inj}}}^{\xi} \frac{d\eta}{\sqrt{1 - \dfrac{m^2c^4}{\gamma^2[(E_{\text{inj}} - \beta\sqrt{E_{\text{inj}}^2 - m^2c^4}) + |e|(\phi(\eta) - \phi(\xi_{\text{inj}}))]^2}}}. \quad (8)$$

Expressions (7) and (8) relate the parameters of the injected electrons (z, E, etc.) at the initial time t_{inj} to the parameters for all subsequent times. If two electrons in the bunch are initially separated by the sufficiently short distance $\Delta\xi_{\text{inj}}$, then the electron trajectories will always be close to one another. The distance $\Delta\xi$ between the trajectories at any time and the energy difference ΔE between the electrons can be determined from expressions (7) and (8). This can be done by expanding these expressions in powers of the small variations of the coordinates, $\Delta\xi_{\text{inj}} = k_p\Delta z_{\text{inj}} \ll 1$ and $\Delta\xi = k_p\Delta z \ll 1$, and energy $\Delta E \ll mc^2$ (recall that, at the initial time, we have $\Delta E_{\text{inj}} = 0$). Since the bunch is injected into the vicinity of the point of the maximum potential, it is convenient to choose as the reference electron (about which the variations will be made) the bunch electron that is injected exactly at the point at which the potential is maximum $\xi_{\text{inj}} = \xi_m$, where $\phi(\xi_m) = \phi_{\max}$. Note that, in this case, we have $d\phi(\xi_{\text{inj}})/d\xi = 0$; consequently, in the expansions, it is necessary to take into account terms on the order of $\sim(\Delta\xi_{\text{inj}})^2$.

In this way, we can solve the corresponding equations to obtain

$$\Delta\xi = \frac{E_{\text{inj}}p'(\xi)}{E(\xi)p'_{\text{inj}}}\Delta\xi_{\text{inj}} + \frac{|e|\gamma^2 p'(\xi)}{2mcE(\xi)}I_1(\xi)\frac{\partial^2\phi(\xi_{\text{inj}})}{\partial\xi^2}(\Delta\xi_{\text{inj}})^2 \equiv \alpha_1(\xi)\Delta\xi_{\text{inj}} + \alpha_2(\xi)(\Delta\xi_{\text{inj}})^2, \quad (9)$$

$$\Delta E = |e|\gamma\left\{\frac{E_{\text{inj}}p(\xi)}{E(\xi)p'_{\text{inj}}}\frac{d\phi(\xi)}{d\xi}\Delta\xi_{\text{inj}} - \frac{\gamma}{2}\left|\frac{d^2\phi(\xi_{\text{inj}})}{d\xi^2}\right|\frac{p(\xi)c}{E(\xi)}\left[\beta + \frac{E'_{\text{inj}}(\xi)}{p'_{\text{inj}}(\xi)c} + I_2\right](\Delta\xi_{\text{inj}})^2\right\}, \quad (10)$$

where

$$I_1(\xi) = \int_{\xi_m}^{\xi} d\eta\{[E'_{\text{inj}} + |e|\gamma(\phi(\eta) - \phi(\xi_m))]^2/m^2c^4 - 1\}^{-3/2},$$

$$I_2(\xi) = \int_{\xi_{\text{inj}}}^{\xi} \frac{d\eta|e|m^2c^4\gamma\left(\dfrac{d\phi}{d\eta} - \dfrac{d\phi}{d\xi}\right)}{\{[E'_{\text{inj}} + \gamma|e|(\phi(\eta) - \phi(\xi_{\text{inj}}))]^2 - m^2c^4\}^{3/2}}.$$

Using formula (9), we can determine the degree to which a bunch of finite length L_{b0} can be compressed, provided that it is properly injected into the vicinity of the point of the maximum potential, i.e., into the region $[\xi_m + \Delta\xi_0, \xi_m]$, where $\Delta\xi_0 = \Delta\xi_{\text{inj}} = -k_pL_{b0}$ is the initial dimensionless bunch length such that $|\Delta\xi_0| < 1$. According to formula (9), the length L_b of a homogeneous monoenergetic electron bunch accelerated by the wakefield in the ξ direction decreases according to the law

$$\frac{L_b(\xi)}{L_{b0}} = \frac{E_{\text{inj}}p'(\xi)}{E(\xi)p'_{inj}} + \frac{|e|\gamma^2 p'(\xi)}{2mcE(\xi)}I_1(\xi)\left|\frac{\partial^2\phi(\xi_m)}{\partial\xi^2}\right|k_pL_{b0} \equiv \alpha_1(\xi) + \alpha_2(\xi)k_pL_{b0}. \quad (11)$$

An important consequence of formula (11) is the fact that the bunch rapidly shortens in the vicinity of the point ξ_{tr} at which the bunch electrons become trapped by the wave and start to move in the reverse direction and $p'(\xi)$ and, accordingly, $\alpha_1(\xi)$ approach zero. The minimum length of the bunch is determined only by its initial length and the shape of the wave potential at the points where the potential is maximum and where the wave traps the electrons:

$$L_b = \alpha_2(\xi_{\text{tr}})k_pL_{b0}^2 = \frac{k_pL_{b0}^2}{2}\frac{\left|\partial^2\phi(\xi_m)/\partial\xi^2\right|}{\partial\phi(\xi_{\text{tr}})/\partial\xi}. \quad (12)$$

In particular, for a linear harmonic wave with the potential $\phi(\xi) = -\phi_0\cos(\xi)$, which is maximum at the point $\xi_m = \pi$, formula (12) implies that the bunch is the shortest when the electrons are trapped by the wave at the point $\xi_{\text{tr}} = \pi/2$, the minimum bunch length being

$$L_b = k_pL_{b0}^2/2. \quad (13)$$

Note that, in a homogeneous plasma (as well as in a plasma channel wider than k_p^{-1}), the three-dimensional structure of a linear wake wave with potential (1) is such that the turning point $\xi_{\text{tr}} = \pi/2$ lies at the boundary of the focusing phase of the wake wave, $\xi \in [\pi/2, 3\pi/2]$, where the radial force of the wave has a focusing effect on the electrons (this is the necessary condition for stable electron acceleration in real three-dimensional geometry) [15, 16].

According to formula (13), for the compression to be efficient, the initial bunch length should not exceed

the skin depth k_p^{-1}. Moreover, the degree of compression L_{b0}/L_b increases with decreasing the initial bunch length and does not depend directly on the amplitude of the wake wave and its phase velocity (of course, provided that the wave traps the injected electrons).

In order for the bunch electrons injected at an energy $E_{\rm inj}$ into the vicinity of the point of the maximum potential $\phi_{\max}$ to be trapped by the wake wave at a given point $\xi_{\rm tr}$, the difference between the maximum wave potential and the wave potential at the trapping point should satisfy the condition

$$|e|[\phi_{\max} - \phi(\xi_{tr})] = E_{\rm inj} - [(1-\gamma^{-2})(E_{\rm inj}^2 - m^2c^4)]^{1/2} - mc^2/\gamma. \quad (14)$$

In this case, in order to achieve stable compression (with allowance for the transverse motion of the bunch electrons), the trapping point should be chosen so that the electrons moving in the wakefield in the longitudinal direction in the region $\xi \in [\xi_{\rm tr}, \xi_m]$ always remain inside the focusing phase of the wave. From formula (14), we can draw the following, physically obvious, conclusion: the higher the phase velocity and the lower the energy of the injected bunch, the higher wakefield amplitude is required for the bunch to be trapped. For present-day injectors operating at $E_{\rm inj} \approx 10mc^2$, the amplitude of the wakefield capable of trapping the injected bunch turns out to be relatively small. Thus, for the bunch energy $E_{\rm inj} = 20mc^2$ and $\gamma = 50$, a wakefield amplitude of $|e|\phi_0/mc^2 \geq 0.01$ is sufficient to trap the injected bunch.

Figure 1 shows the bunch length in the trapping stage as a function of the initial bunch length for two values of the normalized acceleration distance $L_{\rm acc}/L_{\rm ph}$, where $L_{\rm acc}$ is the distance the bunch propagates in the laboratory frame and $L_{\rm ph} = 2\pi\gamma^2 k_p^{-1}$ is the maximum acceleration distance that the bunch passes when moving from the point of the minimum potential $\phi_{\min}$ to the point of the maximum potential $\phi_{\max}$. The bunch is injected at the dimensionless energy $E_{\rm inj}/mc^2 = 20$ into a wake wave with $\gamma = 50$ and $|e|\phi_0/mc^2 = 0.01$. The solid and dotted lines present analytical results obtained for $L_{\rm acc}/L_{\rm ph} \approx 0.1$ and 0.234, respectively, from formula (11), in which coordinate ξ is expressed in terms of $L_{\rm acc}/L_{\rm ph}$ via the solution of the equations of motion; the symbols demonstrate the numerical results obtained from one-dimensional simulations of the bunch dynamics for the same acceleration distances. For a sufficiently short injected bunch such that $k_pL_{b0} \ll 1$, which is the applicability condition for expression (11), Fig. 1 shows a good agreement between the one-dimensional analytical and numerical results on the decrease in the relative bunch length. For a more detailed graphical illustration of the comparison between analytical and numerical (in particular, three-dimensional) results

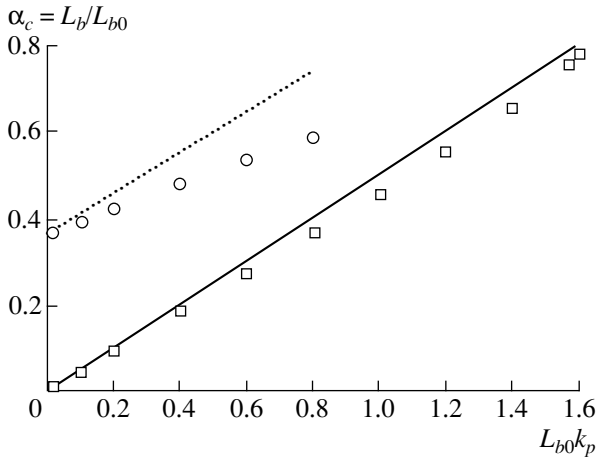

Fig. 1. Compression factor of an electron bunch vs. the initial bunch length k_pL_{b0}. The dotted and solid lines illustrate the analytical results obtained from formula (9) for the acceleration distances $L_{\rm acc}/L_{\rm ph}$ = 0.1 and 0.234, respectively. The numerical results obtained for the same two acceleration distances are demonstrated by circles and squares, respectively.

on bunch compression, we refer the reader to our paper [14]. Note that the applicability range of the simple asymptotic expressions (12) and (13) for the minimum length to which the accelerated bunch is compressed at the trapping instant is broader than the range determined by the condition $k_pL_{b0} \ll 1$, under which formulas (11) and (12) were derived. In fact, according to Fig. 1, the expression for the compression factor at the trapping instant, $\alpha_c = k_pL_{b0}/2$, which follows from formula (13) and is illustrated by the solid line, describes well one-dimensional numerical results for a broad range of the initial bunch lengths up to $k_pL_{b0} \approx \pi/2$, the acceleration distance being $L_{\rm acc}/L_{\rm ph}$ = 0.234, which indicates that the electrons injected at the point $\xi_m = \pi$ where the potential is maximum are trapped at the point $\xi_{\rm tr} = 1.67 \approx \pi/2$. For shorter acceleration distances (see, e.g., the dotted line obtained for $L_{\rm acc}/L_{\rm ph}$ = 0.1), the expression derived for the compression factor from formula (11) is in good quantitative agreement with the numerical results only in the range $k_pL_{b0} \ll 1$.

We now make one more comment on the change in the energy of an electron bunch in the trapping stage. The above analysis revealed that, even in sufficiently short bunches, the electron trajectories, although close to each other, are different. It is this circumstance that provides the possibility of compressing bunches in the acceleration direction. On the other hand, the difference between the electron trajectories inevitably gives rise to the energy spread of the electrons in the initially monoenergetic bunch. Using formula (10), we can obtain the following estimate for the energy spread of a

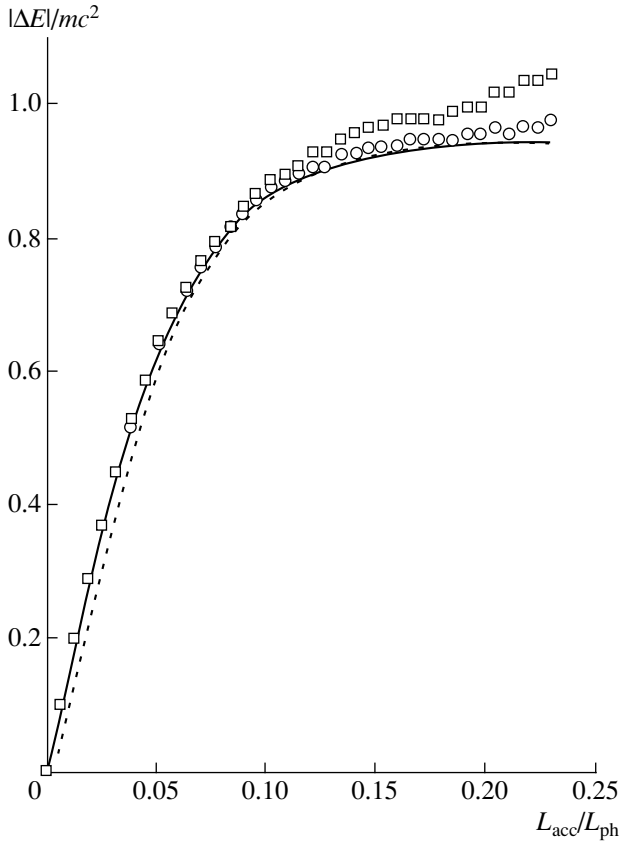

Fig. 2. Energy spread of the electrons in a bunch injected at the energy $E_{inj} = 20mc^2$ into the vicinity of the point of the maximum potential vs. the acceleration length in a wake wave with the parameters $\gamma = 50$ and $|e|\phi_0/mc^2 = 0.01$. The solid curve illustrates the results of one-dimensional numerical simulation, and the dashed curve gives the results obtained from analytic formula (13). The results from three-dimensional simulations for two bunches with R_b/R_p = 0.033 and 0.067 are demonstrated by circles and squares, respectively.

short bunch injected into the vicinity of the point of the maximum potential:

$$\Delta E = -|e|\gamma\left\{\frac{E_{inj}p(\xi)}{E(\xi)p'_{inj}}\frac{d\phi(\xi)}{d\xi}k_pL_{b0}\right.$$
$$\left.+\frac{\gamma}{2}\left|\frac{d^2\phi(\xi_{inj})}{d\xi^2}\right|\frac{p(\xi)c}{E(\xi)}\left[\beta+\frac{E'_{inj}}{p'_{inj}c}+I_2\right](k_pL_{b0})^2\right\}, \quad (15)$$

where ΔE is the difference in energy between the electrons in the trailing and leading edges of the bunch.

Figure 2 illustrates the dependence of the energy spread of an electron bunch with the initial length $L_{b0} = 0.1k_p^{-1}$ on the acceleration distance in the trapping stage. The remaining parameters are the same as in Fig. 1. The solid curve shows the results of one-dimensional numerical simulation, and the dashed curve gives the results obtained from analytic formula (15). The slight discrepancy that remains at short acceleration distances (which, however, are unimportant for practical purposes) stems from the fact that we neglected some terms in the expansions in formulas (9) and (10). In the most important range of sufficiently long acceleration distances over which the bunch is compressed significantly, the analytical and numerical results are seen to agree well.

The symbols in Fig. 2 demonstrate the results of three-dimensional simulations of the electron dynamics [11, 17] for two bunches with the relative dimensionless radii R_b/R_p = 0.033 (circles) and 0.067 (squares) and for $k_pR_p = 3.0$. The simulations were performed for a Gaussian radial profile of the wakefield potential, $\phi(\xi, r) = -\phi_0\cos(\xi)\exp[-(r/R_p)^2]$. The good agreement between the numerical and analytical results completely confirms the following conclusion that was drawn in [14]: the dynamics of the energy characteristics and spatial (in the longitudinal direction) parameters of electron bunches whose radii are much smaller than the radius $R_{max, opt}$ of the optimum injection region (in the example at hand, we have $R_{max, opt} \approx k_p^{-1}$, so that the inequality $R_b \ll R_{max, opt}$ holds) and which as a whole are injected into the optimum region can be estimated using formulas of one-dimensional theory.

Our calculations and estimates also show that, under certain conditions, the second term on the right-hand side of formula (15) may be much smaller than the first term and, thus, can be neglected. As an example, for the above parameter values $\gamma = 50$, $E_{inj}/mc^2 = 20$, and $|e|\phi_m/mc^2 = 0.01$, the energy spread of an electron bunch with the initial length $L_{b0} = 0.1k_p^{-1}$ is calculated to within an error of less than 0.25%. Such a small error is attributed to the fact that, in formula (15), the conditions $|I_2| \ll 1$ and $|\beta + E'_{inj}/cp'_{inj}| \ll 1$ hold for the electron trajectories under consideration, for which the energy of the injected bunch is much lower than the resonant energy for the wave with the above parameters, $E_{inj} \ll \gamma mc^2$, and the bunch is trapped in the region where the wave potential is almost linear (e.g., at $\xi_{tr} = \pi/2$). In this case, the energy spread of the bunch in the trapping stage can be estimated from the approximate formula

$$|\Delta E| = |e|\gamma\left\{\frac{E_{inj}}{|p'_{inj}|c}\frac{d\phi(\xi)}{d\xi}k_pL_{b0}\right\}. \quad (16)$$

For a linear plasma wave with the potential of the form $\phi(\xi, r) = -\phi_0\cos(\xi)$, the energy spread at the boundary of the region of the focusing phase of the corresponding linear three-dimensional wake wave near the point $\xi_{tr} = \pi/2$ can be estimated from formula (16)

with allowance for the trapping condition (14):

$$|\Delta E| = E_{\text{inj}} k_p L_{b0} \sqrt{\frac{E'_{\text{inj}} - mc^2}{E'_{\text{inj}} + mc^2}}. \quad (17)$$

For $E'_{\text{inj}} \gg mc^2$, we obtain the following, simpler estimate for the energy spread of the bunch electrons near the trapping region after the bunch is compressed by the linear wave: $|\Delta E| = E_{\text{inj}} k_p L_{b0}$.

In connection with the problem of optimizing the process of the trapping and acceleration of an electron bunch in order to achieve such bunch parameters in the trapping stage that will not substantially deteriorate during the subsequent acceleration of the bunch to high energies, it is of interest to consider the trapping and acceleration of a one-dimensional bunch. In this respect, the short length of the compressed bunch and the minimized energy spread of the bunch electrons may be used as a criterion of the quality of one-dimensional compression. In order to achieve the desired quality, it is necessary to choose the optimum parameters of the wakefield and injected bunch. Recall that the compression is most efficient when the bunch is trapped near the boundary of the region of the focusing phase of the three-dimensional wake wave. However, from formula (12), we can see that a linear small-amplitude wake wave is not the best means of compressing the bunch, because, for such a wave, $\alpha_2(\xi_{\text{tr}}) = 1$. For a nonlinear wave, the ratio of the derivatives of the potential in the coefficient $\alpha_2(\xi_{\text{tr}})$ can be markedly smaller, because the larger the wakefield amplitude, the smoother the potential profile near its maximum and the steeper the slope of the profile at the trapping point near the boundary of the region of the focusing phase of the wave. It is well known [18] that, in the limiting case of a strongly nonlinear potential wave with the total potential difference $|e|\Delta\phi/mc^2 = |e|2\phi_0/mc^2 \gg 1$, the wave potential over the period is nearly parabolic in shape: $\phi(\xi) = \phi_0(4\xi/\pi - 2\xi^2/\pi^2 - 1)$, where $0 < \xi < 2\pi$. In this case, the boundary of the region of the focusing phase of the corresponding, strongly nonlinear, three-dimensional wake wave lies in the vicinity of the point of the minimum potential (in the case at hand, near the point $\xi = 0$), so that the electron bunch can be trapped in the entire region corresponding to the total potential difference in the wave, $\Delta\phi = 2\phi_0$ [19]. We thus arrive at the coefficient $\alpha_2 = \pi^{-1}$, which indicates that the compression of a bunch by a strongly nonlinear wave is approximately three times higher than that by a linear wave. The energy spread of the electrons in a bunch injected at an energy $E'_{\text{inj}} \gg mc^2$ and then trapped by a strongly nonlinear wave can be estimated as $|\Delta E| = E_{\text{inj}} k_p L_{b0} 2/\pi$, which is smaller than the energy spread of a bunch in a linear wave. That the compression by a nonlinear wave is more efficient than that by a linear wave is also confirmed by relationship (14), which implies that, for the same trapping point, the larger the wave amplitude, the lower the energy of the injection bunch. We thus can conclude that nonlinear large-amplitude wake waves are most preferable from the standpoint of the efficient compression of one-dimensional bunches. Physically, this conclusion is easy to explain: the stronger the wave nonlinearity, the smaller the energy spread of the bunch electrons and the closer the electron trajectories to each other.

3. DYNAMICS OF THE BUNCH PARAMETERS IN THE ACCELERATION STAGE

In the acceleration stage, the electron bunch injected at an energy such that the electron velocity is higher than the phase velocity of the wake wave experiences no longitudinal compression (this point was considered in Section 2). In this case, the wake field immediately starts to accelerate the bunch to high energies on a time scale much longer than the duration of the compression stage. Of course, the bunch should be injected into the region of the appropriate phase of the wake wave. It is obvious that the optimum injection region in the propagation direction of the wave is now the vicinity of the boundary of the focusing phase, where the potential gradient is the largest, provided that the electrons are focused by a positive force. For the wakefield potential $\phi(\xi, r) = -\phi_0\cos(\xi)\exp[-(r/R_p)^2]$, the optimum injection region is $\xi_{\text{inj}} \geq \pi/2$.

In the acceleration stage, the dynamics of the energy characteristics and spatial parameters of an initially monoenergetic, short electron bunch can be investigated by applying the approach described in Section 2 and using relationships analogous to formulas (4) and (5). In this way, we must keep in mind that, in expression (5), the integral over electron trajectories is of the opposite sign, because, in the wave rest frame, the electrons immediately start moving in the positive direction along the z'-axis. In the expansions, we can take into account only the first-order terms in the small variations $\Delta\xi = k_p L_b$ and ΔE, because the condition $d\phi/d\xi \neq 0$ holds over the entire electron trajectory. As the reference electron (about which the variations will be made), we choose the last electron in the bunch, in which case $\Delta\xi$ and ΔE are equal, respectively, to the differences between the coordinates and energies of the first and last electrons in the bunch. As a result, we arrive at the relationships

$$L_b = L_{b0}\frac{\gamma c p'(\xi)}{E(\xi)}\left\{\beta + \frac{\dfrac{d\phi(\xi_{\text{inj}})}{d\xi}}{\dfrac{d\phi(\xi)}{d\xi}}\frac{E'(\xi)}{cp'(\xi)} + I_0(\xi)\right\}, \quad (18)$$

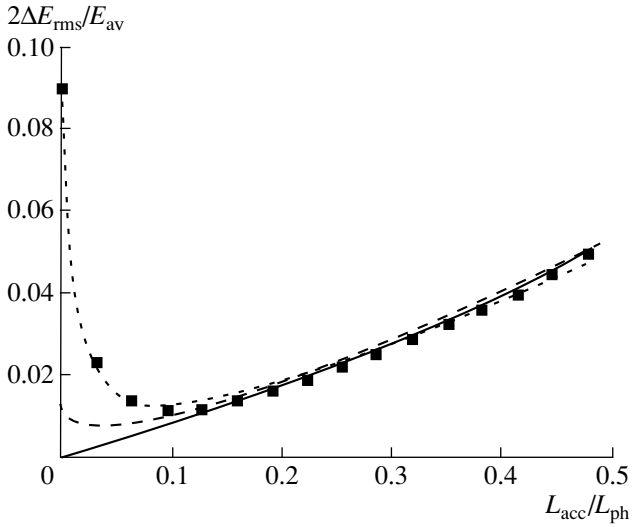

Fig. 3. Energy characteristics of different electron bunches in the acceleration stage vs. the acceleration length (E_{av} is the averaged electron energy and ΔE_{rms} is the root-mean-square energy spread of the bunch electrons). The computation parameters corresponding to different plots are described in the body of the paper.

$$\Delta E = |e|\gamma^2 k_p L_{b0}\frac{cp(\xi)}{E(\xi)} \times\left\{\beta\left(\frac{d\phi(\xi)}{d\xi}-\frac{d\phi(\xi_{inj})}{d\xi}\right)+\frac{d\phi(\xi)}{d\xi}I_0(\xi)\right\}, \quad (19)$$

where

$$I_0(\xi) = \int\limits_{\xi_{inj}}^{\xi}\frac{d\eta\dfrac{d\phi(\xi_{inj})}{d\xi}\dfrac{d^2\phi}{d\eta^2}\left(\dfrac{d\phi}{d\eta}\right)^{-2}}{\{1-m^2c^4[E'_{inj}+\gamma|e|(\phi(\eta)-\phi(\xi_{inj}))]^{-2}\}^{1/2}}. \quad (20)$$

These relationships can be simplified using the simple estimate

$$\frac{1}{\{1-m^2c^4[E'+\gamma|e|(\phi(\eta)-\phi(\xi_{inj}))]^{-2}\}^{1/2}} \geq \frac{E'(\xi)}{cp'(\xi)}, \quad (21)$$

which is valid over the entire electron trajectory (i.e., for $\xi_{inj} < \eta < \xi$). Using inequality (21), we can readily show that, in the acceleration stage, the bunch length does not increase. This is quite evident, because, in the wakefield with the above potential, the last electron in the bunch injected in the above manner always experiences a stronger accelerating force than the first electron. Accordingly, the lower estimate for the energy spread of the bunch electrons after acceleration is

$$|\Delta E(\xi)| > k_p L_{b0}\gamma|e|\frac{p(\xi)}{p'(\xi)}\left|\frac{d\phi(\xi)}{d\xi}-\frac{d\phi(\xi_{inj})}{d\xi}\right|. \quad (22)$$

If, after acceleration, the electron momentum in the wave rest frame is sufficiently large, $p'(\xi) \gg mc$, then the lower estimate for the maximum energy spread of the electrons in an initially monoenergetic accelerated bunch can be obtained from the simpler approximate formula

$$|\Delta E| \approx 2\gamma^2|e|k_p L_{b0}\left\{\frac{d\phi(\xi_{inj})}{d\xi}-\frac{d\phi(\xi)}{d\xi}\right\}, \quad (23)$$

which is, however, far more exact than the corresponding formula derived in [20]. All of the above formulas for the energy spread of the bunch electrons show that, first, the longer the region where the accelerating potential is nonlinear, the larger the energy spread, and, second, the energy spread is linearly proportional to the initial bunch length.

In order to check the above estimates for the energy spread of an accelerated electron bunch, we carried out a series of test simulations. First, we simulated the acceleration of a one-dimensional bunch formed by the compression of a one-dimensional monoenergetic electron bunch with the initial energy $E_{inj} = 20mc^2$ in a plasma wave with the parameters $\gamma = 50$ and $|e|\phi_0/mc^2 = 0.01$. The length of the injected bunch in the trapping stage was chosen such that the electrons occupied the entire optimum injection region in the longitudinal direction [14], in which case, throughout the trapping stage, all of the bunch electrons remained in the focusing phase of the corresponding linear wake wave (this way of forming a compact bunch was described in more detail in [13]). By the time the electrons acquired a resonant energy of about $\approx 50mc^2$ in the trapping stage, the length of the bunch was $L_b = 0.1k_p^{-1}$. After the trapping stage, the bunch was injected into the accelerating stage with the plasma wave parameters $|e|\phi_0/mc^2 = 0.3$ and $\gamma = 50.0$, specifically, into the region of the strongest accelerating field; for the potential $\phi(\xi) = -\phi_0\cos(\xi)$, this is $\xi_{inj} \approx \pi/2$. In Fig. 3, the change in the relative root-mean-square energy spread of an electron bunch accelerated in such a manner is illustrated by the dotted curve.

The solid curve in Fig. 3 demonstrates an increase in the relative root-mean-square energy spread of the bunch electrons accelerated by the same wake wave. This curve was obtained using the analytic formula (23) for an initially monoenergetic electron bunch with the injection energy $E_{inj} = 50mc^2$ and the initial length $L_{b0} = 0.1k_p^{-1}$. The root-mean-square energy spread was estimated under the assumption that the electrons are distributed uniformly over the energy interval determined

by formula (23). We can see that, even when the initial energy spread of the injected bunch is nonzero (as is the case in the first example), the solid and dotted curves approach one another and, after a certain time, remain very close together. Such a coincidence of the curves confirms our analytical results and indicates that the approximate formula (23) for the smallest energy spread of the electrons in the accelerated bunch is actually quite exact and can be used directly for estimates, provided that the acceleration length is not too short in comparison with the maximum acceleration length. The unimportance of the initial energy spread of the electrons at the time at which the bunch is injected into the accelerating stage indicates that, during acceleration, the bunch electrons acquire an additional energy spread: the final energy spread of the bunch eventually becomes larger than the initial energy spread and thus plays the governing role.

The dashed curve in Fig. 3 illustrates the change in the root-mean-square energy spread of the bunch that has the same initial length $L_{b0} = 0.1k_p^{-1}$ and is formed in the same way as in the first example but by the same plasma wave in which the bunch is accelerated, i.e., by the wave with the parameters $|e|\phi_0/mc^2 = 0.3$ and $\gamma = 50.0$. Since the amplitude of this plasma wave is larger than that in the first example, the energy of the injected electron bunch from which the bunch to be accelerated was formed in the compression stage is smaller, $E_{inj} = 1.87mc^2$. This series of simulations differs from the first series only in the initial energy spreads of the bunches injected into the accelerating stage. Note that, in the examples at hand, the initial energy spread is well estimated from formula (17). The good agreement between the results of these two series of simulations for long acceleration distances indicates that, for the same parameters of the acceleration process, the spatial (longitudinal) and energy characteristics of the bunches accelerated to high energies do not differ fundamentally between these two model examples, although the latter example better fits the analytical results.

It is of interest to compare the results of one-dimensional simulations and analytic predictions with the results of three-dimensional simulations. In Fig. 3, the closed squares illustrate the root-mean-square energy spread of the accelerated bunch that is formed from a three-dimensional monoenergetic bunch of radius $R_b = 0.5k_p^{-1}$ and, at the beginning of the compression stage (at the instant of injection), occupies the entire optimum injection region in the longitudinal direction. In three-dimensional simulations, both the compressing and accelerating wake waves were specified by the same potential $\phi(\xi) = -\phi_0\cos(\xi)\exp(-(r/R_p)^2)$ with $R_p = 3.0k_p^{-1}$ and the wakefield parameters were chosen to be $\gamma = 50$ and $|e|\phi_0/mc^2 = 0.01$ (in the compression stage) and $\gamma = 50$ and $|e|\phi_0/mc^2 = 0.3$ (in the acceleration stage). The remaining parameters of the three-dimensional extended injected bunch and the compression and acceleration scheme corresponded to the first example (see [14] for more details). The closed squares are seen to agree well with the plots obtained from one-dimensional simulations and analytic formulas. This agreement is predictable, because the electrons of the given bunch were injected into the optimum injection region and, for the above parameters of the bunch and of the compressing field, the initial radius of the injected bunch in the compression stage was smaller than $R_{max, opt}$.

4. CONCLUSION

Our analytic investigation provides better insight into the mechanism for changes in both the spatial (longitudinal) and energy characteristics of electron bunches injected into wake waves under different conditions.

We have studied the compression of short ($k_pL_b \ll 1$) electron bunches by wake waves when the bunches are injected at energies such that the initial electron velocity is lower than the wave phase velocity. We have shown how the bunch length decreases in the course of the bunch trapping by the wakefield and how the energy spread of an initially monoenergetic bunch increases. We have derived simple analytic formulas that make it possible to estimate these bunch parameters. Our analytical results agree well with the results of numerical simulations. We have shown that the proposed mechanism for compressing an electron bunch can be used to optimize the precompression of the trapped bunches in order to raise the quality of the subsequent acceleration.

We have considered how the parameters of a short electron bunch change in the acceleration stage, provided that the bunch electrons are injected at a velocity higher than the phase velocity of the wake wave. The length of the accelerated bunch is found to change only slightly; at least, it does not increase, whereas the energy spread of the bunch electrons increases. The final energy spread is linearly proportional to the initial bunch length; consequently, for the quality of acceleration to be high, it is desirable to use the shortest possible bunches or to precompress the bunches to be accelerated. Our analytic formulas are shown to provide quite exact estimates for the spatial (longitudinal) and energy characteristics of the electron bunches in both the compression and the acceleration stages, provided that the bunch is injected into the optimum injection region.

ACKNOWLEDGMENTS

This work was supported in part by the Russian Foundation for Basic Research, project no. 98-02-16263.

REFERENCES

1. K. Nakajima, D. Fisher, T. Kawakubo, *et al.*, Phys. Rev. Lett. **74**, 4428 (1995).
2. A. Modena, Z. Najmudin, A. E. Dangor, *et al.*, Nature **377**, 606 (1995).
3. D. Umstadter, S. J. Chen, G. Mourou, *et al.*, Science **273**, 472 (1996).
4. E. Esarey, P. Sprangle, J. Krall, and A. Ting, IEEE Trans. Plasma Sci. **24**, 252 (1996).
5. N. E. Andreev and L. M. Gorbunov, Usp. Fiz. Nauk **169**, 1 (1999).
6. I. V. Pogorelsky, in *Proceedings of the International Conference LASERS'97, New Orleans, 1997*, Ed. by J. J. Carroll and T. A. Goldman (STS Press, McLean, 1998), p. 868.
7. A. Ogata, K. Nakajima, T. Kozawa, and Y. Yoshida, IEEE Trans. Plasma Sci. **24**, 453 (1996).
8. I. V. Pogorelsky, N. E. Andreev, and S. V. Kuznetsov, in *Proceedings of Conference "Advanced Accelerator Concepts," Baltimore, MD, 1998* (American Inst. of Physics, New York, 1999) [AIP Conf. Proc. **472**, 444 (1999)].
9. A. Ogata, K. Nakajima, and N. Andreev, J. Nucl. Mater. **248**, 392 (1997).
10. N. E. Andreev, L. M. Gorbunov, and S. V. Kuznetsov, Fiz. Plazmy **21**, 1099 (1995) [Plasma Phys. Rep. **21**, 1037 (1995)].
11. N. E. Andreev, L. M. Gorbunov, and S. V. Kuznetsov, IEEE Trans. Plasma Sci. **24**, 448 (1996).
12. I. V. Pogorelsky, W. D. Kimura, D. C. Quimby, *et al.*, in *Proceedings of XVII International Conference on Coherent and Nonlinear Optics, Moscow, 1998* [Proc. SPIE **3735**, 175 (1999)].
13. N. E. Andreev and S. V. Kuznetsov, Kratk. Soobshch. Fiz., No. 1, 9 (1999).
14. N. E. Andreev and S. V. Kuznetsov, IEEE Trans. Plasma Sci. **28**, 1170 (2000).
15. L. M. Gorbunov and V. I. Kirsanov, Zh. Éksp. Teor. Fiz. **93**, 509 (1987) [Sov. Phys. JETP **66**, 290 (1987)].
16. N. E. Andreev, L. M. Gorbunov, V. I. Kirsanov, *et al.*, Phys. Plasmas **4**, 1145 (1997).
17. N. E. Andreev, A. A. Frolov, S. V. Kuznetsov, *et al.*, in *Proceedings of the International Conference LASERS'97, New Orleans, 1997*, Ed. by J. J. Carroll and T. A. Goldman (STS Press, McLean, 1998), p. 875.
18. J. M. Dawson, Phys. Rev. **113**, 383 (1959).
19. N. E. Andreev and S. V. Kuznetsov, Fiz. Plazmy **25**, 810 (1999) [Plasma Phys. Rep. **25**, 746 (1999)].
20. S. Wilks, T. Katsouleas, J. M. Dawson, *et al.*, IEEE Trans. Plasma Sci. **15**, 210 (1987).

Translated by G.V. Shepekina

Plasma Physics Reports, Vol. 27, No. 5, 2001, pp. 381–389. Translated from Fizika Plazmy, Vol. 27, No. 5, 2001, pp. 406–414.

BEAMS IN PLASMA

Cherenkov Excitation of Spatial Waves by a Straight Nonrelativistic Electron Beam in a Plasma Waveguide

I. N. Kartashov and M. V. Kuzelev

Institute of General Physics, Russian Academy of Sciences, ul. Vavilova 38, Moscow, 117942 Russia

Received July 12, 2000; in final form, September 19, 2000

Abstract—The problem of the excitation of plasma waves by a thin-walled annular electron beam in a waveguide filled entirely with a plasma is analyzed in the quasistatic approximation. The instability growth rates are derived and are studied as functions of the waveguide parameters. The evolution of different seed perturbations in the nonlinear stage of the instability is investigated. © *2001 MAIK "Nauka/Interperiodica".*

1. Much attention has recently been devoted to experimental [1, 2] and theoretical [3, 4] studies of the Cherenkov mechanism for the excitation of surface waves of an annular plasma by a straight electron beam in a metal waveguide. The spectrum of the surface waves of an annular plasma is fairly sparse (the dispersion curves of the surface waves consist of a small number of branches and the surface waves themselves are easy to excite under both single-particle and collective Cherenkov resonance conditions), which makes it feasible to achieve a single-mode regime of the generation of surface waves and to control the frequency range of the excited waves. These circumstances have stimulated increased interest in the Cherenkov excitation of surface plasma waves in waveguides. However, spatial plasma waves are of no less interest from the standpoint of the Cherenkov excitation mechanism and may also hold great promise for practical applications. A number of distinctive features in which spatial waves differ from the corresponding surface waves are the focus of our theoretical analysis. For simplicity, we restrict ourselves to the quasistatic approximation and, accordingly, consider a nonrelativistic electron beam. A relativistic electron beam in the nonquasistatic approximation will be studied in a separate paper.

2. Let us consider an infinitely thin (needle-shaped) nonrelativistic electron beam in a metal waveguide with an arbitrary, simply connected cross section. Let us assume that the waveguide is filled entirely with a homogeneous (over the waveguide cross section) plasma and is immersed in an external longitudinal magnetic field strong enough for the transverse motion of the beam and plasma electrons to be neglected (the ions are assumed to be immobile). We also assume that the beam and plasma are both cold and that the beam density is sufficiently low so that the motion of the plasma electrons can be described in the linear approximation. It is well known that the only waves that can be excited in a waveguide filled entirely with a plasma are spatial plasma waves [5].

The potential perturbations in the system under consideration are described by the equations

$$\left(\Delta_\perp + \frac{\partial^2}{\partial z^2}\right)\varphi = -4\pi S_b \delta(\mathbf{r}_\perp - \mathbf{r}_b)(\rho_b - \rho_{0b}) - 4\pi\rho_p,$$

$$\frac{\partial^2 \rho_p}{\partial t^2} = \frac{\omega_p^2}{4\pi}\frac{\partial^2 \varphi}{\partial z^2}, \quad \rho_b = e\int f_b(t, z, v)dv, \qquad (1)$$

$$\frac{\partial f_b}{\partial t} + v\frac{\partial f_b}{\partial z} + \frac{e}{m}\left(-\frac{\partial \varphi}{\partial z}\right)\frac{\partial f_b}{\partial v} = 0.$$

Here, φ is the scalar potential, z is the coordinate along the waveguide axis, $\mathbf{r}_\perp$ is the radial coordinate in the waveguide cross section, $\Delta_\perp$ is the transverse Laplace operator, v is the electron velocity, e and m are the charge and mass of an electron, $\omega_p = \sqrt{4\pi e^2 n_{0p}/m}$ and n_{0p} are the Langmuir frequency and unperturbed density of the plasma electrons, ρ_p is the perturbed charge density in a plasma, ρ_b is the beam charge density, ρ_{0b} is the density of the electrostatic charge that neutralizes the beam charge, f_b is the distribution function of the beam electrons, S_b is the cross-sectional area of the beam, and $\mathbf{r}_b$ is the average radial coordinate of the beam in the waveguide cross section. We assume that, at the initial time, the distribution function of the beam electrons satisfies the condition

$$f_b(0, z, v) \equiv f_0(v) = n_{0b}\delta(v - u), \qquad (2)$$

where n_{0b} is the unperturbed beam density and u is the unperturbed beam velocity. Obviously, we have $\rho_{0b} = en_{0b}$.

It is well known [6] that the general solution to the kinetic equation for the distribution function f_b is expressed in terms of the following integral over the

initial solutions to the characteristic system for the Vlasov equation:

$$f_b(t, z, v) = \iint dz_0 dv_0 f_0(v_0)\delta[z - z_b(t, z_0, v_0)] \times \delta[v - v_b(t, z_0, v_0)], \quad (3)$$

where $z_b(t, z_0, v_0)$ and $v_b(t, z_0, v_0)$ are the solutions to the characteristic system

$$\frac{dz_b}{dt} = v_b, \quad \frac{dv_b}{dt} = -\frac{e}{m}\frac{\partial\varphi}{\partial z}, \quad (4)$$

supplemented with the initial conditions

$$z_b|_{t=0} = z_0, \quad v_b|_{t=0} = v_0. \quad (5)$$

We substitute function (3) into Eqs. (1) and, using relationship (2), perform the velocity integration in order to arrive at the following equations, which will serve as a basis for further analysis:

$$\left(\Delta_\perp + \frac{\partial^2}{\partial z^2}\right)\varphi' = \omega_b^2 S_b \delta(\mathbf{r}_\perp - \mathbf{r}_b) \times \{\int dz_0 \delta[z - z_b(t, z_0)] - 1\} + \omega_p^2 \rho_p',$$

$$\frac{\partial^2 \rho_p'}{\partial t^2} = -\frac{\partial^2 \varphi'}{\partial z^2}, \quad (6)$$

$$\frac{dz_b}{dt} = v_b, \quad \frac{dv_b}{dt} = \frac{\partial\varphi'}{\partial z}(t, z_b, \mathbf{r}_b),$$

$$z_b|_{t=0} = z_0, \quad v_b|_{t=0} = u.$$

Here, $\varphi' = -e\varphi/m$, $\rho_p' = \rho_p/en_{0p}$, and $\omega_b = \sqrt{4\pi e^2 n_{0b}/m}$ is the Langmuir frequency of the beam electrons. For the beam, an exact analog of the dimensionless plasma charge density ρ_p' is the function

$$\rho_b' = \int dz_0 \delta[z - z(t, z_0)] - 1, \quad (7)$$

which enters the right-hand side of the first equation in set (6). Note that, in expression (7) [as well as in Eqs. (1) and (6)], we eliminate a constant background charge, because we assume that the electrostatic beam charge in the plasma is completely neutralized [7]. In the linear approximation, we can use the third and fourth equations in set (6) and the initial conditions for these equations in order to show that the beam charge density (7) satisfies the equation

$$\left(\frac{\partial}{\partial t} + u\frac{\partial}{\partial z}\right)^2 \rho_b' = -\frac{\partial^2 \varphi'}{\partial z^2}. \quad (8)$$

Finally, replacing $S_b\delta(\mathbf{r}_\perp - \mathbf{r}_b)$ with unity in the first equation in set (6), we arrive at the equations that describe a waveguide in which the plasma and beam are both uniform over the waveguide cross section. Below, such a waveguide will serve as a certain reference point for a comparative analysis of the results obtained.

3. Let the characteristic longitudinal scale (period) of the initial perturbation in the waveguide under consideration be L. Then, all the perturbed quantities (in particular, the potential φ' and density ρ_p') can be represented as

$$\varphi' = \frac{1}{2}\sum_{n=1} [\varphi_n(\mathbf{r}_\perp, t)\exp(ink z) + \text{c.c.}],$$
$$\rho_p' = \frac{1}{2}\sum_{n=1} [\rho_{pn}(\mathbf{r}_\perp, t)\exp(ink z) + \text{c.c.}], \quad (9)$$

where $k = 2\pi/L$ is the mean longitudinal perturbation wavenumber. Inserting expressions (9) into Eqs. (6) and using the orthogonality of the functions $\exp(ikz)$, we obtain the following equations for the expansion coefficients φ_n and ρ_{pn}:

$$(\Delta_\perp - n^2k^2)\varphi_n = \omega_b^2 S_b \delta(\mathbf{r}_\perp - \mathbf{r}_b)\rho_{bn} + \omega_p^2 \rho_{pn},$$
$$\frac{\partial^2 \rho_{pn}}{\partial t^2} = n^2k^2\varphi_n, \quad (10)$$

where functions ρ_{bn} have the form

$$\rho_{bn} = \frac{1}{\pi}\int_0^{2\pi} \exp(-iny_b)dy_0, \quad y_b = kz_b. \quad (11)$$

Now, we assume that all the transverse eigenfunctions and eigenvalues of the waveguide are known; i.e., we know the solutions to the problem

$$\Delta_\perp \phi_m = -k_{\perp m}^2 \phi_m,$$
$$\phi_m|_{\sigma=0} = 0, \quad (12)$$

where ϕ_m is an eigenfunction, $k_{\perp m}^2$ is the corresponding eigenvalue ($m = 1, 2, \ldots$), and $\sigma \equiv \sigma(\mathbf{r}_\perp) = 0$ is the equation for the metal waveguide surface. With the expansions

$$\varphi_n = \sum_{m=1} \tilde{\varphi}_{n,m}(t)\phi_m(\mathbf{r}_\perp),$$
$$\rho_{pn} = \sum_{m=1} \tilde{\rho}_{n,m}^p(t)\phi_m(\mathbf{r}_\perp), \quad (13)$$

Eqs. (10) become

$$(k_{\perp m}^2 + n^2k^2)\tilde{\varphi}_{n,m} + \omega_p^2 \tilde{\rho}_{n,m}^p = -\frac{\omega_b^2 S_b}{\|\phi_m\|^2}\phi_m(\mathbf{r}_b)\rho_{bn},$$
$$\frac{d^2\tilde{\rho}_{n,m}^p}{dt^2} - n^2k^2\tilde{\varphi}_{n,m} = 0. \quad (14)$$

Here and below, the subscript n specifies the longitudinal (along the z-axis) mode number and the subscript m defines the transverse waveguide mode number (below, we will always put the subscript n in front of the subscript m). Now, we substitute Eqs. (14) with relationships (9) and (13) into the equations of beam electron motion in set (6), in which case it is expedient to exclude coefficients $\tilde{\varphi}_{n,m}$ from consideration. As a result, we arrive at the equations

$$\begin{aligned}
&\frac{d^2\rho^p_{n,m}}{dt^2} + \omega_p^2\alpha_{n,m}\rho^p_{n,m} = -\omega_b^2\beta_{n,m}\rho_{bn},\\
&\frac{d^2y_b}{dt^2} + \frac{1}{2}i\omega_b^2\sum_n\frac{1}{n}[g_n\rho_{bn}\exp(iny) - \text{c.c.}]\\
&= -\frac{1}{2}i\omega_p^2\sum_n\frac{1}{n}\left[\sum_m\alpha_{n,m}\rho^p_{n,m}\exp(iny) - \text{c.c.}\right].
\end{aligned} \tag{15}$$

Here, we set $\rho^p_{n,m} = \phi_m(\mathbf{r}_b)\tilde{\rho}^p_{n,m}$ and introduce the notation

$$\alpha_{n,m} = \frac{n^2k^2}{k_{\perp m}^2 + n^2k^2}, \quad \beta_{n,m} = \frac{S_b\phi_m^2(\mathbf{r}_b)}{\|\phi_m\|^2}\frac{n^2k^2}{k_{\perp m}^2 + n^2k^2}, \tag{16}$$
$$g_n = \sum_m\beta_{n,m}.$$

Equations (15) are rather peculiar and have a complicated structure, because each value of n corresponds to a large (generally, infinite) set of the values $m = 1, 2, \ldots$. In other words, each longitudinal mode ρ_{bn} of the beam wave generates a large number of spatial plasma waves $\rho^p_{n,m}$, which correspond to all possible transverse wavenumbers $k_{\perp m}$. The reason for this is that the modes of a thin beam are surface waves, whereas the modes a continuous plasma are spatial waves. In such a waveguide system, the transverse modes not only interact with each other in a complex manner, but the nonlinear nature of the beam also gives rise to the interaction between longitudinal modes with different numbers n.

4. Let us examine Eqs. (15) in the linear approximation. In accordance with the initial conditions for Eqs. (6), we assume that $y_b = y_0 + kut + \tilde{y}$. Linearizing expression (11) and the second equation from set (15) in $\tilde{y}$ and performing simple manipulations yields the equations

$$\begin{aligned}
&\frac{d^2\rho^p_{n,m}}{dt^2} + \omega_p^2\alpha_{n,m}\rho^p_{n,m} = -\omega_b^2\beta_{n,m}\rho_{bn},\\
&\left(\frac{d}{dt} + inku\right)^2\rho_{bn} + \omega_b^2g_n\rho_{bn} = -\omega_p^2\sum_m\alpha_{n,m}\rho^p_{n,m}.
\end{aligned} \tag{17}$$

Since, in the linear approximation, longitudinal modes with different numbers n do not interact with each other, Eqs. (17) refer to a mode with an arbitrary number n.

In the linear approximation, we as usual seek a solution in the form $\rho_{bn}, \rho^p_{n,m} \sim \exp(-i\omega t)$, in which case we can find the amplitudes $\rho^p_{n,m}$ from the first equation in set (17) and substitute them into the second equation in order to obtain the linear dispersion relation

$$(\omega - nku)^2 = \omega_b^2\sum_m\left[\frac{S_b\phi_m^2(\mathbf{r}_b)}{\|\phi_m\|^2}\frac{n^2k^2}{k_{\perp m}^2 + n^2k^2(1 - \omega_p^2/\omega^2)}\right]. \tag{18}$$

The poles of the right-hand side of Eq. (18), or the zeros of the functions

$$k_{\perp m}^2 + n^2k^2\left(1 - \frac{\omega_p^2}{\omega^2}\right) = 0, \quad m = 1, 2, \ldots, \tag{19}$$

determine the spectra of spatial plasma waves with the longitudinal wavenumber nk in a waveguide free of the electron beam. In Eq. (18), spatial plasma waves with different numbers m are coupled through the surface wave of the beam. This brings about the question of the competition between different plasma modes and of the conditions under which the beam excites a single transverse plasma mode or the desired set of transverse modes. Usually, this question is answered as follows. If the beam density is low, then only those transverse plasma modes can be excited that satisfy the inequality

$$\omega_p^2 > k_{\perp m}^2u^2, \tag{20}$$

the remaining modes being stable. According to the perturbation theory for beam-driven modes [8], the growth rate of the excited mode [which should satisfy inequality (20)] is calculated from Eq. (18), on the right-hand side of which we must retain only the term with the number of the excited mode. Under the conditions of exact Cherenkov resonance between the beam and the mth mode with the longitudinal number

$$nk = \sqrt{\omega_p^2/u^2 - k_{\perp m}^2}, \tag{21}$$

the growth rate of the mth transverse plasma mode is equal to

$$\delta\omega = \frac{-1 + i\sqrt{3}}{2}nku\left(\frac{S_b\phi_m^2(\mathbf{r}_b)}{\|\phi_m\|^2}\frac{\omega_b^2}{2\omega_p^2}\right)^{1/3}. \tag{22}$$

This mode grows as a result of an instability associated with the single-particle Cherenkov effect. As for the collective Cherenkov effect, it does not manifest itself in a waveguide filled entirely with a plasma (at least within the limits of the theory of the interaction

between a thin-walled annular beam and a thin-walled annular plasma [9, 10]). The above analysis applies to a situation in which different spatial plasma waves are excited independently. However, in a waveguide with a thin beam (and, especially, when the beam is dense), the spatial plasma waves are coupled to each other. In this connection, it is of interest to compare the interaction between a thin beam and a continuous plasma with the interaction between a solid beam and a continuous plasma. In the latter case, the linear approximation clearly implies that different transverse plasma modes are decoupled.

Let us specify the geometry of the problem. We consider a thin-walled annular electron beam propagating in a circular waveguide of radius R, which is assumed to be filled entirely with a homogeneous plasma. Such a beam can be regarded as a tube with a mean radius $r_b < R$, the thickness of the tube wall being Δ_b. Under the assumption that $\Delta_b \ll r_b$, the beam cross-sectional area is equal to $S_b = 2\pi\Delta_b r_b$. In a circular waveguide, the eigenfunctions and the associated eigenvalues have the form $\phi_m = J_l(k_{\perp m} r)$ and $k_{\perp m} = \mu_{l,m}/R$, where $\mu_{l,m}$ is the root of the lth order Bessel function. For comparison, we also briefly analyze the case in which the beam is solid and homogeneous, as is the plasma.

For the interaction of an annular electron beam with a homogeneous plasma in a circular waveguide with the adopted parameters, we can use the corresponding formulas of the theory of Bessel functions to rewrite dispersion relation (18) in an explicit form [10]:

$$(\omega - nku)^2 = \omega_b^2 n^2 k^2 \frac{\pi}{2} r_b \Delta_b J_l^2(Xr_b)\left[\frac{N_l(XR)}{J_l(XR)} - \frac{N_l(Xr_b)}{J_l(Xr_b)}\right], \quad (23)$$

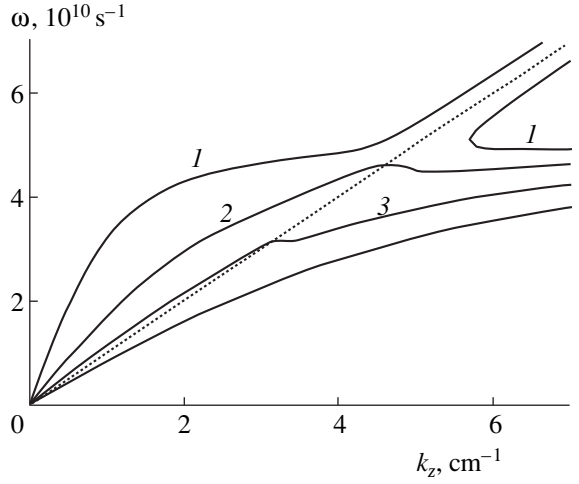

Fig. 1. Dispersion curves for an annular electron beam of radius $r_b = 0.4$ cm in a waveguide filled entirely with a homogeneous plasma at $\nu = 0.01$. The beam is in resonance with the first three transverse plasma modes.

where $X^2 = n^2k^2(\omega_p^2/\omega^2 - 1)$ and $N_l(x)$ is the Neumann function. For the interaction of a solid homogeneous beam with a continuous homogeneous plasma in a circular waveguide, we arrive at an infinite number of independent dispersion relations for the decoupled transverse modes:

$$k_{\perp m}^2 + n^2k^2\left[1 - \frac{\omega_p^2}{\omega^2} - \frac{\omega_b^2}{(\omega - nku)^2}\right] = 0, \quad m = 1, 2, \ldots. \quad (24)$$

Since the structures of dispersion relations (23) and (24) are radically different, the relevant dispersion curves differ in shape. By the dispersion curves, we mean the plots of the real functions $\omega(k_z)$ obtained by solving the corresponding dispersion relations with respect to ω. Parenthetically, we assume that the reader is familiar with the shapes of the dispersion curves of the growing modes under consideration, including those driven by the beam instabilities [3, 4, 9–12]. Dispersion relation (24) is analogous to that describing the excitation of plasma waves when both the beam and the plasma are homogeneous over the entire space. For low-density beams, unstable modes are those with numbers from zero to approximately the number corresponding to the point at which the dispersion curve of the plasma wave intersects the Cherenkov resonance line $\omega = k_z u \equiv nku$. The transverse mode can be either stable or unstable, without any impact on the remaining modes. In other words, when both the beam and the plasma are homogeneous over the entire cross section of a circular waveguide, we may speak of the excitation of an individual transverse mode with a specific number m.

5. Here, we analyze the consequences of the linear dispersion relation (23). To do this, we specify the parameters of the waveguide system. We assume that the waveguide radius is $R = 2$ cm, the beam thickness is $\Delta_b = 0.1$ cm, the azimuthal number is $l = 0$, the plasma frequency is $\omega_p = 5 \times 10^{10}$ rad/s, and the beam density is such that the parameter $\nu = \omega_b^2/\omega_p^2$ takes on the values 0.01 and 5×10^{-5}. We fix these parameters and vary the mean radius r_b of the beam and its velocity u.

First, we choose the beam velocity in such a way that condition (20) is satisfied for the first three transverse modes (with the numbers $m = 1, 2, 3$) and fails to hold for the fourth mode. For example, we set $u = 10^{10}$ cm/s. We also choose the beam radius to be $r_b = 0.4$ cm. With this choice of r_b, the interaction of a beam with the first three transverse modes of the plasma waveguide is fairly efficient. This interaction is illustrated by the dispersion curves in Fig. 1, which were obtained by solving Eq. (23) and are marked by the transverse mode numbers m. In Fig. 1, the abscissa is the longitudinal wavenumber $nk \equiv k_z$ (in cm^{-1}) and the ordinate is frequency ω (in units of 10^{10} rad/s). We can

see that the dispersion curves differ greatly in shape from the familiar dispersion curves obtained for the interaction of a solid beam with a continuous plasma. For a thin-walled annular beam, the only unstable transverse mode is the first one, while the higher modes are stable. However, this does not contradict the situation with a solid beam: we only need to refine the notion of the transverse mode for plasma waveguides with and without a beam.

For a solid beam, each transverse mode with the number $m = 1, 2, \ldots$ is characterized by its own dispersion curve and, accordingly, by the corresponding waveguide mode described by the eigenfunction (the diaphragm function) $\phi_m = J_l(k_{\perp m}r)$ for an empty waveguide. We call such modes transverse modes of a plasma waveguide without a beam. For a thin-walled annular beam, the dispersion curves in Fig. 1 can also be renumbered ($p = 1, 2, \ldots$) in the usual manner (from top to bottom)—see the numerals above the curves. In this case, each dispersion curve is also characterized by a certain waveguide mode, but the corresponding eigenfunction

$$\psi_p(r) = \sum_{m=1} a_m J_l(k_{\perp m}r) \qquad (25)$$

is now determined not only by the plasma but also by the beam. We call these modes transverse modes of a beam–plasma waveguide. From Fig. 1, we can see that, in terms of eigenfunctions (25), the only unstable mode of a plasma waveguide with an annular beam is the first ($p = 1$) transverse mode. In contrast, in terms of the diaphragm functions ϕ_m, at least the first three ($m = 1, 2, 3$) transverse modes of a plasma waveguide are unstable. The latter conclusion is illustrated by Fig. 2a, which shows the function $\mathrm{Im}\,\delta\omega$ versus k_z for the same parameters as in Fig. 1. Here, the complex growth rate $\delta\omega$ is defined as

$$\delta\omega = \omega - k_z u, \qquad (26)$$

where ω is the root of Eq. (23). As is usual for Cherenkov instability, the real part of the complex growth rate $\delta\omega$ is negative, in which case we can say that the beam overtakes the plasma wave. The function $\mathrm{Im}\,\delta\omega$ has three peaks, which reflect the interaction between the beam and the corresponding transverse mode of a plasma waveguide: the right peak is for the $m = 1$ mode, the middle peak is for the $m = 2$ mode, and the left peak is for the $m = 3$ mode. When the beam is not too dense, the growth rate $\delta\omega$ at the point at which its imaginary part is maximum can be calculated from formula (22), in which case we can speak of the Cherenkov excitation of a certain transverse mode of a plasma waveguide by a thin-walled annular beam. However, the denser the beam, the smoother the peaks in the function $\mathrm{Im}\,\delta\omega$, so that the transverse modes of a plasma waveguide become indistinguishable. In this case, eigenfunction (25) is composed of a large number of terms, and it would be more correct to speak of the instability of the first ($p = 1$) transverse mode of a beam–plasma waveguide. Note that, in terms of Eqs. (23) and (24), the limiting transition from a thin-walled annular beam to a solid beam is impossible. The above analysis of a low-density beam is illustrated by Fig. 3a, which refers to the value $\nu = 5 \times 10^{-5}$. We can see that the three peaks,

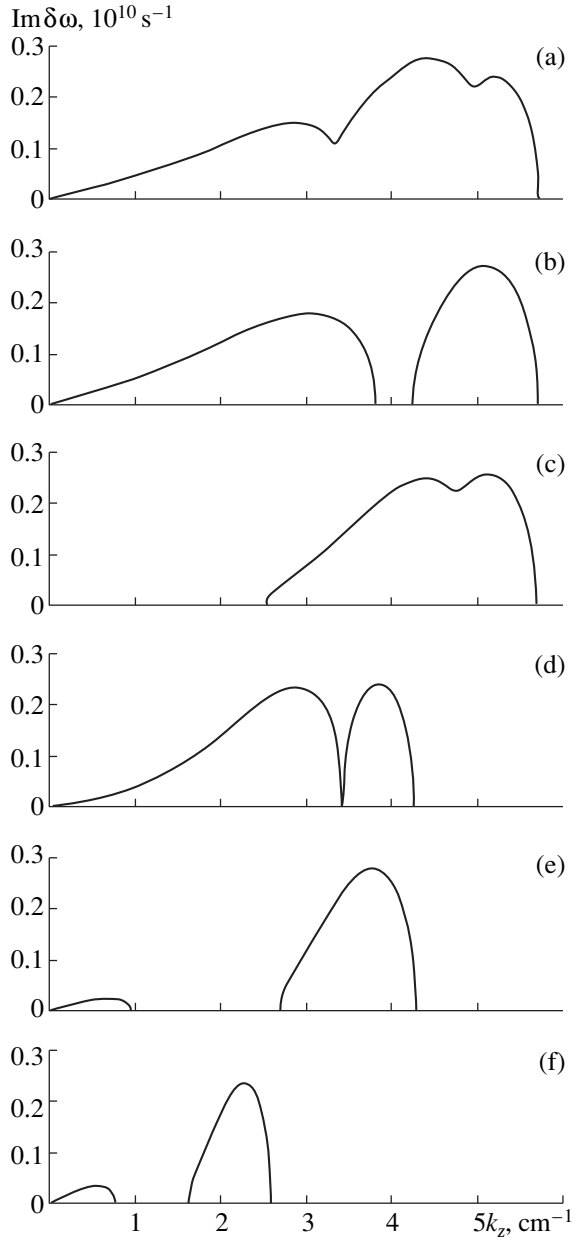

Fig. 2. Growth rate of the instability for a continuous plasma and an annular electron beam at $\nu = 0.01$. The beams of radii r_b = (a) 0.4, (b) 0.871, and (c) 0.556 cm are in resonance with the first three modes; the beams of radii r_b = (d) 0.4 and (e) 0.871 cm are in resonance with the first two modes; and (f) the beam of radius $r_b = 0.4$ cm is in resonance with the first mode.

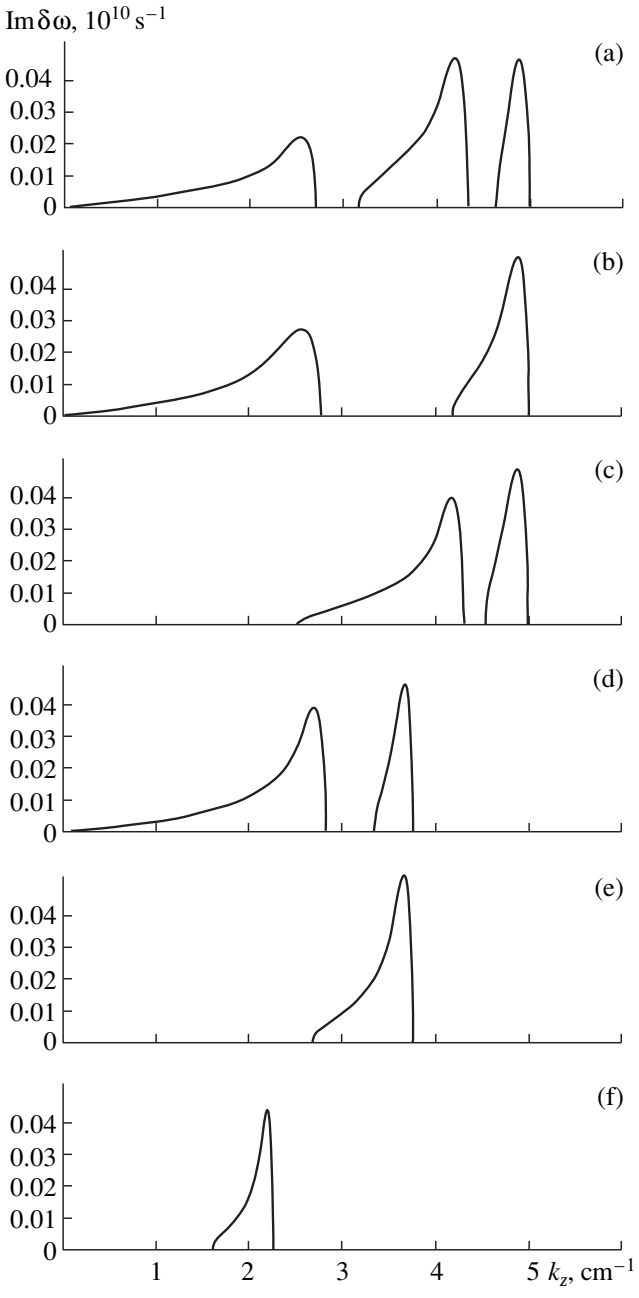

Fig. 3. Dispersion curves for a continuous plasma and an annular electron beam at $\nu = 5 \times 10^{-5}$. The beams of radii r_b = (a) 0.4, (b) 0.871, and (c) 0.556 cm are in resonance with the first three modes; the beams of radii r_b = (d) 0.4 and (e) 0.871 cm are in resonance with the first two modes; and (f) the beam of radius r_b = 0.4 cm is in resonance with the first mode.

which correspond to transverse modes with different numbers *m*, are well separated from each other, thereby providing evidence that, in a plasma waveguide, the modes are excited almost independently.

Now, we set $r_b = R\mu_{0,1}/\mu_{0,2} = 0.871$ cm, keeping the remaining parameters unchanged. A beam with such r_b propagates in the region where the field of the second transverse mode of a plasma waveguide vanishes, so that this mode cannot be excited. For this value of r_b, Figs. 2b and 3b show the growth rates $\mathrm{Im}\,\delta\omega$ calculated from expression (26). One can see two regions in which the growth rate is nonvanishing: the right region reflects the interaction of the beam with the first ($m = 1$) transverse mode of a plasma waveguide and the left region corresponds to the interaction with the third ($m = 3$) transverse plasma mode. The zone between these regions is free of instability, because the beam with the adopted radius r_b cannot interact with the second ($m = 2$) transverse mode of a plasma waveguide. However, this situation can be interpreted in a different way: Figs. 2b and 3b show the growth rates of the first ($p = 1$) unstable mode of a beam–plasma waveguide, in which case eigenfunction (25) is composed of a large number of terms, except for the second one.

Now, we choose $r_b = R\mu_{0,1}/\mu_{0,3} = 0.556$ cm and again fix the remaining parameters. A thin-walled annular beam with such r_b propagates in the region where the field of the third transverse mode of a plasma waveguide vanishes, so that this mode cannot be excited. For this beam, Figs. 2c and 3c show the growth rates $\mathrm{Im}\,\delta\omega$ calculated from expression (26). For small values of k_z, we have $\mathrm{Im}\,\delta\omega = 0$, as expected. For larger wavenumbers, there are two regions where the growth rate is nonzero: the right region reflects the interaction between the beam and the first ($m = 1$) transverse mode and the left region corresponds to the interaction with the second ($m = 2$) mode. The regions in Fig. 2c are seen to overlap; this effect was discussed above.

Now, we again set $r_b = 0.4$ cm but increase the beam velocity to $u = 1.3 \times 10^{10}$ cm/s. With such a beam, condition (20) is satisfied for the first two ($m = 1, 2$) transverse modes of a plasma waveguide and fails to hold for the third mode. The related functions $\mathrm{Im}\,\delta\omega$ are displayed in Figs. 2d and 3d. We can see that the $m = 1$ and $m = 2$ transverse modes of a plasma waveguide do not overlap: the pronounced peaks in their growth rates are separated by the zone where the growth rate vanishes. Then, we set $r_b = R\mu_{0,1}/\mu_{0,2} = 0.871$ cm, keeping the values of the remaining parameters fixed. In this case, the $m = 2$ transverse mode cannot be excited. The corresponding growth rates $\mathrm{Im}\,\delta\omega$ are presented in Figs. 2e and 3e. From Fig. 2e, we can see that $\mathrm{Im}\,\delta\omega = 0$ for k_z from approximately 1 to 3 cm^{-1}: the right high peak corresponds to the $m = 1$ unstable transverse plasma mode and the left low peak refers to the nonresonant instability of the $m = 3$ mode, which can be made unstable only by a sufficiently dense beam and becomes stable as parameter ν decreases (Fig. 3d).

Finally, we again set $r_b = 0.4$ cm but consider a beam with a higher velocity $u = 2 \times 10^{10}$ cm/s, with which condition (20) is satisfied only for the first ($m = 1$)

transverse mode of a plasma waveguide and fails to hold for the second and third modes. The relevant functions $\mathrm{Im}\delta\omega$ are shown in Figs. 2f and 3f. The above analysis makes clear the structure of the figures (e.g., in Fig. 2f, the right peak corresponds to the resonant instability of the first transverse plasma mode and the left peak refers to the nonresonant instability of the second transverse mode of a plasma waveguide).

Hence, even in the linear approximation, different transverse modes of a uniform plasma waveguide with a thin-walled annular electron beam are strongly coupled to each other. The only exceptions are the modes excited by beams with low densities, high velocities u, and specially chosen radii r_b. The results of linear theory (see Figs. 2, 3) show that, by a special choice of the parameters of a beam–plasma waveguide, it is possible to drive unstable modes with different transverse numbers in different wavelength ranges. This makes it feasible (at least according to linear theory) to control the emission spectrum of a thin-walled annular electron beam in a waveguide filled entirely with a homogeneous plasma, which is impossible for a waveguide with a thin-walled annular beam and thin-walled annular plasma [4]. Nonlinear phenomena that occur in an electron beam give rise to an additional coupling between the transverse modes of a plasma waveguide.

6. Here, we turn to nonlinear equations (15) in order to analyze the saturation stage of the beam–plasma instability. The problem as formulated accounts for the nonlinear nature of the beam and describes the plasma by the linearized equations of cold hydrodynamics. We model the beam by the particle method; i.e., we determine the beam density from the positions of quasi-particles, whose motion is traced by solving Newton's equations. We supplement Eqs. (15) with the initial conditions that specify the seed perturbation, the initial positions of the beam particles, and their initial velocities. We examine several different seed perturbations. First, we consider a monochromatic perturbation. To do this, we set the initial parameters of the perturbations driven by the $n = 1$ longitudinal mode to be nonzero and the parameters of the perturbations associated with the remaining longitudinal modes to be zero. Then, we specify the initial parameters of a large number of longitudinal modes, assuming equal mode amplitudes and zero mode phases. This seed perturbation has the form of a regular sequence of pulses at the time $t = 0$. Finally, we specify random phases of a large number of longitudinal modes; i.e., we consider a noisy seed perturbation.

We start with a monochromatic seed perturbation. In the sums over n, we retain the first five terms, and, in the sums over m, we keep at least the first ten terms. We set $u = 10^{10}$ cm/s, $r_b = 0.4$ cm, and $\nu = 0.01$. These parameter values refer to the instability growth rate illustrated in Fig. 2a. We assume that the wavelength of the seed perturbation corresponds to the Cherenkov resonance between the beam and the first ($m = 1$) transverse mode of a plasma waveguide; i.e., we choose $k \approx 4.85$ cm^{-1}. Figure 4 shows the time evolutions of the amplitudes of the first three ($n = 1, 2, 3$) longitudinal modes of the perturbed plasma charge density $\tilde{\rho}_{pn}(r_b)$ at the surface whose radius is equal to the beam radius r_b. It is seen that, in the initial stage, the first longitudinal mode (curve *1*) grows exponentially with the rate $\mathrm{Im}\delta\omega$. As the first mode saturates, the nonlinear effects in the beam come into play and give rise to the second and third longitudinal modes.

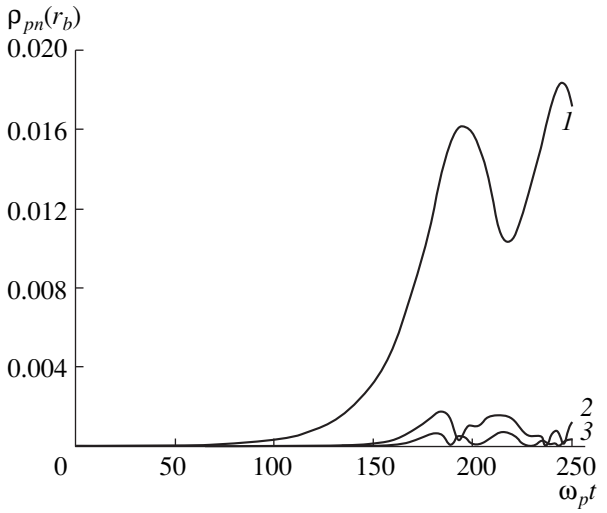

Fig. 4. Time evolutions of the amplitudes of the first three ($n = 1, 2, 3$) longitudinal modes of the perturbed plasma electron density for $\nu = 0.01$ and $r_b = 0.4$ cm.

Now, we analyze the relative roles played by transverse modes with large numbers m for two different beam densities. For $\nu = 0.01$ and 5×10^{-5}, the development of the first several transverse modes driven by the $n = 1$ longitudinal mode is illustrated in Figs. 5 and 6, respectively. Figure 6 demonstrates that a dominant role is played by the first transverse mode, which is in resonance with the beam; the second and third transverse modes are seen to be of lesser importance. For a higher density beam ($\nu = 0.01$), the second and third transverse modes play a greater role, even though the beam interacts resonantly with the first transverse mode. As discussed above, these effects stem from the fact that the transverse structure of the beam differs from that of the plasma.

Let us consider a seed perturbation in the form of a large number of longitudinal modes with different numbers n. The spatial spectra of oscillations calculated at the times $\tau \equiv \omega_p t = 0$, 90, 120, and 240 for the same parameters of the system but for a pulsed (in the form of a regular sequence of pulses) seed perturbation are presented in Fig. 7. At the initial time, the spectrum consists of the first fifty longitudinal modes. In the linear stage of the instability, the longitudinal modes that are in exact (or almost exact) resonance with the beam

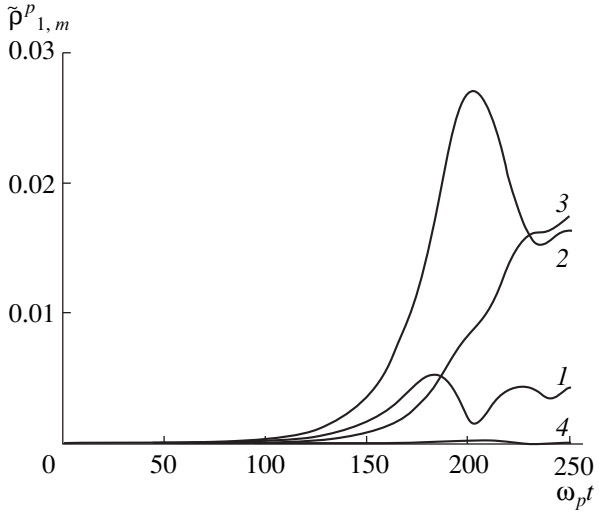

Fig. 5. Time evolutions of the amplitudes of the first four (m = 1, 2, 3, 4) transverse modes of the perturbed plasma electron density for $\nu = 0.01$ and $r_b = 0.4$ cm.

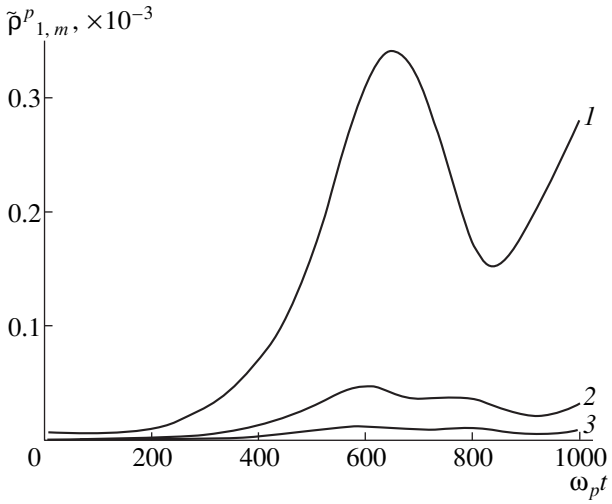

Fig. 6. Time evolutions of the amplitudes of the first three (m = 1, 2, 3) transverse modes of the perturbed plasma electron density for $\nu = 5 \times 10^{-5}$ and $r_b = 0.4$ cm.

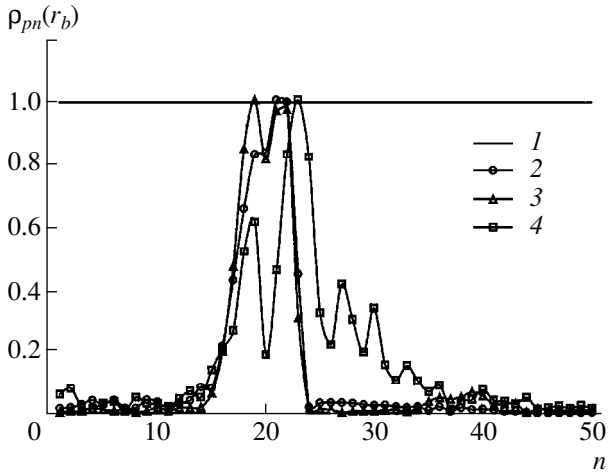

Fig. 7. Spatial mode spectra for a pulsed seed perturbation at the times τ = (*1*) 0, (*2*) 90, (*3*) 120, and (*4*) 240.

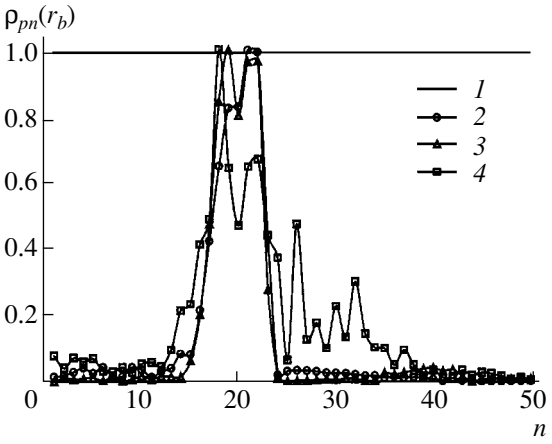

Fig. 8. Spatial mode spectra for a noisy seed perturbation at the times τ = (*1*) 0, (*2*) 90, (*3*) 120, and (*4*) 240.

grow faster than the remaining modes. In the case at hand, the mode that is in exact resonance with the beam is the $n = 20$ longitudinal mode. The growing resonant modes play an increasingly important role, so that the spectrum narrows and thus becomes more monochromatic. Then, the nonlinear effects come into play. Thus, the spectrum calculated at the time $\tau = 120$ is seen to contain a low peak at $n = 40$. Further, the modes with different longitudinal (n) and transverse (m) numbers start to interact with each other, giving rise to more and more modes. As a result, the spectrum again broadens and its structure becomes irregular. From Fig. 8, we can see that similar processes are also characteristic of a system in which the noisy seed perturbation is specified as a set of longitudinal modes with random phases.

Finally, we consider the dynamics of energy transfer from the directed beam motion to plasma waves. Figure 9

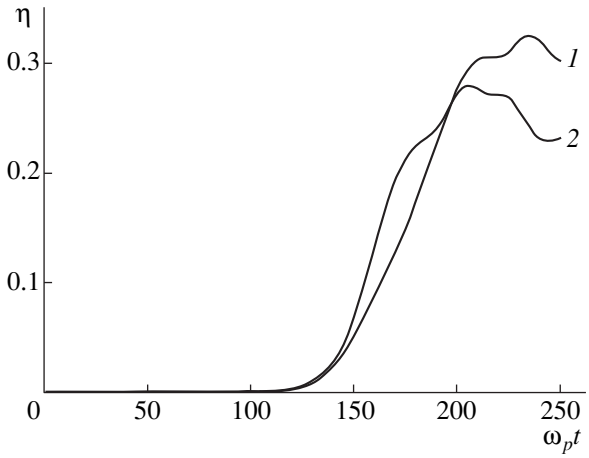

Fig. 9. Time evolutions of the relative energy lost by the beam for (*1*) pulsed and (*2*) noisy seed perturbations.

shows the relative energies lost by the beam electrons for pulsed (curve *1*) and noisy (curve *2*) seed perturbations. In both cases, the energy-conversion efficiency in the saturation stage is about 30%. For a regular seed perturbation when the phases of all the longitudinal modes are the same, the field has the form of a regular sequence of pulses because of the superposition of different harmonics. Consequently, there are spatial regions where the longitudinal component of the electric field is weak and, accordingly, the field itself does not interact with the beam electrons. This effect is illustrated in Fig. 9: for a regular seed perturbation, the beam electrons lose their energy at a slower rate than for a noisy seed perturbation (curve *2* is steeper than curve *1*).

ACKNOWLEDGMENTS

This work was supported in part by the Ministry of Education of the Russian Federation (under the programs "Radio engineering and Electronics" and "Russian Universities") and the Russian Foundation for Basic Research (under the program "Leading Scientific Schools").

REFERENCES

1. A. G. Shkvarunets, A. A. Rukhadze, and P. S. Strelkov, Fiz. Plazmy **20**, 682 (1994) [Plasma Phys. Rep. **20**, 613 (1994)].
2. M. V. Kuzelev, O. T. Loza, A. V. Ponomarev, *et al.*, Zh. Éksp. Teor. Fiz. **109**, 2048 (1996) [JETP **82**, 1102 (1996)].
3. M. V. Kuzelev, O. V. Lazutchenko, and A. A. Rukhadze, Izv. Vyssh. Uchebn. Zaved., Radiofiz. **42**, 958 (1999).
4. M. Biro, M. A. Krasil'nikov, M. V. Kuzelev, and A. A. Rukhadze, Usp. Fiz. Nauk **167**, 1025 (1997) [Phys. Usp. **40**, 975 (1997)].
5. A. F. Aleksandrov and A. A. Rukhadze, *Course on Electrodynamics of Plasmalike Media* (Mosk. Gos. Univ., Moscow, 1999).
6. M. V. Kuzelev and A. A. Rukhadze, Izv. Vyssh. Uchebn. Zaved., Radiofiz. **36**, 867 (1993).
7. A. A. Rukhadze, L. S. Bogdankevich, S. E. Rosinskiĭ, and V. G. Rukhlin, *Physics of High-Current Relativistic Electron Beams* (Atomizdat, Moscow, 1980).
8. R. Briggs, in *Advances in Plasma Physics*, Ed. by A. Simon and W. Thompson (Wiley, New York, 1969, 1971; Mir, Moscow, 1974), Vols. 3, 4.
9. M. V. Kuzelev and A. A. Rukhadze, *Electrodynamics of Dense Electron Beams in a Plasma* (Nauka, Moscow, 1990).
10. M. V. Kuzelev and A. A. Rukhadze, Fiz. Plazmy **25**, 471 (1999).
11. *Plasma Electrodynamics*, Ed. by A. I. Akhiezer, I. A. Akhiezer, R. V. Polovin, *et al.* (Nauka, Moscow, 1974; Pergamon, Oxford, 1975).
12. N. S. Erokhin, M. V. Kuzelev, S. S. Moiseev, A. A. Rukhadze, and A. B. Shvartsburg, *Nonequilibrium and Resonant Processes in Plasma Radiophysics* (Nauka, Moscow, 1982).

Translated by I.A. Kalabalyk

Plasma Physics Reports, Vol. 27, No. 5, 2001, pp. 390–397. Translated from Fizika Plazmy, Vol. 27, No. 5, 2001, pp. 415–422.

PLASMA OSCILLATIONS AND WAVES

Spectral Properties of Plasma Waves in Periodic Plasma-Filled Structures

G. I. Zaginaĭlov

Kharkov National University, pl. Svobody 4, Kharkov, 61077 Ukraine

Received August 16, 2000

Abstract—The dispersion properties and field distribution of plasma waves in a periodic plasma-filled waveguide are correctly analyzed for the first time with allowance for all spatial harmonics. It is shown that the plasma wave spectrum has a zonal structure and a lower cutoff frequency. The widths of the forbidden bands and the lower cutoff frequency are determined by the waveguide corrugation depth. For a planar periodic plasma-filled waveguide, the allowed and forbidden frequency bands are evaluated analytically. The waveguide periodicity substantially influences the field of the plasma waves at frequencies close to the forbidden bands. This leads to the formation of regions in which the energy density of plasma waves exceeds the average level by more than one order of magnitude. This effect is related to the contribution from the higher spatial harmonics. *© 2001 MAIK "Nauka/Interperiodica".*

1. INTRODUCTION

Periodic plasma-filled waveguide structures are widely used in plasma microwave electronics. To date, several types of microwave sources [1–4] that are based on periodic plasma-filled structures and are better than vacuum devices of the same class in a number of technical parameters have been developed. Periodic plasma-filled structures can also be used to develop new efficient methods for charged-particle acceleration and plasma heating.

However, in spite of a number of theoretical and experimental studies (see, e.g., reviews [4, 5]), the mechanisms through which the plasma influences the generation of electromagnetic waves in periodic structures are still poorly understood. To date, several mechanisms have been suggested to describe the effect of a plasma on the increase in the output power and the efficiency of microwave generation in plasma-filled devices. The mechanisms can be divided into three groups, which are briefly analyzed below.

(i) The influence of the plasma as dielectric medium manifests itself in a decrease in the phase velocity of the working mode [6] and an increase in the detuning of the wavenumber of a slow beam wave from the exact beam–plasma resonance $k_z = \omega/V$ [7], where ω is the working frequency and V is the beam velocity. The first effect increases the spatial growth rate of the synchronous mode, whereas the second effect increases the efficiency with which the beam energy is converted into the energy of the working mode. However, the predicted increase in the efficiency is much lower than that observed in experiments. Moreover, an appreciable influence of the plasma is observed at significantly lower densities than those predicted in [6, 7]; at these densities, the plasma permittivity is close to unity and does not affect the electrodynamic properties of the waveguide structure. Note that somewhat different mechanisms for the influence of the plasma as dielectric medium were discussed in [8–10]. However, these mechanisms, as well as those mentioned above, predict an increase in the microwave generation efficiency at substantially higher plasma densities as compared to the experimentally determined optimal density.

(ii) The formation of periodic plasma inhomogeneities under the action of strong electromagnetic fields [11, 12] increases the feedback coupling between the direct and backward electromagnetic waves, which, in turn, substantially decreases the starting current and increases the generation efficiency. The predicted increase in the efficiency is in fact high, but at plasma densities much higher than the experimental ones. In addition, the strong coupling between the direct and backward waves may take place even without plasma filling, when a vacuum device operates near the π-mode; however, the efficiency does not increase so much in this case. On the other hand, with plasma filling, no decrease in the starting current was observed.

(iii) There is a parametric interaction between the plasma waves and electromagnetic waves that are simultaneously excited by the electron beam. Several mechanisms for this interaction were considered in [13–15]. However, all these mechanisms either do not predict such a substantial increase in the efficiency or predict it for higher plasma densities.

Therefore, the mechanisms through which the plasma influences the microwave generation efficiency in plasma-filled microwave sources based on periodic waveguide structures still remain unknown.

Note that an even more special problem of the spectral properties of plasma-filled periodic structures at

1063-780X/01/2705-0390$21.00

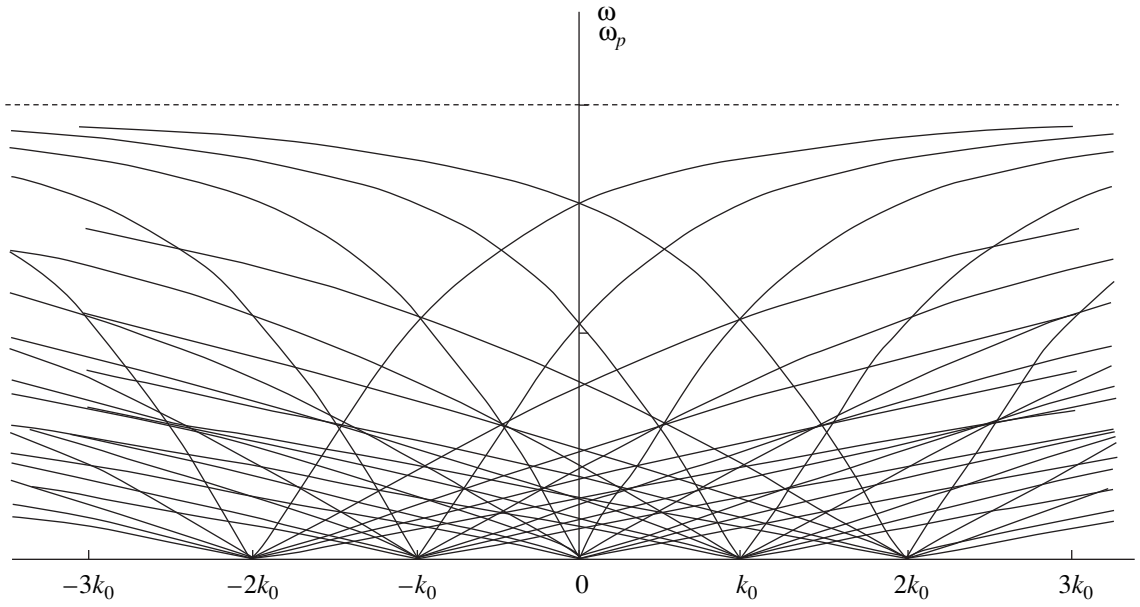

Fig. 1. Qualitative pattern of the dispersion curves of plasma waves forming a dense spectrum. For clarity, only five transverse and five longitudinal harmonics are depicted.

frequencies below the plasma frequency also remains unstudied. However, without knowledge of these properties, an analysis of the mechanisms for the influence of the plasma may be incomplete or incorrect.

As is known, the spectrum of a plasma-filled periodic waveguide structure contains electromagnetic and plasma modes, which, in the simplest case of a transversely uniform plasma, are separated in frequency [16].

The dispersion properties of high-frequency electromagnetic modes do not substantially differ from the corresponding modes of a vacuum periodic structure and can be described using the same technique [13]. Thus, if we represent the waveguide field in the form of a superposition of spatial harmonics and require that the tangential components of the electric field vanish on the periodic surface of the structure, we arrive at the dispersion relation in the form of an infinite determinant. Taking into account a finite number of spatial harmonics, we pass to a finite determinant whose roots can be found numerically. For periodic structures with typical experimental parameters, taking into account five to ten harmonics is usually quite sufficient to achieve the required accuracy, which is confirmed by a comparison with experimental data [17].

The first theoretical investigations of plasma waves in periodic plasma-filled waveguides were also based on the traditional approach [8, 18]. An analysis of the beam–plasma instability in a periodic plasma waveguide with allowance for the fundamental and two neighboring spatial harmonics showed that the growth rate of plasma waves is much less than that of electromagnetic waves. However, it was shown later [19] that, contrary to the Floquet theorem, the dispersion curves of plasma waves become nonperiodical with respect to the wave vector as the number of spatial harmonics increases. In addition, the number of dispersion curves increases as the next spatial harmonic is taken into account (Fig. 1). In this case, the allowed and forbidden bands change substantially as new, even very high, harmonics are taken into account. It seems that the results obtained with any finite number of incorporated harmonics are incorrect. In the limiting case when all transverse and longitudinal harmonics are incorporated, the entire domain below ω_p in the (ω, k_z) plane is compactly filled by the dispersion curves, which thus become indistinguishable.

In fact, each point in the (ω, k_z) plane below ω_p is a solution to the dispersion relation. Therefore, we arrive at a special type of spectrum, the so-called "dense" spectrum, which was first described in [20]. The properties of dense spectra have not yet been studied even qualitatively, although plasma waves in periodic plasma-filled structures have been observed in many experiments [17, 21] and the fact of their existence is beyond question. Nevertheless, the question arises as to whether it is possible, in principle, to adequately describe plasma waves by certain dispersion curves in the (ω, k_z) plane. Theoretical studies reported in this paper provide a positive answer to this question.

The analysis is based on the method proposed in [22]. According to this method, it is possible to pass from representation in the form of spatial harmonics to an integral representation for the fields inside the periodic structure. As a result, instead of a dispersion rela-

tion in the form of an infinite determinant, we obtain a uniform integral equation for the electric field at the axis of the periodic structure. In the quasistatic limit $c \longrightarrow \infty$, this equation transforms into the functional equation. A detailed study of the latter and an analysis of the results obtained are the subject of this paper.

In Section 2, a basic integral equation for the total field at the axis is derived by a new method that is more efficient than that used in [22]. In Section 3, the basic equation is transformed into a form admitting a numerical analysis. In Section 4, possible methods for numerically analyzing the equation obtained are described. In Section 5, the numerical results are analyzed. As an example, a waveguide with sinusoidal corrugation is considered.

It is shown that the dense spectrum has a zonal structure. The widths of the forbidden and allowed bands depend on the corrugation depth. In the range of lower frequencies ($\omega \ll \omega_p$), the forbidden bands overlap and periodic solutions are seemingly absent.

In the Conclusion, the results obtained are summarized and some findings are formulated.

2. FORMULATION OF THE PROBLEM. DERIVATION OF THE BASIC INTEGRAL EQUATION

We consider a simple periodic waveguide structure—a planar waveguide filled with a uniform collisionless cold plasma in an infinitely strong longitudinal magnetic field (Fig. 2). The choice of such a model is reasonable in many aspects, even although experimental plasma-filled periodic structures are, for the most part, cylindrical. First, many specific features of the wave processes in planar geometry do not change qualitatively when passing to cylindrical geometry. Second, planar geometry is of particular interest because it can successfully be used to model coaxial plasma-filled structures [23] and periodic structures with rectangular cross sections. Planar plasma-filled devices have not yet been studied experimentally, but devices with this type of geometry are widely used in vacuum electronics. For harmonic TM waves (E_x, H_y, E_z) ~ exp($-i\omega t$), the set of Maxwell equations reduces to one equation for H_y

$$\left(\frac{\partial^2}{\partial x^2} + \varepsilon\frac{\partial^2}{\partial z^2} + k^2\varepsilon\right)H_y(x, z) = 0, \quad (1)$$

where $\varepsilon = 1 - \omega_p^2/\omega^2$ is the permittivity of a cold collisionless plasma, $k = \omega/c$, and c is the speed of light in a vacuum. The other field components are expressed through H_y by the formulas

$$E_z = -\frac{1}{ik\varepsilon}\frac{\partial H_y}{\partial x}, \quad E_x = \frac{1}{ik}\frac{\partial H_y}{\partial z}. \quad (2)$$

In the range where plasma waves exist ($\omega - \omega_p$), we have $\varepsilon < 0$. Changing to a new variable $|\varepsilon|^{1/2}x = \tilde{x}$, Eq. (1) transforms into

$$\left(\frac{\partial^2}{\partial z^2} - \frac{\partial^2}{\partial \tilde{x}^2} + k^2\right)\tilde{H}_y(\tilde{x}, z) = 0, \quad (3)$$

where $\tilde{H}_y(\tilde{x}, z) = H_y(x, z)$.

Equation (3) is hyperbolic. Its solution can be expressed through integrals of the sought function and its derivative at the waveguide axis ($x = 0$) [24]:

$$\tilde{H}_y(\tilde{x}, z) = \frac{f(z+\tilde{x}) + f(z-\tilde{x})}{2} + \frac{1}{2}\int_{z-\tilde{x}}^{z+\tilde{x}} J_0(k\sqrt{(z-\zeta)^2 - \tilde{x}^2})g(\zeta)d\zeta + \frac{1}{2}k\tilde{x}\int_{z-\tilde{x}}^{z+\tilde{x}} \frac{J_1(k\sqrt{(z-\zeta)^2 - \tilde{x}^2})}{\sqrt{(z-\zeta)^2 - \tilde{x}^2}} f(\zeta)d\zeta, \quad (4)$$

where $f(z) = \tilde{H}_y(0, z)$ and $g(z) = \left.\frac{\partial \tilde{H}_y(\tilde{x}, z)}{\partial \tilde{x}}\right|_{\tilde{x}=0}$.

For the fields symmetric about x ($E_z(-x) = E_z(-x)$), we have $\tilde{H}_y(0, z) = 0$. Then, passing to the old variables, we obtain the following representation for the magnetic field in the waveguide:

$$H_y(x, z) = \frac{1}{2}\int_{z-|\varepsilon|^{1/2}x}^{z+|\varepsilon|^{1/2}x} J_0(k\sqrt{(z-\zeta)^2 - |\varepsilon|x^2})g(\zeta)d\zeta. \quad (5)$$

The requirement that the tangential component of the electric field should vanish at the waveguide wall

$$X'(z)E_x + E_z\big|_{x=X(z)} = 0$$

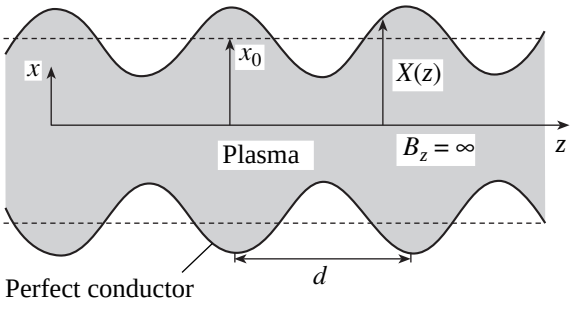

Fig. 2. Geometry of the problem.

is equivalent to the condition for $H_y(x, z)$:

$$\left(X'(z)\frac{\partial H_y}{\partial z} - \frac{1}{\varepsilon}\frac{\partial H_y}{\partial x}\right)\Bigg|_{x = X(z)} = 0, \quad (6)$$

where $x = X(z)$ is the coordinate of the periodic boundary of the waveguide ($X(z + d) = X(z)$) and the prime stands for differentiation with respect to the argument. Substituting Eq. (5) into Eq. (6), after simple manipulations, we arrive at the integral equation

$$g(z + \varphi(z))(1 + \varphi'(z)) + g(z - \varphi(z))(1 - \varphi'(z)) + \int_{z-\varphi(z)}^{z+\varphi(z)} G(z, \zeta)g(\zeta)d\zeta = 0, \quad (7)$$

where $\varphi(z) = |\varepsilon|^{1/2}X(z)$,

$$G(z, \zeta) = \frac{kJ_1(k\sqrt{(z-\zeta)^2 - \varphi^2(z)})}{\sqrt{(z-\zeta)^2 - \varphi^2(z)}}(\varphi(z) - \varphi'(z)(z-\zeta)).$$

In the quasistatic limit $c \longrightarrow \infty$, Eq. (7) coincides with an equation obtained in [22] using a traditional approach based on the expansion of fields in series in spatial harmonics. The full mathematical equivalence of these approaches under the condition $\varphi'(z) \le 1$ is also proved in [25].

Below, we will consider in detail quasistatic oscillations, in which case the integral equation (7) transforms into the functional equation

$$e^{ik_z\varphi(z)}\Psi(z + \varphi(z))(1 + \varphi'(z)) + e^{-ik_z\varphi(z)}\Psi(z - \varphi(z))(1 - \varphi'(z)) = 0, \quad (8)$$

where $\Psi(z) = E_z(0, z)e^{-ik_z z}$ and k_z is the oscillation wavenumber.

Note that taking into account the correction for electromagnetic effects, which contribute to the integral term in Eq. (7), presents no problems. In view of the fact that the kernel of the integral equation (7) is continuously differentiable with respect to both variables, Eq. (7) can be solved by iterations. As an initial function, we can use the solution to Eq. (8). The procedure for solving this equation will be described below.

3. REDUCTION OF THE FUNCTIONAL EQUATION DESCRIBING A DENSE SPECTRUM TO THE EQUATION DESCRIBING AN ORDINARY SPECTRUM

The functional equation (8) is the equation for eigenfunctions and eigenvalues. Although the amplitudes of spatial harmonics do not enter this equation explicitly, it describes, again, a dense spectrum; i.e., any point in the (ω, k_z) plane that lies below ω_p is the solution to Eq. (8). Hence, it is hardly possible to analyze Eq. (8) numerically.

Indeed, let us assume that $k_{zm}(\omega)$ is the eigenvalue corresponding to the eigenfunction $\Psi_m(z)$, where $m = 0, 1, 2, \ldots, \infty$ is the transverse index. A direct substitution shows that the wavenumbers $k_{zmn}(\omega) = k_{zm}(\omega) + nk_0$ shifted by nk_0, where $k_0 = 2\pi/d$, are also the eigenvalues of Eq. (8), which, however, correspond to other eigenfunctions: $\Psi_{mn}(z) = \Psi_m(z)\exp(-ink_0z)$. The latter feature can be used to separate out the shifted branches. Such a separation was performed analytically in [22] for $|\varepsilon(\omega)| \ll 1$.

Below, we will separate out the shifted branches in the general case, without any additional assumptions. It should be noted that all shifted branches determine the same total field; i.e., $E_{zm}(0, z) = \exp(ik_{zm}(\omega)z)\Psi_m(z) \equiv \exp(ik_{zmn}(\omega)z)\Psi_{mn}(z)$. Therefore, to completely determine the field distribution in the waveguide, it is sufficient to know, e.g., $k_{zm}(\omega)$ and $\Psi_m(z)$. The other solutions to Eq. (8) with the same transverse index are spurious and do not provide new information about the waveguide field. The eigenvalues $k_{zm}(\omega)$ and eigenfunctions $\Psi_m(z)$ describe an ordinary spectrum of transverse modes, which correspond to the modes of a smooth plasma-filled waveguide (Trivelpiece–Gould modes).

In order to eliminate spurious solutions, we introduce a new unknown function $F(z) = \int^z E_z(0, z')dz'$. Then, Eq. (8) reduces to the problem

$$F(z + \varphi(z)) + F(z - \varphi(z)) = 0, \quad F(z + d) = e^{ik_z d}F(z). \quad (9)$$

The solution to Eqs. (9) is sought in the form $F(z) = \rho(z)\exp(ik_z z + i\theta(z))$. From Eqs. (9), we obtain two independent problems for two new unknown real functions $\rho(z)$ and $\theta(z)$:

$$\rho(z + \varphi(z)) = \rho(z - \varphi(z)), \quad \rho(z + d) = \rho(z); \quad (10)$$

$$\frac{1}{2}[\theta(z + \varphi(z)) - \theta(z - \varphi(z))] = (m + 1/2)\pi - k_z\varphi(z), \quad (11)$$

$$\theta(z + d) = 2\pi nk_0 z + \theta(z).$$

Equations (10) have a simple and obvious solution $\rho(z) = \text{const}$. According to the uniqueness theorem for the Maxwell equation with boundary conditions, the obtained solution is unique; otherwise, we would have two (or more) field distributions corresponding to the same frequency and the same wavenumber, which are independently determined from Eqs. (11).

A family of Eqs. (11) taken for different n determines a family of shifted branches, index m being the

transverse mode number. Hence, it is Eqs. (11) that provide the separation of shifted branches. In addition, fixing n and m, we not only eliminate spurious solutions, but also arrive at the problem for a fixed transverse mode, which substantially facilitates numerical calculations.

4. NUMERICAL METHODS FOR SOLVING THE FUNCTIONAL EQUATION

Setting $n = 0$ in Eqs. (11), we arrive at the problem

$$\hat{L}\theta(z) = (m + 1/2)\pi - k_z\varphi(z), \quad \theta(z + d) = \theta(z), \tag{12}$$

which describes an ordinary spectrum of transverse modes; here, $\hat{L}\,\theta(z) = \frac{1}{2}[\theta(z + \varphi(z)) - \theta(z - \varphi(z))]$. It is easily seen that, for $X(z) \longrightarrow x_0$, the eigenvalues and eigenfunctions of problem (12) ($k_{zm} \longrightarrow (m + 1/2)\pi/(|\varepsilon|^{1/2}x_0)$ and $\theta_m(z) \longrightarrow$ const, respectively) correspond to the ordinary Trivelpiece–Gould modes of a smooth waveguide filled with a magnetized plasma.

Equations (12) were solved numerically by two different methods. The first method was based on the Fourier expansion of the unknown function $\theta(z)$: $\theta(z) = \sum_{q=-\infty}^{\infty} C_q \exp(iqk_0z)$. As a result, we arrive at a set of linear algebraic equations for the Fourier coefficients C_q, which allows us to determine $\theta(z)$ and k_z with any prescribed accuracy. We took into account at most 90 Fourier harmonics. However, as a rule, it was sufficient to take into account ten to twenty Fourier harmonics in order to calculate $\theta(z)$ accurate to 10^{-2}%.

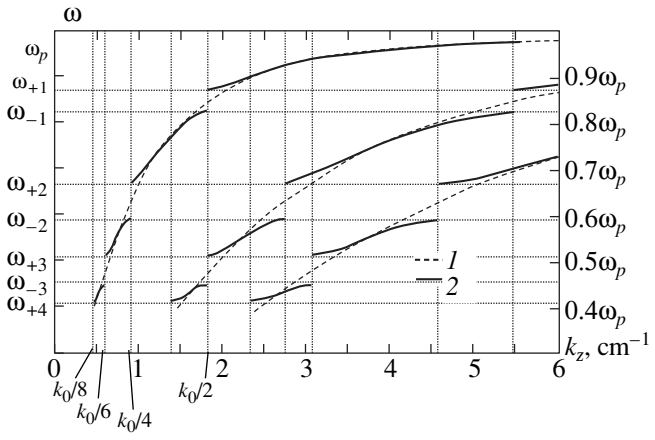

Fig. 3. Dispersion curves for the first three transverse modes of a periodic plasma waveguide: α = (*1*) 0 and (*2*) 0.1, x_0 = 1.4 cm, and $k_0 = 3.67$ cm^{-1}.

The second method was based on the approximation of $\theta(z)$ by the spline functions,

$$\theta(z) = \sum_{i=0}^{N-1} a_i B_i^k(z), \tag{13}$$

where $B_i^k(z)$ are the spline functions of the kth order:

$$B_i^k(z) = \left(\frac{z - z_i}{z_{i+k} - z_i}\right)B_i^{k-1}(z) + \left(\frac{z_{i+k+1} - z}{z_{i+k+1} - z_{i+1}}\right)B_{i+1}^{k-1},$$

$$k \geq 1,$$

$$B_i^0(z) = \begin{cases} 1, & z_i < z < z_{i+1} \\ 0, & z \in (z_i, z_{i+1}) \end{cases} \quad z_i = \frac{i}{N}d,$$

$$i = 0, \ldots, N-1.$$

To achieve an accuracy of $\leq 10^{-2}$%, it is sufficient to take $N \propto 100$ for the spline functions of the first order. The numerical solutions obtained by the two methods coincide within the given accuracy.

5. ANALYSIS OF NUMERICAL RESULTS

Figure 3 shows the dispersion curves for a sinusoidal corrugated plasma waveguide $X(z) = x_0(1 + \alpha\cos(k_0z))$ for $x_0 = 1.4$ cm, $\alpha = 0.1$, and $k_0 = 3.67$ cm^{-1}.

As is seen from Fig. 3, the interaction between the fundamental and higher spatial harmonics produces the forbidden bands $\omega_{-l} < \omega < \omega_{+l}$, where $\omega_{\pm l}$ are the upper and lower boundaries of the lth forbidden band ($l = 1, 2, \ldots, \infty$). The expressions for the boundary frequencies of each forbidden band can be found analytically: $\omega_{\pm l} = \omega_p/(1 + (\pi l/x_0k_0(1 \pm \alpha))^2)^{-1/2}$. It is interesting that, for the frequencies within the forbidden band, operator $\hat{L}$ has a singular point in which $\hat{L}\,\theta(z)|_{z=z_0} = 0$. The singular point is determined by the condition $2\varphi(z_0) = ld$. From here, in view of Eqs. (12), it follows that, at the boundaries of the lth forbidden band, we have $k_{zm}(\omega) \longrightarrow (2m + 1)\pi/(ld)$, where $m = 0, 1, \ldots, \infty$ and $l = 1, 2, \ldots, \infty$. At large l, the forbidden bands overlap; i.e., there is a lower cutoff frequency. The forbidden bands overlap at frequencies satisfying the inequality $\alpha x_0k_0|\varepsilon|^{1/2} \geq \pi/2$; however, our consideration is valid for $\alpha x_0k_0|\varepsilon|^{1/2} \leq 1$ [25]. As is the case of electromagnetic waves, the group velocity of plasma waves tends to zero as the frequency approaches the forbidden band.

To analyze the influence of periodicity on the field distribution, we represent $E_z(0, z)$ in the form $E_z(0, z) = A(z)\exp(ik_zz + i\theta(z))$. For a smooth plasma-filled waveguide, we may assume $A(z) = 1$ and $\theta(z) = 0$.

Figure 4 shows the profiles of the amplitude $A(z)$ for different frequencies. For frequencies far from the forbidden band, the amplitude $A(z)$ differs slightly from unity; i.e., the periodicity slightly perturbs the field of a smooth waveguide. As the frequency approaches the

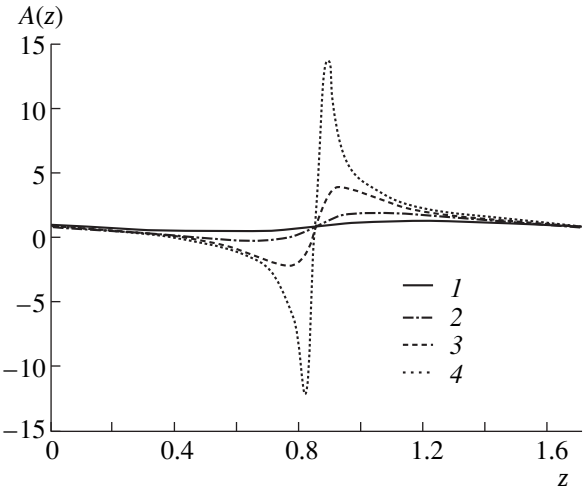

Fig. 4. Effect of periodicity on the profile of the fundamental mode amplitude for different frequencies: ω/ω_p = (*1*) 0.9, (*2*) 0.88, (*3*) 0.875, and (*4*) 0.874.

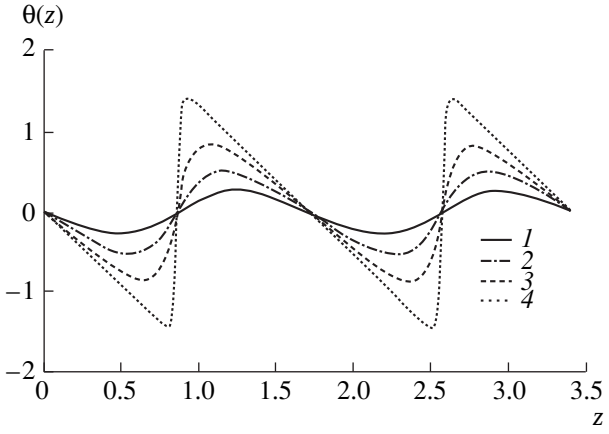

Fig. 5. Effect of periodicity on the phase shift $\theta(z)$ of the fundamental mode for different frequencies: ω/ω_p = (*1*) 0.9, (*2*) 0.88, (*3*) 0.875, and (*4*) 0.874 at $\alpha = 0.1$, $x_0 = 1.4$ cm, and $k_0 = 3.67$ cm^{-1}.

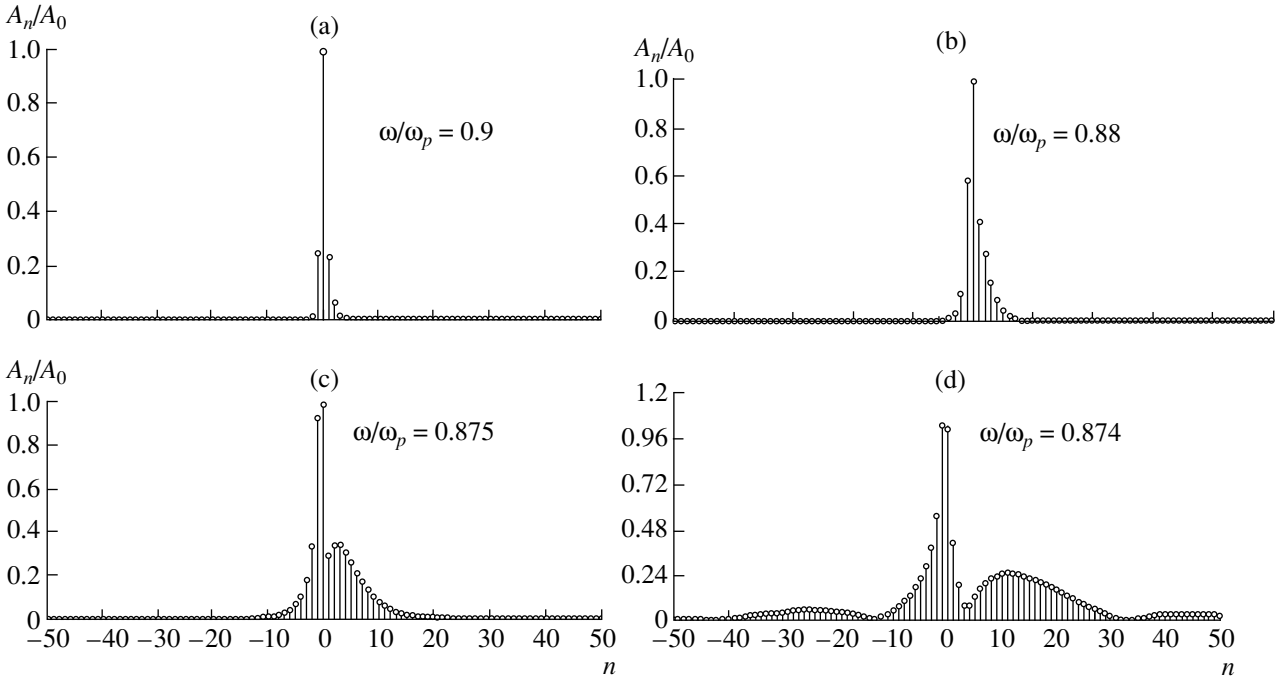

Fig. 6. Amplitudes of the spatial harmonics of the fundamental mode for different frequencies: ω/ω_p = (a) 0.9, (b) 0.88, (c) 0.875, and (d) 0.874.

upper boundary frequency of the first forbidden band ($\omega_{+1} \simeq 0.874\omega_p$ for our parameters), the amplitude perturbation caused by periodicity becomes stronger. Near the boundary frequency ω_{+1}, $A(z)$ has sharp peaks in which $A(z)$ exceeds its averaged value by more than one order of magnitude. In this case, the width of the peaks decreases and the maximum field strongly increases as $\omega \longrightarrow \omega_{+1}$. Similar behavior of the field is observed when the frequency approaches the boundaries of the other forbidden bands.

Figure 5 shows the profiles of the phase shift $\theta(z)$ caused by periodicity for different frequencies. Far

from the boundary frequency ω_{+1}, the profile $\theta(z)$ is nearly sinusoidal and the absolute value of $\theta(z)$ is rather small. As the frequency approaches ω_{+1}, the profile $\theta(z)$ changes substantially: the sinusoidal profile transforms into a sawtooth profile, and the maximal values of $\theta(z)$ increase substantially. It is also of interest to analyze the amplitudes of spatial harmonics.

Figure 6 shows the amplitudes of spatial harmonics of the longitudinal electric field $A_n = \frac{1}{d}\left|\int_0^d E_z(0, z)\exp(-i[k_z(\omega) + nk_0]z)dz\right|$ at different frequencies. As is seen from Figs. 6a–6d, the contribution from higher spatial harmonics to the total field increases substantially as $\omega \longrightarrow \omega_{+1}$. The spatial harmonic with $n = -1$ has a maximum amplitude; its amplitude becomes comparable with the amplitude of the fundamental spatial harmonic in the vicinity of ω_{+1}.

The amplitudes of higher harmonics are significantly lower. However, they fall slowly as the harmonic number increases, so that their total contribution is substantial (especially, near the boundary frequencies), which explains the formation of regions with the high energy density of the electromagnetic field.

6. CONCLUSION

The dispersion properties and field distribution of plasma waves in a periodical plasma-filled waveguide have been thoroughly analyzed for the first time. Using the new approach proposed in [22], the problem of the dense spectrum of plasma waves in a periodic plasma waveguide is solved. Specific features of both the spectrum of plasma waves and the distribution of electromagnetic fields are revealed.

The forbidden bands for plasma waves in periodic plasma waveguides are predicted and correctly investigated for the first time. It is shown that the effect of periodicity is negligibly small for frequencies far from the forbidden bands, even when the corrugation depth is relatively large. As the frequency approaches the boundary of the forbidden band, the effect of periodicity on the dispersion characteristics and the field distribution becomes stronger. At the boundaries of the forbidden bands, the wave group velocity tends to zero. At the same time, the plasma wave field strongly increases in narrow spatial regions: the closer the frequency to the boundary frequency, the higher the field amplitude and the narrower the region where the field is concentrated. Such an unusual behavior is due to the contribution from higher spatial harmonics, which, unlike the case of electromagnetic waves in a periodic vacuum waveguide, are volumetric in character.

Such diversity of the dispersion characteristics and field distributions is favorable for implementing various regimes of the interaction between plasma waves and charged-particle beams. Previously, the modulation of an electron beam in a nearly sinusoidal plasma wave field was studied in detail. However, the modulation character may change substantially as the frequency approaches the forbidden band.

The results obtained may also be of interest for the development of plasma-based charged-particle accelerators, because it is shown that, under certain conditions, the local values of the plasma wave fields in periodic plasma waveguides can be very high.

Although we have considered in detail one of the simplest plasma-filled periodic structures (a planar corrugated waveguide filled with a fully magnetized, cold uniform collisionless plasma), we can anticipate that the results obtained are general in character and the method used may be extended to researching plasma structures that are closer to the experimental ones.

ACKNOWLEDGMENTS

I am grateful to K. Shuenemann for valuable discussions and for his continuing interest in this work. This study was supported in part by the NATO Scientific Affairs Division (grant no. PST.CLG.976412).

REFERENCES

1. D. M. Goebel, E. A. Adler, E. S. Ponti, *et al.*, IEEE Trans. Plasma Sci. **27**, 800 (1999).
2. M. A. Zavjalov, L. A. Mitin, V. I. Perevodchikov, *et al.*, IEEE Trans. Plasma Sci. **22**, 600 (1994).
3. A. N. Antonov, Yu. P. Bliokh, Yu. A. Degtyar', *et al.*, Fiz. Plazmy **20**, 777 (1994) [Plasma Phys. Rep. **20**, 699 (1994)].
4. G. S. Nusinovich, Y. Carmel, T. M. Antonsen, *et al.*, IEEE Trans. Plasma Sci. **26**, 628 (1998).
5. O. T. Loza, A. G. Shkvarunets, and P. S. Strelkov, IEEE Trans. Plasma Sci. **26**, 615 (1998).
6. A. T. Lin and A. Chen, Phys. Rev. Lett. **63**, 2808 (1989).
7. M. M. Ali, K. Minami, K. Ogura, *et al.*, Phys. Rev. Lett. **65**, 855 (1990).
8. V. I. Kurilko, V. I. Kucherov, and A. O. Ostrovskiĭ, Zh. Tekh. Fiz. **51**, 1415 (1981) [Sov. Phys. Tech. Phys. **26**, 812 (1981)].
9. H. Kosai, E. P. Garate, and A. Fisher, IEEE Trans. Plasma Sci. **18**, 1002 (1990).
10. R. Sawhney, K. P. Maheshwari, and Y. Choyal, IEEE Trans. Plasma Sci. **21**, 609 (1993).
11. M. Botton and A. Ron, Phys. Rev. Lett. **66**, 2468 (1991).
12. M. Botton and A. Ron, Phys. Fluids B **4**, 1979 (1992).
13. K. Minami, Y. Carmel, V. L. Granatstein, *et al.*, IEEE Trans. Plasma Sci. **18**, 537 (1990).
14. S. M. Miller, T. M. Antonsen, and B. Levush, IEEE Trans. Plasma Sci. **26**, 680 (1998).
15. C. S. Liu and V. K. Tripathi, IEEE Trans. Plasma Sci. **21**, 191 (1993).
16. N. S. Erokhin, M. V. Kuzelev, S. S. Moiseev, *et al.*, *Nonequilibrium and Resonant Processes in Plasma Radiophysics* (Nauka, Moscow, 1982).
17. Y. Carmel, W. R. Lou, T. M. Antonsen, *et al.*, Phys. Fluids B **4**, 2286 (1992).

18. A. O. Ostrovskiĭ and V. V. Ognivenko, Radiotkh. Élektron. (Moscow) **24**, 2470 (1979).
19. K. Ogura, M. M. Ali, K. Minami, *et al.*, J. Phys. Soc. Jpn. **61**, 4022 (1992).
20. W. R. Lou, Y. Carmel, T. M. Antonsen, *et al.*, Phys. Rev. Lett. **67**, 2481 (1991).
21. X. Zhai, E. Garate, R. Prohaska, and G. Benford, Phys. Rev. A **45**, R8336 (1992).
22. G. I. Zaginaylov, A. A. Rozhkov, and J.-Y. Raguin, Phys. Rev. E **60**, 7391 (1999).
23. Q. Wang, Y. Jiang, and X. Du, IEEE Trans. Plasma Sci. **25**, 763 (1997).
24. A. N. Tikhonov and A. A. Samarskii, *Equations of Mathematical Physics* (Nauka, Moscow, 1966; Pergamon, Oxford, 1964).
25. I. L. Verbitskii and G. I. Zaginaylov, IEEE Trans. Plasma Sci. **27**, 1101 (1999).

Translated by N.F. Larionova

Plasma Physics Reports, Vol. 27, No. 5, 2001, pp. 398–406. Translated from Fizika Plazmy, Vol. 27, No. 5, 2001, pp. 423–431.

PLASMA OSCILLATIONS AND WAVES

Spectra of Electromagnetic Radiation from a Hot Plasma with Langmuir Turbulence in a Magnetic Field

V. V. Tirsky*, V. G. Ledenev, and V. M. Tomozov****

**Institute of Laser Physics, Irkutsk Branch, Siberian Division, Russian Academy of Sciences, Irkutsk, 664033 Russia*

***Institute of Solar and Terrestrial Physics, Siberian Division, Russian Academy of Sciences, Irkutsk, 664033 Russia*

Received July 11, 2000; in final form, November 9, 2000

Abstract—A study is made of the generation of electromagnetic waves during the merging of two Langmuir plasmons in a hot plasma with a magnetic field. It is shown that the frequency of Langmuir plasmons can vary in the range from 0.8 to 1.1 of the electron Langmuir frequency. The spectrum and polarization of the emitted electromagnetic radiation are analyzed. It is found that the thermal motion of plasma particles may lead to the generation of electromagnetic waves in the frequency range from 1.6 to 2.2 of the electron Langmuir frequency. In a plasma with an isotropic Langmuir turbulence spectrum, the degree of circular polarization of the emitted radiation can amount to 50%. *© 2001 MAIK "Nauka/Interperiodica".*

1. INTRODUCTION

Conditions favorable for the onset of Langmuir turbulence may often arise in both laboratory and space plasmas. In a turbulent plasma, electromagnetic radiation can be generated during the merging of two Langmuir plasmons, $l_1 + l_2 \longrightarrow t$ [1]. This process in the absence of a magnetic field was thoroughly examined in monographs [1–3]. The presence of a magnetic field significantly alters the generation of electromagnetic radiation. For a weak magnetic field, the generation process was investigated by Zlotnik [4], who analyzed both the polarization and power of the electromagnetic radiation generated during the merging of two Langmuir plasmons in a cold plasma without allowance for the effect of the thermal motion of plasma particles on the plasma dielectric tensor and, accordingly, on the dispersion of Langmuir waves.

In this paper, we investigate how the thermal motion of plasma particles affects the merging process in a plasma with Langmuir turbulence in a magnetic field. We treat the case in which the electron gyrofrequency is lower than the electron Langmuir frequency. Assuming that the plasma particles obey a Maxwellian energy distribution and taking into account thermal corrections, we investigate the polarization of the generated electromagnetic radiation.

2. DISPERSION RELATION FOR LANGMUIR WAVES IN A HOT PLASMA WITH A MAGNETIC FIELD

The expression for the dielectric tensor of a plasma in a magnetic field can be found, e.g., in monographs [3, 5]. We use the expression presented in the book by V.L. Ginzburg and A.A. Rukhadze [5]. Under the conditions

$$Z_e^3 = ((k_{1\perp}^6 v_{Te}^6)/\omega_{Be}^6) \ll 1,$$
$$\beta_{se}^3 = \left(\frac{\omega_1 - s\omega_{Be}}{|k_{1z}| v_{Te}}\right)^3 \gg 1, \quad (1)$$

where $s = \ldots, -1, 0, 1, \ldots$, the plasma dielectric tensor elements are

$$\varepsilon_{xx} = 1 - \frac{\omega_{pe}^2}{2\omega_1(\omega_1 - \omega_{Be})}\{1 - Z_e + Z_e^2(5/8)\}$$
$$\times \{1 + \beta_{1e}^{-2} + 3\beta_{1e}^{-4} - i\sqrt{(\pi/2)}\beta_{1e}\exp(-\beta_{1e}^2/2)\}$$
$$- \frac{\omega_{pe}^2}{2\omega_1(\omega_1 + \omega_{Be})}\{1 - Z_e + Z_e^2(5/8)\} \quad (2)$$
$$\times \{1 + \beta_{-1e}^{-2} + 3\beta_{-1e}^{-4} - i\sqrt{(\pi/2)}\beta_{-1e}\exp(-\beta_{-1e}^2/2)\},$$

$$\varepsilon_{xz} = \varepsilon_{zx} = \frac{\omega_{pe}^2 k_{1\perp}}{2\omega_1\omega_{Be}k_{1z}}\{1 - Z_e + Z_e^2(5/8)\}$$
$$\times \{\beta_{-1e}^{-2} - \beta_{1e}^{-2} + 3\beta_{-1e}^{-4} - 3\beta_{1e}^{-4} \quad (3)$$
$$+ i\sqrt{(\pi/2)}(\beta_{1e}\exp(-\beta_{1e}^2/2) - \beta_{-1e}\exp(-\beta_{-1e}^2))\}.$$

$$\varepsilon_{zz} = 1 + \frac{\omega_{pe}^2}{k_{1z}^2 v_{Te}^2}\{1 - Z_e + Z_e^2(3/4)\}$$
$$\times \{-\beta_{0e}^{-2} - 3\beta_{0e}^{-4} + i\sqrt{(\pi/2)}\beta_{0e}\exp(-\beta_{0e}^2/2)\}$$
$$+ \frac{\omega_{pe}^2(\omega_1 - \omega_{Be})Z_e}{2\omega_1 k_{1z}^2 v_{Te}^2}\{1 - Z_e + Z_e^2(5/8)\}$$

1063-780X/01/2705-0398$21.00 © 2001 MAIK "Nauka/Interperiodica"

$$\times\{-\beta_{1e}^{-2}-3\beta_{1e}^{-4}+i\sqrt{(\pi/2)}\beta_{1e}\exp(-\beta_{1e}^2/2)\} \quad (4)$$

$$+\frac{\omega_{pe}^2(\omega_1+\omega_{Be})Z_e}{2\omega_1 k_{1z}^2 v_{Te}^2}\{1-Z_e+Z_e^2(5/8)\}$$

$$\times\{-\beta_{-1e}^{-2}-3\beta_{-1e}^{-4}+i\sqrt{(\pi/2)}\beta_{-1e}\exp(-\beta_{-1e}^2/2)\}.$$

The dispersion relation for the longitudinal Langmuir waves in a magnetic field has the form

$$\frac{k_{1i}k_{1j}}{k_1^2}\varepsilon_{ij} = 0. \quad (5)$$

For a hot plasma in which the electron gyrofrequency is lower than the electron Langmuir frequency, the solution to Eq. (5) can always be represented as the sum of the Langmuir frequency and small terms (thermal corrections and corrections introduced by the magnetic field).

We substitute the tensor elements (2)–(4) expanded about the electron Langmuir frequency ω_{pe} into Eq. (5) to obtain the following dispersion relation for Langmuir turbulent pulsations in a plasma with a magnetic field:

$$\frac{\omega_1-\omega_{pe}}{\omega_{pe}} = -\frac{Ax+D+yF}{xC+E+yG}, \quad (6)$$

where

$$A = 1-\frac{1}{2(1-a)}\{1-bxa^{-2}+b^2x^2a^{-4}(5/8)\}$$
$$\times\{1+by(1-a)^{-2}+3b^2y^2(1-a)^{-4}\}$$
$$-\frac{1}{2(1+a)}\{1-bxa^{-2}+b^2x^2a^{-4}(5/8)\} \quad (7)$$
$$\times\{1+by(1+a)^{-2}+3b^2y^2(1+a)^{-4}\},$$

$$C = \frac{1}{2}\{1-bxa^{-2}+b^2x^2a^{-4}(5/8)\}$$
$$\times\left\{\frac{2+a}{(1+a)^2}+\frac{2-a}{(1-a)^2}+by\left[\frac{4+a}{(1+a)^4}+\frac{4-a}{(1-a)^4}\right]\right. \quad (8)$$
$$\left.+3b^2y^2\left[\frac{6+a}{(1+a)^6}+\frac{6-a}{(1-a)^6}\right]\right\},$$

$$F = 1+\{1-bxa^{-2}+b^2x^2a^{-4}(3/4)\}\{-1-3by\}$$
$$+\frac{bx}{2a^2}\{1-bxa^{-2}+b^2x^2a^{-4}(5/8)\} \quad (9)$$
$$\times\left\{-\frac{1}{1-a}-\frac{1}{1+a}-3by\left[\frac{1}{(1-a)^3}+\frac{1}{(1+a)^3}\right]\right\},$$

$$G = \{1-bxa^{-2}+b^2x^2a^{-4}(3/4)\}\{2+12by\}$$
$$+\frac{bx}{2a^2}\{1-bxa^{-2}+b^2x^2a^{-4}(5/8)\} \quad (10)$$
$$\times\left\{\frac{2+a}{(1+a)^2}+\frac{2-a}{(1-a)^2}+3by\left[\frac{4+a}{(1+a)^4}+\frac{4-a}{(1-a)^4}\right]\right\},$$

$$D = \frac{x}{a}\{1-bxa^{-2}+b^2x^2a^{-4}(5/8)\}$$
$$\times\left\{by\left[\frac{1}{(1+a)^2}-\frac{1}{(1-a)^2}\right]\right. \quad (11)$$
$$\left.+3b^2y^2\left[\frac{1}{(1+a)^4}-\frac{1}{(1-a)^4}\right]\right\},$$

$$E = \frac{x}{a}\{1-bxa^{-2}+b^2x^2a^{-4}(5/8)\}$$
$$\times\left\{by\left[\frac{3-a}{(1-a)^3}-\frac{3+a}{(1+a)^3}\right]\right. \quad (12)$$
$$\left.+3b^2y^2\left[\frac{5-a}{(1-a)^5}-\frac{5+a}{(1+a)^5}\right]\right\},$$

$$a = \frac{\omega_{Be}}{\omega_{pe}}, \quad b = \frac{k_1^2v_{Te}^2}{\omega_{pe}^2}, \quad x = \sin^2\theta_1, \quad (13)$$
$$y = \cos^2\theta_1.$$

Expression (6), which is valid under conditions (1), can be reduced to a simpler form containing only first-order (in parameter b) thermal corrections:

$$\frac{\omega^l(\mathbf{k}_1)-\omega_{pe}}{\omega_{pe}} \approx \frac{3}{2}b+\frac{1}{2}a^2x-\frac{b}{2a^2}x^2. \quad (14)$$

Note that, according to expressions (13), the parameter b/a^2 is the squared ratio of the electron gyroradius to the wavelength of the Langmuir plasmon. Figures 1 and 2 show the dependence of the ratio $(\omega-\omega_{pe})/\omega_{pe}$ in formula (6) on the angle θ_1 between the wave vector and the magnetic induction vector for different values of b/a^2 and b. We can see that, under conditions (1), the Langmuir plasmon frequency ω for the maximum possible values of b/a^2 and for θ_1 close to 90° is lower than the electron Langmuir frequency by 20%, whereas for θ_1 close to zero, ω is higher than ω_{pe} by approximately 5–10%. Note that, in accordance with formula (14), this difference is pronounced even in the linear approximation in parameter b. Hence, we can conclude that, if the Langmuir turbulence spectrum contains plasmons with wavelengths close to the electron gyroradius, then the

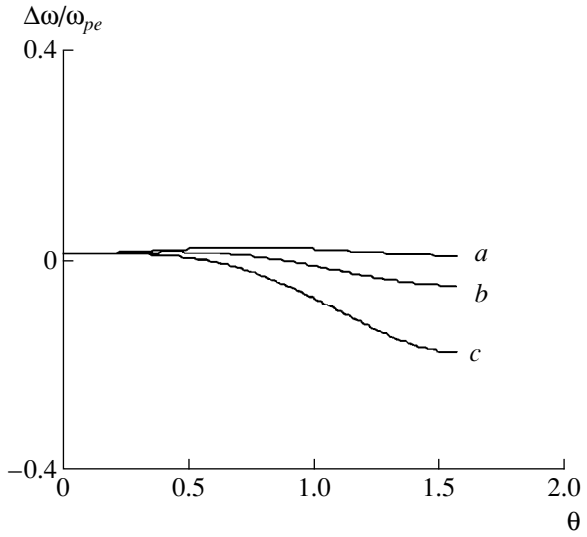

Fig. 1. Dispersion of Langmuir waves ($\Delta\omega = \omega_1 - \omega_{pe}$) vs. the angle between the magnetic induction vector and the wave vector for $b = k_1^2 v_{Te}^2/\omega_{pe}^2 = 0.01$ and different ratios of the squared electron gyroradius to the squared wavelength: $b/a^2 =$ (*a*) 0.09, (*b*) 0.16, and (*c*) 0.36.

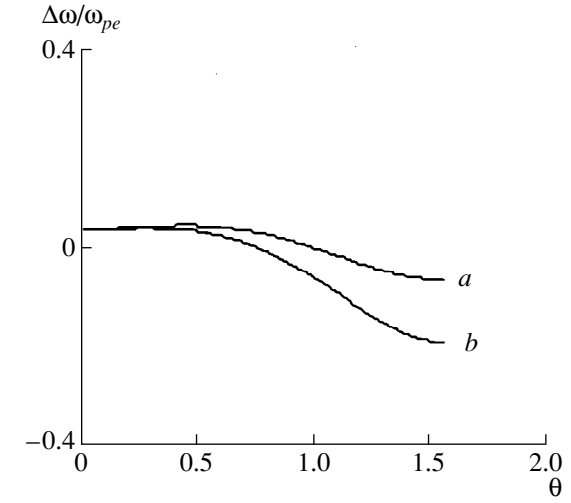

Fig. 2. Same as in Fig. 1, but for $b = 0.03$ and $b/a^2 =$ (*a*) 0.27 and (*b*) 0.48.

merging of two such plasmons can result in the generation of electromagnetic radiation in the frequency band from $1.6\omega_{pe}$ to $2.2\omega_{pe}$ (in accordance with the conservation of energy and momentum during the merging process). Below, we will be interested precisely in these mergings, assuming that the plasmon wavelengths in the Langmuir turbulence spectrum range from 1.4 ($(b/a^2) = 0.5$) to several electron gyroradii.

3. MERGING OF TWO LANGMUIR PLASMONS ACCOMPANIED BY THE GENERATION OF AN ELECTROMAGNETIC WAVE

We consider the merging process in a hot plasma with a magnetic field. We take into account thermal corrections through the first order in the expansion in parameter *b* and assume that $a \le 1/3$. In the Langmuir turbulence spectrum, we are interested in plasmon wavelengths $2\pi/k_1$ that range from 1.4 to several electron gyroradii, in which case the wavenumbers of the Langmuir plasmons are much larger than the wavenumbers of the generated electromagnetic radiation and the conditions $Z_e^2 \ll 1$ and $\beta_{se}^2 \gg 1$ hold.

The merging process under investigation is described by the equation [1]

$$\left[\frac{\partial}{\partial t} + \left(\mathbf{v}_{on}(\kappa)\frac{\partial}{\partial \mathbf{r}}\right)\right] I_{ij}(\kappa) = 4(2\pi)^3\omega^2\left[\frac{\partial}{\partial\omega}(\omega^2\varepsilon_\kappa^t)\right]^{-1}\delta(k^2c^2 - \omega^2\varepsilon_\kappa^t)R_{ij}(\kappa). \quad (15)$$

Here,

$$\mathbf{v}_{on}(\kappa) = \left[\frac{\partial}{\partial\mathbf{k}}(k^2c^2 - \omega^2\varepsilon_\kappa^t)\right]\left[\frac{\partial}{\partial\omega}(\omega^2\varepsilon_\kappa^t)\right]^{-1},$$
$$R_{\kappa,ij} = \int d\kappa_1 d\kappa_2 \delta(\kappa - \kappa_1 - \kappa_2) \quad (16)$$
$$\times I^l(\kappa_1)I^l(\kappa_2)\lambda_i(\kappa, \kappa_1, \kappa_2)\lambda_j^*(\kappa, \kappa_1, \kappa_2),$$

where $\kappa(\omega, \mathbf{k})$ is the four-dimensional wave vector of the generated electromagnetic wave, $\kappa_1(\omega_1, \mathbf{k}_1)$ and $\kappa_2(\omega_2, \mathbf{k}_2)$ are the four-dimensional wave vectors of the Langmuir plasmons, ε_κ^t is the plasma dielectric function, and $I_{ij}(\kappa)$ is the spectral matrix of electromagnetic radiation. When the electron gyrofrequency is much lower than the electron Langmuir frequency (i.e., the dispersion of the Langmuir wave is determined by small corrections introduced by the plasma temperature and magnetic field), we have

$$I^l(\kappa_1) = W^l(\mathbf{k}_1)\delta[\omega_1 - \omega^l(\mathbf{k}_1)]/4\pi^2,$$
$$I^l(\kappa_2) = W^l(\mathbf{k}_2)\delta[\omega_2 - \omega^l(\mathbf{k}_2)]/4\pi^2, \quad (17)$$

where $W^l(\mathbf{k}_1)$ and $W^l(\mathbf{k}_2)$ are the spectral functions of the Langmuir turbulence.

Consequently, we can take the integrals over ω_1 and ω_2 in formula (16) and use expressions (17) to arrive at

$$R_{\kappa,ij} = \int d\mathbf{k}_1 d\mathbf{k}_2 \delta(\mathbf{k} - \mathbf{k}_1 - \mathbf{k}_2)\delta[\omega - \omega^l(\mathbf{k}_1) - \omega^l(\mathbf{k}_2)](4\pi^2)^{-2}W^l(\mathbf{k}_1)W^l(\mathbf{k}_2)\lambda_i\lambda_j^*,$$

where quantities λ_i are functions of variables k, k_1, $k-k_1$, ω, $\omega(k_1)$, and $\omega(k-k_1)$.

In the last expression, we take the integrals over the absolute value of dk_1 and over the vector dk_2. As a result, we obtain

$$R_{\kappa,ij} = \int \sin\theta_1 d\theta_1 d\phi_1 \left\{ \frac{\partial}{\partial k_1} [\omega - \omega^l(\mathbf{k}_1) - \omega^l(\mathbf{k}-\mathbf{k}_1)] \right\}^{-1} \times (4\pi^2)^{-2} W^l(\mathbf{k}_1) W^l(\mathbf{k}-\mathbf{k}_1) \lambda_i \lambda_j^* \Big|_{k_1 = k_{1\text{const}}}, \quad (18)$$

where $k_{1\text{const}}$ is the solution to the following algebraic equation, which reflects the conservation of energy (or, equivalently, frequencies) in the merging process:

$$\omega - \omega^l(\mathbf{k}_1) - \omega^l(\mathbf{k}-\mathbf{k}_1) = 0. \quad (19)$$

To first order in parameter b,

$$\omega^l(\mathbf{k}_1) = \omega_{pe} + \frac{3k_1^2 v_{Te}^2}{2\omega_{pe}} + \frac{\omega_{Be}^2}{2\omega_{pe}} \sin^2\theta_1 - \frac{k_1^2 v_{Te}^2}{2\omega_{Be}^2} \omega_{pe} \sin^4\theta_1, \quad (20)$$

$$\omega^l(\mathbf{k}-\mathbf{k}_1) = \omega_{pe} + \frac{3(\mathbf{k}-\mathbf{k}_1)^2 v_{Te}^2}{2\omega_{pe}} + \frac{\omega_{Be}^2 (k\sin\theta - k_1\sin\theta_1)^2}{2\omega_{pe}(\mathbf{k}-\mathbf{k}_1)^2} - \frac{v_{Te}^2 \omega_{pe} (k\sin\theta - k_1\sin\theta_1)^4}{2\omega_{Be}^2 (\mathbf{k}-\mathbf{k}_1)^2}, \quad (21)$$

where θ is the angle between the wave vector of the electromagnetic wave and the magnetic induction vector.

When the absolute value of vector $\mathbf{k}$ is much smaller than the absolute values of vectors $\mathbf{k}_1$ and $\mathbf{k}_2$, vector $\mathbf{k}_{1\text{const}}$ is related to the frequency of the generated electromagnetic wave by the formula

$$k_{1\text{const}}^2 = (\omega - 2\omega_{pe} - \omega_{pe} a^2 x) \Big/ \left(\frac{3v_{Te}^2}{\omega_{pe}} - \frac{v_{Te}^2 \omega_{pe}}{\omega_{Be}^2} \sin^4\theta_1 \right), \quad (22)$$

in which the terms on the order of k/k_1 are neglected.

It is seen that, under the above conditions, expression (22) with a negative denominator describes the generation of electromagnetic waves whose frequencies are lower than the doubled Langmuir frequency. When the denominator is positive, expression (22) describes the generation of electromagnetic waves at frequencies higher than the doubled Langmuir frequency. Note that, by virtue of the resonant character of the frequency conservation during the generation of electromagnetic waves, the thermal corrections primarily affect the relationship between the absolute value of vector $\mathbf{k}_1$ and the expression for the frequency of the emitted electromagnetic radiation. Note also that, although expression (22) contains terms proportional to a^2, the relationship between the wave vector k_1 of the Langmuir waves and the frequency ω of electromagnetic radiation is described by terms of the first order in parameter a, because the left-hand side of expression (22) is the squared wavenumber of Langmuir turbulent pulsations.

To first order in the parameter k/k_1, we obtain

$$k_{1\text{const}}'^2 = \frac{\omega - 2\omega_{pe} - \dfrac{\omega_{Be}^2 \sin^2\theta_1}{\omega_{pe}} - f_{11}(\theta, \theta_1, k, v_{Te})}{\dfrac{3v_{Te}^2}{\omega_{pe}} - \dfrac{v_{Te}^2 \omega_{pe} \sin^4\theta_1}{\omega_{Be}^2}}, \quad (23)$$

where

$$f_{11} = \frac{k}{k_{1\text{const}}} \left\{ -\frac{3k_{1\text{const}}^2 v_{Te}^2 (\mathbf{k}\mathbf{k}_1)}{\omega_{pe} k k_1} + \frac{\omega_{Be}^2}{\omega_{pe}} \left[\sin^2\theta_1 \frac{(\mathbf{k}\mathbf{k}_1)}{k k_1} - \sin\theta_1 \sin\theta \right] - \frac{v_{Te}^2 \omega_{pe} k_{1\text{const}}^2}{\omega_{Be}^2} \left[\sin^4\theta_1 \frac{(\mathbf{k}\mathbf{k}_1)}{k k_1} - 2\sin\theta \sin\theta_1 \right] \right\}. \quad (24)$$

According to expressions (23) and (24), first-order effects in k/k_1 can only affect the generation of electromagnetic waves at frequencies that differ from the frequency

$$\omega = 2\omega_{pe} + \frac{\omega_{Be}^2 \sin^2\theta_1}{\omega_{pe}}$$

at which the radiation is emitted most intensively by the amount

$$\Delta\omega \approx \pm \frac{v_{Te}^2 k k_1}{2\omega_{Be}^2} \omega_{pe}.$$

Below, when analyzing the generation of electromagnetic radiation during the merging process, we will exclude from consideration this frequency range (under conditions typical of, e.g., the plasma in the solar corona, its width is usually smaller than 5% of the electron plasma frequency).

For high-frequency Langmuir turbulent pulsations in a magnetic field, quantities λ_i can be expanded in powers of the small parameters ω_{Be}/ω and b (the latter parameter accounts for the thermal motion of plasma particles) [1]. In such expansions, it is sufficient to retain terms up to first order in both ω_{Be}/ω and b. The higher order terms are neglected because they are much smaller.

In this approximation, quantities λ_i have the form [1]

$$\lambda_i(\kappa, \kappa_1, \kappa_2) = M^t_{mi}(\mathbf{h}, \mathbf{n}) 2\tilde{S}_{mpl}(\kappa, \kappa_1, \kappa_2) e^l_p(\kappa_1) e^l_l(\kappa_2). \quad (25)$$

Here, $e^l_p(\kappa_1) = \frac{\boldsymbol{\kappa}_1}{\kappa_1}$, $e^l_l(\kappa_2) = \frac{\boldsymbol{\kappa}_2}{\kappa_2}$; the matrices $M^t_{mi}(\mathbf{h}, \mathbf{n})$ describe the transition from the laboratory frame of reference to the frame related to the generated electromagnetic wave [6]; and the tensor elements S_{mpl} have the form [1]

$$S_{x,ip}(\kappa, \kappa_1, \kappa_2) = \left\{\delta_{xi} + i\frac{\omega_{Be}}{\omega}\delta_{yi}\right\} S_p(\kappa_2), \quad (26)$$

$$S_{y,ip}(\kappa, \kappa_1, \kappa_2) = \left\{\delta_{yi} - i\frac{\omega_{Be}}{\omega}\delta_{xi}\right\} S_p(\kappa_2), \quad (27)$$

$$S_{z,ip}(\kappa, \kappa_1, \kappa_2) = \delta_{zi} S_p(\kappa_2), \quad (28)$$

$$S_p(\kappa_2) = \frac{\omega^2_{pe}}{(4\pi)^2 n_0 |e| \omega} k_{2r}[\varepsilon^l_{rp}(\kappa_2) - \delta_{rp}], \quad (29)$$

where n_0 is the electron plasma density, $|e|$ is the absolute value of the electron charge, and ε^l_{rp} is the dielectric tensor for Langmuir plasmons.

In this case, expression (25) reduces to

$$\begin{aligned}\lambda_x(\kappa, \kappa_1, \kappa_2) &= \frac{\omega^2_{pe} k_2 \sin\phi}{(4\pi)^2 n_0 e\omega}\left\{e^l_x(\kappa_1) + i\frac{\omega_{Be}}{\omega}e^l_y(\kappa_1)\right\} \\ &+ \frac{\omega^2_{pe} k_1 \sin\phi}{(4\pi)^2 n_0 e\omega}\left\{e^l_x(\kappa_2) + i\frac{\omega_{Be}}{\omega}e^l_y(\kappa_2)\right\} \\ &- \frac{\omega^2_{pe} k_2 \cos\phi}{(4\pi)^2 n_0 e\omega}\left\{e^l_y(\kappa_1) - i\frac{\omega_{Be}}{\omega}e^l_x(\kappa_1)\right\} \\ &- \frac{\omega^2_{pe} k_1 \cos\phi}{(4\pi)^2 n_0 e\omega}\left\{e^l_y(\kappa_2) - i\frac{\omega_{Be}}{\omega}e^l_x(\kappa_2)\right\},\end{aligned} \quad (30)$$

$$\begin{aligned}\lambda_y(\kappa, \kappa_1, \kappa_2) &= \frac{\omega^2_{pe} k_2 \cos\theta\cos\phi}{(4\pi)^2 n_0 e\omega}\left\{e^l_x(\kappa_1) + i\frac{\omega_{Be}}{\omega}e^l_y(\kappa_1)\right\} \\ &+ \frac{\omega^2_{pe} k_1 \cos\theta\cos\phi}{(4\pi)^2 n_0 e\omega}\left\{e^l_x(\kappa_2) + i\frac{\omega_{Be}}{\omega}e^l_y(\kappa_2)\right\} \\ &+ \frac{\omega^2_{pe} k_2 \cos\theta\sin\phi}{(4\pi)^2 n_0 e\omega}\left\{e^l_y(\kappa_1) - i\frac{\omega_{Be}}{\omega}e^l_x(\kappa_1)\right\} \\ &+ \frac{\omega^2_{pe} k_1 \cos\theta\sin\phi}{(4\pi)^2 n_0 e\omega}\left\{e^l_y(\kappa_2) - i\frac{\omega_{Be}}{\omega}e^l_x(\kappa_2)\right\} \\ &- \frac{\omega^2_{pe}\sin\theta}{(4\pi)^2 n_0 e\omega}\{e^l_z(\kappa_1)k_2 + e^l_z(\kappa_2)k_1\}.\end{aligned} \quad (31)$$

We expand expressions (30) and (31) in powers of the small parameter k/k_1 and retain terms up to second order. As a result, we obtain

$$\begin{aligned}\lambda_x(\kappa, \kappa_1, \kappa_2) &\approx -\frac{\omega^2_{pe} 2k e^l(\kappa_1)\sin\phi}{(4\pi)^2 n_0 e\omega}\left\{e^l_x(\kappa_1) + i\frac{\omega_{Be}}{\omega}e^l_y(\kappa_1)\right\} \\ &+ \frac{\omega^2_{pe} 2k e^l(\kappa_1)\cos\phi}{(4\pi)^2 n_0 e\omega}\left\{e^l_y(\kappa_1) - i\frac{\omega_{Be}}{\omega}e^l_x(\kappa_1)\right\},\end{aligned} \quad (32)$$

$$\begin{aligned}\lambda_y(\kappa, \kappa_1, \kappa_2) &\approx -\frac{\omega^2_{pe} 2k e^l(\kappa_1)\cos\theta\cos\phi}{(4\pi)^2 n_0 e\omega}\left\{e^l_x(\kappa_1) + i\frac{\omega_{Be}}{\omega}e^l_y(\kappa_1)\right\} \\ &- \frac{\omega^2_{pe} 2k e^l(\kappa_1)\cos\theta\sin\phi}{(4\pi)^2 n_0 e\omega}\left\{e^l_y(\kappa_1) - i\frac{\omega_{Be}}{\omega}e^l_x(\kappa_1)\right\} \\ &+ \frac{\omega^2_{pe} 2k e^l(\kappa_1)\sin\theta}{(4\pi)^2 n_0 e\omega}e^l_z(\kappa_1).\end{aligned} \quad (33)$$

In a plasma with a magnetic field, Langmuir turbulence is often generated during the injection of a relativistic electron beam. In laboratory installations (e.g., in the GOL-3 device at the Budker Institute of Nuclear Physics, Siberian Division of the Russian Academy of Sciences), a relativistic electron beam is injected along the magnetic induction vector. In a laboratory plasma with a magnetic field such that the gyrofrequency of the plasma electrons is lower than the electron Langmuir frequency, the ions are, as a rule, unmagnetized and obey an isotropic velocity distribution [7]. Langmuir plasmons scattered by the plasma ions become distributed isotropically on time scales τ on the order of [1]

$$\frac{1}{\tau} \sim \omega_{pe}\frac{W}{n_e T_e}.$$

In such devices, the spectrum of Langmuir plasmons may become isotropic when the characteristic isotropization rate τ^{-1} is much higher than both the frequency of binary collisions between the plasma electrons and the inverse duration of the electron beam. This situation can arise when the plasma density is about 10^{13}–10^{14} cm^{-3} and the density of the relativistic electrons is about 10^{11}–10^{12} cm^{-3} (the energy of relativistic electrons being about 1 MeV); in this case, the gyrofrequency of the plasma electrons is lower than their Langmuir frequency. In space plasmas, the Langmuir turbulence spectrum often becomes isotropic under conditions analogous to those in the solar corona and the Earth's ionosphere. For such space plasmas, the isotropic Langmuir turbulence approximation, which is often used in model calculations, was justified in [1, 8]. Hence, when a relativistic electron beam propagates in laboratory or space plasmas with a magnetic field, the Langmuir turbulence spectrum may often become isotropic.

We consider an isotropic Langmuir turbulence spectrum of the form ($\eta \neq 3$)

$$W^l_{\mathbf{k}_2 = -\mathbf{k}_1} = W^l_{\mathbf{k}_1} = \frac{2\pi^2 W^l (3-\eta)}{k_1^{\eta}(k_{1\max}^{3-\eta} - k_{1\min}^{3-\eta})},$$

such that

$$\int_{k_{1\min}}^{k_{1\max}} W^l_{\mathbf{k}_1} \frac{d\mathbf{k}_1}{(2\pi)^3} = W^l,$$

where W^l is the energy density of Langmuir turbulent pulsations and $k_{1\max}$ and $k_{1\min}$ are the maximum and minimum wavenumbers in the Langmuir turbulence spectrum. We take into account the relationships [1]

$$I_{\mathbf{k}\frac{R}{L}} = \int d\omega [I_{\kappa, xx} + I_{\kappa, yy} \pm i(I_{\kappa, yx} - I_{\kappa, xy})] \times \left(2\pi^2 \frac{\partial(\omega^2 \varepsilon^t_\kappa)}{\partial\omega}\right)^{-1} \delta(\omega - \omega_{\mathbf{k}}),$$

where

$$\frac{\partial(\omega^2 \varepsilon^t_\kappa)}{\partial\omega} = \frac{\partial(\omega^2 n^2)}{\partial\omega}, \quad v_{g\frac{R}{L}} = c n_{\frac{R}{L}}.$$

We also take into account the fact that the functions $I_{R,k}$ and $I_{L,k}$ of electromagnetic waves with left-hand and right-hand circular polarizations are related to the functions $I_{R,\omega}$ and $I_{L,\omega}$ by the expressions [1]

$$I_{\omega\frac{R}{L}} = k^2 I_{\mathbf{k}\frac{R}{L}}.$$

Under the above conditions, we can also use the following expression for the refractive index of the electromagnetic waves [4]:

$$n_{\frac{R}{L}} = \left(1 - \frac{\omega_{pe}^2}{\omega^2}\right)^2 \left\{1 \mp \frac{\omega_{pe}^2 \omega_{Be} |\cos\theta|}{2\omega^3 \left(1 - \frac{\omega_{pe}^2}{\omega^2}\right)}\right\}.$$

Then, substituting expressions (32) and (33) for λ_i into formula (18), we arrive at the equation describing the generation of electromagnetic radiation during the merging of two Langmuir plasmons in a magnetic field:

$$\left[\frac{\partial}{\partial t} + \mathbf{v}^t_{g\frac{R}{L}} \frac{\partial}{\partial \mathbf{r}}\right] I_{\omega\frac{R}{L}} = \frac{\pi}{8} \frac{(W^l)^2}{n_0 m_e c^4} \times \frac{\omega_{pe}^{6-2\eta} (3v_{Te}^2)^{\eta-1.5} (3-\eta)^2}{(k_{1\max}^{3-\eta} - k_{1\min}^{3-\eta})^2} \frac{(1-p^2)^2}{p^2} \times \left[1 \mp \frac{ap^3 |\cos\theta|}{2} \frac{(5-p^2)}{(1-p^2)}\right] \int_{\xi}^{u} \sin\theta_1 d\theta_1 [U_1(\theta, \theta_1) \pm 2apU_2(\theta, \theta_1)] f_1^{0.5-\eta}(\omega, \theta_1) f_2^{\eta-1.5}(\theta_1), \tag{34}$$

where

$$U_1(\theta, \theta_1) = \sin^2\theta \sin^2\theta_1 - 0.75 \sin^4\theta \sin^4\theta_1 - 6\sin^2\theta \cos^2\theta \sin^2\theta_1 \cos^2\theta_1 + 2\cos^2\theta \cos^2\theta_1 - 2\cos^4\theta \cos^4\theta_1,$$

$$U_2(\theta, \theta_1) = \sin^2\theta \cos\theta \sin^4\theta_1 - 2\sin^2\theta \cos\theta \sin^2\theta_1 \cos^2\theta_1 + \cos^3\theta \sin^2\theta_1 \cos^2\theta_1,$$

$$p = \omega_{pe}/\omega.$$

For $\omega < 2\omega_{pe}$, we have

$$f_1(\omega, \theta_1) = 2 - p^{-1} + a^2 \sin^2\theta_1,$$

$$f_2(\theta_1) = \frac{1}{3a^2} \sin^4\theta_1 - 1,$$

$$\xi = \theta_{1\lim} = \arcsin\left\{3^{0.25}\left(\frac{\omega_{Be}}{\omega_{pe}}\right)^{0.5}\right\},$$

$$u = \pi - \theta_{1\lim}, \quad 0 \leq \theta_{1\lim} \leq \pi/2.$$

For $\omega \geq 2\omega_{pe}$, we have

$$f_1(\omega, \theta_1) = p^{-1} - 2 - a^2 \sin^2\theta_1,$$

$$f_2(\theta_1) = 1 - \frac{1}{3a^2} \sin^4\theta_1, \quad \xi = 0, \quad u = \theta_{1\lim}.$$

Formula (34) implies that, for $\eta = 2$, the power of electromagnetic radiation (right- and left-polarized waves) emitted into a unit solid angle from the unit volume of

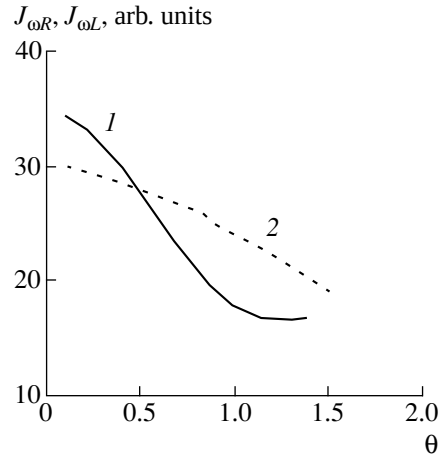

Fig. 3. Spectral powers (*1*) $J_{\omega R}$ and (*2*) $J_{\omega L}$ of the generated electromagnetic waves with right- and left-hand circular polarizations vs. the angle between the wave vector and the magnetic field for $a = \omega_{Be}/\omega_{pe} = 1/3$ and $(1/p) = \omega/\omega_{pe} = 2.1$.

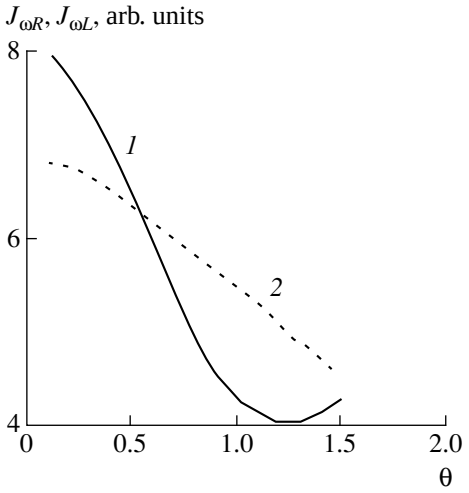

Fig. 4. Same as in Fig. 3, but for $1/p = 2.2$.

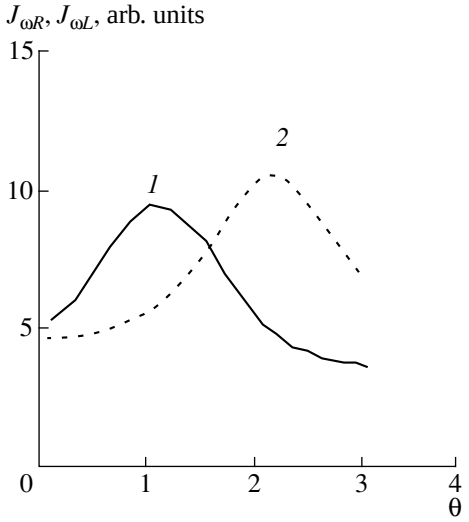

Fig. 5. Same as in Fig. 3, but for $1/p = 1.95$.

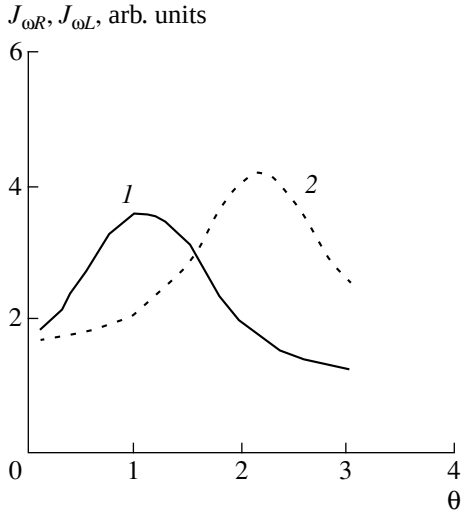

Fig. 6. Same as in Fig. 3, but for $1/p = 1.8$.

a turbulent plasma per unit frequency interval is equal to

$$J_{\omega\frac{R}{L}} = \frac{\pi}{8}\frac{(W^l)^2}{n_0 m_e c^5}\frac{\sqrt{3}\omega_{pe}^2 v_{Te}}{(k_{1\max}-k_{1\min})^2}\frac{(1-p^2)}{p^2}$$

$$\times\left[1 \pm \frac{ap^3|\cos\theta|}{2(1-p^2)} \mp \frac{ap^3|\cos\theta|(5-p^2)}{2(1-p^2)}\right] \qquad (35)$$

$$\times\int \sin\theta_1 d\theta_1 [U_1(\theta,\theta_1) \pm 2apU_2(\theta,\theta_1)]\frac{f_2^{1/2}(\theta_1)}{f_1^{3/2}(\omega,\theta_1)}.$$

For estimates, we consider the case in which $k_{1\max} = k_{De}/4$, where k_{De} is the wavenumber corresponding to the Debye radius. The spectral power of the generated right- and left-polarized waves as a function of the angle between the magnetic induction vector and the direction along which electromagnetic radiation is emitted is illustrated in Figs. 3–7, which were obtained for different values of parameter p and for $a = 1/3$. One can see that, for $p^{-1} > 2$, the maximum intensities of the emitted right- and left-polarized waves are nearly the same and the corresponding intensity profiles are peaked in the angular range $0 \le \theta < 1$. The degree to which the generated radiation is polarized is smaller than 0.1.

For $p^{-1} < 2$, the right-polarized waves are emitted preferentially in the angular range $\theta \sim 1$, while the intensity profile of the generated left-polarized waves is

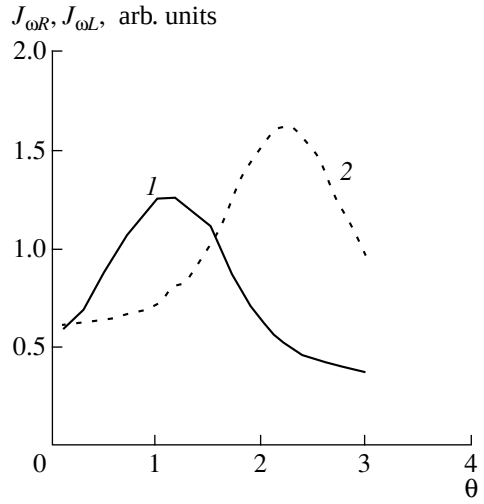

Fig. 7. Same as in Fig. 3, but for $1/p = 1.6$.

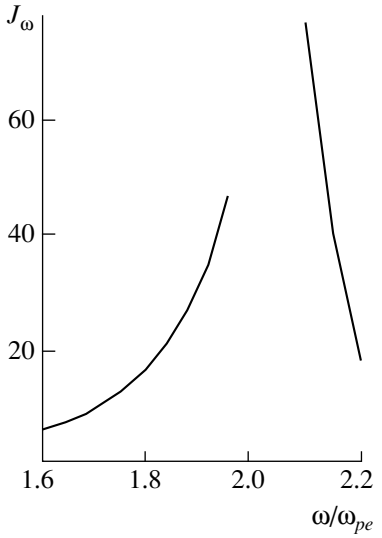

Fig. 8. Angle-averaged spectrum of the generated electromagnetic radiation for $a = 1/3$.

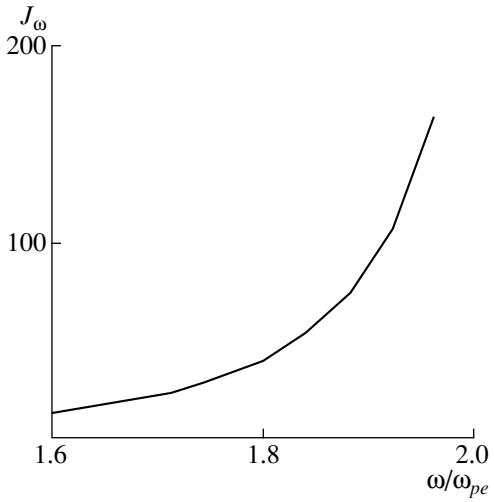

Fig. 9. Same as in Fig. 8, but for $a = 1.4$.

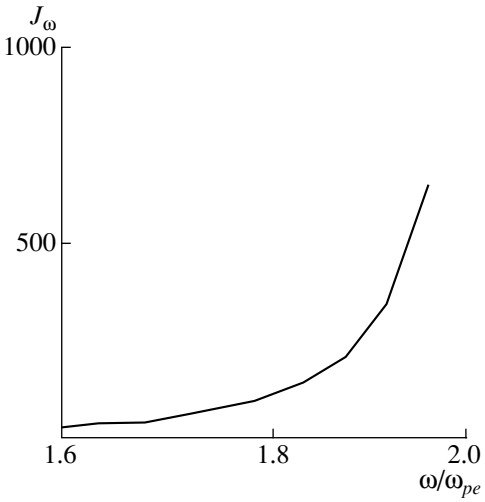

Fig. 10. Same as in Fig. 8, but for $a = 1.6$.

peaked at $\theta \sim 2$. The degree of polarization can amount to 0.5 (for $p^{-1} \approx 1.6$ and $\theta \approx 2$).

Figures 8–10 display the radiation spectra obtained by integrating the spectral power of the generated right- and left-polarized waves over the angle in the ranges $\omega > 2\omega_{pe}$ and $\omega < 2\omega_{pe}$ for different values of the parameter a and for $k_{1\max} v_{Te}/\omega_{Be} = 1/1.4$. From Fig. 8, we can see that, for $a = 1/3$, electromagnetic radiation is primarily generated at frequencies in the range $\omega > 2\omega_{pe}$. On the other hand, for smaller a values (i.e., for weaker magnetic fields), the radiation spectrum is peaked in the frequency range $\omega < 2\omega_{pe}$, because, in dispersion relation (14), the term that accounts for the magnetic field effect becomes smaller. That is why, in Figs. 9 and 10, we present radiation spectra precisely in this frequency range.

Note that, in formula (35), the frequency band of the emitted radiation does not depend explicitly on the plasma temperature. However, from relationships (19)–(21), we can find that the minimum frequency in the emission spectrum is approximately equal to $\omega_{\min} \approx 2\omega_{pe} + \frac{\omega_{Be}^2}{\omega_{pe}} - \frac{k_{l\max}^2 v_{Te}^2}{\omega_{Be}^2}\omega_{pe}$ and the maximum frequency is about $\omega_{\max} \approx 2\omega_{pe} + \frac{3k_{l\max}^2 v_{Te}^2}{\omega_{pe}}$; i.e., the bandwidth of the radiation spectrum is governed by the plasma temperature. For the parameter values $a = 1/3$ and

$k_{1\max} v_{Te}/\omega_{Be} = 1/1.4$, for which formulas (19)–(21) indicate that the frequency spectrum of the Langmuir turbulence extends between 0.8 and 1.1 of the electron Langmuir frequency, the electromagnetic radiation is seen to be generated at frequencies from $\omega_{\min} \approx 1.6\omega_{pe}$ to a $\omega_{\max} \approx 2.2\omega_{pe}$.

4. CONCLUSION

We have shown that, when the ratio of the electron Langmuir frequency to the electron gyrofrequency lies in the range 3–8, the frequency of the electron Langmuir waves in a hot plasma with a magnetic field can vary from $1.1\omega_{pe}$ (for oscillations in the direction of the magnetic induction vector) to $0.8\omega_{pe}$ (for oscillations in the transverse direction). According to the energy conservation law, this circumstance provides the possibility of generating electromagnetic radiation in the frequency band from $1.6\omega_{pe}$ to $2.2\omega_{pe}$ in the $l_1 + l_2 \longrightarrow t$ merging process. The closer the radiation frequency to $2\omega_{pe}$, the higher the radiation power (this is valid for generation at frequencies both above and below $2\omega_{pe}$). However, for a sufficiently strong magnetic field such that the ratio of the electron Langmuir frequency to the electron gyrofrequency is equal to three, the radiation is generated predominantly at frequencies in the range $\omega > 2\omega_{pe}$. As the magnetic field decreases, the peak in the radiation spectrum is displaced into the frequency range $\omega < 2\omega_{pe}$.

The degree of circular polarization of the generated electromagnetic radiation can be as high as 50%.

When the minimum wavenumber of the Langmuir turbulence spectrum is much larger (by a factor of ten or more) than the inverse gyroradius of the plasma electrons, electromagnetic radiation can only be generated at frequencies equal to the doubled electron Langmuir frequency or higher (this process was investigated by Tsytovich [1]). When the maximum wavenumber of the Langmuir turbulence spectrum is much smaller than the inverse electron gyroradius, the energy conservation law (19) and dispersion relations (20) and (21) for the frequencies of Langmuir plasmons imply that electromagnetic radiation is also generated exclusively at frequencies above the doubled electron Langmuir frequency.

For an arbitrary Langmuir turbulence spectrum (i.e., for an arbitrary anisotropic Langmuir turbulence spectrum with arbitrary ratios of the minimum and maximum wavelengths to the gyroradius of the plasma electrons), the minimum and maximum frequencies of the spectrum of the generated electromagnetic waves are determined from the energy conservation law (19) and dispersion relation (20) for the frequency of Langmuir plasmons.

ACKNOWLEDGMENTS

This work was supported by the Russian Foundation for Basic Research, project no. 98-02-17727.

REFERENCES

1. V. N. Tsytovich, *Theory of Turbulent Plasma* (Atomizdat, Moscow, 1971; Plenum, New York, 1974).
2. V. V. Zheleznyakov, *Electromagnetic Waves in Space Plasma* (Nauka, Moscow, 1977).
3. *Plasma Electrodynamics*, Ed. by A. I. Akhiezer *et al.* (Nauka, Moscow, 1974; Pergamon, Oxford, 1975).
4. E. Ya. Zlotnik, Astron. Astrophys. **101**, 250 (1981).
5. V. L. Ginzburg and A. A. Rukhadze, *Waves in Magnetized Plasmas* (Nauka, Moscow, 1970).
6. A. Z. Dolginov, Yu. N. Gnedin, and N. A. Silant'ev, *Radiation Propagation and Polarization in Space Media* (Nauka, Moscow, 1979).
7. L. N. Vyacheslavov, L. M. Gorbach, I. V. Kandaurov, *et al.*, Fiz. Plazmy **20**, 51 (1994) [Plasma Phys. Rep. **20**, 45 (1994)].
8. S. A. Kaplan and V. N. Tsytovich, *Plasma Astrophysics* (Nauka, Moscow, 1972; Pergamon, Oxford, 1974).

Translated by I.A. Kalabalyk

Plasma Physics Reports, Vol. 27, No. 5, 2001, pp. 407–411. Translated from Fizika Plazmy, Vol. 27, No. 5, 2001, pp. 432–436.

DUSTY PLASMA

Skin Effects in a Dusty Plasma

V. Yu. Zaburdaev

Russian Research Centre Kurchatov Institute, pl. Kurchatova 1, Moscow, 123182 Russia

Received July 18, 2000; in final form, September 28, 2000

Abstract—A multifluid MHD model is applied to study the magnetic field dynamics in a dusty plasma. The motion of plasma electrons and ions is treated against the background of arbitrarily charged, immobile dust grains. When the dust density gradient is nonzero and when the inertia of the ions and electrons and the dissipation from their collisions with dust grains are neglected, we are dealing with a nonlinear convective penetration of the magnetic field into the plasma. When the dust density is uniform, the magnetic field dynamics is described by the nonlinear diffusion equations. The limiting cases of diffusion equations are analyzed for different parameter values of the problem (i.e., different rates of the collisions of ions and electrons with the dust grains and different ratios between the concentrations of the plasma components), and some of their solutions (including self-similar ones) are found. The results obtained can also be useful for research in solid-state physics, in which case the electrons and holes in a semiconductor may be analogues of plasma electrons and ions and the role of dust grains may be played by the crystal lattice and impurity atoms. © *2001 MAIK "Nauka/Interperiodica".*

Dust structures are frequently encountered in space plasma: these are, e.g., planetary rings, interstellar clouds, and comet tails. It is inevitable that the dust is present in plasmas of experimental and industrial devices. Thus, the dust adversely affects the performance of computer chips produced by the plasma-etching method. This important and challenging problem has stimulated theoretical and experimental efforts aimed at studying dust-related processes in plasmas [1].

The presence of dust in plasmas substantially modifies the picture of plasma phenomena that is usually found in the two-fluid MHD approach [2]. There are many papers devoted to charge-exchange and recombination processes in real dusty plasmas. Here, in order to concentrate our attention on the characteristic features of the magnetic field dynamics in a multicomponent plasma, we assume that the dust plasma component is represented by point grains having a constant charge (see, e.g., [3]), in which case the plasma electrons and ions experience purely Coulomb collisions with the grains. In the steady-state and linear approximations, analogous problems have been treated in solid-state physics [4], in which case the electrons and holes are analogs of plasma electrons and ions and the role of dust grains is played by the crystal lattice of a semiconductor. In this paper, we derive equations for the magnetic field dynamics in a dusty plasma. In particular, we describe an effect that is analogous to the magnetoresistance effect, which is well known in solid-state physics. The term "magnetoresistance" has not yet found widespread use in plasma physics, although the effect itself has been rediscovered by many plasma physicists.

We describe the magnetic field dynamics in a dusty plasma by the standard set of equations consisting of the equation of motion for ions and electrons without consideration of the inertial terms (Aristotle's equations)

$$-e\mathbf{E} - \frac{e}{c}[\mathbf{v}_e, \mathbf{B}] - \frac{m}{\tau}(\mathbf{v}_i - \mathbf{v}_e) - m\nu_{ed}\mathbf{v}_e = 0, \quad (1)$$

$$Z_i e\mathbf{E} + \frac{Z_i e}{c}[\mathbf{v}_i, \mathbf{B}] + \frac{m}{\tau}\frac{n_e}{n_i}(\mathbf{v}_i - \mathbf{v}_e) - M\nu_{id}\mathbf{v}_i = 0, \quad (2)$$

$$\mathbf{j} = eZ_i n_i \mathbf{v}_i - en_e \mathbf{v}_e, \quad (3)$$

where ν_{ed} and ν_{id} are the rates of the collisions of plasma electrons and ions with the dust grains and $\tau = \tau_{ei} = \nu_{ei}^{-1}$, ν_{ei} is the electron–ion collision rate; the continuity equation

$$\frac{\partial n_\alpha}{\partial t} + \operatorname{div} n_\alpha \mathbf{v}_\alpha = 0, \quad \alpha = i, e; \quad (4)$$

the condition for the plasma to be electrically neutral (the electroneutrality condition)

$$Z_i n_i + Z_d n_d - n_e = 0, \quad (5)$$

where Z_d is the grain charge and n_d is the grain density; and Maxwell's equations

$$\operatorname{curl} \mathbf{E} = -\frac{1}{c}\frac{\partial \mathbf{B}}{\partial t}, \quad (6)$$

$$\operatorname{curl} \mathbf{B} = \frac{4\pi}{c}\mathbf{j}. \quad (7)$$

The main difference of the set of equations presented here from the standard two-fluid MHD equations is that we incorporate the dust component into the electroneutrality condition (5), which now implies that

1063-780X/01/2705-0407$21.00

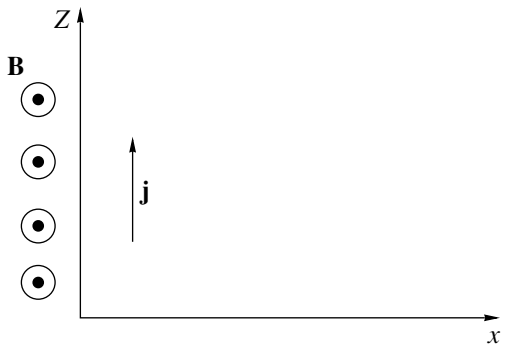

Fig. 1. Geometry of the problem.

the plasma electrons and ions are not directly coupled to each other, but occupy such spatial positions that the difference between their charge densities is equal to the prescribed dust charge density.

In Eqs. (1) and (2), we neglect electron and ion inertia, respectively, and, in Eq. (6), we ignore the displacement current. The corresponding strong inequalities under which these simplifying assumptions are valid will be presented below. In Eqs. (1) and (2), we discard terms with the gas-kinetic pressure and thermal forces; i.e., we assume that

$$n_\alpha T_\alpha \ll B^2, \quad \alpha = i, e.$$

If, in Eqs. (1) and (2), we also omit terms accounting for collisions of plasma electrons and ions with the dust grains, we can sum Eqs. (1) and (2) multiplied by n_e and $Z_i n_i$, respectively, to obtain

$$-Z_d n_d e\mathbf{E} + \left[\frac{\mathbf{j}}{c}, \mathbf{B}\right] = 0. \tag{8}$$

Under this condition, the characteristic spatial and temporal scales a and τ on which the inertial terms in Eqs. (1) and (2) can be disregarded satisfy the inequalities

$$a \gg \frac{c}{\omega_{pi}}\frac{Z_i n_i}{Z_d n_d}, \quad \tau^{-1} \ll \omega_{Bi}.$$

We divide Eq. (8) by the dust density and take a curl of the resulting equation:

$$\frac{\partial \mathbf{B}}{\partial t} + \mathrm{curl}\left[\frac{\mathbf{j}}{Z_d n_d e}, \mathbf{B}\right] = 0.$$

When the transverse (with respect to the magnetic field) dust density gradient is nonzero, we are faced with a situation similar to that described by Kingsep *et al.* [5]. The exact solution that they derived in terms of the electron magnetohydrodynamic (EMHD) model, which makes it possible to treat electron motion against the background of immobile ions, implies that the magnetic field either penetrates into the plasma due to the transverse ion density gradient or is locked at the plasma boundary. In our problem, the role of the ion density gradient is played by the dust density gradient [6].

The equation for the magnetic field dynamics (the Hopf equation) has the form

$$\frac{\partial B}{\partial t} + kB\frac{\partial B}{\partial x} = 0, \quad k = \frac{c}{4\pi e}\frac{\partial}{\partial z}\left(\frac{1}{Z_d n_d}\right).$$

The magnetic field penetrates into the plasma in the form of a shock wave moving at a constant speed $v = \frac{kB_0}{2}$. In [5], the shock front is assumed to be governed by the competition between the nonlinear effects and diffusion. In our problem, the diffusion term is omitted. However, as the shock front steepens, the spatial scale a shortens; when it becomes as short as $a \approx (c/\omega_{pi})Z_i n_i/Z_d n_d$, electron and ion inertia should be taken into account (see [7]).

In order to clarify the consequences of the electron–grain and ion–grain collisions, we consider the simplest one-dimensional problem, setting $\sigma = \infty$. Since the ions are much heavier than the electrons, $M \gg m$ (see also [2]), we take into account only ion–grain collisions. Stricter inequalities, under which electron–grain collisions may be neglected, will be presented below. We direct the y-axis along the magnetic field ($B \equiv B_y$) and consider the magnetic field dynamics along the x-axis only (Fig. 1). We also assume a uniform dust distribution.

In planar geometry, Eq. (6) reduces to the simple equation

$$\mathrm{curl}\,\mathbf{E} = \mathbf{e}_y \frac{1}{c}\frac{\partial}{\partial x} v_{ex} B. \tag{9}$$

We find the electron velocity from Eqs. (1)–(3) and use Maxwell's equation (7) to obtain

$$v_{ex} = -\frac{Z_i^2 n_i \dfrac{\partial B^2}{\partial x}}{8\pi Z_d^2 n_d^2 M \nu_{id}\left(\omega_{Bi}^2 \tau_{id}^2 + \dfrac{n_e^2}{Z_d^2 n_d^2}\right)}. \tag{10}$$

Substituting expression (10) into Eq. (9) yields (cf. [3])

$$\frac{\partial B}{\partial t} = \frac{1}{8\pi Z_d^2 n_d^2 M \nu_{id}}\frac{\partial}{\partial x}\left(\frac{Z_i^2 n_i B \dfrac{\partial B^2}{\partial x}}{\omega_{Bi}^2 \tau_{id}^2 + \dfrac{n_e^2}{Z_d^2 n_d^2}}\right). \tag{11}$$

Since the electroneutrality condition (5) indicates that the dust grains redistribute plasma electrons and ions in space, we must supplement the equation for the magnetic field dynamics with the continuity equation for one of the plasma components, e.g., for plasma elec-

trons. To do this, we insert the electron velocity (10) into the continuity equation (4):

$$\frac{\partial n_e}{\partial t} = \frac{1}{8\pi Z_d^2 n_d^2 M\nu_{id}}\frac{\partial}{\partial x}\frac{Z_i^2 n_i n_e \dfrac{\partial B^2}{\partial x}}{\left(\omega_{Bi}^2\tau_{id}^2 + \dfrac{n_e^2}{Z_d^2 n_d^2}\right)}. \qquad (12)$$

According to Eq. (9), the magnetic field is frozen in the electron plasma component. However, since the magnetic pressure forces the plasma electrons and ions to "squeeze" between the immobile grains, we deal with diffusion-like equations in which the diffusion coefficients depend on the magnetic field strength and the electron and ion densities. Consequently, the plasma resistivity also depends on the magnetic field strength. In solid-state physics, this effect is known as the magnetoresistance effect (see, e.g., [8]); in plasma physics, this effect was revealed in many theoretical and experimental studies (see, e.g., [3, 9]).

Now, we examine the different limiting cases of Eqs. (11) and (12).

1. First, we assume that the magnetization parameter is large in comparison with the ratio of the total charge of the plasma electrons to the total dust charge:

$$\omega_{Bi}^2\tau_{id}^2 \gg \frac{n_e^2}{Z_d^2 n_d^2}.$$

Recall that, in the equations of motion, the inertial terms are omitted. In the limiting case under consideration, this can be done under the following conditions on the characteristic spatial (a) and temporal (τ) scales of the problem:

$$a^2 \gg \frac{\nu_{id}}{\omega_{Bi}}\frac{c^2}{\omega_{pi}^2}\left(\frac{Z_i n_i}{Z_d n_d}\right)^2, \quad \tau^{-1} \ll \omega_{Bi}, \quad \nu_{id}.$$

We thus arrive at the equations

$$\frac{\partial B}{\partial t} = \frac{D}{|Z_d n_d|}\frac{\partial}{\partial x}\left(Z_i n_i \frac{\partial B}{\partial x}\right),$$

$$\frac{\partial n_i}{\partial t} = \frac{D}{|Z_d n_d|}\frac{\partial}{\partial x}\left(\frac{n_i(Z_i n_i + Z_d n_d)}{B}\frac{\partial B}{\partial x}\right),$$

where

$$D = \frac{c^2}{4\pi\sigma}, \quad \sigma = \frac{Z_i|Z_d|n_d e^2}{M\nu_{id}}.$$

Depending on the sign of the dust charge Z_d, we can distinguish between the following four cases.

1.1. The dust charge is negative, $Z_d < 0$.

1.1.1. If the dust charge is much smaller than the ion charge, $\left|\dfrac{n_e}{Z_d n_d}\right| \gg 1$, we can follow the evolution of the given initial profile of the magnetic field by performing the self-similar change of variables $t = t_0\tilde{t}$, $x = x_0\tilde{x}$, $\xi = \dfrac{\tilde{x}}{\tilde{t}^{1/3}}$, $B(x, t) = \dfrac{B_0}{\tilde{t}^{1/3}}\tilde{B}(\xi)$, and $n(x, t) = \dfrac{n_0}{\tilde{t}^{1/3}}\tilde{n}(\xi)$, where the zero subscript refers to the dimensional quantities and the tilde identifies the dimensionless quantities. One of the solutions to our problem has the form

$$\tilde{n} = \tilde{n}(\tilde{B}) = \tilde{B}^\gamma,$$

$$\tilde{B}^\gamma(\xi) = \frac{\gamma Z_d n_d}{6 Z_i n_0 D}\frac{x_0^2}{t_0}(\xi_0^2 - \xi^2), \quad \gamma > 0.$$

1.1.2. If the plasma contains only a few electrons, then the ions are confined to the dust component and the magnetic field evolves in the usual way, with the diffusion coefficient

$$D = \frac{c^2}{4\pi\sigma}, \quad \sigma = \frac{Z_i|Z_d|n_d e^2}{M\nu_{id}}.$$

1.2. The dust charge is positive, $Z_d > 0$.

1.2.1. If the plasma contains many more ions than the grains, $\dfrac{n_e}{Z_d n_d} \gg 1$, the magnetic field dynamics is analogous to that in case 1.1.1.

1.2.3. The opposite case, in which the grain positive charge substantially exceeds the ion charge, $\dfrac{Z_i n_i}{Z_d n_d} \ll 1$, is described by the equations

$$\frac{\partial B}{\partial t} = \frac{D}{Z_d n_d}\frac{\partial}{\partial x}\left(Z_i n_i \frac{\partial B}{\partial x}\right), \qquad (13)$$

$$\frac{\partial n_i}{\partial t} = D\frac{\partial}{\partial x}\left(\frac{n_i}{B}\frac{\partial B}{\partial x}\right). \qquad (14)$$

We can see that the magnetic field evolves much more slowly than the ion density: it varies at a rate proportional to the small quantity $Z_i n_i/Z_d n_d$, which drops out of the ion continuity equation (14). Consequently, we can follow the behavior of the ion plasma component while keeping the magnetic field profile fixed, in which case the magnetic field gradient is found to expel the ions from the plasma. Thus, for a magnetic field of the form $B(x) = B_0 e^{-x^2}$, Eq. (14) can be integrated by the method of characteristics (Fig. 2):

$$n_i(x, t) = n_{0i}(xe^{-2Dt})e^{-2Dt},$$

where n_{0i} is the initial ion density profile. In contrast, for the initial magnetic field profile in the shape of a well, $B(x) = B_0 e^{x^2}$, the ions tend to concentrate in the magnetic well (Fig. 3):

$$n_i(x, t) = n_{0i}(xe^{2Dt})e^{2Dt}.$$

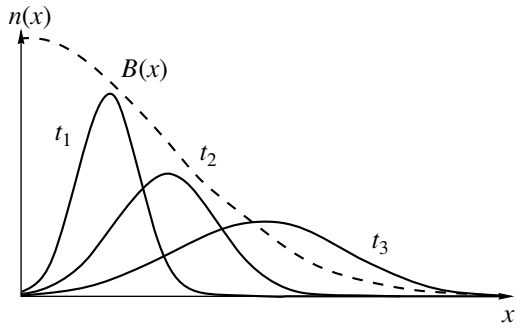

Fig. 2. Evolution of the ion density in a magnetic field with a profile in the shape of a hump. The ion density profiles calculated at successive times $t_1 < t_2 < t_3$ are shown.

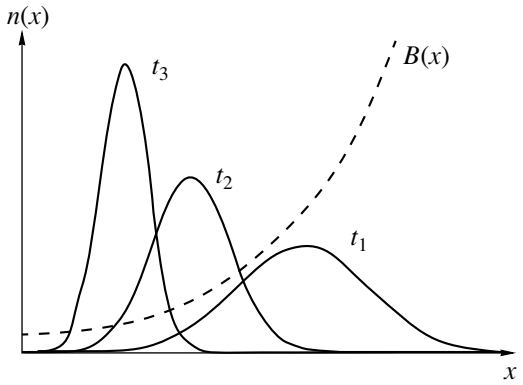

Fig. 3. Evolution of the ion density in a magnetic field with a profile in the shape of a well. The ion density profiles calculated at successive times $t_1 < t_2 < t_3$ are shown.

2. Now, we analyze another limiting case of Eqs. (11) and (12); i.e., we assume that the magnetization parameter is much smaller than the ratio of the total charge of the plasma electrons to the total dust charge: $\omega_{Bi}^2\tau_{id}^2 \ll \frac{n_e^2}{Z_d^2 n_d^2}$. In this limit, the inertial terms in the equations of motion can be neglected if the characteristic scales of the problem satisfy the conditions

$$a^2 \gg \frac{\omega_{Bi}}{\nu_{id}}\frac{c^2}{\omega_{pi}^2}\left(\frac{n_e}{Z_i n_i}\right)^2, \quad \tau^{-1} \ll \omega_{Bi}, \quad \nu_{id}.$$

Under these conditions, the evolutions of the magnetic field and electron density are described by the equations

$$\frac{\partial B}{\partial t} = \frac{Z_i}{4\pi M\nu_{id}}\frac{\partial}{\partial x}\left(\frac{n_e - Z_d n_d}{n_e^2}B^2\frac{\partial B}{\partial x}\right), \tag{15}$$

$$\frac{\partial n_e}{\partial t} = \frac{Z_i}{4\pi M\nu_{id}}\frac{\partial}{\partial x}\left(\frac{n_e - Z_d n_d}{n_e}B\frac{\partial B}{\partial x}\right). \tag{16}$$

As before, depending on the sign of the dust charge and on the dust-to-electron and dust-to-ion density ratios, we can distinguish between several cases.

2.1. The dust charge is negative, $Z_d < 0$.

2.1.1. If the dust component is insignificant in comparison with the electron component, $\left|\frac{Z_d n_d}{n_e}\right| \ll 1$, then, by analogy to case 1.1.1, we again arrive at a solution in terms of the self-similar variables

$$t = t_0\tilde{t}, \quad x = x_0\tilde{x}, \quad \xi = \frac{\tilde{x}}{\tilde{t}^{1/3}},$$

$$B(x, t) = \frac{B_0}{\tilde{t}^{1/3}}\tilde{B}(\xi), \quad n(x, t) = \frac{n_0}{\tilde{t}^{1/3}}\tilde{n}(\xi),$$

specifically,

$$\tilde{n} = \tilde{n}(\tilde{B}) = \tilde{B}^\gamma, \quad \tilde{B}^\gamma(\xi) = \frac{2\gamma\pi M\nu_{id}n_0}{3Z_i B_0^2}\frac{x_0^2}{t_0}(\xi_0^2 - \xi^2),$$

$$\gamma > 0.$$

2.1.2. If the dust component dominates over the electron component, $\left|\frac{Z_d n_d}{n_e}\right| \gg 1$, Eqs. (15) and (16) have another self-similar solution, which can also be obtained by switching to the self-similar variables $\xi = \frac{\tilde{x}}{\tilde{t}^{1/2}}$, $t = t_0\tilde{t}$, $x = x_0\tilde{x}$, $B(x, t) = \frac{1}{\tilde{t}^{1/2}}\tilde{B}(\xi)$, and $n(x, t) = \frac{1}{\tilde{t}^{1/2}}\tilde{n}(\xi)$:

$$\tilde{n} = \tilde{n}(\tilde{B}) = \tilde{B}^\gamma, \quad B^{2(1-\gamma)}(\xi) = \frac{1-\gamma}{A}(\xi_0^2 - \xi^2),$$

$$A = \frac{Z_i|Z_d|n_d}{4\pi M\nu_{id}}, \quad 0 \le \gamma < 1.$$

2.2.1. Finally, if the dust component is charged positively, $Z_d > 0$, and if the ion component dominates, we arrive at a self-similar solution analogous to that in case 2.1.1.

It should be noted that the symmetry properties of the equations of motion (1) and (2) allow us to apply an analogous treatment to the problem in which the major role is played by the electron–grain collisions and the ion–grain collisions are neglected.

The general equations for a dusty plasma in which the electron–grain and ion–grain collisions are both important is far more complicated. Thus, the dynamic equation for the magnetic field has the form

$$\frac{\partial B}{\partial t} = \frac{1}{4\pi}\frac{\partial}{\partial x}\left(\left[\frac{B^2(M\nu_{id}n_i + m\nu_{ed}n_e) + \dfrac{mM\nu_{id}\nu_{ed}c^2}{e^2Z_i^2}(Z_i^2 m\nu_{ed}n_i + M\nu_{id}n_e)}{\left(\dfrac{(Z_i^2 m\nu_{ed}n_i + M\nu_{id}n_e)^2}{Z_i^2} + \dfrac{e^2Z_d^2n_d^2}{c^2}B^2\right)}\right]\frac{\partial B}{\partial x}\right).$$

This equation makes it possible to determine the conditions for the rates of the collisions of electrons and ions with the grains under which the electron–grain collisions can be ignored (cf. [2]):

$$\frac{\nu_{id}}{\nu_{ed}} \gg \frac{m}{M}\frac{n_e}{n_i}, \quad \frac{m}{M}\frac{Z_i^2 n_i}{n_e}, \quad \frac{m}{M}\frac{n_e}{n_i}\frac{1}{\omega_{Bi}^2\tau_i^2}.$$

Hence, we have established that, in a dusty plasma in which the electron–grain collisions are unimportant, the magnetic field is frozen in the plasma electrons, which move under the action of the magnetic pressure force. Although, in an electrically neutral dusty plasma, the electrons are coupled to the ions, they are freer to move than predicted by the standard two-fluid MHD theory. As a result, the time evolution of the magnetic field and plasma components is described by the nonlinear diffusion equations. In such a plasma, heat is released from the friction between the plasma ions and immobile grains, in which case the plasma resistivity depends on the magnetic field strength.

ACKNOWLEDGMENTS

I am grateful to K.V. Chukbar for his guidance and support throughout the work. This work was supported in part by the Ministry of Science of the Russian Federation (under the program "Fundamental Problems of Nonlinear Dynamics") and INTAS (grant no. 97-0021).

REFERENCES

1. V. N. Tsytovich, Usp. Fiz. Nauk **167**, 57 (1997) [Phys. Usp. **40**, 53 (1997)].
2. S. I. Braginskii, in *Reviews of Plasma Physics*, Ed. by M. A. Leontovich (Gosatomizdat, Moscow, 1963; Consultants Bureau, New York, 1963), Vol. 1.
3. A. V. Gordeev, Fiz. Plazmy **13**, 1235 (1987) [Sov. J. Plasma Phys. **13**, 713 (1987)].
4. A. G. Kollyukh, Yu. M. Malozovskiĭ, and V. K. Malyutenko, Zh. Éksp. Teor. Fiz. **89**, 1018 (1985) [Sov. Phys. JETP **62**, 586 (1985)].
5. A. S. Kingsep, Yu. V. Mokhov, and K. V. Chukbar, Fiz. Plazmy **10**, 854 (1984) [Sov. J. Plasma Phys. **10**, 495 (1984)].
6. L. I. Rudakov, A. V. Gretchikha, C. S. Liu, and G. D. Milikh, Phys. Plasmas **8** (2001) (in press).
7. Ya. P. Kalda and A. S. Kingsep, Fiz. Plazmy **15**, 874 (1989) [Sov. J. Plasma Phys. **15**, 508 (1989)].
8. V. V. Vladimirov, A. F. Volkov, and E. Z. Meĭlikhov, *Semiconductor Plasma* (Atomizdat, Moscow, 1979).
9. A. I. Smolyakov and K. Khabibrakhmanov, Phys. Rev. Lett. **81**, 4871 (1998).

Translated by O.E. Khadin

Plasma Physics Reports, Vol. 27, No. 5, 2001, pp. 412–417. Translated from Fizika Plazmy, Vol. 27, No. 5, 2001, pp. 437–442.

NONLINEAR PHENOMENA IN PLASMAS

Calculation of the Second-Order Polarizability of a Warm Magnetized Plasma

E. Z. Gusakov and A. Yu. Popov

Ioffe Physicotechnical Institute, Russian Academy of Sciences, Politekhnicheskaya ul. 26, St. Petersburg, 194021 Russia

Received September 10, 2000

Abstract—An analysis is made of the general expression for the density of a nonlinear charge induced in a magnetized plasma in the interaction between two arbitrary waves. Asymptotic expressions for the nonlinear induced charge density are derived for the first time in the case where both of the interacting waves are short-scale. © *2001 MAIK "Nauka/Interperiodica".*

1. INTRODUCTION

In plasma physics, the theory of nonlinear phenomena has been developed fairly well. There is substantial literature on the analysis of three-wave interactions and the derivation of explicit expressions for the nonlinear current in the second-order approximation (see, e.g., [1–3]). Thus, we can mention the familiar expression for the nonlinear current in an isotropic plasma, which is widely used to describe waves with arbitrary wavelengths [1]. An explicit expression for the nonlinear current in an anisotropic plasma in an external magnetic field was derived only in the hydrodynamic approximation and applies exclusively to an interaction between large-scale waves [2, 3]. Recently, Bindslev [4] has generalized this approach to the scattering problem in which the "cold" hydrodynamic approximation can only be used to describe the scattered wave. On the other hand, a number of physical applications require an analysis of the interaction between three short-scale waves, none of which can be correctly described using the hydrodynamic approach. We can mention, e.g., the problem of describing wave scattering from the upper hybrid resonance region (this phenomenon is used to diagnose spontaneous small-scale plasma fluctuations and regular short-wavelength plasma oscillations [5]). The only thing simplifying the theoretical analysis of such experiments is that the frequency of the scattered signal deviates from the frequency of the probing signal only slightly and that the short-wavelength oscillations are, as a rule, potential. The latter circumstance allows one to restrict analysis to the expression for the nonlinear induced charge density.

In this paper, we develop a systematic kinetic theory of three-wave interaction under the assumption that the frequency of the scattered wave differs insignificantly from the frequency of the probing wave. We derive and analyze an expression for the induced charge density, which provides an adequate description of the interaction between three short-scale waves, regardless of their dispersion properties.

2. KINETIC MODEL

In a collisionless plasma, the dynamics of the electron distribution function f is described by the kinetic equation

$$\frac{\partial f}{\partial t} + \mathbf{v}\frac{\partial f}{\partial \mathbf{r}} - \frac{|e|}{m_e}\left(\mathbf{E} + \frac{\mathbf{v}\times\mathbf{B}}{c}\right)\frac{\partial f}{\partial \mathbf{v}} = 0. \quad (1)$$

Equation (1) can be solved by expanding function f in a power series in the parameter $\delta \propto v_E/v_t$, where v_E is the electron oscillatory velocity in the wave field and $v_t = \sqrt{T_e/m_e}$ is the electron thermal velocity:

$$f = f^{(0)}(\mathbf{p}) + f^{(1)}(\mathbf{p}, \mathbf{r}, t) + f^{(2)}(\mathbf{p}, \mathbf{r}, t) + \ldots. \quad (2)$$

Here, $f^{(0)}$ is a Maxwellian distribution function and $f^{(n)}(\mathbf{p}, \mathbf{r}, t) \propto \delta^{(n)}$.

To first order in δ, the function $f^{(1)}(\mathbf{p}, \mathbf{r}, t)$ is found from the equation

$$\hat{L} f^{(1)} = -\mathbf{F}^{(1)}\frac{\partial f^{(0)}}{\partial \mathbf{v}}. \quad (3)$$

Here, the linear operator $\hat{L}$ has the form

$$\hat{L} = \frac{\partial}{\partial t} + \mathbf{v}\frac{\partial}{\partial \mathbf{r}} - \frac{|e|}{m_e}\frac{\mathbf{v}\times\mathbf{B}^{(0)}}{c}\frac{\partial}{\partial \mathbf{v}} \quad (4)$$

$$\text{and} \quad \mathbf{F}^{(1\gamma)} = -\frac{|e|}{m_e}\left(\mathbf{E}^{(1\gamma)} + \frac{\mathbf{v}}{c}\times\mathbf{B}^{(1\gamma)}\right), \quad \gamma = a, b.$$

For two harmonic plasma waves with frequencies $\omega(a)$ and $\omega(b)$ and wave vectors $\mathbf{k}(a)$ and $\mathbf{k}(b)$, we have $\mathbf{F}^{(1)} = \mathbf{F}^{(1a)} + \mathbf{F}^{(1b)}$ and $f^{(1)} = f^{(1a)} + f^{(1b)}$, where the solutions $f^{(1a)}$ and $f^{(1b)}$ to Eq. (3) are well known from linear theory (see, e.g., [1, 3]):

$$f^{(1\gamma)} = \frac{ie}{m_e}e^{-i\beta_\perp(\gamma)\sin\phi}\sum_{n=-\infty}^{\infty}\frac{\mathbf{a}^{(n)}\mathbf{E}^{(\gamma)}\exp(-in\phi)}{k_z(\gamma)v_z + n\omega_{ce} - \omega(\gamma)},$$

1063-780X/01/2705-0412$21.00

$$a_x^{(n)} = \left[\frac{k_z(\gamma)v_\perp}{\omega(\gamma)}\frac{\partial f^{(0)}}{\partial v_z} + \left(1 - \frac{k_z(\gamma)v_z}{\omega(\gamma)}\right)\frac{\partial f^{(0)}}{\partial v_\perp}\right]\frac{n}{\beta_\perp(\gamma)}J_n(\beta_\perp(\gamma)),$$

$$a_y^{(n)} = \left[\frac{k_z(\gamma)v_\perp}{\omega(\gamma)}\frac{\partial f^{(0)}}{\partial v_z} + \left(1 - \frac{k_z(\gamma)v_z}{\omega(\gamma)}\right)\frac{\partial f^{(0)}}{\partial v_\perp}\right]iJ_n'(\beta_\perp(\gamma)), \quad (5)$$

$$a_z^{(n)} = \frac{\partial f^{(0)}}{\partial v_z}J_n(\beta_\perp(\gamma)) + \left[\frac{k_z(\gamma)v_\perp}{\omega(\gamma)}\frac{\partial f^0}{\partial v_\perp} - \frac{k_x(\gamma)v_z}{\omega(\gamma)}\frac{\partial f^{(0)}}{\partial v_z}\right]\frac{n}{\beta_\perp(\gamma)}J_n(\beta_\perp(\gamma)),$$

Here, $\beta_\perp(\gamma) = v_\perp k_\perp(\gamma)/\omega_{ce}$ and $k_\perp(\gamma) = \sqrt{k_x^2(\gamma) + k_y^2(\gamma)}$ with $\gamma = a$ and b.

The nonlinear interaction of two harmonic waves gives rise to harmonic oscillations of the induced charge density $\rho^{(2\sigma)} = e\int f^{(2\sigma)}d^3v$, whose frequency $\omega(\sigma)$ and wave vector $\mathbf{k}(\sigma)$ satisfy the resonant decay conditions

$$\omega(\sigma) = \omega(a) + \omega(b), \quad \mathbf{k}(\sigma) = \mathbf{k}(a) + \mathbf{k}(b). \quad (6)$$

For convenience, we choose a coordinate system in which

$$\mathbf{k}(a) = (k_x(a), 0, k_z(a)).$$

At the combination frequency, the second-order (in δ) correction $f^{(2\sigma)}$ to the distribution function is found from the equation

$$\hat{L}f^{(2\sigma)} = -\mathbf{F}^{(1a)}\frac{\partial f^{(1b)}}{\partial \mathbf{v}} - \mathbf{F}^{(1b)}\frac{\partial f^{(1a)}}{\partial \mathbf{v}}. \quad (7)$$

Since we are interested in the interaction between almost potential short-scale waves, we define $\mathbf{F}^{(1\gamma)}$ by $\mathbf{F}^{(1\gamma)} = \frac{-|e|}{m_e}\mathbf{E}^{(1\gamma)}$ with $\gamma = a, b$. Note also that, when the frequency of the scattered wave is close to the frequency of the probing wave, $\omega^{(b)}/\omega^{(a)} \ll 1$, we can retain only the first (main) term on the right-hand side of Eq. (7), because the second term is small. In this case, the solution to Eq. (7) is

$$f^{(2\sigma)} = \frac{1}{\omega_{ce}}e^{-i\beta_\perp(\sigma)\sin(\phi+\theta(\sigma))} \times \int_0^\infty e^{-i\alpha(\sigma)\tau + i\beta_\perp(\sigma)\sin(\phi-\tau+\theta(\sigma))}\Theta(\phi-\tau, v_\perp, v_z)d\tau, \quad (8)$$

where $\beta_\perp(\sigma) = v_\perp k_\perp(\sigma)/\omega_{ce}$, $\alpha(\sigma) = (v_z k_z(\sigma) - \omega(\sigma))/\omega_{ce}$, $\phi = \arccos(v_x/v_\perp)$, and

$$\theta(\gamma) = \arccos(k_x(\gamma)/k_\perp(\gamma)), \quad \gamma = a, b, \sigma,$$
$$\Theta(\phi, v_\perp, v_z) = -\mathbf{F}^{(1a)}\frac{\partial f^{(1b)}}{\partial \mathbf{v}}. \quad (9)$$

The corresponding expression for the induced charge density has the form

$$\rho^{(2\sigma)} = \frac{e}{\omega_{ce}}\int\left[e^{-i\beta_\perp(\sigma)\sin(\phi+\theta(\sigma))} \times \int_0^\infty e^{-(i\alpha(\sigma)\tau + i\beta_\perp(\sigma)\sin(\phi-\tau+\theta(\sigma)))}\Theta(\phi-\tau)d\tau\right]d\mathbf{v}, \quad (10)$$

where $d\mathbf{v} = v_\perp dv_\perp dv_z d\phi$.

In expression (10), we pass over from ϕ to the variable $\phi + \tau$ to obtain

$$\rho^{(2\sigma)} = \frac{e}{\omega_{ce}}\int\left[e^{i\beta_\perp(\sigma)\sin(\phi+\theta(\sigma))} \times \int_0^\infty e^{-i\alpha(\sigma)\tau + i\beta_\perp(\sigma)\sin(\phi+\tau+\theta(\sigma))}\Theta(\phi)d\tau\right]d\mathbf{v}. \quad (11)$$

According to formulas (9), expression (11) can be structurally represented as

$$\rho^{(2\sigma)} = \int g(\mathbf{v})F_j^{(1a)}\frac{\partial f^{(1b)}}{\partial v_j}d\mathbf{v}.$$

This allows us to integrate expression (11) by part:

$$\rho^{(2\sigma)} = \frac{e}{\omega_{ce}}\int\left[\frac{\partial}{\partial v_k}\left\{e^{i\beta_\perp(\sigma)\sin(\phi+\theta(\sigma))} \times \int_0^\infty e^{-i\alpha(\sigma)\tau - i\beta_\perp(\sigma)\sin(\phi+\tau+\theta(\sigma))}d\tau\right\}F_k^{(1a)}f^{(1b)}\right]d\mathbf{v}. \quad (12)$$

Taking the derivative within an integral sign yields

$$\rho^{(2\sigma)} = \frac{e}{\omega_{ce}}\int\left[\left\{e^{i\beta_\perp(\sigma)\sin(\phi+\theta(\sigma))} \times \int_0^\infty T_k e^{-i\alpha(\sigma)\tau - i\beta_\perp(\sigma)\sin(\phi+\tau+\theta(\sigma))}d\tau\right\}F_k^{(1a)}f^{(1b)}\right]d\mathbf{v}, \quad (13)$$

where vector T_k has the components

$$\left\{ i\frac{k_\perp(\sigma)}{\omega_{ce}}(\sin\theta(\sigma) - \sin(\tau + \theta(\sigma))), \right.$$
$$\left. i\frac{k_\perp(\sigma)}{\omega_{ce}}(\cos\theta(\sigma) - \cos(\tau + \theta(\sigma))), -i\frac{k_z(\sigma)}{\omega_{ce}}\tau \right\}. \quad (14)$$

The condition $\omega(b)/\omega_{ce} \ll 1$ allows us to retain only the main term (with $n = 0$) in the sum in expression (5) for the linear correction to the distribution function introduced by the low-frequency wave:

$$f^{(1b)} = \frac{ie}{m_e}e^{-i\beta_\perp(b)\sin(\phi + \theta(b))}\frac{a_j^{(0)}E_j^{(1b)}}{k_z(b)v_z - \omega(b)}. \quad (15)$$

We substitute formula (15) into expression (13) and, using decay conditions (6), reduce the product of two oscillating exponential functions to one exponential function:

$$e^{i\beta_\perp(\sigma)\sin(\phi + \theta(\sigma))}e^{-i\beta_\perp(b)\sin(\phi + \theta(b))}$$
$$= \exp\left(i\frac{v_\perp k_\perp(a)}{\omega_{ce}}\sin\phi\right).$$

Hence, in order to obtain the desired expression for $\rho^{(2\sigma)}$, we must calculate the fourfold multiple integral

$$\rho^{(2\sigma)} = \frac{i}{4\pi}\frac{\omega_{pe}^2}{\omega_{ce}}\int[\{e^{i\beta_\perp(a)\sin\phi} \quad (16)$$
$$\times\int_0^\infty T_k e^{-i\alpha(\sigma)\tau - i\beta_\perp(\sigma)\sin(\phi + \tau + \theta(\sigma))}d\tau\left\{\frac{F_k^{(1a)}a_n^{(0)}E_n^{(1b)}}{k_z(b)v_z - \omega(b)}\right]d\mathbf{v}.$$

Here, according to formulas (5), vector $\mathbf{a}^{(0)}$ has the components

$$\left\{0; -\frac{v_\perp}{v_t^2}iJ_0'(\beta_\perp(b))f^{(0)}; -\frac{v_z}{v_t^2}J_0(\beta_\perp(b))f^{(0)}\right\}.$$

Now, we turn to the familiar representation of the Bessel function, $e^{-i\beta_\perp\sin(\phi)} = \sum_{n=-\infty}^{\infty}J_n(\beta_\perp)e^{-in\phi}$, in order to rewrite expression (16) in terms of the product of two infinite series:

$$\rho^{(2\sigma)} = \frac{i}{4\pi}\frac{\omega_{pe}^2}{\omega_{ce}}\int\left[\left\{\sum_n\sum_m\int_0^\infty T_k J_m(\beta_\perp(a))\right.\right.$$
$$\left.\times J_n(\beta_\perp(\sigma))e^{im\phi - in(\phi + \tau + \theta(\sigma))}e^{-i\alpha(\sigma)\tau}d\tau\right\}$$
$$\left.\times\frac{F_k^{(1a)}a_n^{(0)}E_n^{(1b)}}{k_z(b)v_z - \omega(b)}\right]d\mathbf{v}.$$

Integrating this expression with respect to ϕ, we obtain a delta function, which makes one of the infinite series summable:

$$\rho^{(2\sigma)} = \frac{i}{2}\frac{\omega_{pe}^2}{\omega_{ce}}\int dv_z v_\perp dv_\perp\{\int_0^\infty T_k R(\tau)e^{-i\alpha(\sigma)\tau}d\tau\}$$
$$\times\frac{e}{m_e}\frac{E_k^{(1a)}a_n^{(0)}E_n^{(1b)}}{k_z(b)v_z - \omega(b)}.$$

Here, we have introduced the notation $R(\tau) = \sum e^{-im(\tau + \theta(\sigma))}J_m(\beta_\perp(a))J_m(\beta_\perp(\sigma))$. Using the addition theorem for Bessel functions, $J_0(\beta_3) = \sum_{n=-\infty}^{\infty}J_n(\beta_1)J_n(\beta_2)e^{-in\psi}$, where the argument is $\psi = (\tau + \theta(\sigma))$ and $\beta_3 = \sqrt{\beta_1^2 + \beta_2^2 - 2\beta_1\beta_2\cos\psi}$, we can take the sum of the remaining series. As a result, we arrive at the following expression for the induced charge density:

$$\rho^{(2\sigma)} = \frac{i}{2}\frac{\omega_{pe}^2}{\omega_{ce}}\int dv_z v_\perp dv_\perp$$
$$\times\left\{\int_0^\infty T_k J_0(\zeta)e^{-i\alpha(\sigma)\tau}d\tau\right\}\frac{e}{m_e}\frac{E_k^{(1a)}a_n^{(0)}E_n^{(1b)}}{k_z(b)v_z - \omega(b)}, \quad (17)$$

where

$$\zeta = \frac{v_\perp}{\omega_{ce}}\sqrt{k_\perp^2(a) + k_\perp^2(\sigma) - 2k_\perp(a)k_\perp(\sigma)\cos(\tau + \theta(\sigma))}.$$

Note that, in expression (17), integration over variable $v_\perp$ can be performed with the help of the familiar formulas for the second Weber exponential integral:

$$\int_0^\infty \exp(-p^2t^2)J_0(\alpha t)J_0(\beta t)tdt$$
$$= \frac{1}{2p^2}\exp\left(-\frac{(\alpha^2 + \beta^2)}{4p^2}\right)I_0\left(\frac{\alpha\beta}{2p^2}\right) \equiv \frac{1}{2p^2}A\left[\frac{\alpha}{p}, \frac{\beta}{p}\right],$$

where

$$p = \frac{1}{\sqrt{2}v_t}, \quad \alpha = \frac{k_\perp(b)}{\omega_{ce}},$$

$$\beta = \frac{1}{\omega_{ce}}\sqrt{k_\perp^2(a) + k_\perp^2(\sigma) - 2k_\perp(a)k_\perp(\sigma)\cos(\tau + \theta(\sigma))}.$$

Performing integration over variable v_z in expression (17) gives the probability integral

$$Z(\xi) = 1/\sqrt{\pi}\int_{-\infty}^{\infty}\frac{\exp(-x^2)dx}{x - \xi},$$

in which case the above expression for the induced charge density becomes

$$\rho^{(2\sigma)} = \frac{i}{2\pi\sqrt{2}}\frac{\omega_{pe}^2}{\omega_{ce}}\frac{eE_k^{(1a)}E_l^{(1b)}}{mk_z(b)v_t^2} \times \int_0^\infty d\tau T_k(\tau) W_l(\tau) \exp\left(-\left(\frac{\lambda_z^T(\sigma)\tau}{2}\right)^2 + i\frac{\omega(\sigma)}{\omega_{ce}}\tau\right). \quad (18)$$

Here, vector W_l has the components $\left\{0;\ -i\frac{Z(\tilde{\mu})}{\beta_\perp^T(b)}\frac{\partial}{\partial\beta_\perp^T(b)}A(\beta_\perp^T(b), \zeta^T);\ -(1 + \mu Z(\tilde{\mu}))A(\beta_\perp^T(b), \zeta^T)\right\}$, the components of vector T_k are given by formulas (14),

$\zeta^T = \sqrt{\beta_\perp^T(a)^2 + \beta_\perp^T(\sigma)^2 - 2\beta_\perp^T(a)\beta_\perp^T(\sigma)\cos(\tau + \theta(\sigma))}$, $\beta_\perp^T = \frac{\sqrt{2}k_\perp v_t}{\omega_{ce}}$, $\lambda_z^T = \frac{\sqrt{2}k_z v_t}{\omega_{ce}}$, $\mu = \frac{\omega(b)}{\omega_{ce}\lambda_z^T(b)}$, and $\tilde{\mu} = \frac{\omega(b)}{\omega_{ce}\lambda_z^T(b)} + i\frac{\lambda_z^T(\sigma)}{2}\tau$.

3. LONG-WAVELENGTH LIMIT

Expression (18) makes it possible to determine the asymptotics of the nonlinear charge density for different relationships between the wave vectors of the three waves. We start by considering the long-wavelength limit for a probing or a scattered wave: $\beta_\perp^T(\sigma) \ll 1$ or $\beta_\perp^T(a) \ll 1$. We also assume that $\lambda_z^T(\sigma)\lambda_z^T(b)\omega_{ce}/\omega(b) \ll 1$.

Note that, in the long-wavelength limit, $\theta(\sigma)$ is the angle that vector $k_\perp(\sigma)$ makes with the X-axis and, accordingly, with the vector $k_\perp(a)$, in which case expression (18) is symmetric in the vectors $k_\perp(\sigma)$ and $k_\perp(a)$. Consequently, we can treat only the first case, namely, $\beta_\perp^T(\sigma) \ll 1$, because the corresponding result in the second case ($\beta_\perp^T(a) \ll 1$) can be obtained simply by changing the indices.

In order to expand expression (18) in powers of $\beta_\perp^T(\sigma)$ and $\lambda_z^T(\sigma)$, we need to determine $W_l \approx W_l^{(0)} + W_l^{(1)}$, in which case vector $W_l^{(0)}$ has the components $\{0,\ -iZ(\mu)A_0';\ -(1 + \mu Z(\mu))A_0\}$, where $A_0 = \exp\left(-\frac{\beta_\perp^T(b)^2}{2}\right)I_0\left(\frac{\beta_\perp^T(b)^2}{2}\right)$. In turn, vector $W_l^{(1)}$ can be represented as the sum of two vectors, $W_l^{(1)} = W_l^{(1,1)} + W_l^{(1,2)}$, whose components are equal to

$$W_l^{(1,1)} = \tilde{W}_l^{(1,1)}\frac{ik_z(\sigma)v_t}{\sqrt{2}\omega_{ce}}\tau,$$

$$\tilde{W}_l^{(1,1)} = \{0; -iA_0'; -\mu A_0\}\cdot Z'(\mu).$$

$$W_l^{(1,2)} = \tilde{W}_l^{(1,2)}\frac{k_\perp(\sigma)v_t}{\sqrt{2}\omega_{ce}}(\cos\theta(\sigma) - \cos(\tau + \theta(\sigma))),$$

$$\tilde{W}_l^{(1,2)} = \{0; -i\beta_\perp^T(b)Z(\mu)A_0''; -\beta_\perp^T(b)(1 + \mu Z(\mu))A_0'\}.$$

We thus arrive at the final expression for the induced charge density:

$$\rho^{(2\sigma)} = \rho^{(2\sigma)(0)} + \rho^{(2\sigma)(1)}, \quad (19)$$

where

$$\rho^{(2\sigma)(0)} = \frac{1}{2\pi}\frac{n^{(1b)}}{N_0}\hat{\sigma}_k^{(0)}[\omega(\sigma)]E_k^{(1a)}, \quad (20)$$

N_0 is the unperturbed plasma density, and $n^{(1b)} = \int d\mathbf{v} f^{(1b)}$. Here, we use summation over repeated indices and introduce the vector $\hat{\sigma}_k^{(0)}[\omega(\sigma)]$ representing the convolution of the conductivity tensor $\sigma_{ik}[\omega(\sigma)]$ of a cold plasma at the frequency $\omega(\sigma)$: $\hat{\sigma}_k^{(0)}[\omega(\sigma)] = k_i(\sigma)\sigma_{ik}[\omega(\sigma)]/\omega(\sigma)$.

The second term on the right-hand side of expression (19) has the form

$$\rho^{(2\sigma)(1)} = \frac{1}{2\pi}\left[\frac{\tilde{n}(b)}{N_0}\hat{\sigma}_k^{(1,1)} + \frac{\check{n}(b)}{N_0}\hat{\sigma}_k^{(1,2)}\right]E_k^{(1a)},$$

where

$$\tilde{n}(b) = \frac{i2eE_k^{(1b)}\tilde{W}_k^{(1,1)}}{m_e v_t^2 k_z(b)}N_0,$$

$$\check{n}(b) = \frac{i2eE_k^{(1b)}\tilde{W}_k^{(1,2)}}{m_e v_t^2 k_z(b)}N_0,$$

$$\hat{\sigma}_k^{(1,1)} = \frac{k_z(\sigma)v_t}{\sqrt{2}}\frac{\partial}{\partial\omega(\sigma)}\hat{\sigma}_k^{(0)}[\omega(\sigma)],$$

$$\hat{\sigma}_k^{(1,2)} = \frac{v_t}{\sqrt{2}\omega_{ce}}\left\{k_x(\sigma)\left(\hat{\sigma}_k^{(0)}[\omega(\sigma)] - \frac{1}{2}(\hat{\sigma}_k^{(0)}[\omega(\sigma)+\omega_{ce}] + \hat{\sigma}_k^{(0)}[\omega(\sigma)-\omega_{ce}])\right) + k_y(\sigma)\left(\frac{1}{2i}(\hat{\sigma}_k^{(0)}[\omega(\sigma)+\omega_{ce}] - \hat{\sigma}_k^{(0)}[\omega(\sigma)-\omega_{ce}])\right)\right\},$$

where $\hat{\sigma}_k^{(0)}[\omega(\sigma)\pm\omega_{ce}] = k_i(\sigma)\sigma_{ik}[\omega(\sigma)\pm\omega_{ce}]/\omega(\sigma)$.

In expression (19), the first term coincides with that obtained by Bindslev [4] and the remaining two terms are corrections that are linear in the parameters $\beta_\perp^T(\sigma) \ll 1$ and $\lambda_z^T(\sigma) \ll 1$. Recall that taking limit $\beta_\perp^T(a) \ll 1$ and $\lambda_z^T(\sigma)\lambda_z^T(b)\omega_{ce}/\omega(b) \ll 1$ requires a simple replacement $\sigma \longleftrightarrow a$ in the expressions for $\beta_\perp^T$ in formula (20).

4. SHORT-WAVELENGTH LIMIT

Here, we consider the interaction of short-scale waves satisfying the conditions $1 \ll \beta_\perp^T(a)$, $\beta_\perp^T(b)$, $\beta_\perp^T(\sigma)$. We also assume that $\lambda_z^T(\sigma)\lambda_z^T(b)\omega_{ce}/\omega(b) \ll 1$. Note that this limiting case is, in particular, characteristic of the scattering of a high-frequency wave (after it has been converted in the upper hybrid resonance region) by a low-frequency Bernstein wave [6]. In the short-wavelength limit, the desired asymptotics of expression (18) can be obtained by the method of steepest descent:

$$\rho^{(2\sigma)} \propto \int d\tau T_k(\tau)\exp\left(-\left(\frac{\lambda_z^T(\sigma)\tau}{2}\right)^2 + i\frac{\omega(\sigma)}{\omega_{ce}}\tau\right)\exp(\Theta(\tau)).$$

The main contribution to the integral over $d\tau$ comes from the points at which the function $\Theta(\tau) = -\zeta^{T2}/4 + \ln\left(I_0\left(\frac{\zeta^T\beta_\perp^T(b)}{2}\right)\right)$ is maximum. The extremes of $\Theta(\tau)$ are determined from the formula

$$\Theta'(\tau) = -\frac{\zeta^{T'}}{2}(\zeta^T - I_0'(\zeta^T\beta_\perp^T(b))/I_0(\zeta^T\beta_\perp^T(b))\beta_\perp^T(b)) = 0,$$

in which case the relationship

$$\zeta^T - I_0'(\zeta^T\beta_\perp^T(b))/I_0(\zeta^T\beta_\perp^T(b))\beta_\perp^T(b) = 0 \qquad (21)$$

gives the maximum $\Theta(\tau)$ of this function, while the relationship

$$\zeta^{T'} = 0 \qquad (22)$$

gives its minimum.

Using the approximate equality $\beta_\perp^T(b)\zeta^T \gg 1$, which holds under the condition $I_0'(\zeta^T\beta_\perp^T(b))/I_0(\zeta^T\beta_\perp^T(b)) \approx 1$, we can rewrite solution (21) as

$$\zeta^T = \beta_\perp^T(b). \qquad (23)$$

The corresponding values of τ_{max} are equal to $\tau_{max}^{(1)} = 2\pi n$ and $\tau_{max}^{(2)} = 2\pi n - 2\theta(\sigma)$ with $n \in (0, \infty)$. The value of the derivative $\Theta''(\tau)$ at the point at which the function itself is maximum is determined by the relationship

$$\Theta''(\tau_{max}^{(1,2)}) = -\frac{\zeta^{T'}}{2}(\zeta^{T'} - \beta_\perp^T(b)(I_0'/I_0)') \approx -\frac{1}{2}(\beta_\perp^T(a)\beta_\perp^T(\sigma)\sin(\theta(\sigma))/|\beta_\perp^T(b)|)^2 < 0.$$

To apply the method of steepest descent, we need to impose the restriction $|\Theta''(\tau_{max})| \gg 1$, which can be reduced to the following condition for the transverse components of the three interacting waves: $\beta_\perp^T(a)\beta_\perp^T(\sigma)\sin(\theta(\sigma))/|\beta_\perp^T(b)| \gg 1$.

The sum of the remaining series

$$\sum_{n=0}^{\infty}\exp\left(i2\pi n\frac{\omega(\sigma)}{\omega_{ce}} - \left(\frac{2\pi\lambda_z^T(\sigma)}{2}\right)^2 n^2\right)$$

can be taken as follows. Introducing the notation $\eta = \frac{2\pi\omega(\sigma)}{\omega_{ce}}$ and $\gamma = \left(\frac{2\pi\lambda_z^T(\sigma)}{2}\right)^2$, we rewrite the series as $\Phi(\gamma, \eta) = \sum_{n=0}^{\infty}\exp(in\eta - \gamma n^2)$. The function $\Phi(\gamma, \eta)$ satisfies the diffusion equation $\frac{\partial}{\partial\gamma}\Phi(\gamma, \eta) = \frac{\partial^2}{\partial\eta^2}\Phi(\gamma, \eta)$ with the initial condition $\Phi(0, \eta) = \sum_{n=0}^{\infty}\exp(in\eta)$.

Since the series in the initial condition is an infinite geometric series, we have

$$\sum_{n=0}^{\infty}\exp(in\eta) = \frac{1}{1-\exp(i\eta)},$$

which allows us to represent the solution to the diffusion equation for the function $\Phi(\gamma, \eta)$ as

$$\Phi(\gamma, \eta) = \int G(\eta - \eta')\Phi(0, \eta')d\eta',$$

where $G(\eta) = \frac{1}{\sqrt{\gamma}}\exp\left(-\frac{\eta^2}{\gamma}\right)$ is the Green's function of the diffusion equation.

For $\frac{\omega(\sigma) - m\omega_{ce}}{k_z(\sigma)v_t} \gg 1$ with $m \in Z$, we obtain

$$\int G(\eta - \eta')\Phi(0, \eta')d\eta' \simeq$$
$$\simeq \Phi(0, \eta)\int G(\eta - \eta')d\eta' = \Phi(0, \eta).$$

Hence, we arrive at the asymptotics

$$\hat{\sigma}_x = 4\sqrt{\pi}i\frac{\omega_{pe}^2}{\omega_{ce}v_t}\frac{k_\perp(b)}{k_\perp(a)}$$
$$\times \exp\left\{-i2\theta(\sigma)\frac{\omega(\sigma)}{\omega_{ce}}\right\}/\left(1 - \exp i\frac{\omega(\sigma)}{\omega_{ce}}\right), \quad (24)$$

where $\rho^{(2\sigma)} = \frac{1}{2\pi}\frac{n^{(1b)}}{N_0}\hat{\sigma}_x E_x^{(1a)}$.

When the frequency of the scattered wave is close to a multiple of the cyclotron frequency, $\frac{\omega(\sigma) - m\omega_{ce}}{k_z(\sigma)v_t} \leq 1$ with $m \in Z$ and $\frac{\omega_{ce}}{k_z(\sigma)v_t} \gg 1$, we have

$$\rho^{(2\sigma)} = \frac{1}{2\pi}\frac{n^{(1b)}}{N_0}\hat{\sigma}_x E_x^{(1a)}, \quad (25)$$

where

$$\hat{\sigma}_x$$
$$= \frac{2\omega_{pe}^2}{k_z(\sigma)v_t^2}\frac{k_\perp(b)}{k_\perp(a)}Z\left(\frac{\omega(\sigma) - m\omega_{ce}}{k_z(\sigma)v_t}\right)\exp\left\{-i2\theta(\sigma)\frac{\omega(\sigma)}{\omega_{ce}}\right\}, \quad (26)$$

and Z is the dispersion function.

A comparison of expressions (24) and (25) with expression (20) enables us to conclude that the MHD expression (20) substantially (by a factor of $k_\perp(\sigma)\rho_e$) overestimates the nonlinear induced charge density.

5. CONCLUSION

We have analyzed the general expression for the density of a nonlinear charge induced in a magnetized plasma in the interaction between two arbitrary waves. The proposed approach for calculating the induced charge density is based on the addition theorem for Bessel functions and thus provides the most complete analytic treatment. This enabled us to derive for the first time asymptotic expressions for the density of a nonlinear charge induced in the interaction between three short-scale waves. This limiting case is of interest for a theoretical description of the diagnostics of spontaneous short-scale plasma fluctuations or regular short-wavelength oscillations by means of the scattering in the upper hybrid resonance region [6]. We have shown that, for a long-scale scattered wave, the nonlinear charge density is described by the same expression as in the MHD theory [4], whereas, in the opposite limit $k_\perp(\sigma)\rho_e \gg 1$, the MHD expression substantially (by a factor of $k_\perp(\sigma)\rho_e$) overestimates the nonlinear induced charge density. Presumably, this result explains the comparatively low intensity of the waves backscattered by the ion Bernstein modes in the upper hybrid resonance region [6].

ACKNOWLEDGMENTS

This work was supported in part by the Russian Foundation for Basic Research (project no. 99-02-17975) and INTAS (grant no. 97-11018).

REFERENCES

1. A. F. Alexandrov, L. S. Bogdankevich, and A. A. Rukhadze, *Principles of Plasma Electrocdynamics* (Vysshaya Shkola, Moscow, 1978; Springer-Verlag, Berlin, 1984).
2. V. N. Tsytovich, *Theory of Turbulent Plasma* (Atomizdat, Moscow, 1971; Plenum, New York, 1974).
3. Plasma Electrodynamics, Ed. by A. I. Akhiezer, I. A. Akhiezer, R. V. Polovin, *et al.* (Nauka, Moscow, 1974; Pergamon, Oxford, 1975).
4. H. Bindslev, Plasma Phys. Controlled Fusion **35**, 1615 (1993).
5. K. M. Novik and A. D. Piliya, Plasma Phys. Controlled Fusion **36**, 1 (1994).
6. D. G. Bulyginskii, A. D. Gurchenko, E. Z. Gusakov, *et al.*, in *Proceedings of the 26th EPS Conference on Controlled Fusion and Plasma Physics, Maastricht, 1999*, Vol. 1, p. 328.

Translated by O.E. Khadin

Plasma Physics Reports, Vol. 27, No. 5, 2001, pp. 418–423. Translated from Fizika Plazmy, Vol. 27, No. 5, 2001, pp. 443–449.

LOW-TEMPERATURE PLASMA

Characteristics of the Electrode Plasma of an Electrode Microwave Discharge in Hydrogen

Yu. A. Lebedev and M. V. Mokeev

Topchiev Institute of Petrochemical Synthesis, Russian Academy of Sciences, Leninskiĭ pr. 29, Moscow, 117912 Russia

Received June 27, 2000; in final form, October 9, 2000

Abstract—The electrode region of an electrode microwave discharge in hydrogen at pressures of 0.5–4 torr and absorbed powers of up to 12 W is studied using emission spectroscopy and actinometry. It is shown that the gas temperature is at most 700 K and the degree of dissociation does not exceed several percent. Direct electron impact is shown to be the main factor governing all the processes in the electrode region of the discharge, including the excitation of the recorded emission. In particular, the Balmer-series H_α line emission is related to the dissociative electron-impact excitation of hydrogen molecules in the ground state. © *2001 MAIK "Nauka/Interperiodica".*

1. INTRODUCTION

At present, initiated microwave discharges attract considerable interest [1–3]. This interest is related to both the fundamental problems of the interaction of a highly nonuniform electromagnetic field with the plasma created by this field and numerous possible applications of such discharges. A characteristic feature of the electrode microwave discharge (EMD), which belongs to this type of discharges, is that energy is supplied to the discharge chamber along an initiating antenna. Although EMDs possess a number of interesting features and there is a wide range of their possible applications (e.g., in plasmochemistry [4]), they still remain the least studied microwave discharges. The EMD phenomenology, the spatial structure of a discharge for different electrode configurations, and the results of optical and probe measurements are described in [5–9]. The observed discharge structure was suggested to be a superposition of two discharges with different properties, namely, a bright thin region near the electrode and an external spherical region. It was also shown that an EMD could be an efficient source of charged particles, whose density is fairly high throughout the entire discharge chamber. Thus, it is important to study physicochemical processes in different discharge regions and the mechanisms for sustaining the EMD.

The aim of this study is to investigate the electrode plasma of an EMD in a mixture of hydrogen with 5 vol % of argon at pressures of 0.5–4 torr using emission spectroscopy and actinometry.

2. EXPERIMENTAL SETUP

The discharge chamber was a metal cylinder 8.5 cm in diameter with an antenna inserted through its end via a vacuum joint [8]. The antenna (a cylindrical stainless steel tube 6 mm in diameter) was part of a coaxial-to-waveguide converter, which was adjusted with the help of a short-circuiting piston. The dimensions of the discharge, which was excited around the antenna (the igniting electrode), were much less than the chamber diameter and the distance from the chamber lower end. The measurements were carried out in a gas flow. The output power of the microwave generator operating at a frequency of 2.45 GHz was up to 170 W. The discharge emission was withdrawn from the discharge chamber through a window on its side wall. Then, it was focused by a collecting lens onto the entrance slit of an MDR-4 monochromator. A spectral range of 400–800 nm was investigated. An FEU-79 was used as an emission detector. For actinometry measurements, 5 vol % of argon was added to hydrogen.

The power absorbed in a plasma is usually determined from the difference between the incident power and the power reflected from the discharge section. In this case, it is not known *a priori* what fraction of the power is absorbed in the plasma and what fraction is lost in the feeding system. To determine the latter, we measured the powers absorbed with and without igniting the discharge. The difference between them was assumed to be the power absorbed in the plasma (Fig. 1), although it is not improbable that igniting the discharge changes the field distribution and, correspondingly, the fraction of the power lost in the feeding system.

3. RESULTS AND DISCUSSION

3.1. Spectral Characteristics of the Discharge and Comparison with an Electrodeless Microwave Discharge in a Cavity

The spectral measurements of plasma emission in the mixture H_2 + 5 vol % Ar showed that, as in the case

1063-780X/01/2705-0418$21.00

of an electrodeless microwave discharge in a cavity [10], the emission spectrum in the range 400–800 nm consists of hydrogen molecular bands corresponding to the $^1\Sigma_g^+ \longrightarrow {}^1\Sigma_u^+$, $^1\Pi_g \longrightarrow {}^1\Sigma_u^+$, $^3\Sigma_g^+ \longrightarrow {}^3\Sigma_u^+$, $^3\Pi_g \longrightarrow {}^3\Pi_u$, and $^3\Pi_u \longrightarrow {}^3\Sigma_g^+$ transitions and atomic hydrogen and Ar lines. The most intense band is the Fulcher α system ($d^3\Pi_u \longrightarrow a^3\Sigma_g$ transition), whose intensity is used to determine the gas temperature. The most intense atomic lines are the Balmer-series hydrogen lines H_α, H_β, and H_γ and Ar lines corresponding to the $4p \longrightarrow 4s$ transitions. It was shown in [10] that emission lines and bands can be divided into two groups with different dependences of the integral (over the discharge volume) intensity on the power absorbed in the plasma. The first group consists of hydrogen molecular bands and the Ar $4p \longrightarrow 4s$ lines, whose intensities linearly increase with power. The other group consists of atomic hydrogen lines, whose intensities depend nonlinearly on the absorbed power. In [10], this fact was explained by the difference in the excitation mechanisms—stepwise excitation of atomic hydrogen lines and direct electron-impact excitation of hydrogen molecular bands and Ar lines.

In an EMD, the observed emission intensities of the Balmer-series atomic hydrogen lines H_α, H_β, and H_γ; the Ar 696.5-nm line; and the H_2 752.4-nm band increase linearly with power (Figs. 2–5). The difference between the above two groups manifests itself in that the intensities of atomic hydrogen lines increase somewhat faster. For the same change in power, the intensities of the Ar 696.5-nm line and H_2 752.4-nm band increase by a factor of 1.5–2, whereas the intensities of atomic hydrogen lines increase by a factor of 2–5 (Fig. 6).

3.2. Spatial Structure of Emission

An interpretation of the measurements of the emission intensity is hindered by the complicated structure of the discharge, which consists of two regions—a bright thin region near the electrode and a less bright spherical region surrounding the first one. A comparison of the integral emission intensities of the two regions shows that the electrode region contributes most to the observed emission [8]. Space-resolved measurements show that the contribution from the electrode region to the line emission is also much larger than that from the spherical region. Although the relative contribution from the spherical region increases with power, the contribution from the electrode region remains dominant throughout the entire power and pressure ranges under study. This indicates that the data from spectral measurements are mainly related to the bright layer near the electrode.

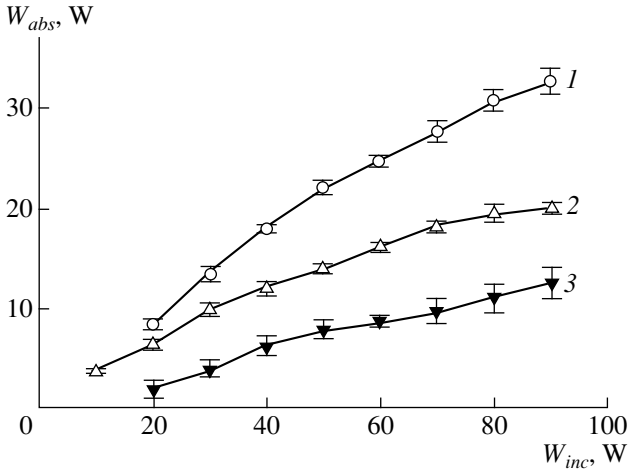

Fig. 1. The powers W_{abs} absorbed in the system (*1*) with and (*2*) without igniting the discharge and (*3*) the difference between them vs. the incident power W_{inc}.

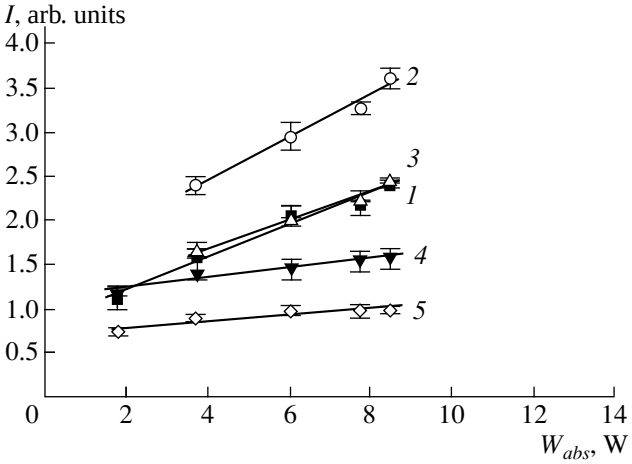

Fig. 2. The line intensities vs. the absorbed power W_{abs}, at a pressure of 0.5 torr: (*1*) H(H_γ, 434.0 nm), (*2*) H(H_β, 486.1 nm), (*3*) H(H_α, 656.3 nm), (*4*) Ar(696.5 nm), and (*5*) H_2 (752.4 nm).

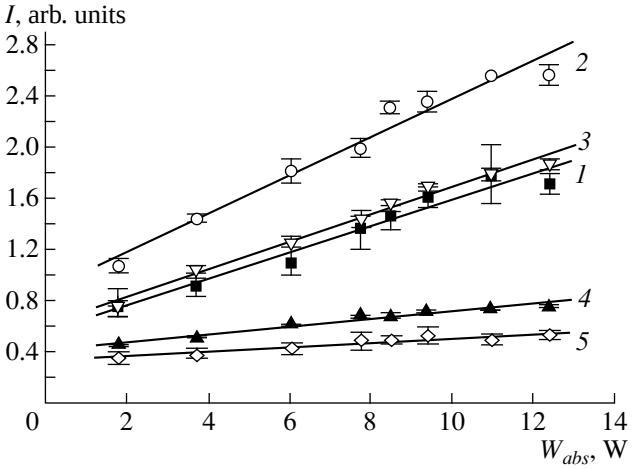

Fig. 3. Same as in Fig. 2 at a pressure of 1 torr.

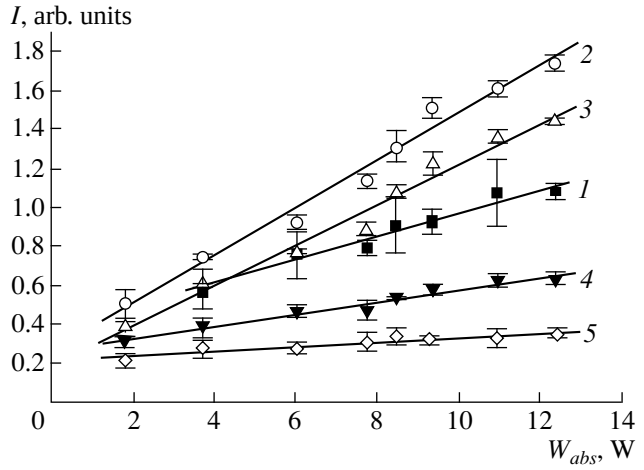

Fig. 4. Same as in Fig. 2 at a pressure of 2 torr.

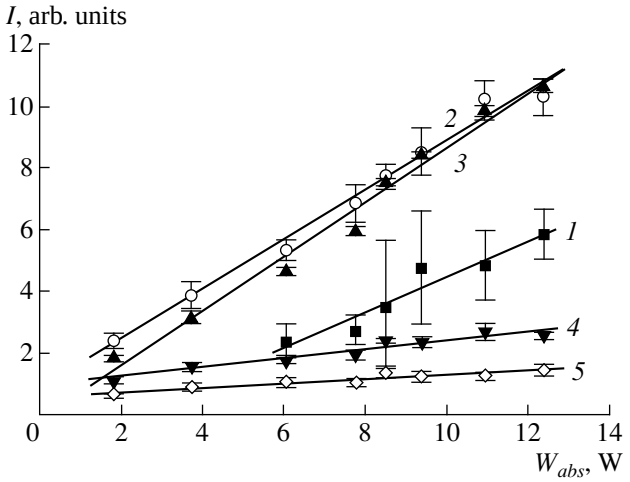

Fig. 5. Same as in Fig. 2 at a pressure of 4 torr.

3.3. Gas Temperature near the Electrode

The gas temperature is an important parameter that determines both the interaction of the electromagnetic field with the plasma (via the ratio ν/ω, where ν is the effective collision frequency of electrons with heavy particles) and the kinetics of the plasma processes. The gas temperature can be determined from the relative intensities of the vibrational lines that belong to the Fulcher α system of electronically excited molecular hydrogen [11] (the $H_2(d^3\Pi_u \longrightarrow a^3\Sigma_g)$ radiative transition). Strictly speaking, the Fulcher α system allows one to determine the rotational temperature of the upper excited state $d^3\Pi_u$ of molecular hydrogen. The relation between the rotational and gas temperatures was studied in detail in [12–14]. In view of the above said, the obtained gas temperature is related to the electrode region. The gas temperature was calculated from the intensities of the Q and R branches of the diagonal ($v' = v'' = 0$, 1, and 2) bands of the Fulcher α system. The rotational temperature of the $d^3\Pi_u$ state was calculated by the formula

$$\ln\left(\frac{I_{'\to''}}{\nu^4_{'\to''}S_{j',j''}}\right) = -\frac{hc}{kT^*_{\rm rot}}F(j') + \text{const}, \qquad (1)$$

where $I_{'\to''}$ is the intensity of emission corresponding to the transition between the rotational levels of the vibrationally excited electronic molecular states, $\nu_{'\to''}$ is the frequency of this transition, $S_{j',j''}$ is the Hönl–London factor, and $F(j')$ is the rotational energy of the upper state. The temperature is determined from the slope of the linear dependence of $\ln\left(\frac{I_{'\to''}}{\nu^4_{'\to''}S_{j',j''}}\right)$ on $F(j')$. The rotational temperature of the ground state is calculated by the formula [11, 15]

$$T^0_{\rm rot} = T^*_{\rm rot}\frac{B^0}{B'}, \qquad (2)$$

where B^0 and B' are the rotational constants of the ground and excited states, respectively. The rotational temperature of the ground state was assumed to be equal to the gas temperature. The estimated rotational temperature of the excited state is $T^*_{\rm rot} = 310 \pm 40$ K; the gas temperature is twice as high due to the difference between the rotational constants.

Thus, estimates show that the gas heating is insignificant and the gas temperature near the electrode is no higher than 700 K. This result is of importance for determining the mechanisms responsible for sustaining

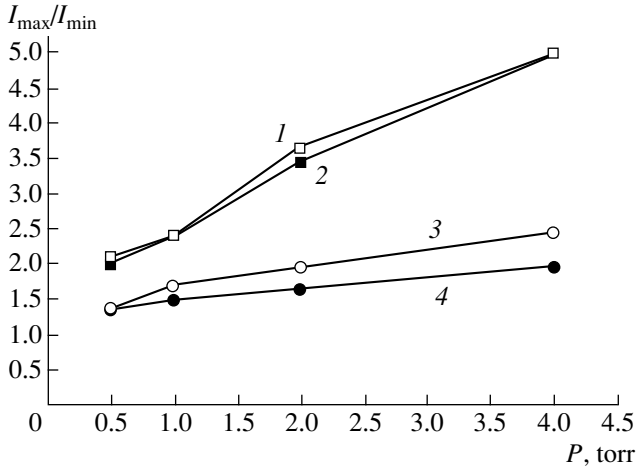

Fig. 6. The ratios between the line intensities $I_{\max}/I_{\min}$ at the maximum (12.4 W) and minimum (1.8 W) values of W_{abs} at different pressures P: (*1*) $H(H_\beta$, 486.1 nm), (*2*) $H(H_\alpha$, 656.3 nm), (*3*) Ar(696.5 nm), and (*4*) H_2 (752.4 nm).

the discharge. One of these mechanisms may be energy absorption in the plasma resonance region. The role of this mechanism decreases as the ratio ν/ω increases. Under our experimental conditions, this resonance is feasible. However, taking into account that identical discharge structures were observed at a pressure of 15 torr and approximately the same power [7], it is reasonable to assume that the gas heating does not ensure the conditions under which the resonant mechanism plays a decisive role in the formation of the electrode layer within the entire pressure range under study.

3.4. Plasma Processes near the Discharge Electrode

The linear dependences of the intensities of the atomic hydrogen lines on the absorbed power (and, consequently, on the electron density [10, 16]) and an analysis of the balance of the excited particles allow us to conclude that the excitation of atomic lines in the discharge is not caused by stepwise processes of the form $H(2S, 2D) + e \longrightarrow H^*$ (here, the two lowest metastable states and two resonant hydrogen states are considered a single state H(2*S*, 2*D*)), which would result in a stronger dependence on n_e. Indeed, in this case, the balance equation for excited particles would be

$$k_{st}N_{H(2S,\,2D)}n_e = k_{em}N_{H^*}, \qquad (3)$$

where $k_{st} = 4 \times 10^{-7}$ cm^3/s [17] is the coefficient of excitation from the metastable state, $N_{H(2S,\,2D)}$ is the density of metastable particles, $k_{em} = 1/\tau = 4.4 \times 10^{10}$ s^{-1} [18] is the coefficient determined by the lifetime of the excited (emitting) state, and N_{H^*} is the density of the excited atoms. Comparing the contributions from different excitation and deexcitation channels, such as [17]

(i) direct electron-impact excitation, $H + e \longrightarrow H(2S, 2D)$, with a threshold of 10.2 eV;

(ii) excitation due to the radiative transition from a higher level, $H^* \longrightarrow H(2S, 2D) + h\nu$, with the rate constant $k = 5 \times 10^8$ s^{-1};

(iii) dissociative excitation, $H_2 + e \longrightarrow H(2S, 2D) + H + e$, with a threshold of 15 eV and $k = 10^{-11} - 10^{-10}$ cm^3/s;

(iv) diffusion toward the electrode surface;

(v) electron-impact quenching, $H(2S, 2D) + e \longrightarrow H + e$, with $k = 6.8 \times 10^{-9}$ cm^3/s;

(vi) electron-impact ionization, $H(2S, 2D) + e \longrightarrow H^+ + 2e$, with a threshold of 3.4 eV and $k = 7.3 \times 10^{-8}$ cm^3/s;

(vii) stepwise electron-impact ionization, $H(2S, 2D) + e \longrightarrow H^* + e$, with a threshold of 1.9 eV and $k_{st} = 4 \times 10^{-7}$ cm^3/s;

(viii) emission via the transition $H(2S, 2D) \longrightarrow H + h\nu$ with $\tau_{eff} = 2.1 \times 10^{-9}/(g_{esc}$ s) (one can find the expression for g_{esc} in [19, 20]);

(ix) quenching in collisions with molecules, $H(2S, 2D) + H_2 \longrightarrow H + H + H$, with $k = 1.3 \times 10^{-9}$ cm^3/s; and

(x) quenching in collisions with atoms, $H(2S, 2D) + H \longrightarrow H + H$, with $k = 3 \times 10^{-11}$ cm^3/s,

and taking into account the main processes, we arrive at the following balance equation for metastable particles:

$$k_mN_Hn_e + k_dN_{H_2}n_e = k_qN_{H_2}N_{H(2S,\,2D)}. \qquad (4)$$

Here, k_m is the coefficient of the direct electron-impact excitation of a metastable state, N_H is the atom density, k_d is the coefficient of dissociative excitation, N_{H_2} is the density of hydrogen molecules calculated taking into account the gas temperature near the electrode, and k_q is the coefficient of quenching in collisions with molecules. Thus, we obtain $N_{H^*} \propto n_eN_{H(2S,\,2D)} \propto n_e^2$, which disagrees with experimental results. A comparison between the stepwise and direct processes based on the value of $N_{H(2S,\,2D)}$ derived from Eq. (4) shows that the former process is of minor importance.

There are two possible channels of direct electron-impact excitation, namely, the excitation from the ground atomic state, $H + e \longrightarrow H^* + e$, and dissociative excitation, $H_2 + e \longrightarrow H^* + H + e$. Thus, we can write

$$k_{ex}N_Hn_e + k_{dex}N_{H_2}n_e = k_{em}N_{H^*}, \qquad (5)$$

where k_{ex} is the coefficient of direct electron-impact excitation and k_{dex} is the coefficient of dissociative excitation.

An analysis of the balance of hydrogen atoms shows that direct electron-impact dissociation is the main mechanism for their formation. Here, the following processes are taken into account:

(i) direct electron-impact dissociation, $H_2 + e \longrightarrow H + H + e$, with a threshold of 9 eV and $k = 3.7 \times 10^{-10}$ cm^3/s;

(ii) dissociation in collisions of metastable particles with molecules, $H(2S, 2D) + H_2 \longrightarrow H + H + H$, with $k = 1.3 \times 10^{-9}$ cm^3/s;

(iii) dissociation in collisions of excited particles with molecules, $H^* + H_2 \longrightarrow H + H + H$, with $k = 2.2 \times 10^{-9}$ cm^3/s; and

(iv) recombination on the electrode surface, $H + H \longrightarrow H_2$ [17].

Under our conditions, the main channel of the loss of hydrogen atoms is recombination on the electrode surface with a characteristic time of

$$\tau_s = \tau_k + \tau_d, \quad \tau_k = \frac{2R}{v_t\gamma}, \quad \tau_d = \frac{R^2}{6D}. \qquad (6)$$

Here, τ_k is the characteristic time of reaction at the electrode surface; τ_d is the characteristic diffusion time; $R \approx$

Degree of dissociation (%) calculated based on the experimental data (the minimum and maximum absorbed powers are 3.7 and 9.4 W for a pressure of 0.5 torr and 1.8 and 12.4 W for other pressures)

E, V/cm	0.5 torr		1 torr		2 torr		4 torr	
	min	max	min	max	min	max	min	max
60	0.89	1.29	0.60	0.90	0.42	0.80	0.23	0.59
100	1.37	2.06	0.86	1.40	0.57	1.25	0.31	1.02
150	1.59	2.58	0.88	1.64	0.49	1.46	0.18	1.23
200	1.66	2.89	0.78	1.73	0.30	1.52	–	1.27
300	1.64	3.23	0.5	1.74	–	1.48	–	1.21
400	1.53	3.38	0.21	1.65	–	1.36	–	1.07
500	1.38	3.42	–	1.51	–	1.20	–	0.90

1 mm is the distance from the electrode; v_t is the thermal velocity of atoms; $\gamma = 0.05$ [21] is the coefficient of recombination on steel; and D is the diffusion coefficient

$$D = D_0\left(\frac{T}{273}\right)^a/(1.3\times10^{-3}P), \tag{7}$$

where $D_0 = 0.184$ cm^2 s, T is the gas temperature in K, $a = 1.728$, and P is the pressure in torr.

The balance equation for atoms is

$$k_{\text{diss}}N_{\text{H}_2}n_e = \frac{v_t\gamma}{R}N_{\text{H}}, \tag{8}$$

where k_{diss} is the diffusion coefficient, $N_{\text{H}_2} = N^0_{\text{H}_2} - 0.5N_{\text{H}}$ is the density of hydrogen molecules, and $N^0_{\text{H}_2}$ is the density of molecules at zero dissociation. As a result, a high degree of dissociation in the discharge is required to ensure the linear dependences of the intensities on the electron density in the case of direct electron-impact excitation from the ground atomic state. Otherwise, we have $N_{\text{H}} \propto n_e$, which leads to a square-law dependence $I \propto n_eN_{\text{H}} \propto n_e^2$. However, it follows from Eq. (8) that, under our conditions ($n_e \approx 10^{11}$ cm^{-3} [7]), the degree of dissociation should be within the range 10^{-2}–10^{-3}. Therefore, dissociative excitation is the main process responsible for the atomic line emission. It is seen from Eq. (5) that it takes place when

$$\frac{N_{\text{H}}}{N_{\text{H}_2}} < \frac{k_{dex}}{k_{ex}}. \tag{9}$$

Estimates made with allowance for the ratio of the rate constants k_{dex}/k_{ex} calculated from the Boltzmann equation [17] show that condition (9) is satisfied when the degree of dissociation is less than 0.1–3%. Since the microwave field amplitude near the electrode is unknown, the calculations were carried out for E = 100–500 V/cm.

The threshold for dissociative excitation (17 eV for H_α) is higher than that for direct electron-impact excitation of hydrogen molecular bands (9–15 eV) and Ar lines (13.3 eV for $\lambda = 696.5$ nm). The processes with a higher threshold are much more sensitive to the change in the microwave field amplitude, which can increase with power. This circumstance can explain the fact that the intensities of atomic hydrogen lines increase faster than the intensities of hydrogen molecular bands and Ar lines as the power increases (Fig. 6).

3.5. Determination of the Degree of Dissociation

The degree of dissociation was measured using actinometry. For this purpose, 5 vol % of argon was added to hydrogen. In [10], it was shown that, at low argon concentrations in a molecular gas, Ar line emission is related to direct electron-impact excitation from the ground state, which is confirmed by the linear dependence of the intensity of the Ar 696.5-nm line on the absorbed power. This result is also applicable for our experiments. With allowance for process (5), the ratio of the intensities of H_α and Ar 696.5-nm lines is

$$\frac{I_{\text{H}_\alpha}}{I_{\text{Ar}}} = \frac{k_{dex}N_{\text{H}_2} + k_{ex}N_{\text{H}}}{k_{\text{Ar}}N_{\text{Ar}}} = \frac{k_{dex}N^0_{\text{H}_2} + (k_{ex} - 0.5k_{dex})N_{\text{H}}}{k_{\text{Ar}}N_{\text{Ar}}}, \tag{10}$$

hence,

$$N_{\text{H}} = N_{\text{Ar}}\frac{k_{\text{Ar}}}{k_{ex} - 0.5k_{dex}}\left(\frac{I_{\text{H}_\alpha}}{I_{\text{Ar}}} - \frac{N^0_{\text{H}_2}}{N_{\text{Ar}}}\frac{k_{dex}}{k_{\text{Ar}}}\right), \tag{11}$$

where k_{Ar} is the coefficient of electron-impact excitation of the emitting argon state and N_{Ar} is the argon atom density.

The table presents the ranges of the degree of dissociation calculated from the measured ratios I_{H_α}/I_{Ar} at different pressures and powers. The estimates were obtained for different values of the microwave field amplitude because its actual value was unknown. It is seen that, within the range of pressures and powers under study, the degree of dissociation near the electrode is no more than 3.5%.

4. CONCLUSION

An EMD in hydrogen at pressures of 0.5–4 torr and absorbed powers up to 12 W has been studied using spectroscopy methods. The volume-averaged emission intensities of lines and bands are measured within the wavelength range 400–800 nm. It is shown that, due to the substantial inhomogeneity of the discharge, the observed emission stems from the bright region near the electrode. Based on the relative intensities of the rotational lines, the rotational temperature of the excited state is determined and, taking into account the rotational constant, the rotational temperature of the ground state of hydrogen in the electrode region is estimated. This temperature is at most 700 K. Taking into account the fact that a similar discharge structure was previously observed at much higher pressures, we can conclude that gas heating is insufficient for the plasma resonance regime to be realized within the entire pressure range under study.

It is shown experimentally that the intensities of all the lines and bands depend linearly on the absorbed power. An analysis of plasma processes shows that the recorded emission lines and bands are excited by direct electron impact; in particular, the H_α line emission is related to the dissociative electron-impact excitation from the H_2 ground state. The degree of hydrogen dissociation in the electrode region is determined using actinometry and is shown to be no higher than several percent. All this indicates that the microwave field amplitude in the bright electrode region is high (as predicted for the electrodynamic system under study). At the same time, the steady-state densities of the particles whose decay is determined by diffusion (e.g., atoms and metastable states) cannot be high because the distance from the electrode and, accordingly, the diffusion time are short.

ACKNOWLEDGMENTS

We are grateful to I.V. Soldatova for help in determining the gas temperature. This study was supported in part by the Netherland Organization for Scientific Research (NWO), grant no. 047.011.000.01.

REFERENCES

1. Yu. A. Lebedev, J. Phys. IV **8**, 369 (1998).
2. G. M. Batanov, N. K. Berezhetskaya, E. F. Bol'shakov, *et al.*, Plasma Sources Sci. Technol. **2**, 164 (1993).
3. V. G. Brovkin, Yu. F. Kolesnichenko, and D. V. Khmara, *Ball Lightning in Laboratory* (Khimiya, Moscow, 1994), p. 119.
4. V. G. Brovkin, Yu. F. Kolesnichenko, and D. V. Khmara, Prikl. Fiz. **4**, 5 (1994).
5. L. Bardos, H. Barankova, Yu. A. Lebedev, *et al.*, Diamond Relat. Mater. **6**, 224 (1997).
6. L. Bardosh and Yu. A. Lebedev, Fiz. Plazmy **24**, 956 (1998) [Plasma Phys. Rep. **24**, 891 (1998)].
7. L. Bardosh and Yu. A. Lebedev, Zh. Tekh. Fiz. **68** (12), 29 (1998) [Tech. Phys. **43**, 1428 (1998)].
8. Yu. A. Lebedev, M. V. Mokeev, and A. V. Tatarinov, Fiz. Plazmy **26**, 293 (2000) [Plasma Phys. Rep. **26**, 272 (2000)].
9. Yu. A. Lebedev and M. V. Mokeev, Teplofiz. Vys. Temp. **38**, 381 (2000) [High Temp. **38**, 338 (2000)].
10. Yu. A. Lebedev, I. V. Soldatova, I. L. Épshteĭn, and O. I. Kholodkevich, Teplofiz. Vys. Temp. **36**, 5 (1998) [High Temp. **36**, 1 (1998)].
11. Zhou Qing, D. K. Otorbaev, G. J. H. Brussaard, *et al.*, J. Appl. Phys. **80**, 1312 (1996).
12. D. K. Otorbaev, V. N. Ochkin, S. Yu. Savinov, and N. N. Sobolev, Preprint No. 3, FIAN (Lebedev Institute of Physics, USSR Academy of Sciences, Moscow, 1979).
13. P. B. Lavrov, V. N. Ostrovskiĭ, and V. I. Ustinov, in *Proceedings of the VIII All-Union Conference on Physics of Electron and Atomic Collisions, Leningrad, 1981*, Review papers, p. 42.
14. B. N. Lavrov and D. K. Otorbaev, Pis'ma Zh. Tekh. Fiz. **4**, 1419 (1978) [Sov. Tech. Phys. Lett. **4**, 574 (1978)].
15. L. Tomasini, A. Rousseau, G. Gousset, and P. Leprince, J. Phys. D **29**, 1006 (1996).
16. Yu. A. Lebedev, Teplofiz. Vys. Temp. **33**, 850 (1995) [High Temp. **33**, 846 (1995)].
17. Yu. A. Lebedev and I. L. Epstein, J. Mosc. Phys. Soc. **5**, 103 (1995).
18. G. A. Kasabov and V. V. Eliseev, *Spectroscopic Tables for Low-Temperature Plasma. Handbook* (Atomizdat, Moscow, 1973).
19. T. Holstein, Phys. Rev. **83**, 1159 (1951).
20. P. Walsh, Phys. Rev. **116**, 551 (1959).
21. A. D. Tserepi, J. R. Dunlop, B. L. Preppernau, and T. A. Miller, J. Appl. Phys. **72**, 2638 (1992).

Translated by N.N. Ustinovskiĭ

Plasma Physics Reports, Vol. 27, No. 5, 2001, pp. 424–431. Translated from Fizika Plazmy, Vol. 27, No. 5, 2001, pp. 450–457.

LOW-TEMPERATURE PLASMA

Glow Pause in a Helium Plasma at Room and Liquid Nitrogen Temperatures on Applying a Nanosecond Voltage Pulse to a Glow Discharge

R. Kh. Amirov, É. I. Asinovskiĭ, and V. V. Markovets

Associated Institute of High Temperatures, Russian Academy of Sciences, Izhorskaya ul. 13/19, Moscow, 127412 Russia

Received October 12, 2000

Abstract—The features of the relaxation of a quasi-steady glow discharge after extra excitation by a nanosecond high-voltage pulse are studied experimentally. It is shown that the plasma relaxation is characterized by the existence of a time interval with a low emission intensity—a glow pause. A kinetic model of the helium plasma relaxation is developed. It is shown that the nanosecond discharge that creates extra ionization and metastable atoms enables one to keep the electron temperature at a quasi-steady level within the range 0.05–0.5 eV for several hundred microseconds during the glow pause. The effect of the helium temperature on the glow pause features is investigated. *© 2001 MAIK "Nauka/Interperiodica".*

1. INTRODUCTION

A combined discharge in which the main ionization is produced by a short pulsed discharge has a number of advantages. Applying nanosecond pulses to a current-carrying plasma enables efficient ionization and makes it possible to easily control the electron temperature. Between the pulses, the electric field may be maintained at a lower level. Such a scheme was used when creating powerful lasers pumped by a combined discharge [1, 2].

When applying nanosecond pulses to a glow discharge, a specific time interval during plasma decay in which the intensity of plasma emission was lower than in the glow discharge was found in [3, 4]. Apparently, a similar effect was observed in [5] at the instant of discharge ignition. This paper is devoted to studying the decay of a helium plasma carrying a dc current.

The recombination of a current-free helium plasma after pulsed excitation has been extensively studied [6, 7]. An analysis of the results obtained shows that metastable atoms and molecules substantially affect the helium plasma decay. Long-lived metastable states, which accumulate the excitation energy, act as sources of fast electrons with an energy of ~18 eV. Cooling helium to cryogenic temperatures (e.g., $T \approx 77$ K) decelerates the decay of atoms in metastable states and increases their total density.

Metastable atoms significantly affect the voltage–current characteristic of a glow discharge in helium at cryogenic temperatures [8]. At low currents, there is a region in which $dE/di > 0$ (where E and i are the electric field and current, respectively) and E is one-half of the field in a glow discharge at room temperature.

In this study, we investigate a plasma state that, on the one hand, resembles an ordinary afterglow and, on the other hand, is similar to a cryogenic glow discharge. Immediately after the nanosecond discharge, recombination occurs as in an ordinary afterglow; then, the plasma relaxation is mainly governed by metastables and the glow discharge current, as is the case with a cryogenic glow discharge.

2. EXPERIMENTAL SETUP

The schematic of the experimental device is shown in Fig. 1. A steady-state glow discharge was ignited in a discharge cell (*1*) with the help of a microsecond pulse generator (*2*). The discharge cell was a 7-cm-long and 1.6-cm-diameter molybdenum glass tube, which was placed between two molybdenum electrodes and was surrounded by a metal shield. The duration of a glow discharge, which could be varied within the range 100–1200 μs, was determined by the duration of the pulse produced by a G5-7A synchronizing generator (*3*). When the glow discharge current had relaxed to a steady-state value, the same synchronizing generator triggered the generator of nanosecond pulses (*4*), which initiated a nanosecond discharge in the discharge cell. The glow discharge current was kept constant during the plasma decay and was determined by a ballast resistor (*5*) and the internal resistance of the microsecond pulse generator (*2*). The current varied within the range 1–15 mA, and the voltage and duration of the nanosecond pulse varied within the ranges 1.5–3.5 kV and 2–40 ns, respectively. The synchronizing generator (*3*) ensured repetitive operation at a repetition rate of 10–100 Hz. To cool the gas to cryogenic temperatures ($T \approx 77$ K), the gas-discharge tube was housed in a cell filled

1063-780X/01/2705-0424$21.00 © 2001 MAIK "Nauka/Interperiodica"

with liquid nitrogen. The reduced pressure of helium in the discharge tube varied from 2 to 50 torr. The total average specific power of a combined discharge did not exceed 200 mW/cm^3; at such powers, the estimated difference between the gas temperatures at the tube axis and wall attained several percent.

We measured the glow discharge current and voltage and the plasma emission intensity (both integral and in individual helium spectral lines) during plasma decay. A D6-1 capacitive divider (*9*) with an attenuation factor of 1 : 100 and a passband of 10 MHz was used to measure the voltage. The glow discharge current was measured by a shunt (*8*) with a resistance of 1 kΩ.

Radiation emitted from the plasma in the transverse direction was applied to an SPM-2 monochromator (*11*) with the help of an optical fiber and a lens. Emission from different discharge regions was recorded by displacing the fiber along the discharge tube. Emission detectors (*6*) (FEU-97 and FEU-84-3 photomultipliers) were gated for a time of 1–10 μs by a pulse supplied from a G5-15 generator (*10*), which was synchronized with the G5-7A generator (*3*). The delay time of the gating pulse was controlled by the G5-15 generator. All the electrical and optical parameters were recorded with an HP-1701B oscillograph (*12*).

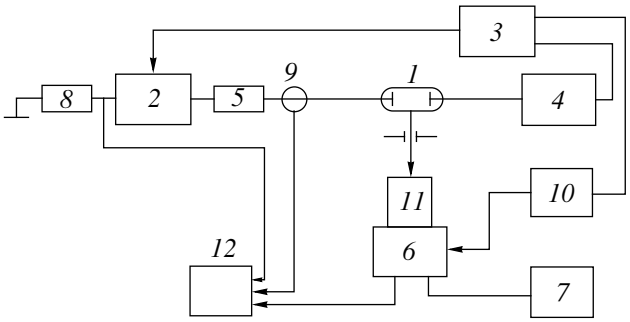

Fig. 1. Schematic of the experimental device for studying the decay of a current–carrying plasma: (*1*) discharge cell, (*2*) microsecond pulse generator, (*3*) G5-7A synchronizing generator, (*4*) nanosecond pulse generator, (*5*) ballast resistor, (*6*) FEU 84-3 photomultiplier, (*7*) VSV-1 power supply, (*8*) shunt, (*9*) D6-1 capacitive divider, (*10*) G5-15 generator, (*11*) SPM-2 monochromator, and (*12*) HP-1701B oscillograph.

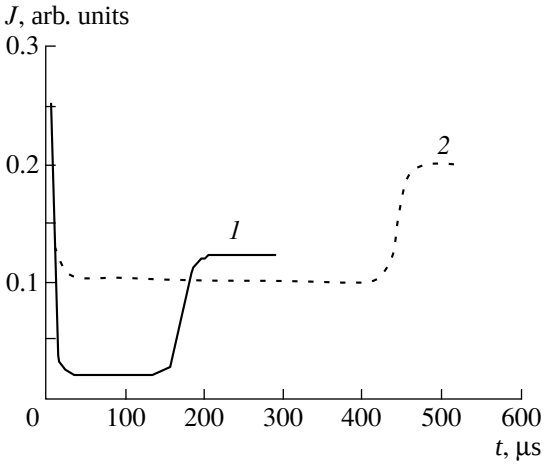

Fig. 2. Time evolution of the intensity of the HeI 587.6-nm spectral line after applying a nanosecond pulse to the glow discharge (at $t = 0$) at gas temperatures of (*1*) 298 and (*2*) 77 K; the helium atom density and the glow discharge current are equal to 6.8×10^{17} cm^{-3} and 4.8 mA, respectively.

3. EXPERIMENTAL RESULTS

The main feature of the relaxation of the plasma of a glow discharge positive column after extra excitation with a nanosecond discharge is the existence of a time interval (a glow pause) in which the emission intensity is substantially lower than in an unperturbed glow discharge.

Figure 2 shows the time evolution of the intensity of the HeI 587.6-nm spectral line for two different gas temperatures. After the nanosecond discharge, the line intensity sharply drops and remains at a low steady-state level for several tens or even hundreds of microseconds. Then, the intensity rapidly increases and reaches the initial value characteristic of a glow discharge. During this process, the discharge current remains constant and equal to that before applying the nanosecond pulse.

The intensities of the following spectral lines were measured: 706.5 nm ($2^3S \Rightarrow 2^3P$), 388.8 nm ($3^3P \Rightarrow 2^3S$), 587.6 nm ($3^3D \Rightarrow 2^3P$), 667.8 nm ($3^1D \Rightarrow 2^1P$), 501.5 nm ($3^1P \Rightarrow 2^1S$), 447.2 nm ($4^3D \Rightarrow 3^3P$), and 396.4 nm ($4^3P \Rightarrow 3^1S$). The glow pause with the same duration of the steady-state phase was observed simultaneously in all these lines. However, the ratio between the intensities in the glow pause and the glow discharge phase varied in a wide range for different lines.

A qualitative explanation of the glow pause is as follows. Applying the high-voltage nanosecond pulse sharply increases the electron density in the plasma. At a constant glow discharge current, the voltage drop across the plasma column and, consequently, the electric field decrease due to the decrease in the discharge resistance; this is confirmed by the recorded voltage oscillograms. The electron temperature T_e in the discharge is determined by the reduced electric field E/N (where N is the atom density); as the field decreases, T_e and, consequently, the emission intensity decrease.

There is no glow pause in the cathode sheath of a glow discharge. After extra excitation of the plasma, the emission intensity of the cathode sheath rapidly increases and then monotonically relaxes to the value typical of a steady-state discharge. The characteristic relaxation time is about several microseconds. It is rea-

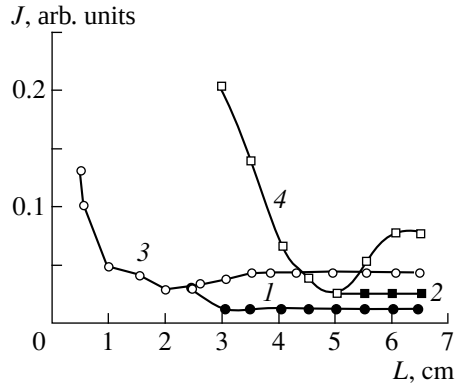

Fig. 3. Profile of the intensity of the HeI 587.6-nm spectral line along the discharge tube in (*1*, *2*) the glow pause and (*3*, *4*) the glow discharge phase for different gas pressures *P* and discharge currents *i*: (*1*, *3*) *P* = 23.3 torr and *i* = 13 mA and (*2*, *4*) *P* = 5 torr and *i* = 10 mA.

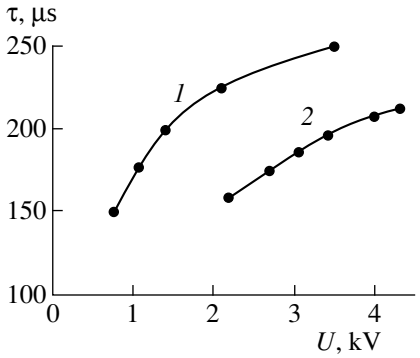

Fig. 4. Duration of the glow pause vs. the nanosecond pulse amplitude for the pulse rise time of (*1*) 2 and (*2*) 5 ns at *P* = 22 torr and *i* = 3 mA.

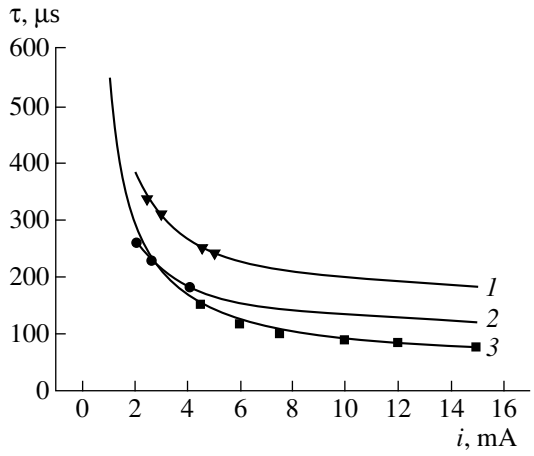

Fig. 5. Duration of the glow pause vs. the glow discharge current for different helium pressures: *P* = (*1*) 21, (*2*) 13.7, and (*3*) 9.5 torr. Solid curves are the simulated dependences; dots show the experimental results.

sonable to assume that the structure of the cathode sheath does not appreciably change during relaxation, because it depends mainly on the electron emission from the cathode surface. Thus, during the glow pause, which lasts for several tens or hundreds of microseconds, the cathode sheath is adjacent to the plasma column that carries the same current as in the steady-state glow discharge, but at a higher electron density and lower electron temperature.

The distribution of the plasma emission intensity in the HeI 587.6-nm spectral line along the discharge tube for different gas pressures and discharge currents is shown in Fig. 3 for both the glow discharge phase and the glow pause. It is seen that the length of the region in which the glow pause occurs coincides with the length of the positive column in the glow discharge phase.

The duration of the glow pause is determined by the time during which the excessive electron density relaxes, which, in turn, depends on the amplitude of the high-voltage nanosecond pulse; as the amplitude increases, the duration of the glow pause monotonically increases (Fig. 4). Moreover, the difference between curves *1* and *2* in Fig. 4 indicates that the degree of extra ionization increases as the rise time of the voltage pulse decreases.

The relaxation time of the excessive electron density depends also on the helium pressure and glow discharge current (Fig. 5). The increase in the gas pressure increases the glow pause duration, whereas the increase in the glow discharge current reduces it. Lowering the helium temperature from the room temperature to 77 K increases the glow pause duration and changes the distribution of the emission intensity along the discharge tube in both the glow discharge phase and the glow pause. Figure 6 shows the distribution of the emission intensity in the HeI 587.6-nm spectral line along the discharge tube during the glow discharge phase and the glow pause for both of these temperatures. At a constant current and helium atom density, the line intensity in the glow pause, as well as the pause duration, increases as the temperature decreases.

4. KINETICS OF HELIUM PLASMA DURING THE GLOW PAUSE

Plasma decay is determined by the plasma composition. The ion composition of helium plasma depends on the pressure and can vary in time. Immediately after the nanosecond discharge, the most abundant ions are the He^+ ions, which are produced by electron-impact ionization of helium atoms. The He_2^+ ions are produced both in the Hornbeck–Molnar reaction $He^* + He \Rightarrow He_2^+$ with the participation of the He* excited state and the conversion reaction $He^+ + 2He \Rightarrow He_2^+ + He$. The conversion rate is equal to $\nu_{1-2} = 3 \times 10^{-29} T^{-1} N^2\ s^{-1}$ [8]; here and below, the temperature *T* is in K and the atom

density N is in cm^{-3}. The diatomic ions can convert into triatomic ones in the reaction $He_2^+ + 2He \Rightarrow He_3^+ + He$. At $T = 77$ K, the rate constant of the latter reaction is $k_{2-3} > 1.7 \times 10^{-31}$ cm^6 s^{-1} [8]. Thus, the increase in the pressure and decrease in the temperature enhance the fraction of heavy ions.

The most abundant metastable particles in helium are $He_2 2^3\Sigma_u^+$, $He2^1S$, and $He2^3S$. The $He_2 2^3\Sigma_u^+$ molecules are produced via the conversion of atomic particles, $He2^3S + 2He \Rightarrow He_2 2^3\Sigma_u^+ + He$ (with a rate constant of 1.8×10^{-34} cm^6 s^{-1} [6]), and the electron–ion recombination of He_2^+ ions. We do not take into account the $He_2 2^3\Sigma_u^+$ molecules because the conversion time of $He2^3S$ exceeds the glow pause duration; the production of $He_2 2^3\Sigma_u^+$ molecules via recombination is also inefficient due to the relatively low electron density.

The density of $He2^1S$ singlet metastable atoms is less than that of $He2^3S$ atoms due to the different statistical weights and high rate of the conversion reaction $He2^1S + e \Rightarrow He2^3S$ (with a rate constant of 3.5×10^{-7} cm^3 s^{-1} [9]). Taking into account the high conversion rate and minor difference in the rates of reactions involving $He2^1S$ and $He2^3S$ atoms, we assume that only $He2^3S$ atoms take part in the reactions characteristic of metastable atoms.

The main channels of electron losses are the recombination and ambipolar diffusion with the coefficient $D_a = \frac{\mu_i}{e}(T_e + T)$, where μ_i is the ion mobility and T_e and T are the temperatures of electrons and neutrals, respectively. The electron recombination rate depends on the ion species. For the He^+ ions, three-body recombination with an electron as a third body is the dominant loss channel. According to [6], the coefficient of three-body recombination is $\alpha_1 = \frac{8.1 \times 10^{-20}}{1 + 0.079P}\left(\frac{T_e}{T}\right)^{-4.4} n_e$ cm^3 s^{-1}, where n_e is in cm^{-3} and P is in torr. At cryogenic temperatures, when the He_2^+ ions can be dominant, dissociative recombination prevails. We considered the following recombination mechanisms involving He_2^+ [6, 10]:

$$He_2^+ + 2e \Rightarrow He2^3S + He + e,$$

$$\alpha_e = 4 \times 10^{-20} n_e \left(\frac{T_e}{T}\right)^{-4} \text{ cm}^3 \text{ s}^{-1},$$

$$He_2^+ + e + He \Rightarrow He2^3S + 2He,$$

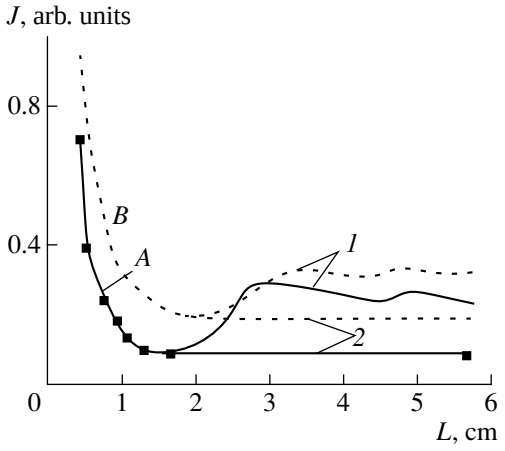

Fig. 6. Profile of the intensity of the HeI 587.6-nm spectral line along the discharge tube in (*1*) the glow discharge phase and (*2*) the glow pause for different gas temperatures: (*A*) 293 and (*B*) 77 K.

$$\alpha_a = 5 \times 10^{-27} N \left(\frac{T_e}{T}\right)^{-1} \text{ cm}^3 \text{ s}^{-1},$$

$$He_2^+ + e \Rightarrow He^* + He,$$

$$\alpha_d = 1.8 \times 10^{-8} \left(\frac{T_e}{T}\right)^{-1.5} \text{ cm}^3 \text{ s}^{-1}.$$

To evaluate the rates of the excitation and ionization of metastable atoms, we used the Fabrikant approximation [11] for the energy dependences of the corresponding cross sections. The electron energy distribution function (EEDF) was assumed to be Maxwellian; cross sections for atomic metastable states and cross sections for ionization from the ground state were taken from [12] and [13], respectively. The cross sections for electron elastic collisions were taken from [14].

Collisions between metastable atoms lead to their deexcitation and the formation of fast electrons in the reactions

$$He2^3S + He2^3S \Rightarrow He^+ + He + e + 15 \text{ eV},$$

$$He2^3S + He2^3S \Rightarrow He_2^+ + e + 17.4 \text{ eV}.$$

Metastable atoms are the so-called S-source of fast electrons [8], whose intensity can be represented as $J_s = 0.5\beta[He2^3S]^2$, where $\beta = (1.5 \pm 0.3) \times 10^{-9}$ cm^3 s^{-1} [6] is the total rate constant of the two latter reactions. Diffusion decreases the excessive metastable atom density. For $He2^3S$ atoms, in the temperature range under study ($T = 77$–293 K), the diffusion coefficient is approximated by the formula [15, 16]

$$D_M = 1.2 \times 10^{-18} N^{-1} T/(11.5 + T^{1/2}) \text{ cm}^2 \text{ s}^{-1}.$$

In accordance with the above processes, the equations for the electron temperature, electron balance, and $He2^3S$ metastable atom balance are incorporated into the set of kinetic equations describing the plasma behavior during the glow pause. These equations are complemented with the requirement that the current be constant during the helium plasma relaxation. The set is written for the densities averaged over the tube radius under the assumptions that the electron radial distribution is diffusive and the ion temperature is equal to the gas temperature.

The equation for the electron temperature is

$$\frac{dT_e}{dt} = -2\frac{m_e}{M_a}\nu(T_e - T) - \frac{2}{3}T\frac{D_a}{\Lambda^2}q + \frac{2}{3}\frac{e^2E^2}{m_e\nu} + Q,$$

where m_e and e are the electron mass and charge and M_a is helium atom mass. The first term on the right-hand side describes the cooling of electrons due to elastic collisions with atoms (with the collision frequency ν); it is taken into account that inelastic collisions are of no importance at electron temperatures T_e less than 10 eV. The second term describes diffusive cooling; here, Λ is the diffusion radius and the parameter q, which depends on the plasma parameters and tube radius, is taken from calculations [17]. Electron heating is determined by the electric field strength and fast electrons, which are produced in reactions involving metastable atoms. The metastable atom density determines the quantity $Q = \frac{1}{3}\beta[He2^3S]^2\frac{1}{n_e}\Delta\varepsilon + \frac{2}{3}\gamma[He2^3S]\Delta\varepsilon$, where $\gamma = (4.2 \pm 0.6) \times 10^{-9}$ cm^3 s^{-1} [6] is the rate constant of superelastic collisions between electrons and metastable atoms,

$$He2^3S + e \Rightarrow He + e + 19.8\ \text{eV}.$$

The quantity $\Delta\varepsilon$ is the average energy transferred by a fast electron to the bulk electrons. According to [6], it is equal to $\Delta\varepsilon = 1.39 \times 10^{-6}(n_eT/P)^{1/2}$, where P is the pressure in torr. The latter expression is valid for $(n_e/P) < 2 \times 10^{11}$ cm^{-3} torr^{-1}. At low pressures, $\Delta\varepsilon = 3.3 \times 10^{-14}n_eT/P$ for the fast electron energies from 18 to 20 eV and $\Delta\varepsilon = 5.7 \times 10^{-14}n_eT/P$ for the fast electron energies ≤15 eV [6].

For the diffusive radial electron distribution, the balance equation for the average electron density in a cylindrically symmetric plasma is

$$\frac{dn_e}{dt} = -\frac{D_a}{\Lambda^2}n_e - \alpha n_e^2 + n_e\nu_i + J_s.$$

Here, the first and second terms on the right-hand side describe the electron losses due to ambipolar diffusion and recombination, respectively; the third term describes ionization (both direct and stepwise); and the last term is the intensity of the S-source.

The balance of $He2^3S$ metastable atoms is determined by the losses due to diffusion toward the tube wall, deexcitation by electrons, conversion into molecular metastable states, and pair collisions between atoms. The $He2^3S$ atoms are produced due to electron-impact excitation from the ground state and electron–ion recombination. The metastable atom balance equation is

$$\frac{dM}{dt} = -\frac{D_M}{\Lambda^2}M - \beta M - \gamma n_eM - \delta NM + n_e\nu_M + k_1\alpha_1n_e[He^+] + k_2\alpha_2n_e[He_2^+],$$

where δ is the rate constant of conversion into molecular metastable states, ν_M is the rate of electron-impact excitation of metastable atoms from the ground state, and α_2 is the total recombination rate constant of the He_2^+ ions. In this equation, the quantities k_1 and k_2 (which are equal to 1 and 0.7, respectively [5]) characterize the relative contributions of atomic and molecular ions to the recombination processes that yield $He2^3S$ atoms.

In our experiments, the current is determined by the external circuit and remains constant during relaxation; hence, the electric field in the plasma obeys Ohm's law,

$$E = j\frac{m_e\nu}{e^2n_e},$$

where j is the current density.

In simulations, the initial conditions are set at a certain instant after the nanosecond pulse when the rapid collisional cooling of electrons has already occurred,

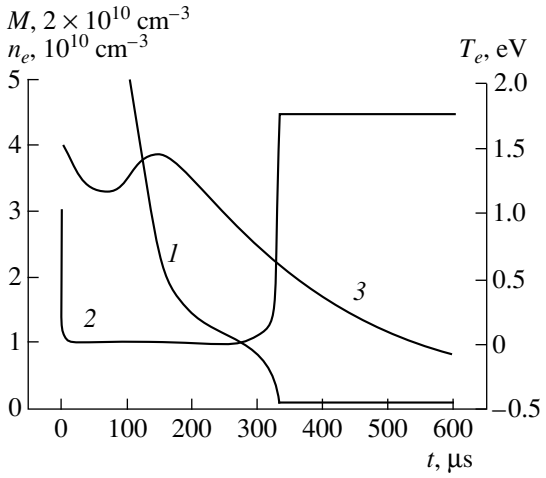

Fig. 7. Calculated relaxation of (*1*) the electron density N_e, (*2*) electron temperature T_e, and (*3*) the density of metastable atoms $He2^3S_1$; the pressure is P = 9.5 torr, the glow discharge current is i = 5 mA, and the gas temperature is T = 293 K.

but the particle density has not yet changed. The densities of electrons and He2^3S atoms are chosen such that the calculations match the experimental data. To estimate the ratio between the excessive density of metastable atoms and the electron density, we calculated the EEDF for the reduced electric field that is characteristic of the nanosecond discharge. Simulations were performed using the code based on the approach developed in [18]. The electric field was estimated as $E = 2U/L$, where U is the amplitude of the high-voltage pulse and L is the discharge tube length. The coefficient 2 is related to the doubling of the pulse voltage due to the mismatch between the impedances of the cable and the discharge tube.

Figure 7 shows the calculated relaxation of the electron temperature, electron density, and metastable atom density. We emphasize the quasi-steady behavior of T_e during the glow pause and its abrupt rise at the end of the pause. We can distinguish three characteristic stages of plasma decay: first, the early afterglow with a rapid decrease in the electron temperature due to collisions; then, the glow pause, during which T_e varies only slightly; and, finally, a rapid increase in T_e to the value typical of a glow discharge. The end of the T_e relaxation exactly coincides with the decay of the excessive electron density. The excessive metastable atom density relaxes more slowly than n_e.

Figure 5 presents the calculated duration of the glow pause versus the glow discharge current for different helium pressures. It is seen that the calculated dependence is in good agreement with the experimental results. The calculated initial densities of the electrons and metastable atoms are proportional to the current. The increase in the duration of the glow pause with pressure is explained by the decrease in the rate of electron loss due to diffusion. The decrease in the duration of the glow pause with increasing the discharge current is related to the increase in the electric field, which raises the electron temperature and the rate of diffusion toward the discharge tube wall.

Metastable atoms determine the behavior of the electron temperature during the glow pause. The calculated relaxation of the electron temperature for different initial densities of He2^3S metastable atoms is shown in Fig. 8. The higher the metastable atom density during the decay, the fewer the variations in the electron temperature and the lower the temperature T_e during the glow pause. The increase in the duration of the glow pause is related to the decrease in the loss rate of excessive electrons due to the action of the S-source. The increase in T_e is due to heating by the fast electrons that are produced in superelastic collisions and pair collisions between metastable atoms.

The quasi-steady behavior of the electron temperature is related to the combined action of the electric field and metastable atoms on T_e. In the initial stage of the glow pause, the densities of electrons and He2^3S atoms are high; hence, electron heating caused by the electric field is weak ($E \sim 1/n_e$) and T_e is mainly determined by heating caused by metastable atoms. As the excessive densities of electrons and metastable atoms decrease, the contribution of the electric field to heating increases, whereas the role of metastable atoms decreases; i.e., the decrease in heating due to the internal source is balanced by the increase in heating caused by the external electric field.

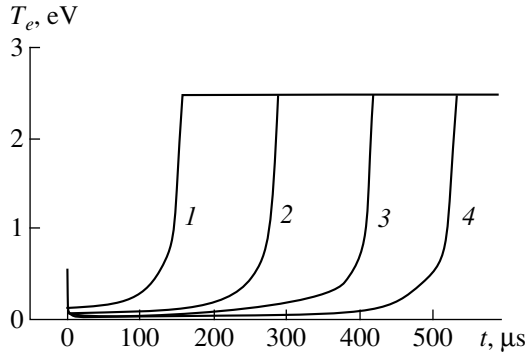

Fig. 8. Calculated relaxation of the electron temperature for different initial densities of He2^3S_1 metastable atoms: (*1*) 4×10^{10}, (*2*) 6×10^{10}, (*3*) 8×10^{10}, and (*4*) 10^{11} cm^{-3}; the pressure is $P = 8$ torr, the glow discharge current is $i = 5$ mA, and the gas temperature is $T = 293$ K.

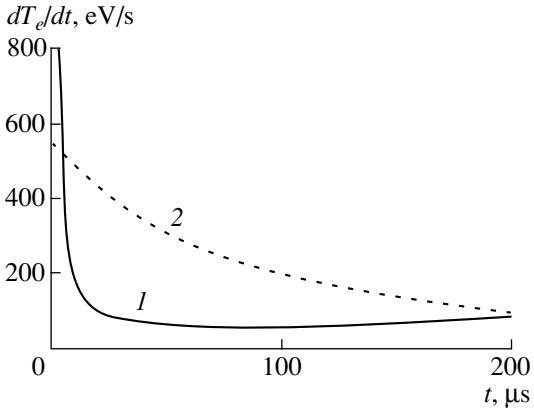

Fig. 9. Time evolution of the electron heating rate during the glow pause: (*1*) heating caused by the electric field and (*2*) heating caused by metastable atoms. Initial conditions are $T_e = 5.5$ eV, [He2^3S_1] $= 1.6 \times 10^{12}$ cm^{-3}, $n_e = 2 \times 10^{11}$ cm^{-3}, the pressure is $P = 4$ torr, and the glow discharge current is $i = 5$ mA.

Figure 9 shows the contribution from different terms in the electron temperature balance equation to electron heating during relaxation. It is seen in Fig. 9 that, within 200 μs after the start of plasma decay, heating

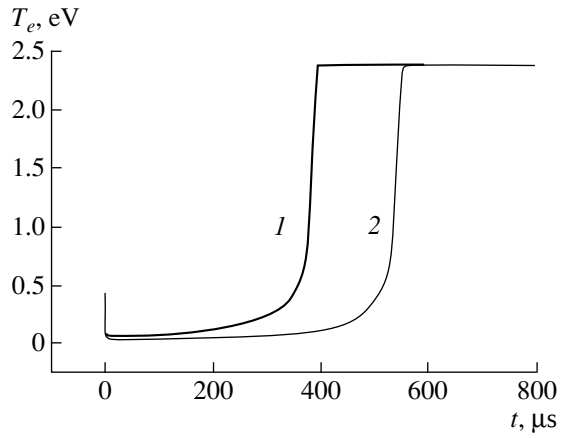

Fig. 10. Calculated relaxation of the electron temperature for different gas temperatures (other conditions being the same): (*1*) 293 and (*2*) 77 K.

caused by the electric field is weaker than that caused by metastable atoms because

$$\frac{2}{3}j^2\frac{m_e\nu}{e^2n_e^2} < \frac{1}{3}\beta[\mathrm{He}2^3S]^2\frac{1}{n_e}\Delta\varepsilon + \frac{2}{3}\gamma[\mathrm{He}2^3S]\Delta\varepsilon,$$

where the term on the left-hand side characterizes Joule heating. After the recombination of a certain fraction of the excessive electrons, the inequality changes its sign; i.e., heating caused by the electric field, which maintains the constant current through the plasma, becomes dominant. The total heating remains almost constant and equal to the total cooling of electrons due to elastic collisions and diffusion. Such a behavior of the electron heating sources ensures that the electron temperature varies insignificantly.

Lowering the gas temperature from room temperature to 77 K leads to a threefold decrease in the diffusion coefficient of metastable atoms, which, in turn, results in an increase in the metastable atom density during plasma decay. An analysis shows that the increase in the duration of the glow pause as the gas temperature decreases is mainly due to this effect. Figure 10 shows the relaxation of the electron temperature during the glow pause for two different gas temperatures.

Plasma decay in a glow discharge resembles a cryogenic dc discharge, namely, T-discharge [19]. In both cases, the current flows at an anomalously low electric field in the plasma. In the glow pause, the electric field is such that the electron-impact ionization rate is not equal to the rate of electron loss due to ambipolar diffusion.

A characteristic feature of the glow pause is the quasi-steady behavior of the electron temperature at a level that cannot be realized in steady-state discharges. This temperature can be controlled by varying the current, pressure, or the parameters of the nanosecond pulse.

Metastable atoms act as sources of fast electrons, which enrich the EEDF near the thresholds for inelastic processes, thus increasing the corresponding rate constants. Moreover, at a high density of metastable atoms, stepwise excitation becomes important. Accurate calculations of the spectral line intensities monitored in the experiment during the plasma relaxation require calculating the EEDF with allowance for the time evolution of the electric field and the density of $\mathrm{He}2^3S$ metastable atoms.

5. CONCLUSION

The kinetic model of decay of a helium plasma carrying a dc current has been developed. The results of computer simulations are compared with the experimental data. Plasma decay is characterized by the existence of a time interval with a low emission intensity—a glow pause. It is shown that the $\mathrm{He}2^3S$ metastable atoms affect the duration of the glow pause and the behavior of the electron temperature. Lowering the gas temperature decreases the rate of $\mathrm{He}2^3S$ losses and increases the glow pause duration. During the glow pause in helium plasma, the electron temperature varies only slightly and is much less than that in a glow discharge.

ACKNOWLEDGMENTS

This study was supported in part by the Russian Foundation for Basic Research, project no. 99-02-16182.

REFERENCES

1. A. E. Hill, Appl. Phys. Lett. **22**, 670 (1973).
2. N. A. Generalov, V. D. Kosynkin, V. P. Zimakov, *et al.*, Fiz. Plazmy **3**, 626 (1977) [Sov. J. Plasma Phys. **3**, 354 (1977)].
3. R. Kh. Amirov, É. I. Asinovskiĭ, and V. V. Markovets, in *Proceedings of the 5th All-Union Conference on Physics of Low-Temperature Plasma, Kiev, 1979*, Part 1, p. 40.
4. R. Kh. Amirov, É. I. Asinovskiĭ, and V. V. Markovets, Teplofiz. Vys. Temp. **9**, 47 (1981).
5. Yu. Z. Ionikh, Yu. G. Utkin, N. V. Chernysheva, and A. S. Evdokimenko, Fiz. Plazmy **22**, 289 (1996) [Plasma Phys. Rep. **22**, 267 (1996)].
6. R. Deloche, P. Monchicourt, M. Cheret, and F. Lambert, Phys. Rev. A **13**, 1140 (1976).
7. V. N. Samovarov, in *Plasma Chemistry*, Ed. by B. M. Smirnov (Atomizdat, Moscow, 1981), Vol. 8, p. 38.
8. É. I. Asinovskiĭ and A. V. Kirillin, in *Plasma Chemistry*, Ed. by B. M. Smirnov (Atomizdat, Moscow, 1978), Vol. 5, p. 66.
9. A. V. Phelps, Phys. Rev. **99**, 1307 (1955).

10. L. P. Khuzeev, Candidate's Dissertation in Mathematical Physics (Inst. Sil'notochnoĭ Élektroniki Akad. Nauk SSSR, Tomsk, 1979).
11. S. É. Frish, *Spectroscopy of Gas-Discharge Plasmas* (Nauka, Leningrad, 1970), p. 244.
12. E. W. McDaniel, *Collision Phenomena in Ionized Gases* (Wiley, New York, 1964; Mir, Moscow, 1967).
13. B. M. Smirnov, *Atomic Collisions and Elementary Processes in Plasma* (Atomizdat, Moscow, 1968).
14. L. G. H. Huxley and R. W. Crompton, *The Diffusion and Drift of Electrons in Gases* (Wiley, New York, 1974; Mir, Moscow, 1977).
15. I. Ya. Fugol', Doctoral Dissertation in Mathematical Physics (FTINT, Kharkov, 1971).
16. W. A. Fitzimos, N. F. Lane, and G. K. Walter, Phys. Rev. **174**, 193 (1968).
17. V. E. Golant, A. P. Zhilinskii, and S. A. Sakharov, *Fundamentals of Plasma Physics* (Atomizdat, Moscow, 1977; Wiley, New York, 1980).
18. L. C. Pitchford, Phys. Rev. A **23**, 294 (1981).
19. A. V. Kirillin and V. V. Markovets, Teplofiz. Vys. Temp. **11**, 706 (1973).

Translated by N.N. Ustinovskiĭ

Plasma Physics Reports, Vol. 27, No. 5, 2001, pp. 432–439. Translated from Fizika Plazmy, Vol. 27, No. 5, 2001, pp. 458–465.

LOW-TEMPERATURE PLASMA

Effect of Resonant Radiation Transport on the Parameters of RF and DC Discharges in a He–Ar–Xe Mixture

S. A. Starostin*, P. J. M. Peters*, G. van der Poel*, Yu. B. Udalov, W. J. Witteman*, I. V. Kochetov***, and A. P. Napartovich*****

**Twente University, Enschede, 7500 AE, Netherlands*

***Netherlands Laser Research Center, Enschede, 7500 CK, Netherlands*

****Troitsk Institute for Innovation and Thermonuclear Research, Troitsk, Moscow oblast, 142190 Russia*

Received July 20, 2000; in final form, November 15, 2000

Abstract—A study is made of the effect of the transport of Xe 147-nm resonant radiation on the parameters of a low-temperature plasma of DC and RF discharges in gas mixtures used as the working medium in lasers based on infrared transitions in xenon. RF discharges are treated in the planar geometry typical of slab lasers. DC discharges in tubes are treated in cylindrical geometry. The trapping of resonant radiation is described using different approximate models: the decay time approximation for a plasma slab (the Holstein approximation) and the effective lifetime approximation (the Biberman approximation). The transport equation for resonant radiation is solved numerically. The effect of the radiation transport on both the current–voltage characteristics of a discharge and the spatial distribution of the excited Xe atoms is investigated. The current–voltage characteristics calculated for a DC discharge with allowance for the resonant radiation transport agree well with the experimental characteristics. It is found that, for an RF discharge, the effective lifetime approximation overestimates the density of the excited Xe atoms near the electrodes by several times and underestimates this density at the midplane of the discharge gap. © *2001 MAIK "Nauka/Interperiodica"*.

1. INTRODUCTION

The efficiency of electric-discharge lasers based on atomic transitions in Xe excited by a DC current in a tube is low and decreases sharply with pressure because of the discharge current contraction. The excitation of a gas by RF discharges [1, 2] has made it possible to increase the laser efficiency and to create fairly compact slab lasers capable of generating output powers of several watts in the continuous mode at wavelengths corresponding to the atmospheric transparency region. The parameters of the RF capacitive discharge are usually calculated for pure noble gases at pressures of several torr and lower (see, e.g., review [3]). A numerical model of RF discharges for lasers operating with Xe-containing gas mixtures was developed by Il'yukhin *et al.* [4].

The typical pressure of the working mixture of a laser is 100–200 torr. The gas mixture consists of almost equal proportions of He and Ar, with a small (about 0.5%) amount of Xe. The distance between the electrodes is 1–2 mm, the frequency of the exciting electric field is about 100 MHz, and the specific excitation power is about 100 W/cm^3 [1, 2]. It was shown experimentally that the amplification coefficient of a weak signal has high sharp peaks near the electrodes [5]. Such a shape of the amplification coefficient is explained as being due to the increase in the electric field near the electrode surfaces [2, 4]. The laser and discharge parameters are largely governed by the distribution of the electronically excited states of Xe atoms in the interelectrode gap. One of the two lowest electronic states of Xe atoms—specifically, the $6s[3/2]_1^0\,(^3P_1)$ state—is resonant ($\lambda = 147$ nm), the radiation lifetime being $\tau_R = 3.79$ ns [6]. Under the conditions corresponding to a highly nonuniform distribution of the density of the excited atoms, an important role may be played by the excitation transfer by resonant radiation, which lowers the density of the excited atoms near the electrodes and raises their density at the midplane of the discharge.

The aim of this study is to analyze how the excitation transfer by resonant radiation affects the calculated parameters of a DC discharge and an RF discharge. We consider a DC discharge in a tube and investigate the effect of the resonant radiation transport on the current–voltage (*I–V*) characteristic of a DC discharge. The computed *I–V* characteristics are compared with the measured ones. The structure of an RF discharge under the conditions prevailing in lasers is numerically calculated.

There are several approximate models for describing the trapping of radiation, such as the decay time approximation for a plasma slab or cylinder (the Holstein approximation [7]) and the effective lifetime approximation (the Biberman approximation; see, e.g., [8]). We compare the results calculated using different approximate models with the results from the numerical solution of the transport equation for resonant radi-

ation. A significant difference in the spatial distributions of the population density of the lowest excited resonant state of Xe atoms is revealed.

2. DESCRIPTION OF THE EXPERIMENT

Figure 1 shows the scheme of the experimental device for measuring the *I–V* characteristic of a DC discharge. The discharge is initiated in a quartz tube with an inner diameter of 0.3 cm, which is cooled by running water. The discharge length is 28 cm. The discharge is initiated by a controlled high-voltage source connected to the cathode through a 94-kΩ ballast resistor. The device is capable of sustaining stable discharges up to a pressure of 100 torr. As the pressure increases, the luminous column becomes smaller in diameter. The voltage drop across the discharge and the discharge current are measured with two FLUKE 8026B multimeters. The electric field is calculated without allowance for the voltage drop at the cathode. Note that, in an Ar : He : Xe = 50 : 50 : 1 mixture at a pressure of 38 torr, we achieved an output power of 0.4 mW, which was mostly generated at a wavelength of 2.65 μm.

3. DISCHARGE MODEL

3.1. DC Discharge

The radial profiles of the parameters of DC discharges were calculated under the assumption that the plasma column is uniform along the discharge axis. We solved a time-dependent equation for the plasma density with allowance for ambipolar diffusion in the radial direction and the processes of direct ionization, stepwise ionization, and dissociative recombination. In our model, we took into account only one effective excited state of Xe atoms, specifically, the Xe* state, which is a combination of the $6s[3/2]_2^0$ metastable state and the $6s[3/2]_1^0$ resonant state. For this effective state, we solved a time-dependent balance equation. The populations of the sublevels were assumed to be proportional to the statistical weights. We took into account the excitation from the ground state, stepwise ionization, and the production of excited atoms via dissociative recombination. The model for describing the excitation transfer by resonant radiation will be discussed in Section 4. The radial profile of the translational temperature was determined by solving the time-independent heat conduction equation at a constant pressure. The basic set of equations was supplemented with the relevant boundary and initial conditions. All of the transport and kinetic coefficients were calculated as functions of the reduced electric field *E*/*N* by numerically solving the Boltzmann equation for the spherically symmetric part of the electron energy distribution function.

The basic set of equations was solved in finite differences by direct integration on a mesh with 25–51 mesh points along the radial coordinate.

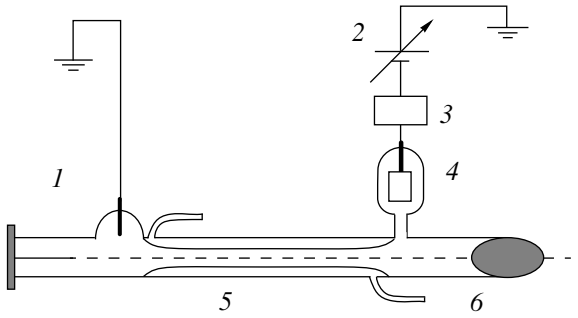

Fig. 1. Scheme of the experimental device: (*1*) anode, (*2*) controlled high-voltage source, (*3*) ballast resistor, (*4*) cathode, (*5*) water-cooled tube, (*6*) output window installed at the Brewster angle.

3.2. RF Discharge

In accordance with [4, 9], our model of an RF discharge was developed with allowance for three species of positive ions (Xe^+, $ArXe^+$, and Xe_2^+) and one effective excited state of Xe atoms (Xe*). The basic set of equations consisting of the balance equations for the densities of the above four plasma components, the equation for the electron density, and Poisson's equation for the electric field was integrated over space and time with allowance for drift and diffusion of the charged particles. The gas temperature and density were determined by solving the time-independent heat conduction equation.

Under the conditions of our experiments with RF discharges in a He–Ar–Xe mixture, the electron energy relaxation rate at the midplane of the interelectrode gap is lower than the frequency of the exciting electric field, whereas at the electrodes, it is higher than the field frequency. The electron energy relaxation length is comparable to the electrode sheath thickness. Consequently, nonlocal effects play an important role near the electrodes. In order to describe these nonlocal effects correctly, it is necessary to solve the Boltzmann equation with allowance for the spatial distributions of the discharge parameters. However, since this problem is very involved (a similar problem for pure He was solved by Feoktistov *et al.* [9]), we applied a simplified approach described in [3]: a time-independent equation for the mean electron energy was solved with allowance for both electron drift and diffusion [10]. At each time step, the mean electron energy was calculated at every mesh point within the interelectrode gap. Then, the mesh values of the mean electron energy were used to calculate the rate constants (found in advance as functions of the mean electron energy by numerically solving the Boltzmann equation for the electron energy distribution function) of direct ionization, stepwise ionization, and the excitation of the effective Xe* level. We also tabulated the transport coefficients that were used to solve the time-independent equation for the mean

electron energy and the balance equations. The terms that describe the excitation transfer by resonant radiation will be discussed in Section 4. The basic equations were supplemented with the corresponding boundary and initial conditions. The voltage drop across the discharge was found from the given RF field power. The basic set of equations was solved numerically by the difference scheme that was developed by Sharfetter and Gummel [11] in order to describe the processes in semiconductor devices (Boeuf [12] was the first to apply this scheme to model RF discharges).

The basic equations were integrated on a nonuniform grid with a spatial step that was shortened when approaching the electrodes. As a rule, we used about 100 spatial steps. In order to achieve a steady-state solution, it was necessary to simulate several thousands of periods of the RF field, so that the calculation of one version took about 20 hours of computer time on an IBM-compatible computer with a Celeron-466 microprocessor.

4. MODELS OF THE RESONANT RADIATION TRANSPORT

The balance equation for the density of the excited atoms in the Xe* state with allowance for collisional and radiative processes has the form [8]

$$\frac{\partial \mathrm{Xe}^*}{\partial t} = K_{ex} n_e \mathrm{Xe} - K_{dex} n_e \mathrm{Xe}^* + \beta_{\mathrm{Xe}_2^+} n_e \mathrm{Xe}_2^+ + \beta_{\mathrm{ArXe}^+} n_e \mathrm{ArXe}^+ - K_i^{\mathrm{Xe}^*} n_e \mathrm{Xe}^* - K_{k\mathrm{ArAr}} \mathrm{Xe}^* \mathrm{ArAr} - K_{k\mathrm{XeHe}} \mathrm{Xe}^* \mathrm{XeHe} - K_{k\mathrm{XeAr}} \mathrm{Xe}^* \mathrm{XeAr} - K_q \mathrm{Xe}^* \mathrm{Xe} + \int \mathrm{Xe}^*(\mathbf{r}') K(|\mathbf{r} - \mathbf{r}'|) d\mathbf{r}' - \frac{\mathrm{Xe}^*}{\tau}. \quad (1)$$

Here, K_{ex} is the rate constant of the electron-impact excitation of the Xe* state from the ground state; K_{dex} is the rate constant of the electron-impact deexcitation of the Xe* state; $\beta_{\mathrm{Xe}_2^+}$ and β_{ArXe^+} are the rate constants of dissociative recombination of electrons with Xe_2^+ and ArXe^+ ions, respectively; $K_i^{\mathrm{Xe}^*}$ is the stepwise-ionization rate constant; $K_{k\mathrm{ArAr}}$, $K_{k\mathrm{XeHe}}$, and $K_{k\mathrm{XeAr}}$ are the rate constants of three-body reactions producing the ArXe* and Xe_2^* excimer molecules; and K_q is the quenching rate of excimer molecules by heavy particles. Being the function of the absolute value of the coordinate difference $r = |\mathbf{r} - \mathbf{r}'|$, the kernel of the integral equation (1) has the form

$$K(r) = -\frac{1}{4\pi r^2 \tau} \frac{\partial f(r)}{\partial r}. \quad (2)$$

Here, the spontaneous lifetime τ of the Xe* state is defined as $\tau = \tau_R \frac{g_R}{g_R + g_m}$; τ_R is the lifetime of the resonant state; and g_R and g_m are the statistical weights of the resonant and metastable states, respectively. In the case of a collisional spectral line broadening, the probability $f(r)$ for a photon to move a certain distance r without being absorbed or scattered is described by the asymptotic expression $f(r) = 1/\sqrt{\pi k_0 r}$, where k_0 is the absorption coefficient at the line center (we assume that the rate of mixing of the metastable and resonant states is much higher than the spontaneous deexcitation rate). In pure Xe at room temperature, the collisional broadening becomes comparable to the Doppler broadening at a pressure of several torr. However, in order to describe the trapping of radiation, it is important to know the radiation transport at the collision-induced line wings. For discharges with sufficiently large geometric dimensions (larger than 1 mm) in pure Xe [13], the Doppler broadening can be neglected, in particular, in the pressure range $P > 10^{-2}$ torr. Consequently, in simulations, we took into account only the collisional spectral line broadening. The data on the broadening of the spectral lines due to collisions with Xe and He atoms were taken from [13] (these data are needed to calculate the absorption coefficient). The broadening due to collisions with Ar atoms was assumed to be two times smaller than that due to collisions with He atoms. Under the conditions of our experiments, the typical value of k_0 was 1.4×10^5 cm^{-1}.

The rate constants of the elementary processes incorporated into Eq. (1) are summarized in Table 1. An analysis of the results obtained shows that the main contribution to the quenching rate of the Xe* state comes from stepwise ionization.

The method proposed by Holstein [7] to describe the trapping of radiation consists in the replacement of the last two terms in Eq. (1) by the term Xe^*/τ_H, where τ_H is the deexcitation time of a plasma slab or cylinder. In the literature, this time is also called the effective decay time of the fundamental mode [17]. For a collisional broadening in the case of a planar plasma slab, the decay time of the fundamental mode is calculated from the formula [7]

$$\tau_H = \frac{\tau \sqrt{\pi k_0 d}}{1.150}, \quad (3)$$

where d is the slab thickness.

For a collisional broadening in the case of a cylindrical plasma, the decay time of the fundamental mode is calculated from the formula [7]

$$\tau_H = \frac{\tau \sqrt{\pi k_0 R}}{1.115}, \quad (4)$$

where R is the radius of the plasma cylinder.

Table 1. Collisional processes of the excitation and quenching of Xe* states

Reaction	Designation	K, $\mathrm{cm}^{3(n-1)}\ \mathrm{s}^{-1}$	Reference
$Xe + e \longleftrightarrow Xe^* + e$	K_{ex}, K_{dex}	Defined from the Boltzmann equation	
$Xe_2^+ + e \longrightarrow Xe^* + Xe$	$\beta_{Xe_2^+}$	1.7×10^{-7} $[1 - \exp(-180/T)]\,T_e^{-1/2}$	
$ArXe^+ + e \longrightarrow Xe^* + Ar$	β_{ArXe^+}	8.2×10^{-7} $[1 - \exp(-180/T)]\,T_e^{-1/2}$	
$Xe^* + e \longrightarrow Xe^+ + e + e$	$K_i^{Xe^*}$	Defined from the Boltzmann equation	
$Xe^* + Ar + Ar \longrightarrow ArXe^* + Ar$	$K_{k\mathrm{ArAr}}$	10^{-35}	[14]
$Xe^* + Xe + He \longrightarrow Xe_2^* + He$	$K_{k\mathrm{XeHe}}$	$1.7 \times 10^{-32}(300/T)^{0.66}$	[15]
$Xe^* + Xe + Ar \longrightarrow Xe_2^* + Ar$	$K_{k\mathrm{XeAr}}$	$2.3 \times 10^{-32}(300/T)^{0.66}$	[16]
$Xe^* + Xe \longrightarrow Xe + Xe$	K_q	3.2×10^{-15}	[17]

n is the number of reagents; the gas temperature T and electron temperature T_e are expressed in degrees and electronvolts, respectively.

The approximation proposed by L.M. Biberman (see, e.g., [8]) incorporates the dependence of the effective lifetime on the distance from the plasma boundary. For a planar discharge, the asymptotic expression for the effective lifetime has the form

$$\tau_{\mathrm{eff}}(x) = \tau \Big/ \left[\frac{1}{2 + 3\sqrt{\pi k_0 x}} + \frac{1}{2 + 3\sqrt{\pi k_0 (d - x)}} \right], \quad (5)$$

where x is the distance from the boundary of the plasma slab. For a cylindrical discharge, the analytic expression for the effective lifetime in terms of hypergeometric functions is presented in [17].

An exact solution to Eq. (1), supplemented with the other equations required for describing the discharge, was found numerically using the algorithm developed in [18, 19].

5. DISCUSSION OF THE RESULTS OBTAINED

In discharges in noble gases, the main ionization mechanism is stepwise ionization. Consequently, we can expect that the reduced electric field E/N (where E is the electric field strength and N is the density of neutral particles) at which the discharge is sustained is highly sensitive to the quenching rate constant of the electronically excited states. The collisional quenching rate of the lowest electronic states is low in comparison with the stepwise ionization rate because of the large energy defect. In the pressure range under investigation, the quenching rate of the lowest electronic states in three-body collisions producing Xe_2^* and ArXe* excimer molecules is also unimportant (see Table 1).

5.1. DC Discharge

The results obtained when studying the effect of the radiative lifetime of a DC discharge on the reduced electric field E/N can be interpreted very simply. The corresponding calculations were carried out for the conditions of our experiments with DC discharges in a tube of radius $R = 0.15$ cm filled with an Ar : He : Xe = 50 : 50 : 1 mixture at a pressure of 76 torr. In Fig. 2, we compare the I–V characteristics calculated using different approximation models for the resonant radiation

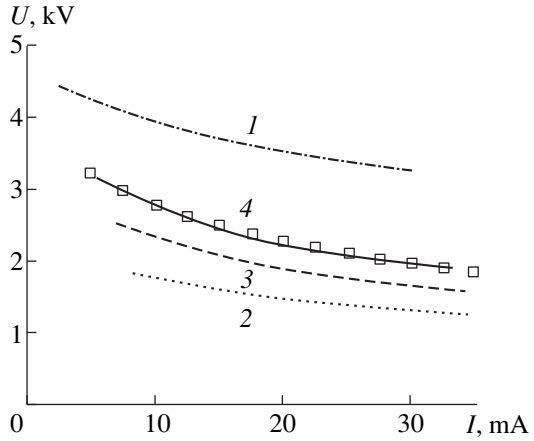

Fig. 2. Comparison between the calculated and measured I–V characteristics of a DC discharge in an Ar : He : Xe = 50 : 50 : 1 mixture at a pressure of $P = 76$ torr: the experimental results are represented by the squares; curves *1* and *2* refer to an optically thin and optically thick medium, respectively; curve *3* is obtained using the decay time approximation for a plasma cylinder; and curve *4* is calculated by solving Eq. (1) numerically.

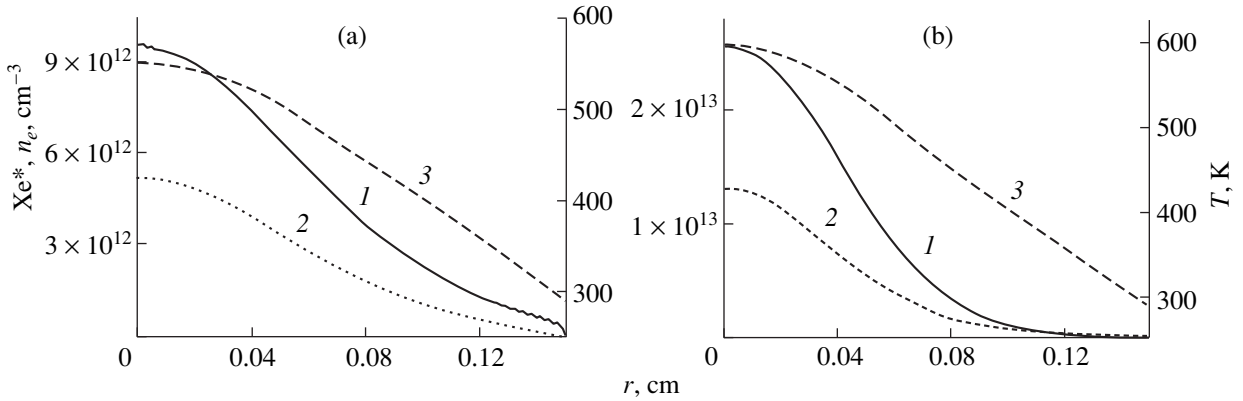

Fig. 3. Radial profiles of (*1*) the density of Xe* atoms, (*2*) the electron density, and (*3*) the translational gas temperature in a DC discharge in an Ar : He : Xe = 59 : 40 : 1 mixture at a pressure of P = 50 torr and a mean power density of W = 14 W/cm^3: (a) the results of solving Eq. (1) numerically and (b) the results obtained using the decay time approximation for a plasma cylinder.

transport with the experimentally measured *I–V* characteristic (squares). The calculations were carried out for an optically thin medium (curve *1*) and a medium with an infinitely large optical thickness (curve *2*). The figure also shows the *I–V* characteristics calculated by using the Holstein approximation (curve *3*) and by solving Eq. (1) numerically (curve *4*). The limiting *I–V* characteristics for an optically thin medium and a medium with an infinitely large optical thickness are presented in order to illustrate the role played by the balance of the excited particles in the formation of the *I–V* characteristic of a discharge. The results obtained are seen to differ markedly among different approximations for resonant radiation transport. We find good agreement between the curve calculated by solving Eq. (1) exactly and the experimental curve. Figure 3 displays the radial profiles of the electron density and the density of the excited atoms in the Xe* state; the corresponding calculations were carried out by applying the decay time approximation for a plasma cylinder (Fig. 3a) and by solving Eq. (1) numerically (Fig. 3b). The figure also shows the radial profiles of the translational gas temperature. A comparative analysis of the profiles in Figs. 3a and 3b shows that the decay time approximation overestimates the density of Xe* atoms at the tube axis by a factor of two and gives a two times smaller full width at half-maximum (FWHM) of the radial profile of the density of Xe* atoms. This is also true for the electron density. Because of the gas heating, the reduced electric field E/N is the strongest at the tube axis; as a result, the ionization and excitation processes are most intense in the central region of the discharge. The resonant radiation transport smoothes the degree of excitation over the tube cross section and increases the discharge current density in the peripheral region, thereby resulting in the expansion of the discharge plasma.

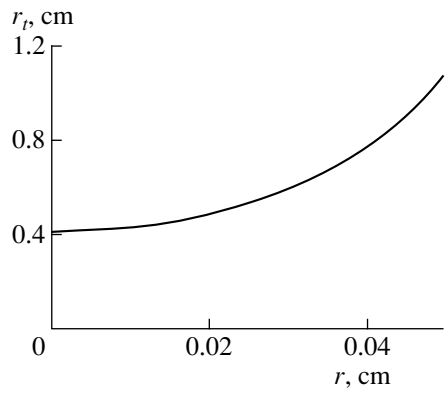

Fig. 4. Radial profile of the thermalization length r_t calculated for the same parameter values as in Fig. 3.

The efficiency of resonant radiation transport can be characterized in terms of the thermalization length [20], which satisfies the following relationship in the case of collisional spectral line broadening:

$$r_t = \left(\frac{\nu_{st}}{\frac{1}{\tau} + \nu_{st}}\right)^{-2} \frac{1}{k_0}, \qquad (6)$$

where τ is the spontaneous lifetime of the Xe* state and ν_{st} is the total collisional quenching rate of this state. Since, for Lorentzian broadening, the probability for a photon to be emitted at the spectral line wings is proportional to $(k_0 r)^{-1/2}$, where r is the distance from the plasma boundary, the thermalization length can be regarded as the spatial scale on which the emitted radiation strongly affects the balance of Xe* atoms. Deep in the discharge plasma (at distances from the plasma boundary greater than the thermalization length), the density of the Xe* atoms is governed exclusively by collisional processes, so that the emitted radiation plays a negligible role. Figure 4 shows the radial profile of the

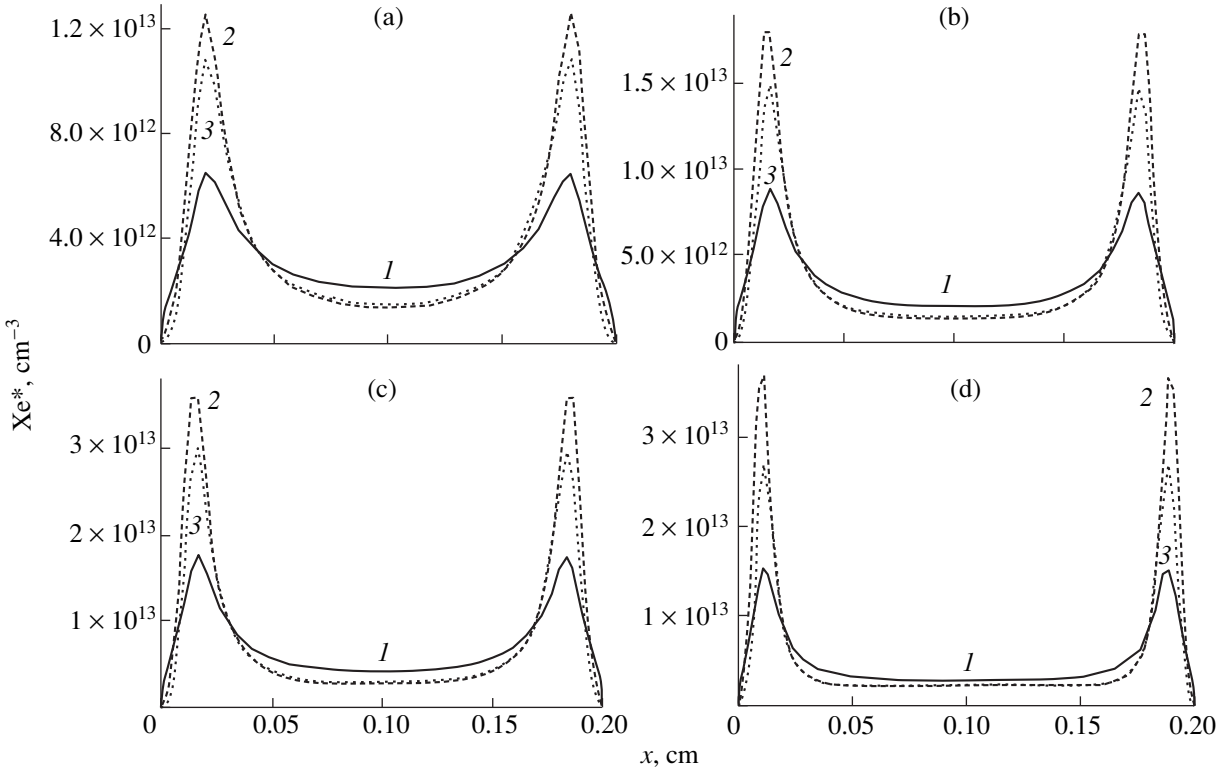

Fig. 5. Profiles of the density of Xe* atoms in the plasma of an RF discharge in an Ar : He : Xe = 50 : 50 : 0.5 mixture for (a) W = 50 W/cm^3 and P = 60 torr, (b) W = 50 W/cm^3 and P = 120 torr, (c) W = 100 W/cm^3 and P = 120 torr, and (d) W = 100 W/cm^3 and P = 240 torr: (*1*) the results of solving Eq. (1) numerically, (*2*) the results obtained using the decay time approximation for a plasma slab, and (*3*) the results obtained using the effective lifetime approximation.

thermalization length r_t calculated from formula (6) for the same parameter values as those in Fig. 3. Since the thermalization length is the shortest at the discharge axis, Fig. 4 refers only to a small axial region. We can see that, even in this region, the thermalization length markedly exceeds the tube radius, thereby evidencing the crucial role of the resonant radiation transport.

5.2. RF Discharge

We simulated an RF discharge in a 2-mm plane gap in a He : Ar : Xe = 50 : 50 : 0.5 mixture at pressures of 60–240 torr, mean power densities of W = 50–100 W/cm^3, and the frequency of the exciting electric field of 100 MHz. Figure 5 shows the profiles of the density of Xe* atoms in the discharge gap. The profiles were calculated by using the decay time approximation for a plasma slab and the effective lifetime approximation, as well as by solving Eq. (1) numerically, for the following values of the power density and pressure: 50/60, 50/120, 100/120, and 100/240, where the first numerals refer to the power density in W/cm^3 and the second numerals refer to the gas pressure in torr. It is seen that the approximate methods overestimate the density of the Xe* atoms near the electrodes by a factor of about 2 to 3 in comparison with the density obtained by exact numerical integration. At the same time, the approximate methods give somewhat lower central

Table 2. Period-averaged absolute values of the reduced electric field E/N [Td] and the translational gas temperature [K] (in parentheses) at the midplane of the discharge

W, W/cm^3	P, torr	Equation (1)	Holstein approximation (3)	Biberman approximation (5)
50	60	2.49 (447)	3.07 (453)	2.93 (452)
50	120	3.23 (507)	3.80 (519)	3.70 (517)
100	120	3.25 (586)	3.82 (602)	3.72 (599)
100	240	3.36 (692)	3.61 (710)	3.57 (706)

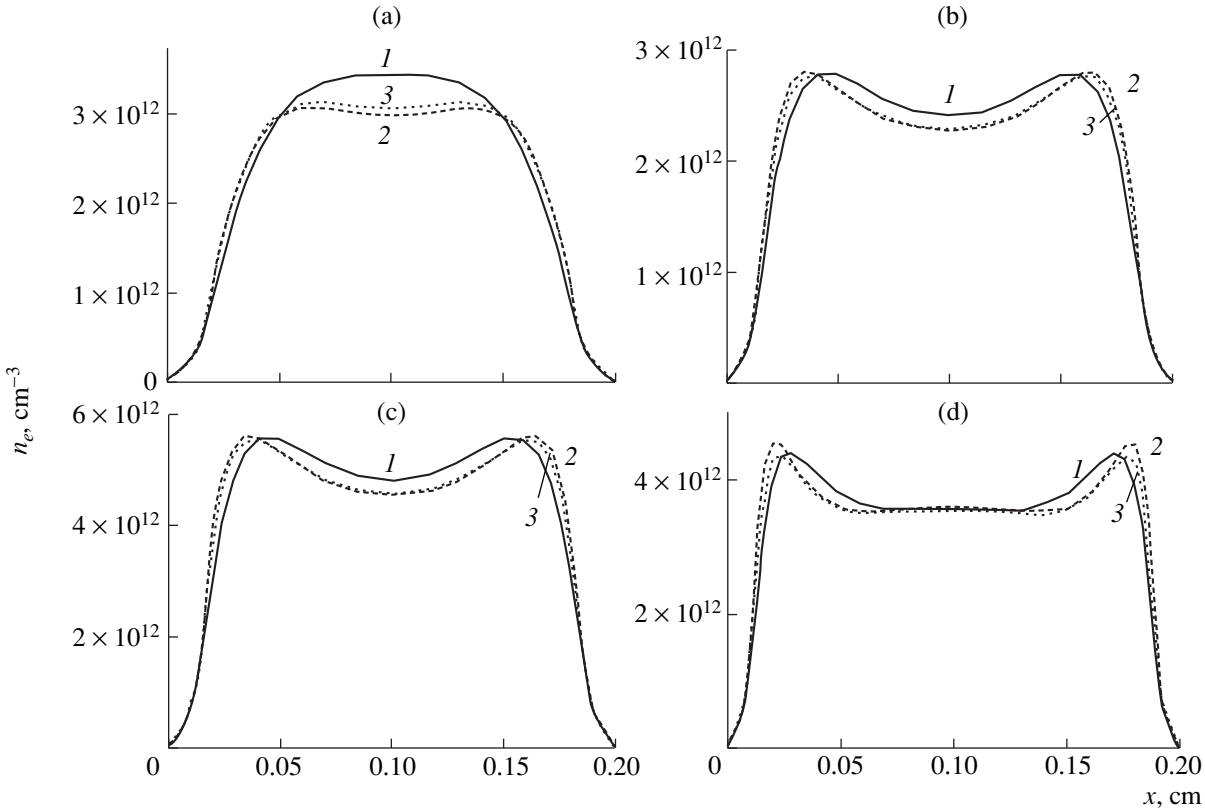

Fig. 6. Profiles of the period-averaged electron density in the plasma of an RF discharge in an Ar : He : Xe = 50 : 50 : 0.5 mixture for (a) W = 50 W/cm^3 and P = 60 torr, (b) W = 50 W/cm^3 and P = 120 torr, (c) W = 100 W/cm^3 and P = 120 torr, and (d) W = 100 W/cm^3 and P = 240 torr: (*1*) the results of solving Eq. (1) numerically, (*2*) the results obtained using the decay time approximation for a plasma slab, and (*3*) the results obtained using the effective lifetime approximation.

densities of the Xe* atoms in comparison with the numerical density, in which case results obtained from the effective lifetime approximation are in better agreement with the exact numerical integration. Table 2 lists the period-averaged absolute values of the reduced electric field E/N and the translational gas temperatures at the midplane of the discharge. An analysis of the calculated results shows that, at the midplane, the electron density remains in local balance: the stepwise ionization rate is equal to the recombination loss rate. According to the numerical solution of Eq. (1), which exactly describes the resonant radiation transport, the excitation is transferred from the peripheral to the central region, the density of the excited xenon atoms increases, and the reduced electric field E/N at which the ionization–recombination balance is maintained decreases. Note that, in contrast to a DC discharge, different approximations for modeling an RF discharge give nearly the same values of the voltage applied to the discharge gap. This circumstance can be explained by the fact that, across the positive column of an RF discharge, the voltage drops only slightly. Figure 6 presents the electron density profiles averaged over the electric field period for the same parameter values as in Fig. 5. We can see that different approximate models for resonant radiation transport and the exact solution of Eq. (1) yield close results. The approximate methods somewhat underestimate the electron density at the midplane and somewhat overestimate it near the elec-

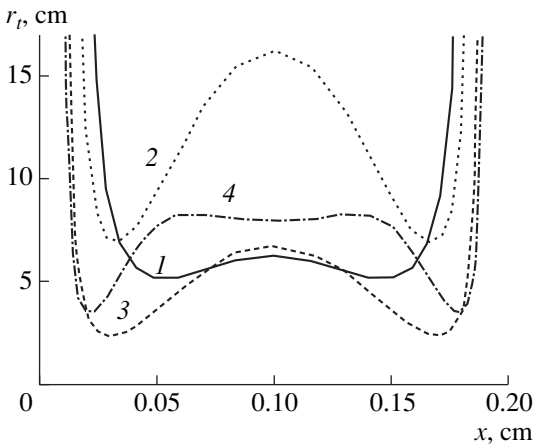

Fig. 7. Calculated profiles of the thermalization length r_t in the plasma of an RF discharge in an Ar : He : Xe = 50 : 50 : 0.5 mixture for (*1*) W = 50 W/cm^3 and P = 60 torr, (*2*) W = 50 W/cm^3 and P = 120 torr, (*3*) W = 100 W/cm^3 and P = 120 torr, and (*4*) W = 100 W/cm^3 and P = 240 torr.

trodes. Figure 7 illustrates the thermalization length for different excitation conditions corresponding to Fig. 5. Since, under all conditions, the thermalization length is markedly longer than the slab thickness, the resonant radiation transport plays an important role.

Note that, for the Xe $5d[3/2]_1$ state, which is the highest excited state for laser transitions at 2.65, 2.03, and 1.73 μm, the thermalization length is about 3×10^{-2} cm (because of the strong collisional relaxation), so that the resonant excitation transfer ($\lambda = 119$ nm) plays an insignificant role in the population balance of this state.

6. CONCLUSION

We have investigated the effect of the transport of Xe 147-nm resonant radiation on the parameters of low-temperature plasmas of DC and RF discharges in gas mixtures used in lasers based on infrared transitions in Xe. Applying the Biberman–Holstein equation, we have developed for the first time a realistic approach to describing resonant radiation transport in the gas-discharge model.

For DC discharges, we have achieved good agreement between the *I–V* characteristics calculated with allowance for the resonant radiation transport and the experimentally measured *I–V* characteristics. We have revealed that the radiation transport weakens the contraction of the discharge column. It is found that, when modeling an RF discharge, the effective lifetime approximation for a plasma slab (the Biberman approximation) and the decay time approximation (the Holstein approximation) overestimate the density of the excited Xe atoms near the electrodes by several times and underestimate this density at the midplane of the discharge gap. For the distribution of the excited Xe atoms under the conditions prevailing in our experiments, the results from the Biberman approximation are closer to the exact ones than the results from the Holstein approximation.

ACKNOWLEDGMENTS

This work was supported in part by the Netherlands Organization for Scientific Research (NWO).

REFERENCES

1. Y. B. Udalov, P. J. M. Peters, M. B. Heeman-Ilieva, *et al.*, Appl. Phys. Lett. **63**, 721 (1993).
2. P. P. Vitruk, R. J. Morley, H. J. Baker, and D. R. Hall, Appl. Phys. Lett. **67**, 1366 (1995).
3. J. P. Boeuf and Ph. Belenguer, in *Nonequilibrium Processes in Partially Ionized Gases*, Ed. by M. Capitelli and J. N. Bardsley (Plenium, New York, 1990), p. 155.
4. B. I. Il'yukhin, V. N. Ochkin, S. N. Tskhaĭ, *et al.*, Kvantovaya Élektron. (Moscow) **25**, 512 (1998).
5. S. N. Tskhai, F. J. Blok, Yu. B. Udalov, *et al.*, Appl. Phys. Lett. **70**, 1921 (1997).
6. D. K. Anderson, Phys. Rev. A **137**, 21 (1965).
7. T. Holstein, Phys. Rev. **83**, 1159 (1951).
8. L. M. Biberman, V. S. Vorob'ev, and I. T. Yakubov, *Kinetics of Nonequilibrium Low-Temperature Plasmas* (Nauka, Moscow, 1982; Consultants Bureau, New York, 1987).
9. V. A. Feoktistov, A. M. Popov, O. B. Popovicheva, *et al.*, IEEE Trans. Plasma Sci. **19**, 163 (1991).
10. S. A. Starostin, I. V. Kochetov, P. J. M. Peters, *et al.*, Appl. Phys. B: Lasers Opt. **B71**, 491 (2000).
11. D. L. Sharfetter and H. K. Gummel, IEEE Trans. Electron Devices **ED-16**, 64 (1969).
12. J.-B. Boeuf, Phys. Rev. A **36**, 2782 (1987).
13. K. Igarashi, S. Mikoshiba, Y. Watanabe, *et al.*, J. Phys. D **28**, 1377 (1995).
14. D. A. Zayarnyĭ, L. V. Semenova, N. N. Ustinovskiĭ, *et al.*, Kvantovaya Élektron. (Moscow) **24**, 987 (1997).
15. D. A. Zayarnyĭ, L. V. Semenova, N. N. Ustinovskiĭ, *et al.*, Kvantovaya Élektron. (Moscow) **25**, 229 (1998).
16. F. Kanari, A. Suda, M. Obara, and T. Fujioka, IEEE J. Quantum Electron. **19**, 1587 (1983).
17. *Reference Book of Constants of Elementary Processes Involving Atoms, Ions, Electrons, and Photons*, Ed. by A. G. Zhiglinskiĭ (St. Petersb. Gos. Univ., St. Petersburg, 1994).
18. J. E. Lawler, G. J. Parker, and W. N. G. Hitchon, J. Quant. Spectrosc. Radiat. Transf. **49**, 627 (1993).
19. G. J. Parker, W. N. G. Hitchon, and J. E. Lawler, J. Phys. B **51**, 211 (1995).
20. V. V. Ivanov, *Radiative Transfer and Celestial Body Spectra* (Nauka, Moscow, 1969).

Translated by G.V. Shepekina

Plasma Physics Reports, Vol. 27, No. 5, 2001, pp. 440–447. Translated from Fizika Plazmy, Vol. 27, No. 5, 2001, pp. 466–474.

LOW-TEMPERATURE PLASMA

Emission Efficiency and Amplification Properties of the Plasma of a Pulsed Discharge in Ar at Elevated Pressures

A. V. Dem'yanov* and D. Lo**

**Troitsk Institute for Innovation and Thermonuclear Research, Troitsk, Moscow oblast, 142190 Russia*

***Faculty of Physics of China University, Hong Kong, China*

Received July 18, 2000; in final form, November 13, 2000

Abstract—The spontaneous emission efficiency of an Ar_2^* excimer and its amplification properties at a wavelength of 126 nm are studied using a numerical model of the weakly ionized plasma of a pulsed discharge in Ar at elevated pressures. It is shown that, under real experimental conditions, it is possible to achieve a net gain coefficient of the active medium equal to ≈ 0.065 cm^{-1} by increasing the gas density up to 4.0×10^{20} cm^{-3} at an initial gas temperature of 170 K. The internal conversion efficiency of discharge energy into spontaneous emission depends weakly on the gas temperature and attains 75% for a gas density of 2.7×10^{20} cm^{-3}, but with excitation powers much lower than for the maximum gain. The applicability of the model at low excitation powers is tested by comparison with the experimental data. © *2001 MAIK "Nauka/Interperiodica".*

1. INTRODUCTION

Progress in microelectronics is largely related to increasingly smaller scale technology. High-power efficient short-wavelength radiation sources are needed for this purpose. The use of high-energy photons is also more preferable in other applications, such as medicine and chemistry. At present, Ar_2^* excimer molecules emit coherent radiation with the shortest wavelength (for Ne_2^* excimers, only fluorescence was observed). Generation with the Ar_2^* excimer was achieved only by exciting a gas at pressures higher than 10–20 atm by a high-power electron beam [1, 2]. From a practical standpoint, the use of pulsed electric discharges is more attractive. However, attempts to achieve generation in pulsed discharges have been unsuccessful. To our knowledge, there are only two papers concerning the possibility of achieving generation using dimers of inert gases in electric discharges [3, 4]. In [3], stable homogeneous discharges with a duration of 50–200 ns were produced in pure Kr at pressures of up to 1.5 atm and in a Kr/Ne mixture at pressures of up to 10 atm. In [4], the amplification at a wavelength of 126 nm for the Ar_2^* excimer was observed at pressures of up to 3.5 atm in pure Ar. In recent papers [5–7], the kinetics of the Ar_2^* excimer excited by a beam of fast electrons was studied in detail. Based on recent experimental data [4–7], we have developed a modified zero-dimensional model [8, 9] describing the kinetics of the Ar_2^* excimer excited by a beam of fast electrons or by a pulsed electric discharge [10]. The model in [10] provides a good description of the experimental data obtained by different authors on excimer excitation by an electron beam and satisfactorily describes experiments with pulsed discharges. Thus, the small-signal gain coefficient (corrected for absorption) predicted by this model is 0.002 cm^{-1}, which is nearly one-third of its value estimated from the amplification of spontaneous emission [4]. In this paper, the model [10], whose applicability at low excitation powers has been tested by comparison with experimental data, is used for simulations and theoretical studies of the amplification properties and emission efficiency of pure Ar plasma excited by a pulsed electric discharge. For definiteness, here we use the parameters of device [4]; i.e., the discharge is excited with the use of the same electric circuit at the same voltages and the same interelectrode distances as in [4]. It is also assumed that, by varying the electrode width, it is possible to vary the discharge area. In addition, the gas density is chosen to be a parameter of the problem. In fact, both these parameters affect the excitation power of the active medium.

2. NUMERICAL MODEL

The numerical model is described in detail in [10]. Here, we only present a brief description of it. The model is based on the package of programs for zero-dimensional modeling of Ar and Xe electric-discharge excimer lamps [8] and also a Xe_2^* electric-discharge laser using Xe/Ne or Xe/He mixtures [9]. The model includes

(i) electric-circuit equations;

(ii) the quasistatic Boltzmann equation in the two-term approximation;

(iii) balance equations for neutral, charged, and excited plasma particles and photons;

1063-780X/01/2705-0440$21.00

(iv) an equation for calculating the gas temperature; and

(v) equations describing the excitation and ionization of Ar by an electron beam.

In [4], the discharge was excited with a Blumlein double forming line. The model uses an equivalent LC electric circuit (Fig. 1). The capacitances C and C_1 are known [4], and the values of the inductances L_s, L_0, and L_m and resistances R_s, R_0, and R_m are chosen in model [10] by comparing the calculated and measured oscillograms of the voltage U_m and the intensity of excimer radiation. The voltage U_m in the prebreakdown phase is determined by the parameters R_s and L_s, whereas the voltage and radiation oscillations after breakdown depend on the total inductance $L = L_0 + L_m$ and total resistance $R = R_0 + R_m$. The oscillogram shape is very sensitive to these parameters, which makes it possible to determine their values.

As was noted in [5, 6], gas heating affects the ion composition. Good agreement with experimental data was achieved in [5] assuming the gas temperature to be ~350 K (for an initial temperature of 300 K). In [5, 6], it was also noted that the gain coefficient of the active medium increases as the gas temperature decreases. For this reason, in order to describe the temperature effects, the model was supplemented with an equation for calculating the gas temperature. The gas temperature is calculated from the energy balance. Gas motion is ignored because the characteristic times of processes observed ($\leq 10^{-6}$ s) are short compared to the gas-expansion time ($\geq 10^{-5}$ s). As the temperature varies, the values of the constants and cross sections dependent on it are recalculated. The temperature effects are discussed in more detail in [10].

The set of kinetic equations was modified in accordance with new data on Ar plasma [4–7]. The scheme of the main processes is illustrated in Fig. 2a.

The kinetic scheme includes three basic parts:

(i) processes involving electrons (the constants and rates are taken from [7, 8]);

(ii) processes involving Ar^+, Ar_2^+, and Ar_3^+ ions (the constants and rates are taken from [6, 7]); and

(iii) processes involving excited particles (the constants and rates are taken from [5, 6, 8]).

Unlike previous models [5–8], model [10] includes the vibrational relaxation of lower levels of the Ar_2^* ($^1\Sigma$) and Ar_2^* ($^3\Sigma$) states (Fig. 2b). This is necessary for correctly determining the gain coefficient of the active medium when the gas temperature varies. The following expression for the gain coefficient of the active medium is used: $g = \sigma N_{Ar_2^*(^1\Sigma,\, v=0)}$, where σ is the cross section for stimulated radiation and $N_{Ar_2^*(^1\Sigma,\, v=0)}$ is the population of the lower vibrational singlet state of an

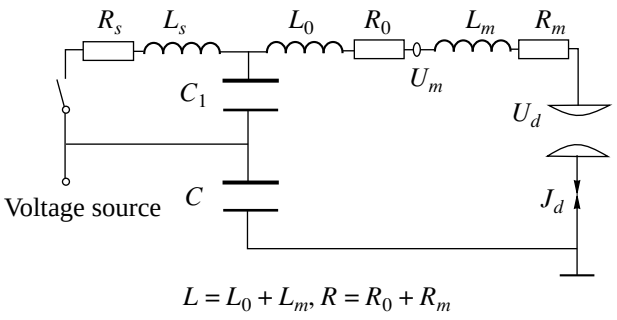

Fig. 1. Equivalent electric circuit of discharge excitation: $R = R_s = 0.3\ \Omega$, $L_s = 9$ nH, $L = 4.5$ nH, and $C = C_1 = 4.25$ nF; the distance between the electrodes is $d = 2.2$ mm.

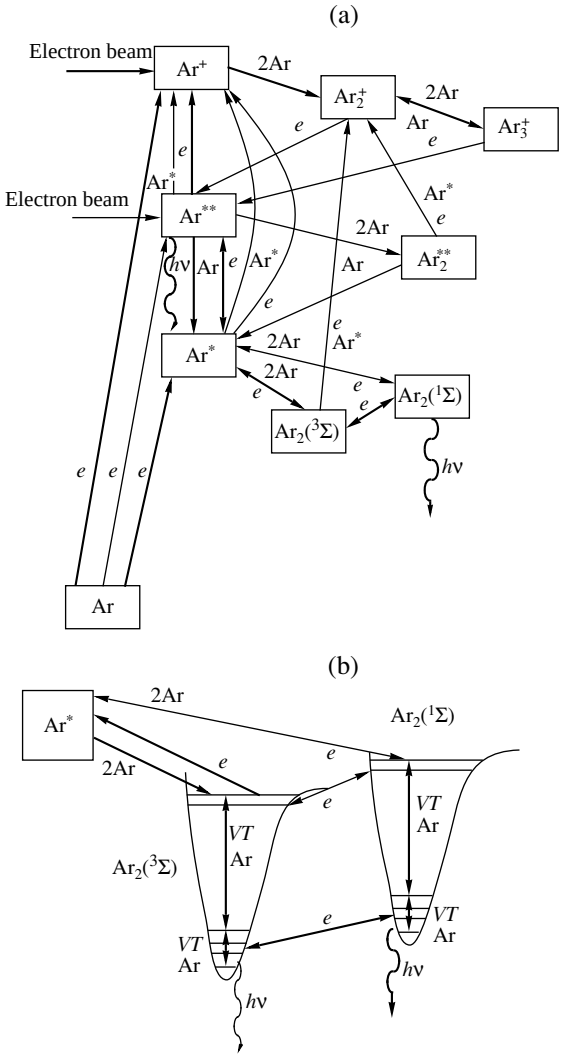

Fig. 2. (a) Diagram of the processes in pure argon plasma excited by an electric discharge or a fast-electron beam, and (b) a detailed diagram of the excitation of singlet and triplet states of the Ar_2^* excimer. The main processes are indicated by heavy arrows.

excimer. The data on the cross section for stimulated radiation are given in [10].

Unfortunately, experimental data on the VT constants of vibrational relaxation are lacking. However, indirect data from spectral measurements [11, 12] allow us to conclude that the rates of these processes are high. At pressures above 1 atm, the Boltzmann distribution over vibrational levels with the vibrational temperature equal to the translational gas temperature is established. In this case, the ratio between the population of the lower vibrational level, which determines the gain coefficient of the active medium, and the total population at lower vibrational states depends on the gas temperature and equals

$$\gamma = \frac{f_0}{\Sigma f_i} = 1 - \exp\left(-\frac{E_{10}}{KT}\right),$$

where E_{10} is the energy of the vibrational transition $\nu = 1 \longrightarrow \nu = 0$ (E_{10} = 292 cm^{-1} = 420 K). Accordingly, incorporating vibrational relaxation in the model decreases the gain coefficient by a factor of about γ. Since γ depends on the gas temperature, incorporating vibrational relaxation under high energy deposition and, consequently, strong heating can affect the time dependence of the gain.

In view of the insufficient information on the vibrational relaxation constants, it is reasonable to use a simplified approach to describing the vibrational kinetics of excimer molecules, which was previously used to describe a XeCl laser [13]. In this case, vibrational relaxation is described by an effective process of energy exchange between the "reservoir" of vibrational energy and the $\nu = 0$ state:

$$Ar_2(^3\Sigma) + Ar \underset{K_r}{\overset{K_f}{\rightleftharpoons}} Ar_2(^3\Sigma, \nu = 0) + Ar,$$

$$Ar_2(^1\Sigma) + Ar \underset{K_r}{\overset{K_f}{\rightleftharpoons}} Ar_2(^1\Sigma, \nu = 0) + Ar.$$

For the constant of the forward reaction, we take a typical value $k_f = 9 \times 10^{-11}$ cm^3/s. The reverse rate constant is chosen to be $k_r = k_f/\gamma$. Note that, to describe the vibrational relaxation more adequately, an experimental study of this process is required.

Hence, the reduced electric field E/N (where E is the electric field strength and N is the total particle density) or the source of secondary electrons (when the excitation is produced by an electron beam) are used in the model as entry parameters when solving the quasistatic Boltzmann equation in the two-term approximation. The model incorporates electron–ion recombination and elastic and inelastic electron losses in collisions of electrons with atoms and molecules in the ground and excited electronic states; electron–electron collisions and superelastic collisions are also taken into account. The constants of direct processes are determined from the calculated electron energy distribution function and from the cross sections for corresponding processes; the constants of reverse processes are calculated from the detailed balance principle. The constants of the processes involving electrons are used to determine the densities of the plasma components and photons from the balance equations solved simultaneously with the equations for the gas temperature and electric circuit. To solve the balance equations, the Kirchhoff equation for the electric circuit, and the temperature equation, we use the Gear method as the most appropriate method for stiff systems typical of the problems under consideration. Note that the time variation of the electron and excited-particle densities is taken into account when solving the Boltzmann equation. The density of electrons and their mobility, which are found from the Boltzmann equation, determine the plasma conductivity needed to calculate the currents and voltages in the electric circuit and, finally, E/N.

In [10], the model was tested using the experimental results [4–6] obtained at high excitation powers (>10 MW/cm^3) needed to achieve generation with the Ar_2^* excimer. For efficient fluorescence (see below), such conditions are not optimal because of the fast quenching of excimer molecules by electrons. For this reason, model [10] was tested for low currents of the fast-electron beam and, accordingly, low pump powers. In Fig. 3, the measurement results [7] are compared with the calculated dependences of the electron density on pressure over a wide range of fast-electron beam currents J_{eb} (from 0.023 to 10 A/cm^2). It is seen that model [10] is also applicable for low pump powers. Note that, for a fast-electron beam current of 0.1 A/cm^2, the plasma-excitation power is nearly the same as for

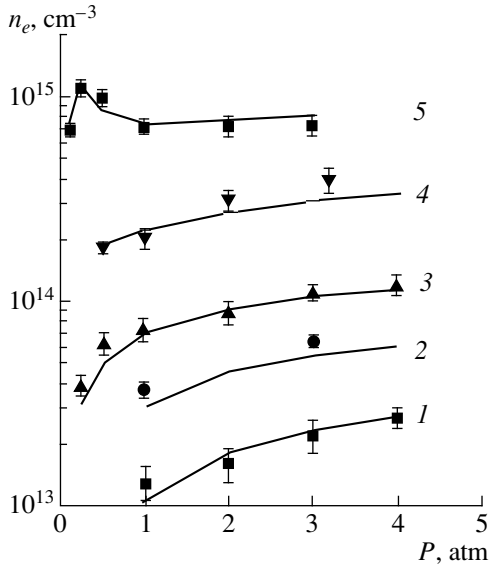

Fig. 3. Comparison of the measured (symbols) and calculated electron densities n_e as a function of the argon pressure P for different currents of a fast-electron beam: J_{eb} = (*1*) 0.023, (*2*) 0.086, (*3*) 0.28, (*4*) 2, and (*5*) 10 A/ cm^2.

the electric-discharge excitation in device [4], but for a discharge area of $S \approx 1500$ cm^2. In this case, the maximum discharge-current density is ~10 A/cm^2.

3. AMPLIFICATION PROPERTIES

In [4], the gain coefficient at a pressure of 3.5 atm was too small (~0.006 cm^{-1}). Hence, the question arises of whether it is possible to achieve a higher gain by using the same device with the same discharge voltage and interelectrode distance. Obviously, the higher the pump power of the active medium, the higher the gain. Taking into account that the discharge current is controlled by the electric circuit, the excitation power for a given discharge area (and, accordingly, a given electron density) increases as the gas density increases due to the increase in the discharge voltage. However, at too high a gas density, the discharge may not be ignited. In our case (see Fig. 4), the highest relative density n ($n = N/N_L$, where $N_L = 2.7 \times 10^{19}$ cm^{-3} is the Loschmidt number) at which the discharge can occur is equal to $n \sim 15$.

Here, we assume that instabilities have no time to develop. The plasma stability is a separate complicated problem, which is beyond the scope of this study.

As the discharge area decreases, the excitation power increases due to an increase in the electron density. Note that, in [4], knifelike electrodes with a thickness of 6 mm and total length of 40 cm were used. To improve the discharge stability, the electrodes were rounded, so that the maximum discharge area in device [4] was at most 24 cm^2 (most likely, it was even smaller because the discharge was contracted toward the center of the discharge gap). The closest agreement of calculations [10] with experiment [4] was achieved for a discharge area of 4 cm^2. As the electron density increases, the quenching rate of excimer molecules by electrons and the dissociation rate of excimer molecules in upper vibrational states increase [10], thus decreasing the pumping rate of excimer molecules. In addition, the gas temperature increases with the pumping power, which also decreases the gain [10]. The existence of an optimal value of the discharge area S is illustrated in Fig. 5, which shows the maximum net gain coefficient of the active medium $g - \alpha$ and the absorption coefficient α as functions of the discharge area. For the relative gas density $n = 10$, the net gain is maximum for $S \approx 2$ cm^2, whereas for $n = 15$, the maximum of the dependence is displaced toward smaller areas ($S \approx 1$ cm^2), because the decrease in the net gain is primarily due to gas heating, which reduces the cross section for stimulated emission [10]. For $n = 15$ and $S \approx 1$ cm^2, the increase in the gas temperature attains $\Delta T \approx 270$ K. For $n = 10$ and $S \approx 2$ cm^2, the gas temperature increases by nearly the same value: $\Delta T \approx 240$ K. As the discharge area increases, the gas temperature increases approximately in inverse proportion to the discharge area. For a discharge area $S > 10$ cm^2 and $n = 10$–15, gas heating can

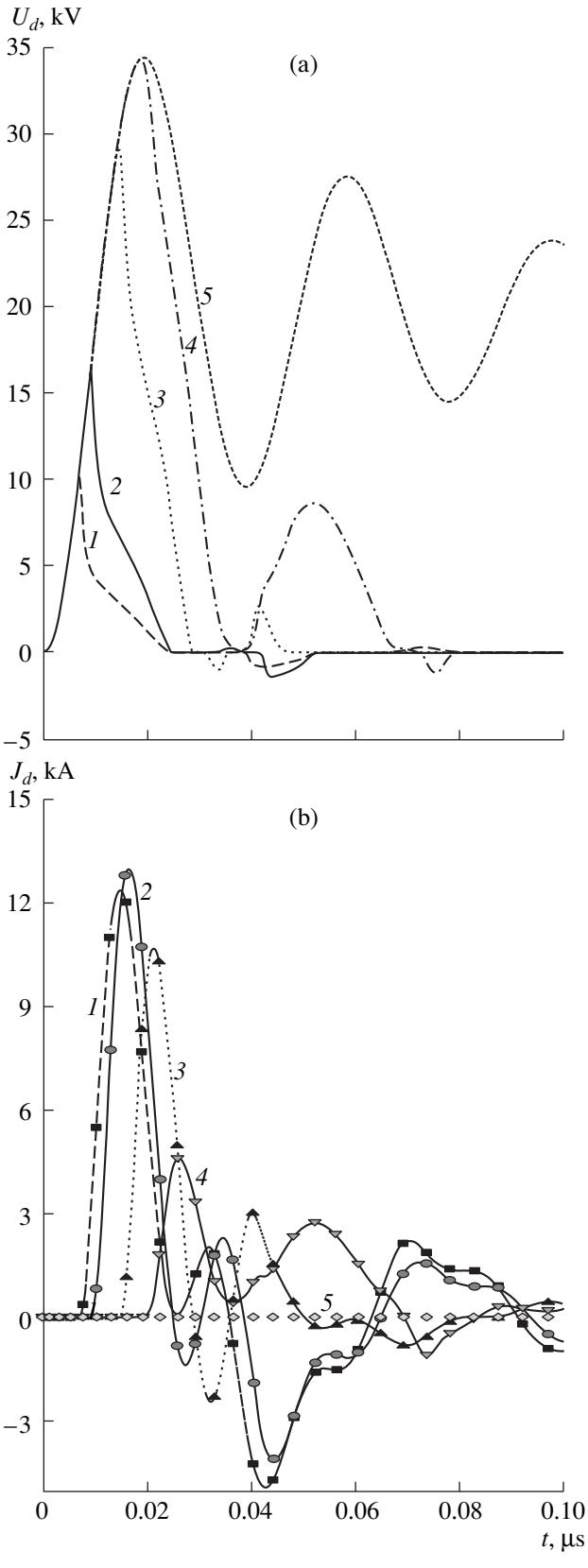

Fig. 4. Time dependence of (a) the discharge voltage U_d and (b) discharge current J_d for relative gas densities n = (*1*) 1.5, (*2*) 3.5, (*3*) 10, (*4*) 15, and (*5*) 20 atm and T_0 = 300 K.

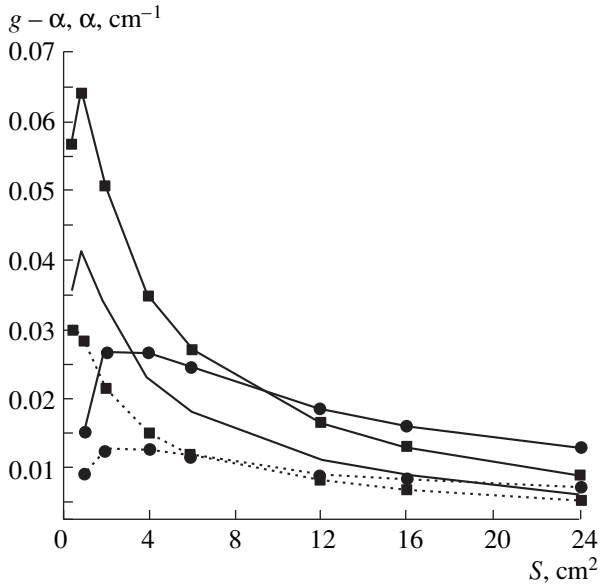

Fig. 5. Maximum net gain, $g - \alpha$ (solid lines), and the absorption coefficient α (dotted lines) vs. discharge area S for $n = 15$ and $T_0 = 300$ K (without symbols); $n = 15$ and $T_0 = 170$ K (squares); and $n = 10$ and $T_0 = 170$ K (circles).

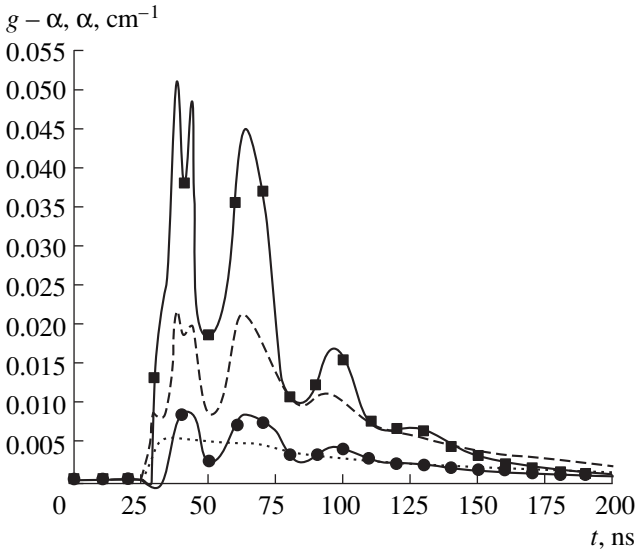

Fig. 6. Time dependences of the net gain, $g - \alpha$ (solid lines), and the absorption coefficient α (dashed-and-dotted lines) at $n = 15$ and $T_0 = 170$ K for a discharge area of $S = 2$ cm^2 (squares and dashed line) and 24 cm^2 (circles and dotted line).

be neglected. As is expected, the net gain coefficient is maximum for the relative gas density $n = 15$ and the low initial temperature $T_0 = 170$ K and can attain 0.065 cm^{-1}, which is one order of magnitude higher than the estimate of [4].

Because of the large difference between the breakdown voltage and the discharge voltage, it is impossible to match the impedances of the Blumlein line and the electric discharge at high excitation powers. For this reason, the current oscillations in the circuit result in oscillations in the time dependences of the net gain and the absorption coefficient α (Fig. 6). The smaller the discharge area, the sharper the spikes and the greater their number. The maximum net gain occurs at the first spike (at a time of ~40 ns). Note that, at this time, discharge instabilities probably have no time to develop.

The efficiency with which the energy is extracted from the active medium in a resonator is determined by the ratio of the small-signal gain coefficient to the absorption coefficient; the higher this ratio, the higher the resonator efficiency. Thus, for excimer lasers, the typical values of g/α are ≥ 10. In our case, i.e., for $n = 15$, $T_0 = 170$ K, and a discharge area of ~2 cm^2, this ratio is relatively low—about 3.4 (Fig. 7).

4. FLUORESCENCE EFFICIENCY

The intensity of the spontaneous emission of the Ar_2^* dimer is proportional to the Ar_2^* density and increases (along with the gain coefficient) as the pressure increases or the discharge area decreases (i.e., the electron density increases). Thus, as the discharge area varies from 24 to 1 cm^2, the intensity increases by almost one order of magnitude (Fig. 8). The difference between the time dependences of the net gain (Fig. 6) and the intensity of spontaneous emission (Fig. 8) is explained by the increase in the gas temperature with time, which results in the decrease in the net gain in the second and third spikes compared to the first one (Fig. 6).

The spontaneous emission energy (Fig. 9) and the conversion efficiency η_{in} of the discharge energy into radiation (Fig. 10) decrease as the discharge area decreases, because the quenching rate due to collisions with electrons increases and the excitation rate of dimers decreases due to dissociation of upper vibrational dimer states by electrons [10]. Figure 9 also shows the dependences of the energy deposited in the discharge on the discharge area. In this case, the energy stored in the Blumlein line ($C = C_1 = 4.25$ nF and $U_0 = 20$ kV) is equal to 1.7 J.

The total emission efficiency η (i.e., the conversion efficiency of the energy stored in capacitors into radiation) is determined by the efficiency η_c with which the energy is transferred from the electric circuit to the discharge and the internal conversion efficiency η_{in} of the discharge energy into radiation. In turn, the internal efficiency η_{in} can be represented as the product of the efficiency η_* of the production of Ar_2^* excited states and the conversion efficiency η_{sp} of the excited states

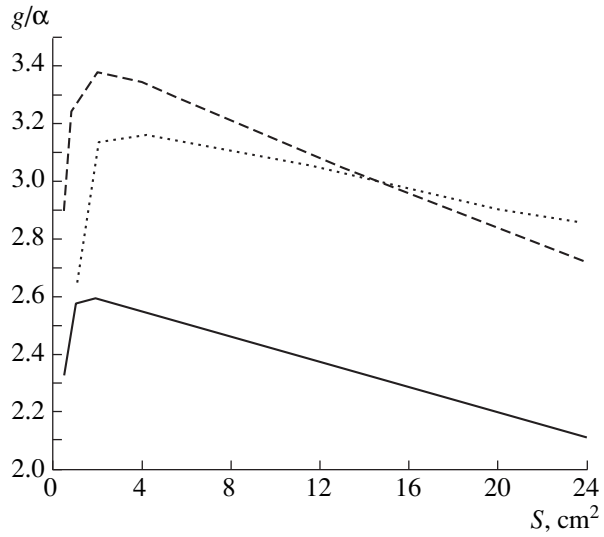

Fig. 7. Maximum ratio of the small-signal gain coefficient to the absorption coefficient g/α vs. discharge area S for n = 15 and T_0 = 300 K (solid line); n = 15 and T_0 = 170 K (dashed line); and n = 10 and T_0 = 170 K (dotted line).

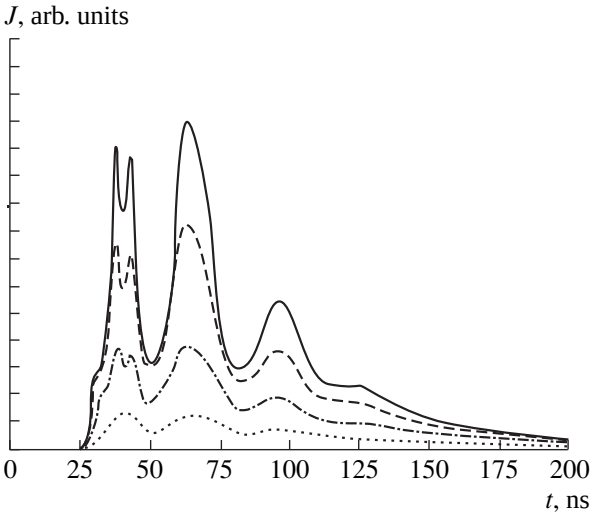

Fig. 8. Effect of the discharge area S on the time dependence of the spontaneous emission intensity for n = 15 and T_0 = 170 K: S = 1 (solid line), 2 (dashed line), 6 (dashed-and-dotted line), and 24 cm^2 (dotted line).

into the Ar_2^* excimer and its spontaneous emission:

$$\eta = \eta_c \eta_{in},$$

where $\eta_{in} = \eta_* \eta_{sp}$.

The lower the resistive losses in the circuit and the better the matching between the wave impedance of the circuit and the resistance of the discharge gap (here, we only consider the forming lines or circuits that contain inductances and are commonly used for exciting electric-discharge lasers), the higher the electric circuit efficiency η_c. Thus, for an ideal LC circuit (with zero resistance), matching is achieved when the circuit wave impedance is equal to the discharge resistance. In this case, the total energy stored in the capacitor is transferred to the discharge during the first half-period of current oscillations. In the absence of matching, the energy stored in the capacitor is also completely transferred to the discharge, but over a longer period of time (the discharge resistance is usually smaller than the circuit wave impedance), until oscillations in the electric circuit relax. Actual circuits always have nonzero resistance; hence, the improvement of matching reduces energy losses in an actual electric circuit. As is seen from Fig. 9, for n = 10–15 and S < 100 cm^2, only one-third of the stored energy is transferred to the discharge because of poor matching between the supply circuit and discharge and, accordingly, large losses in the resistances R_0, R_s, and R_m (Fig. 1). For lower gas densities, matching becomes even poorer, losses increase, and the fraction of the energy deposited in the discharge decreases. Thus, for n = 3.5 and 1.5, the deposited energy decreases to 1/6 and 1/10 of the energy stored in the line, respectively. This is due to the fact that, as the gas density decreases, the discharge voltage decreases, whereas the discharge current is controlled by the external circuit and increases only slightly. Poor matching at small discharge areas is a consequence of the large difference between the breakdown voltage, determined by direct ionization, and the discharge voltage, determined by stepwise ionization (Fig. 11a). Note that, for S = 10 cm^2, the electron density attains the value $n_e \sim 10^{16}$ cm^{-3} and, as is seen in Fig. 11a, the exci-

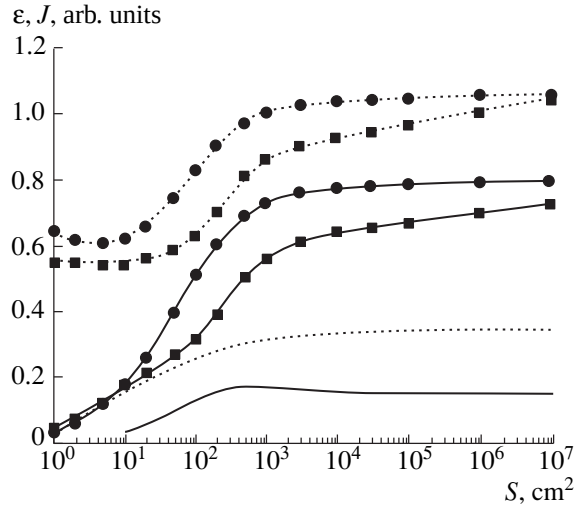

Fig. 9. Discharge energy (dashed line) and spontaneous emission intensity (solid lines) vs. discharge area S for n = 1.5 and T_0 = 300 K (without symbols); n = 10 and T_0 = 170 K (circles); and n = 15 and T_0 = 170 K (squares).

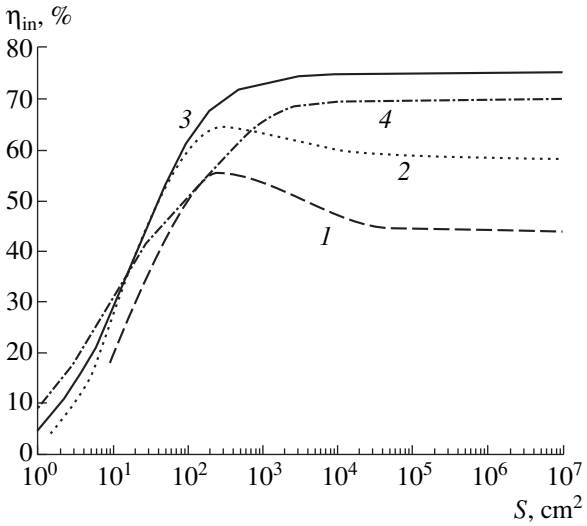

Fig. 10. Efficiency of spontaneous emission (relative to the energy deposited in the discharge) vs. discharge area S for n = (*1*) 1.5, (*2*) 3.5, (*3*) 10, and (*4*) 15.

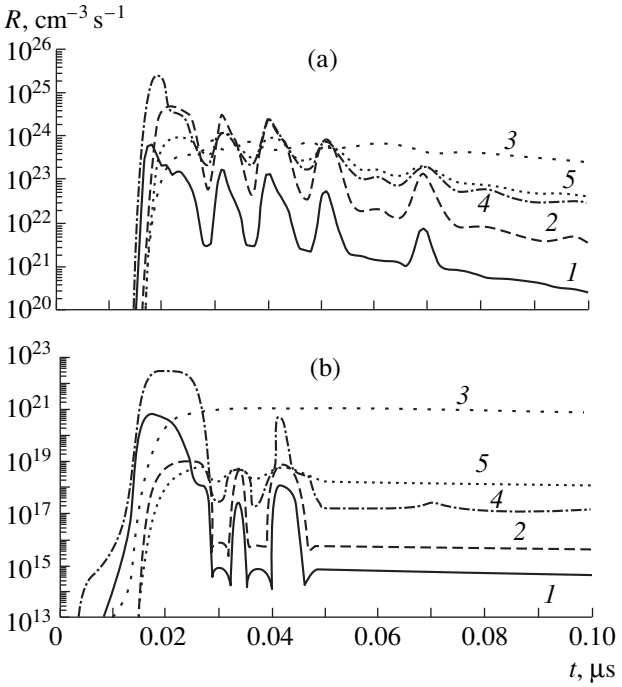

Fig. 11. Time dependences of the total rate R of (*1*) direct ionization, (*2*) stepwise ionization, (*3*) spontaneous emission, (*4*) electron-impact ionization, and (*5*) quenching due to collisions with electrons for Ar_2^* at discharge areas of S = (a) 10 and (b) 10^4 cm^2.

tation rate of Ar electronic states and the stepwise ionization rate are nearly equal to each other. As the discharge area increases ($S > 100$ cm^2), the stepwise ionization rate and the electron density decrease (thus, for $S = 10^4$ cm^2, the maximum value of n_e is $\sim 5 \times 10^{12}$ cm^{-3}) and, starting from $S > 10^3$ cm^2, direct ionization becomes dominant. For $S = 10^4$ cm^2, the direct ionization rate exceeds the stepwise ionization rate during the first spike (Fig. 11b). Only starting from nearly 25 ns, when the discharge voltage decreases, does the direct ionization rate become less than the stepwise ionization rate. The small rate of stepwise ionization is due to the fact that, in this case, the excited-particle density is determined by radiative losses and is insufficient for intense stepwise ionization. As is seen from Fig. 11b, the radiative loss rate for $S = 10^4$ cm^2 is two orders of magnitude higher than the stepwise ionization rate. The prevailing role of direct ionization leads to an increase in the discharge voltage (and also to better matching) and, consequently, to an increase in the energy deposited in the discharge up to ~1J for n = 10–15 and $S > 10^3$ cm^2 (Fig. 9). Calculations with zero resistances R_0, R_s, and R_m showed that, for $S = 10^4$ cm^2 and $n = 10$, the energy deposited in the discharge increases to 1.5 J during the first spike and, as early as at 250 ns, almost the entire energy stored in the capacitors C and C_1 is transferred to the discharge.

The internal conversion efficiency η_{in} of the discharge energy into spontaneous emission depends weakly on the gas temperature and increases as the discharge area increases, attaining ~75% at $n = 10$ and $S > 10^3$ cm^2 (Fig. 10). In this case, the discharge current density decreases to ~1.5 A/cm^2, so that it is necessary to test the numerical model at such low excitation powers (see above). As the gas density decreases, the efficiency η_{in} decreases (to ~ 55% at $n = 1.5$) primarily due to the decrease in the rate of dimer formation in three-body processes and also due to the increase in the relative role of quenching Ar_2^* dimers and their dissociation by electrons. As the relative density n increases above 10, η_{in} decreases insignificantly.

Such a high internal efficiency (higher than an efficiency of ~40–50%, characteristic of the excitation by a fast-electron beam [15, 16]) is ensured by high values of both the efficiencies η_* and η_{sp}. At low pumping powers and, accordingly, low electron densities, the quenching rate of Ar_2^* excimer molecules due to collisions with electrons (this is the main process of Ar_2^* loss) is negligibly small compared to the radiative loss rate (Fig. 11b); for this reason, η_{sp} is close to 100% and $\eta_{in} \approx \eta_*$. Most of the discharge energy is expended on the argon excitation. This is seen in Fig. 12, which shows the time dependences of the ratio between the total density of excited states (Ar*, Ar**, Ar_2^* ($^1\Sigma$), Ar_2^* ($^3\Sigma$), and Ar_2^{**}) and the electron density for $n = 10$. For $S = 10^4$ cm^2, this ratio reaches 40 in the second excitation spike, whereas for $S = 10$ and 100 cm^2, the maximum value of this ratio is reached even in the first spike and is equal to 26. The excitation efficiency of electronic states η_* at electron densities lower than the

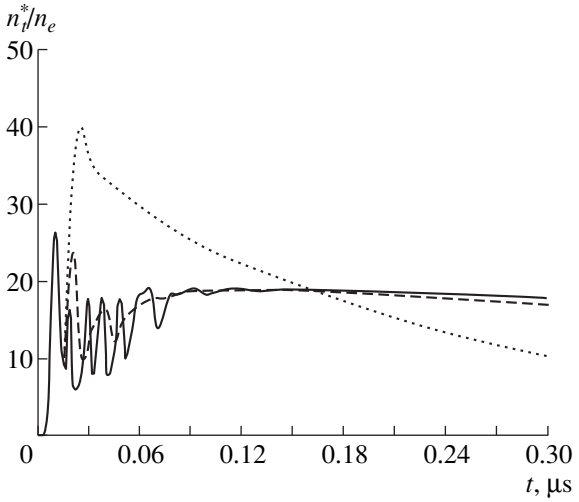

Fig. 12. Time dependences of the ratio of the total excited-particle density to the electron density for the gas density $n = 10$ and discharge areas of $S = 10$ (solid line), 100 (dashed line), and 10^4 cm^2 (dotted line).

excited-particle density tends to the value $h\nu(1 - \eta_{el})/\varepsilon^* \approx 87\%$, where $h\nu = 10.9$ eV is the emission photon energy, $\varepsilon^* = 11.6$ eV is the excitation energy of the lower excited state of Ar*, and $\eta_{el} \approx 6\%$ is the fraction of discharge energy lost due to elastic processes. A smaller value of the calculation efficiency η_{in} (~75%) can be explained by the fact that a certain fraction of discharge energy is expended on the excitation of Ar** states and ionization; another reason is that losses due to elastic collisions are underestimated because of the discharge voltage oscillations. To estimate η_*, we used the value of η_{el} at the maximum of the discharge power.

5. CONCLUSION

We have shown that, under the conditions of experiment [4], it is possible to achieve a net gain coefficient of the active medium equal to $g - \alpha \approx 0.065$ cm^{-1} by increasing the relative gas density n to 15 at an initial gas temperature of 170 K, or 0.04 cm^{-1} at room temperature. In addition, it is necessary to reduce the discharge area to 1 cm^2 and, accordingly, increase the excitation power to 40 MW/cm^3 at normal conditions. In such regimes, the Blumlein line cannot ensure the optimum pumping of the active medium. At best (at relative densities of $n \approx 10$–15), only one-third of the energy stored in the line is transferred to the discharge. For better matching between the electric circuit and the discharge gap, it is necessary to use supply circuits that ensure both the high breakdown voltage and the optimum discharge voltage (e.g., double-pulse excitation circuits).

The internal conversion efficiency of the discharge energy into spontaneous emission depends weakly on the gas temperature and increases as the discharge power decreases, attaining ~75% at $n = 10$ and an excitation power of <700 kW/cm^3. Under these conditions, the discharge voltage is close to the breakdown voltage; consequently, simple electric circuits (e.g., a single-contour LC circuit) can be used to efficiently excite the discharge.

ACKNOWLEDGMENTS

We thank A.P. Napartovich for fruitful discussions of the results obtained. This work was supported in part by the Russian Foundation for Basic Research, project no. 99-02-16545.

REFERENCES

1. W. M. Hughes, J. Shannon, and R. Hunter, Appl. Phys. Lett. **24**, 488 (1974).
2. W. G. Wrobel, H. Rohr, and K. H. Steyer, Appl. Phys. Lett. **36**, 113 (1980).
3. T. Sakurai, N. Goto, C. E. Webb, *et al.*, J. Phys. D **20**, 709 (1987).
4. H. Ninomiya and K. Nakamura, Opt. Commun. **134**, 521 (1997).
5. S. Neeser, T. Kunz, and H. Langhoff, J. Phys. D **30**, 1489 (1997).
6. S. Neeser, M. Schumann, and H. Langhoff, Appl. Phys. B: Lasers Opt. **B63**, 103 (1996).
7. E. Elson and M. Rokni, J. Phys. D **29**, 716 (1996).
8. K. S. Gochelashvily, A. V. Dem'yanov, I. V. Kochetov, *et al.*, Opt. Commun. **91**, 66 (1992).
9. I. V. Kochetov and D. Lo, Opt. Commun. **113**, 54 (1995).
10. S. K. Lam, C.-E. Zheng, D. Lo, *et al.*, J. Phys. D **33**, 242 (2000).
11. P. Dube, M. J. Kiik, and B. P. Stoicheff, J. Chem. Phys. **103**, 7708 (1995).
12. A. Kvaran, M. J. Shaw, and J. P. Simons, Appl. Phys. B: Photophys. Laser Chem. **B46**, 95 (1988).
13. V. A. Adamovich, A. V. Dem'yanov, I. V. Kochetov, *et al.*, Kvantovaya Élektron. (Moscow) **17**, 1395 (1990).
14. J. W. Shon, M. J. Kushner, G. A. Hebner, *et al.*, J. Appl. Phys. **73**, 2686 (1993).
15. D. J. Eckstrom, H. H. Nakano, D. C. Lorents, *et al.*, J. Appl. Phys. **64**, 1679 (1988).
16. D. J. Eckstrom, H. H. Nakano, D. C. Lorents, *et al.*, J. Appl. Phys. **64**, 1691 (1988).

Translated by N.F. Larionova

Plasma Physics Reports, Vol. 27, No. 5, 2001, pp. 448–450. Translated from Fizika Plazmy, Vol. 27, No. 5, 2001, pp. 475–477.

BRIEF COMMUNICATIONS

Threshold Energy Density of Lower Hybrid Waves in the Freja Experiment

S. I. Popel

Institute of Geosphere Dynamics, Leninskiĭ pr. 38-6, Moscow, 117979 Russia

Received October 17, 2000

Abstract—Data from the Freja satellite experiment on the lower hybrid turbulence in the Earth's magnetosphere are analyzed. It is shown that the observed threshold energy density of lower hybrid waves required for the excitation of localized wave packets is in good agreement with theoretical predictions. © *2001 MAIK "Nauka/Interperiodica".*

Observations from the instrumented Freja satellite indicated the existence of localized wave packets in the lower hybrid (LH) frequency range in the Earth's magnetosphere [1–5]. In this paper, we consider the origin of these localized wave packets. The excitation of LH turbulence in the magnetospheric plasma is characterized by a certain threshold value of the LH wave energy density. We compare the threshold LH wave energy density predicted by the theory of the modulational interaction of broad wave spectra [6] with that obtained from observations [4].

The Freja project is a joint Swedish–German research project. Its purpose is to investigate the interaction between the hot magnetospheric plasma and the upper atmosphere (ionosphere). This interaction results in a significant increase in the energy of magnetospheric and ionospheric plasmas and is associated with loss of substance from the Earth's atmosphere. The Freja satellite was launched on October 6, 1992, into a 63°-inclination orbit with a 1760-km apogee over the Northern Hemisphere and a 600-km perigee over the Southern Hemisphere. The most outstanding feature of this mission was the high resolution of the plasma and field (both electric and magnetic) measurements and a high telemetry rate (up to 512 kbits/s) [7, 8].

The high resolution and high telemetry rate ensured the observation of electrostatic fields in the LH frequency range. The measurements were carried out at altitudes of about 1760 km. Purely electrostatic wave fields were observed (no perturbations of the magnetic field were detected). The characteristic feature of these fields was the presence of density cavities in the regions where the field was localized (Fig. 1) [1–5]. The characteristic frequency range of LH waves was [4] $\omega \approx 2\pi(3.5\text{–}4.5) \times 10^3\ \mathrm{s}^{-1}$. The characteristic LH resonance frequency was $\omega_{\mathrm{LH}} \equiv \omega_{pi}(1 + \omega_{pe}^2/\omega_{Be}^2)^{-1/2} \sim 2\pi \times 10^3\ \mathrm{s}^{-1}$ [3], where $\omega_{pe(i)}$ is the electron (ion) plasma frequency and ω_{Be} is the electron gyrofrequency. We note that the above value of ω_{LH} is only an estimate. The measured values of the plasma parameters were the following [3]: the unperturbed electron density was $n_0 \approx 1.1 \times 10^3\ \mathrm{cm}^{-3}$, the electron plasma frequency was $\omega_{pe} \approx 1.87 \times 10^6\ \mathrm{s}^{-1}$, and the proton gyrofrequency was $\omega_{Bp} \approx 2\pi \times 400\ \mathrm{s}^{-1}$. The latter corresponds to an external magnetic field of $|\mathbf{B}_0| \approx 0.263$ G. The most abundant ions in the region of the magnetosphere where the measurements were performed were O^+, He^+, and H^+.

An important result of the instrumented Freja satellite experiment was that it proved the existence of a threshold for the excitation of localized LH oscillations. The dependence of the energy density of LH oscillations on the magnitudes of relative perturbations of the plasma density in the regions where the oscillations were localized was investigated (Fig. 2) [4]. It was shown that the relative perturbations of the plasma density correlated with the energy density of LH oscillations. The threshold energy density was defined as the energy density at which the density perturbations vanish. The threshold for the excitation of wave packets corresponds to the energy density of LH oscillations, which is on the order of $W^{\mathrm{LH}} \sim 10^{-14}\ \mathrm{J/m}^3$.

Localized LH oscillations observed in the Freja experiment were associated [3–5] with the envelope LH solitons that can be formed due to the modulational interaction between LH waves (see, e.g., [9, 10]). Thus, it is of interest to calculate the threshold energy density for the modulational instability under the conditions of the Freja experiment and to compare it with the observed value. Let us compare the threshold LH wave energy density obtained from the instrumented Freja satellite with the theoretical value, which can be found from the following condition [6]:

$$\left[\int \frac{d\mathbf{k} W_{\mathbf{k}}^{\mathrm{LH}}}{n_0 T_e} \frac{\omega_{pe}^2}{|\mathbf{k}|^2 v_{Te}^2}\right]_{\mathrm{th}} \approx \frac{m_e}{m_i}\left(\frac{\omega_{Be}}{\omega_{pe}}\right)^2 \left(1 + \frac{\omega_{pe}^2}{\omega_{Be}^2}\right)^2, \qquad (1)$$

1063-780X/01/2705-0448$21.00

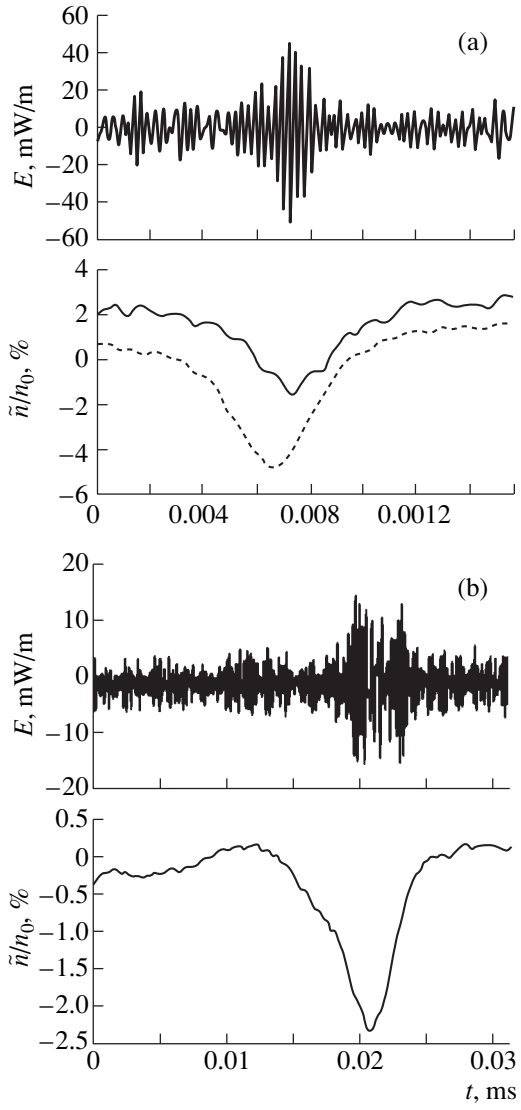

Fig. 1. Two examples of localized LH wave packets in the Earth's magnetosphere (data from the Freja satellite [4]). The LH wave electric fields are shown in the upper panels. The signal has a bandwidth of 0–16 kHz. The lower panels show the low-frequency relative plasma density perturbations. Solid and dashed curves refer to the signals from two Langmuir probes with which the plasma density was measured. The correlation between the regions where the wave field is localized and the plasma density cavities is clearly seen.

where T_e is the electron temperature, $\mathbf{k}$ is the wave vector, $W^{\mathrm{LH}} = \int W_{\mathbf{k}}^{\mathrm{LH}} d\mathbf{k}$, $v_{Te} = (T_e/m_e)^{1/2}$ is the electron thermal velocity, and $m_{e(i)}$ is the electron (ion) mass. Condition (1) is obtained for LH waves propagating under the angles θ with respect to the external magnetic field such that the inequalities

$$\left(\frac{m_e}{m_i}\right)^{1/2} \le |\cos\theta| \ll 1 \qquad (2)$$

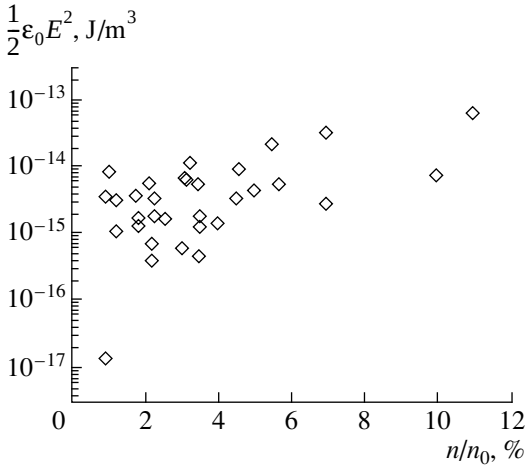

Fig. 2. The dependence [4] of the LH wave energy density on the ratio of the plasma density perturbation to the unperturbed plasma density.

are satisfied. In this case, the linear dispersion relation for LH waves is

$$\omega_{\mathbf{k}} \approx \omega_{\mathrm{LH}}\left(1 + \frac{m_i}{m_e}\cos^2\theta\right)^{1/2}. \qquad (3)$$

When deriving Eq. (1), it is also assumed [6] that (i) the inequality $|\delta\mathbf{k}|v_s < \delta\omega$ is satisfied (here, $\delta\mathbf{k}$ is the spectral width in $\mathbf{k}$ space, $\delta\omega$ is the spectral width in frequency space, and $v_s = (T_e/m_i)^{1/2}$ is the ion acoustic velocity) and (ii) the spectrum occupies the entire region in $\mathbf{k}$ space where LH waves can exist; i.e., $(2–3)|k_\parallel|v_{Te} \le \omega_{\mathbf{k}}$, where the subscript $\parallel$ denotes the vector component parallel to the external magnetic field (for $(2–3)|k_\parallel|v_{Te} \ge \omega_{\mathbf{k}}$, waves rapidly decay due to Landau damping). It is these spectra for which the threshold for the LH wave modulational interaction exists [6].

The parameters of the plasma and waves to which Eq. (1) applies correspond to the conditions of the Freja experiment. Indeed, the broad frequency range of LH waves ($\delta\omega \sim \omega_{\mathrm{LH}} \sim \omega_{\mathrm{ch}}$, where ω_{ch} is the characteristic frequency of the spectrum) indicates that the waves satisfying dispersion relation (3), which corresponds to the situation $(m_e/m_i)^{1/2} \le |\cos\theta| \ll 1$, play an important role. Furthermore, an LH soliton contains harmonics with all the possible $\mathbf{k}$ for which LH waves can exist ($(2–3)|k_\parallel|v_{Te} \le \omega_{\mathrm{ch}}$). This means that the LH wave spectrum can be considered broad; thus, it is meaningful to use the concept of the modulational instability threshold. In addition, the following inequalities are satisfied:

$$|\delta\mathbf{k}|v_s \approx |\delta k_\parallel| v_{Te}(m_e/m_i)^{1/2}/|\cos\theta|$$

$$\sim |k_\parallel| v_{Te}(m_e/m_i)^{1/2}/|\cos\theta| < \omega_{\mathrm{ch}} \sim \delta\omega.$$

When calculating the theoretical threshold energy density of LH waves from Eq. (1), it is natural to assume that the characteristic value of (1 +

$\omega_{pe}^2/\omega_{Be}^2)^{-1}\omega_{pe}^2/|\mathbf{k}|^2 v_{Te}^2 \approx \omega_{ch}^2/k_\parallel^2 v_{Te}^2$ is on the order of ten. Indeed, if the LH wave energy density tends to zero and the broad LH wave spectrum includes all possible **k** (for which LH waves can exist), then the only characteristic wave vector of the problem under study is that satisfying the condition $(2–3)|k_\parallel|v_{Te} \approx \omega_{ch}$. Using the characteristic value of the electron temperature of the magnetospheric plasma at an altitude of about 1760 km (T_e = 0.3–1 eV [11]), we obtain from Eq. (1) that $W^{LH} \sim 2.1 \times 10^{-13}$ erg/cm^3 (here, for definiteness, we assume that T_e = 0.3 eV and that the most abundant ions are H^+ ions). For T_e = 0.3 eV and O^+ ions, we obtain $W^{LH} \sim 1.3 \times 10^{-14}$ erg/cm^3.

Thus, the theoretical values of the threshold LH wave energy density obtained from Eq. (1) agree well with the results of the Freja experiment. This also allows us to conclude that the formation of localized wave structures in the Earth's magnetosphere is indeed associated with the development of modulational processes.

ACKNOWLEDGMENTS

I thank H.L. Pécseli for providing the data from the Freja experiment and helpful discussions.

REFERENCES

1. P.-O. Dovner, A. I. Eriksson, R. Boström, and B. Holback, Geophys. Res. Lett. **21**, 1827 (1994).
2. A. I. Eriksson, B. Holback, P.-O. Dovner, *et al.*, Geophys. Res. Lett. **21**, 1843 (1994).
3. R. Lundin, L. Eliasson, O. Norberg, *et al.*, in *Solar System Plasmas in Space and Time*, Ed. by J. Bruch and J. H. Waite, Jr. (American Geophysical Union, Washington, 1994) [Geophys. Monograph **84**, 247 (1994)].
4. H. L. Pécseli, B. Lybekk, J. Trulsen, and A. Eriksson, Plasma Phys. Controlled Fusion **39** (5A), A227 (1997).
5. S. H. Kjus, H. L. Pécseli, B. Lybekk, *et al.*, J. Geophys. Res. **103**, 26633 (1998).
6. S. I. Popel, Fiz. Plazmy **24**, 1093 (1998) [Plasma Phys. Rep. **24**, 1022 (1998)].
7. R. Lundin, G. Haerendel, and S. Grahn, Geophys. Res. Lett. **21**, 1823 (1994).
8. G. T. Marklund, Plasma Phys. Controlled Fusion **39** (5A), A195 (1997).
9. A. A. Veryaev and V. N. Tsytovich, Izv. Vyssh. Uchebn. Zaved., Radiofiz. **22**, 398 (1979).
10. S. V. Vladimirov, V. N. Tsytovich, S. I. Popel, and F. Kh. Khakimov, *Modulational Interactions in Plasmas* (Kluwer, Dordrecht, 1995).
11. L. Lyons and D. Williams, *Quantitative Aspects of Magnitospheric Physics* (Reidel, Dordrecht, 1984; Mir, Moscow, 1987).

Translated by the author

Plasma Physics Reports, Vol. 27, No. 5, 2001, p. 451. Translated from Fizika Plazmy, Vol. 27, No. 5, 2001, p. 478.

Ksenia Aleksandrovna Razumova (In Honor of Her 70th Birthday)

On January 23, we celebrated the 70th birthday of Ksenia Aleksandrovna Razumova, a doctor of sciences and laboratory head at the Institute of Nuclear Fusion, Russian Research Centre Kurchatov Institute. Her scientific activity is related to experimental research in the field of high-temperature plasma physics. She took part in the pioneering works on the magnetic confinement of a plasma in toroidal systems. In 1962, K.A. Razumova and her colleagues were the first to observe the disruption instability in a tokamak.

Experiments carried out by K.A. Razumova in the TM-2 tokamak, along with the results of experiments in the T-3 and T-4 tokamaks, convinced the scientific community that the pessimistic forecasts concerning the prospects of magnetic confinement that follow from the Bohm formula are unfounded. In 1971, K.A. Razumova, together with her colleagues, was awarded a State Prize for creating and investigating high-temperature thermonuclear plasmas in tokamaks. The investigations carried out by K.A. Razumova led to the tokamak becoming the leader of nuclear fusion research in the world.

During the past twenty years, her scientific interests have been related to investigations of the interaction of electron-cyclotron waves with a tokamak plasma. In 1983, for the second time, K.A. Razumova, together with her colleagues from Nizhni Novgorod, was awarded a State Prize for their cycle of investigations on creating powerful gyrotrons and applying them to plasma heating in nuclear fusion devices. In 1992, for her investigations on EC heating and EC current drive, she was awarded the Academician Artsimovich Prize, which was given for the first time by the Presidium of the Russian Academy of Sciences. During the entire 25-year cycle of experiments in the T-10 tokamak, she has participated in all of the experimental programs and headed many of them.

Time has no power over Ksenia Aleksandrovna. She is as active now as she was in her younger years is as engaged in her work as before, and is always eager to discuss new ideas and experiments. Until recently, every summer, she went on rowing tours. She has two children and, during her vacations, looks after her three grandchildren at her country house, 450 km from Moscow.

The friends and colleagues of Ksenia Aleksandrovna heartily congratulate her and wish her many more years of fruitful scientific activity.

E.P. Velikhov, V.P. Smirnov, V.A. Alikaev, Yu.N. Dnestrovskij, G.E. Notkin, A.M. Stefanovskiĭ, V.S. Strelkov, and V.D. Shafranov

1063-780X/01/2705-0451$21.00 © 2001 MAIK “Nauka/Interperiodica”

Plasma Physics Reports, Vol. 27, No. 5, 2001, pp. 452–453. Translated from Fizika Plazmy, Vol. 27, No. 5, 2001, pp. 479–480.

Viktor Pavlovich Silin (In Honor of His 75th Birthday)

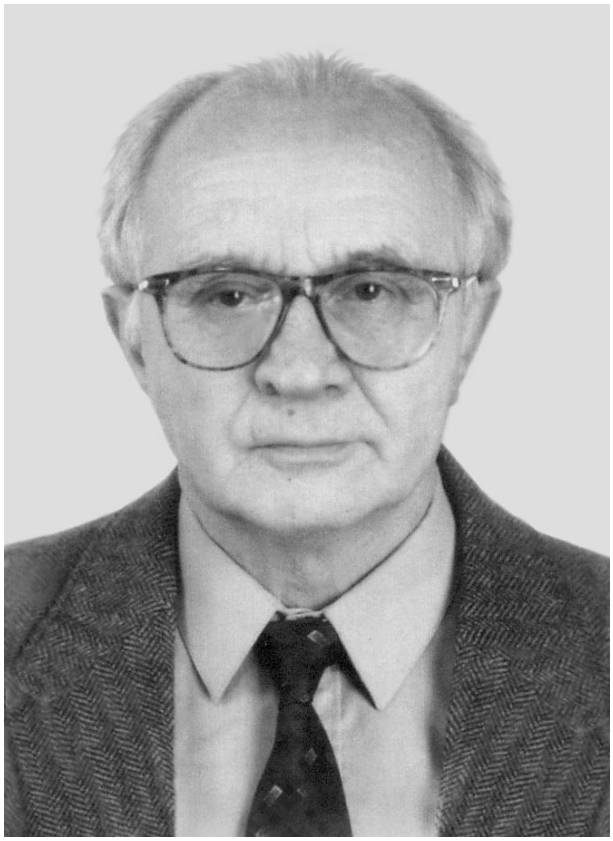

On May 26, we celebrate the 75th birthday of Viktor Pavlovich Silin, a world-famous theoretical physicist, a sector head at the Lebedev Institute of Physics of the Russian Academy of Sciences, and a corresponding member of the Russian Academy of Sciences.

His entire professional life has been linked with the Lebedev Institute of Physics, where he began to work after graduating in 1949 from Moscow State University and where he progressed from a junior researcher to head of the Division of Solid-State Physics (1989–1995). Over this period, he published more than 600 papers in different fields of physics and four monographs, which are well known among plasma physicists.

During the first ten years, when working in the Theoretical Department at the Lebedev Institute of Physics, V.P. Silin was occupied with the quantum field theory and the theory of elementary particles. Among his studies in this field, it is necessary to mention his works on the development of the Tamm–Dankov method; these works provided a better understanding of the nature of nuclear interactions. At that time, V.P. Silin began to work on the theory of many particles and obtained a number of important results on the theory of Fermi gas of weakly interacting charged particles; these results laid the foundations of the Fermi fluid theory. His studies in this field led to the development of two lines of investigations—the theory of normal metals and the physics of a gaseous plasma.

Silin's works on the physics of metals were further developed by his numerous followers. This concerns not only his works on the theory of a normal-metal electron fluid, but also the theory of sound absorption in metals, the quantum theory of transport in a magnetic field, the theory of quantum electron spin-acoustic waves, and the theory of electron fluids of magnetically ordered metals. At present, he is actively working on the theory of Josephson junctions.

In the field of gaseous plasma physics, it is worth noting, first of all, his works on the collision integrals of charged particles in high-frequency and strong fields. In the 1960s, the kinetic theory of various transport effects in plasmas was developed based on these studies. His works on the theory of relativistic plasma, the theory of fluctuations of microscopic distributions, the theory of transport caused by ion-acoustic waves, the kinetic theory of drift-dissipative instabilities, and the kinetic theory of plasma wave interaction are also widely recognized.

Silin's paper on the parametric resonance in plasma, which was published in 1965, received much attention and provided a basis for many subsequent investigations. Since that time, his scientific interests have been concentrated on the development of the theory of parametric instabilities and parametric turbulence and applying this theory to the problem of the interaction of strong laser radiation with plasma. Among the works on the theory of laser plasmas, it is worth noting his investigations on the generation of laser radiation harmonics, which he has continued since the 1960s.

A series of his works on nonlinear electrodynamics (a theory of self-consistent nonlinear waveguides and a dynamical theory of the action of strong radiation on a moving plasma) is devoted to the theory of penetration of a strong electromagnetic field into a plasma. Many of the results of these studies have been verified experimentally.

1063-780X/01/2705-0452$21.00 © 2001 MAIK "Nauka/Interperiodica"

V.P. Silin was twice awarded the USSR State Prize: in 1970, for the cycle of works on the Fermi fluid theory and, in 1987, for the works on the nonlinear plasma theory. For his scientific activity, V.P. Silin was awarded two Orders of the Red Banner of Labor. He was conferred the title of an Honored Scientist of the Russian Federation. V.P. Silin is a member of the editorial boards of several scientific journals. He is a member of a number of scientific councils and a member of the Scientific Council on Plasma Physics of the Russian Academy of Sciences.

Along with intensive scientific activity, V.P. Silin devotes much time to the education of young scientists. For many years, he has been engaged in pedagogical work. He is a professor at the Moscow Engineering Physics Institute (Technical University). As a consultant to UNESCO, he gave lectures on plasma theory at Delhi University (India).

V.P. Silin is a founder and leader of a powerful scientific school. Among his pupils are more than 30 candidates of science and ten doctors of science. For many years, he has guided a seminar on plasma and solid-state physics, whose meetings sometimes transform into heated, long, and temperamental discussions.

Being a socially active man, V.P. Silin has long worked in various social organizations and has held administrative positions in science. However, his persistent interest in physics and his passion for knowledge has not let him turn aside from actual science. Now, as in youth, he works with enthusiasm and publishes about ten papers every year. He is surrounded by students and young scientists, as well as by his older, established pupils. V.P. Silin shows a particular concern for young scientists, tries to support them, and passes on to them his deep interest and devotion to science, which has had a very difficult time over the last decade in Russia.

Viktor Pavlovich greets his 75th birthday full of ideas and plans. His friends and colleagues wish him robust health and fulfillment of all of his creative intentions.

Yu.M. Aliev, N.E. Andreev, L.M. Anosova, G.M. Batanov, K.Yu. Vagin, L.M. Gorbunov, S.E. Grebenshchikov, A.V. Gurevich, A.M. Ignatov, A.I. Isakov, L.M. Kovrizhnykh, A.S. Malishevskiĭ, R.R. Ramazashvili, A.Yu. Romanov, A.A. Rukhadze, P.S. Strelkov, S.A. Uryupin, and A.A. Frolov